Regularized Estimation of Main and RF Field Inhomogeneity and Longitudinal Relaxation Rate in Magnetic Resonance Imaging

by

Amanda K. Funai

A dissertation submitted in partial fulfillment
of the requirements for the degree of
Doctor of Philosophy
(Electrical Engineering: Systems)
in The University of Michigan
2011

Doctoral Committee:

Professor Jeffrey A. Fessler, Chair
Professor Thomas L. Chenevert
Professor Douglas C. Noll
Associate Professor Anna C. Gilbert
Assistant Professor Clayton D. Scott

To my husband, Katsu, and my two sons, Andrew and Seth

ACKNOWLEDGEMENTS

I would like to acknowledge the following people who have been instrumental in me finishing this dissertation. First, my committee. Most especially, my advisor Jeff for his invaluable advice and encouragement. Also, especially Doug for his indispensible knowledge of MRI. I would also like to thank all the members of Jeff and Doug's lab groups - their comments and support throughout graduate school have been invaluable. I would like to especially thank those who collected MRI data for me, Will Grissom and Jon Nielsen. A thank you to all support staff at Rackham and EECS, especially Becky Turanski and her support and encouragement. A very hearty thanks to all my sources of funding, including Rackham, EECS, NSF, and NIH. And most of all, thanks to my family and friends, most especially my husband and his unwavering support through these busy and stressful years of graduate school.

TABLE OF CONTENTS

CHAPTER

LIST OF FIGURES

Figure

LIST OF TABLES

Table

LIST OF APPENDICES

Appendix

ABSTRACT

Regularized Estimation of Main and RF Field Inhomogeneity and Longitudinal Relaxation Rate in Magnetic Resonance Imaging

by

Amanda K. Funai

Chair: Jeffrey A. Fessler

In designing pulses and algorithms for magnetic resonance imaging, several simplifications to the Bloch equation are used. However, as magnetic resonance (MR) imaging requires higher temporal resolution and faster pulses are used, simplifications such as uniform main field (B_0) strength and uniform radio-frequency (RF) transmit coil field (B_1^+) strength no longer apply. Ignoring these non-uniformities can cause significant distortions. Accurate maps of the main and RF transmit coil field inhomogeneity are required for accurate pulse design and imaging. Standard estimation methods yield noisy maps, particularly in image regions having low spin density, and ignore other important factors, such as slice selection effects in B_1 mapping and T_2 effects in B_0 mapping. This thesis uses more accurate signal models for the MR scans to derive iterative regularized estimators that show improvements over the conventional unregularized methods through Cramér-Rao Bound analysis, simulations, and real MR data.

In fast MR imaging with long readout times, field inhomogeneity causes image distortion and blurring. This thesis first describes regularized methods for estimation of the off-resonance frequency at each voxel from two or more MR scans having different echo

times, using algorithms that decrease monotonically a regularized least-squares cost function.

A second challenge is that RF transmit coils produce non-uniform field strengths, so an excitation pulse will produce tip angles that vary substantially over the field of view. This thesis secondly describes a regularized method for B_1^+ map estimation for each coil and for two or more tip angles. Using these scans and known slice profile, the iterative algorithm estimates both the magnitude and phase of each coil's B_1^+ map.

To circumvent the challenge in conventional B_1^+ mapping sequences of an long repetition time, this thesis thirdly describes a regularized method for joint B_1^+ and T_1 map estimation using a regularized method based on a penalized-likelihood cost function using the steady-state incoherent (SSI) imaging sequence with several scans with varying tip angles or repetition times.

CHAPTER I

Introduction

Magnetic resonance imaging (MRI) is a very important and powerful imaging modality, being both safe and non-invasive, while still sensitive to a large variety of tissue properties. Careful manipulation of magnetic fields allows for imaging of an object's interior and its structure, metabolism, and function. MR uses three main magnetic fields, the main field (B_0), a radio-frequency field (B_1), and gradient fields. The final measured MR signal depends greatly on the applied magnetic fields magnitude and phase. Estimation of these fields using statistical signal processing techniques is essential to create the most accurate images possible.

A governing assumption throughout magnetic resonance (MR) is perfectly homogeneous main and radio-frequency fields (B_0 and B_1). However, homogeneous fields are not feasible in the real world. For example, inhomogeneity in the main field arises both from the physical design of the magnet (although this can be improved with shimming) and also from differences in bulk magnetic susceptibility, especially on the boundary of air and tissues, as in the sinuses. This is especially problematic at higher B_0 field strengths. Similarly, B_1 (radio-frequency or RF) inhomogeneity arises from increasing distance from transmit coils, use of surface coils, and interaction of a subject with the RF wavelength. Homogeneity of either the main field or RF field can not be assured due to the physical properties of MR.

Homogeneity assumptions were generally appropriate under low B_0 field strengths and short read out times. However, demand for faster, higher resolution scans and methods such as functional magnetic resonance imaging (fMRI) require fast methods and higher B_0 field strengths. As fast imaging techniques such as echo-planar imaging (EPI) and spiral scans gain popularity, image artifacts from B_0 field inhomogeneity are visible. These artifacts cause signal loss and result in shifts or blurring in the final MR images, making qualitative and quantitative analysis difficult. These effects are exacerbated in high B_0 fields. Similarly, as MR main fields grow in strength, image artifacts from B_1 field inhomogeneity are visible. At higher field strengths, the RF wavelength is shortened, and experiences further shortening due to changes in the tissue dielectric constant, resulting in higher inhomogeneity at higher main field strengths. The nonuniform effect in each voxel gives a possibly different tip angle in each voxel. This gives spatially varying signal and intensity in the image, making both qualitative and quantitative analysis difficult. Therefore, the speed and field strength requirements of state-of-the-art MR technology further exacerbate the problems of inhomogeneity.

Correcting for these artifacts is possible using the appropriate field map. Given a smooth field map of B_0 inhomogeneity, conjugate phase methods can compensate for phase accrual at each voxel, tailored RF pulses can compensate for signal loss, or iterative reconstruction methods can be used to obtain corrected final MR images under the condition of an inhomogeneous B_0 field. Similarly, given a map of B_1 inhomogeneity, tailored RF pulses, parallel transmit excitation, and dynamic adjustment of RF power can compensate for B_1 inhomogeneity. Highly accurate and reliable field map estimators are required in these intensive imaging environments.

Previous estimators have often been based on heuristic algorithms rather than on a statistical estimation theory. These estimators are often limited in scope, dependent on a strict measurement scheme, specific imaging parameters, or ignore complicating physical effects. Additionally, these estimators often satisfy the requirement for smooth field maps through low pass filtering and smoothing of calculated field maps. New statistically based estimators that are based on more comprehensive models are needed. Estimators are needed that incorporate the knowledge that true field maps are smooth with an understanding of the effect of smoothing on image spatial resolution. This thesis presents three separate estimators that satisfy these desired estimator properties.

Chapter II first presents a short introduction to MRI. Section 2.4 follows with a brief discussion of the effects on field inhomogeneity - the motivation for new statistical estimators. Chapter III overviews some principles of iterative penalized estimator design, which are used as the solution in this report. Chapter IV tackles the problem of main field map estimation, considering both current solution and proposing the new solution as well as demonstrating its effectiveness. Chapter V similarly looks at B_1 map estimators, considering current solutions and proposing a new iterative estimator and demonstrating its effectiveness. Chapter VI, noting the interdependence of B_1 and the longitudinal relaxation time T_1, considers current solutions to T_1 mapping and joint B_1, T_1 mapping and their limitations and proposes a new joint estimator for T_1 and B_1 which incorporates slice profile effects and Bloch non-linearity. Finally, Chapter VII concludes, summarizing the proposed solutions in this work and giving future work in the goal of estimating parameter maps in MRI.

1.1 Contribution of Thesis

This thesis proposes three new penalized-likelihood (PL) estimators based on comprehensive statistical models with regularization.

First, the field map PL estimator uses two or more scans to estimate field maps that interpolate smoothly in voxels with low spin density and includes a simple weighting scheme to partially account for R_2^* decay. A Cramer Rao Bound analysis aids in selection of echo times. This estimate improves the conventional field map estimates, shown both in simulation studies, as well as with real MR phantom data. The resulting improved reconstructed images dramatically affects the final image quality.

Second, the B_1^+ PL estimator uses multiple scans and an arbitrary selection of tip angles to estimate both the B_1 magnitude and relative phase of one or more coils assuming a very long repetition time. This method accounts for slice selection effects by using the correct slice profile in the model, improving results at higher tip angles. This method also smoothly interpolates in regions with low spin density. The simulation results have less error that the conventional estimate, even when using the standard two angles. Results are also shown with MR phantom data.

Third, the joint B_1^+/T_1 PL estimator uses multiple scans and an arbitrary selection of tip angles and repetition times to estimate both the B_1 magnitude and relative phase of one or more coils. The estimator uses the steady-state incoherent (SSI) method based on a Cramer Rao Bound analysis of various B_1/T_1 joint estimation schemes and aids in selection of imaging parameters. This method allows for shortened repetition times, and thus faster scanning, than the previous regularized B_1 method. The regularized B_1 estimates interpolate smoothly in low spin density areas with a user-chosen desired full-width half-maximum (FWHM). Simulation results show lower error than those of the previous estimator due to inclusion of T_1 effects.

The thesis contributes three new PL estimators that incorporate important physical effects and smooth in areas of low data magnitude in a controlled manner via a user-selected β value. Cramer Rao bound analyses help select imaging parameters. The estimators aid the field of MR parameter mapping to ultimately improve pulse design and imaging.

CHAPTER II

MRI Background

First, a brief overview of MRI, the magnetic fields used, and the basic equations which govern MRI and their assumptions will be given.

Magnetic resonance imaging (MRI) is a medical imaging modality that uses magnetic fields to image the body non-invasively and without ionizing radiation. Certain atoms (those with an odd number of neutrons or protons) possess a characteristic called nuclear spin angular momentum. Hydrogen, located throughout the human body in the form of water, has a single proton and is the atom used in conventional MRI. We can visualize these atoms as tiny spheres spinning around an axis, or a “spin”. The spins create a small magnetic moment in the same direction as the angular momentum. Manipulating these spins through interactions with magnetic fields creates the signal measured in MRI. Many of these signals, fit to a Cartesian grid, are then transformed via a 2D (or 3D) Fourier Transform to create the final image.

2.1 Three Magnetic Fields

Three magnetic fields are used in signal acquisition in MRI: 1) B_0, the main field, 2) B_1, the radio frequency field, and 3) affine perturbations of B_0 called field gradients.

2.1.1 B_0, the Main Field

Normally, the spins are in random directions, creating a net magnetic moment of zero. However, when a magnetic field is introduced (by convention in the z, or longitudinal, direction), magnetic moments can only be oriented parallel or anti parallel to the field, as explained by quantum physics. The parallel state is a lower energy state, while the anti parallel state is a higher energy state. Thus, slightly more atoms (only a few parts per million) will align in the parallel state, creating a net magnetic moment (referred to as the net magnetization) aligned parallel to the main field, B_0.

These atoms also possess a second important characteristic: magnetic resonance. This property causes the spins to precess about the z direction like a spinning top when the magnetic field B_0 is applied. The frequency of precession is governed by the Larmor equation

$$\omega = \gamma \cdot B_0, \tag{2.1}$$

where γ is the gyromagnetic ratio (for hydrogen, $\gamma/2\pi = 42.57$ MHz/T). Based on this equation, typical resonant frequencies are 63 MHz for a 1.5T field. If no excitation is applied, the net magnetization is proportional to the spin density, the number of spins per unit volume. We define the net magnetization as

$$\boldsymbol{M} = M_x\vec{\imath} + M_y\vec{\jmath} + M_z\vec{k}.$$

A homogeneous main field is important in MRI so that the resonant frequency is constant across the field. Shimming, using small coils or magnets, can be used to make a more homogeneous main field. Main fields are usually in the range of a few Tesla. However, as field strengths become higher (for example, 3T and higher), making the main field homogeneous becomes more and more difficult.

2.1.2 Radio frequency field (B_1), Excitation and Relaxation

The second magnetic field applied is a radio frequency field, called B_1. This alternating electromagnetic field (*i.e.*, a radio frequency (RF) field) is applied, tuned to the Larmor frequency, during the excitation phase of scanning to tip the magnetization into the transverse plane.. This applies a torque to the net magnetization vector, causing that vector to tip. The tip angle is governed by the strength of the RF field and the length of time it is applied. Typically, an angle of 90 degrees is desired so that the net magnetization is in the x-y plane.

If the radio frequency field is inhomogeneous, then the net magnetization vector will be tipped by a different angle at each location in the ROI. This can cause problems in excitation.

After excitation, the net magnetization returns to equilibrium in the longitudinal plane. The vector continues to precess at the Larmor frequency during relaxation. This is called relaxation. Relaxation is governed by two constants (T_1 and T_2) which depend on the object's material. T_1 is the spin-lattice constant and involves energy exchange between spins and the surrounding electrons. The values are in the range of hundreds of milliseconds. T_1 specifies how the longitudinal magnetization recovers:

$$M_z(t) = M_0(1 - \mathrm{e}^{-t/T_1}), \tag{2.2}$$

where M_0 is the equilibrium nuclear magnetization. T_2 is the spin-spin time constant and involves interactions between the spins. T_2 is normally in the tens of milliseconds. T_2 specifies how the magnitude of the transverse magnetization (in the XY plane) decays:

$$M_{xy}(t) = M_0\,\mathrm{e}^{-t/T_2}\,, \tag{2.3}$$

where $M_{xy} = M_x + iM_y$. T_1 and T_2 do not affect the precession of the net magnetization vector, but do affect its length. Interestingly, the net magnetization vector can change length and differ from its equilibrium value during relaxation depending on the values of T_1 and T_2. In fact, magnetization can even disappear for a time and then return.

The magnetization vector precesses at the Larmor frequency while returning to equilibrium. This precession, by Faraday's Law, causes an electromagnetic force in a RF coil that is measured. This signal is the MRI signal. This signal, therefore, depends not only on spin density, but also on T_1 and T_2.

2.1.3 Field Gradients

To create an image, there needs to be spatially dependent information. The addition of field gradients which, encode this information earned its inventor, Paul C Lauterbur and Peter Mansfield, a Nobel Prize in 2003. Linear field gradients are applied to the main field. The field perturbation is the same in the direction as B_0, but its magnitude varies at spatial coordinates. A general gradient can be expressed as

$$\boldsymbol{G} = G_x\vec{i} + G_y\vec{j} + G_z\vec{k}, \tag{2.4}$$

where $\vec{i}, \vec{j},$ and $\vec{k}$ are unit vectors. The main field can then be expressed as

$$\vec{B}(r) = (B_0 + G_x x + G_y y + G_z z)\vec{k} = (B_0 + \boldsymbol{G} \cdot \vec{r})\vec{k}.$$

By varying these field gradients, many signals can be collected and then arranged on a Cartesian grid. Then, a simple 2D Fourier transform of the collected signal gives the final image.

2.2 Bloch Equation

The behavior of the magnetization vector is governed by a phenomenological equation called the Bloch equation. This equation describes the precession and relaxation effects in the previous section. The Bloch equation is given below:

$$\frac{d\boldsymbol{M}}{dt} = \boldsymbol{M} \times \gamma \boldsymbol{B} - \frac{M_x\vec{i} + M_y\vec{j}}{T_2} - \frac{(M_z - M_o)\vec{k}}{T_1}. \tag{2.5}$$

The first term describes precession and influences the direction of the net magnetization. For example, the change in magnetization is proportional to the cross product of $\boldsymbol{M}$ and $\boldsymbol{B}$. If $\boldsymbol{B}$ remains constant (*i.e.*, our main field), then the angle between $\boldsymbol{M}$ and $\boldsymbol{B}$ will not change and we will have precession as specified by the Larmor equation. The second term describes the relaxation controlled by the relaxation rates T_1 and T_2 and influences the length of the net magnetization.

There is no known general solution to the Bloch equation; however, when certain simplifications are made, the differential equation can be solved. One important example is when $RF = 0$, which applies during relaxation when the RF is not applied. Using the expression for a general gradient (2.4), the transverse (X-Y plane) component of the Bloch equation is

$$\frac{dM_{xy}}{dt} = -\left(\frac{1}{T_2(\vec{r})} + i(\omega_0 + \omega(\vec{r}, t))\right) M_{xy}.$$

This simple differential equation thus has the solution

$$M_{xy}(\vec{r}, t) = M_0(\vec{r})\, \mathrm{e}^{-t/T_2(\vec{r})}\, \mathrm{e}^{-\imath\omega_0 t}\, \mathrm{e}^{-\imath\gamma \boldsymbol{G}\cdot\vec{r}t}\, . \tag{2.6}$$

2.3 Imaging

Creating an MR image requires two basic steps. Excitation consists of using a RF pulse to excite the volume (or a portion thereof). Then, gradients are used to spatially encode the information. Finally, during readout, the transverse component of the magnetization signal is read. Usually, this process is repeated several times by waiting until equilibrium is reached between excitations. The collection of recorded signals are rearranged into a 2D array and then the Fourier transform yields a two-dimensional image.

2.3.1 Excitation

Excitation involves using an RF pulse to "excite" spins, or tip spins by some angle. Non-selective excitation excites the entire volume, while selective excitation excites just a slice of the volume. Excitation is based on the principles discussed in Section 2.1.2.

2.3.1.1 Non-selective Excitation

In non-selective excitation, all the spins in the entire volume are excited by the RF pulse, causing them to tip by an angle determined by the duration and power of the pulse.

To analytically solve the Bloch equation in this situation, one uses a few simplifications. First, no gradients are applied - the only operating magnetic fields are the RF pulse (the B_1 field) and the main field, B_0. Relaxation is ignored because the typical length of an RF pulse is very short (less than 1 millisecond).

Two RF coils are used in MR: one coil, the transmit coil, creates the RF field that excites the spins; the second coil, the receive coil receives the RF signal from the precessing spins. Sometimes, one coil will be used for both of these two purposes or multiple coils will be used for either the transmit coil or the receive coil or both. While ideally each of these coils would have a uniform response (*e.g.*, for the receive coil, two identical precessing spins in different locations would generate the same emf), real RF coils have a coil response function that varies as a function of space, $\mathrm{B}_1^+(\vec{r})$ (response of the transmit coil(s)) and $\mathrm{B}^{\mathrm{receive}}(\vec{r})$ (response of the receive coil(s)), where $\vec{r}$ is the space variable. (Note - if more than one coil is used for transmitting or receiving, each will have its own unique response.) The inhomogeneity of the coil response can be very problematic. A non-uniform receive coil response creates intensity differences - those areas with a smaller $\mathrm{B}^{\mathrm{receive}}$ will appear darker compared to areas with a larger value of $\mathrm{B}^{\mathrm{receive}}$. This can make MR images more difficult to interpret. A non-uniform transmit coil response, however, is much more problematic because it leads directly to varying flip angle and influences the signal equation in a more complicated way. Non-uniform flip angles, or B_1 field inhomogeneity, is explained further in Section 2.4.

When an amplitude-modulated signal is injected into either coil, the coil induces a magnetic field called $\boldsymbol{B}_1^{lin}(\vec{r},t)$:

$$\boldsymbol{B}_1^{lin}(\vec{r},t) = a_1(t)\cos(\omega t + \phi_1(t) + \phi_k')\mathrm{B}_1^+(\vec{r}), \tag{2.7}$$

where $a_1(t)$ and $\phi_1(t)$ are the input amplitude and phase to the coil and ϕ_k' is the modulator phase offset. We assume here that B_1^{lin} is exactly on-resonance and ω is the Larmor frequency. The transverse component of this field, or the part of the field that is perpendicular to B_0, influences spins. We can break this field into two circularly polarized fields, a right and a left-handed field; because the left-handed field rotates in the same direction as the rotating spins, this field is more resonant with the spins and the right-handed field has only a negligible effect on the spins (and is thus ignored) [92]. $\boldsymbol{B}_1$ is the left-handed circularly polarized field and is expressed as:

$$\boldsymbol{B}_1(\vec{r},t) = \mathrm{B}_1^+(\vec{r})a_1(t)[\cos(\omega t + \phi_1(t) + \phi_k')\vec{i} - \sin(\omega t + \phi_1(t) + \phi_k')\vec{j}]. \tag{2.8}$$

This field is referred to as the B_1^+ field and is the active field during transmission (in this thesis, we are referring to this circularly polarized field when we are estimating the B_1 field and inhomogeneity in Chapter V and Chapter VI).

Because $\boldsymbol{B}_1$ is precessing, changing our unit directional vectors to vectors that are rotating clockwise at an angular frequency ω can greatly simplify description of these fields. This is called a rotating frame. We can choose a rotating frame that is precessing at the Larmor frequency or at the RF frequency. Here, we assume on-resonance (*i.e.*, the Larmor frequency is exactly the same as that of B_1) and then these rotating frames are identical.

Then, the new directional vectors are defined as

$$\begin{aligned}
\vec{i'} &\triangleq \cos(\omega t)\,\vec{i} - \sin(\omega t)\,\vec{j} \\
\vec{j'} &\triangleq \sin(\omega t)\,\vec{i} + \cos(\omega t)\,\vec{j} \\
\vec{k'} &\triangleq \vec{k},
\end{aligned}$$

and the rotation matrix R_x is given by

$$R_z(\theta) = \begin{bmatrix} \cos(\theta) & \sin(\theta) & 0 \\ -\sin(\theta) & \cos(\theta) & 0 \\ 0 & 0 & 1 \end{bmatrix},$$

and the magnetization vector in the rotating frame is given by

$$\boldsymbol{M}_{rot} = \begin{bmatrix} M_{x'} & M_{y'} & M_{z'} \end{bmatrix}^T.$$

Then,

$$\boldsymbol{M}_{rot}(\vec{r}, t) = \boldsymbol{R}_z(\theta(\vec{r}))\boldsymbol{M}_{rot}(\vec{r}, 0), \tag{2.9}$$

where the tip angle is defined as

$$\theta(\vec{r}) = \int_0^t \omega_1(\vec{r}, s)ds, \tag{2.10}$$

where $\omega_1(\vec{r}, t) = \gamma \mathrm{B}_1^+(\vec{r})b_1(t)$ and $b_1(t) \triangleq a_1(t)\,\mathrm{e}^{-i\phi_1(t)}$ and the oscillator offset has been absorbed by the B_1^+.

In the rotating frame, the RF field rotates the magnetization vector from the longitudinal. The magnetization vector thus precesses along this path as it is tipped.

In the case of multiple transmit coils driven by the same RF signal $b_1(t)$ with individual coil patters ${\rm B}_1^+{}_k$ and different relative amplitudes α_k, the complex coil patterns add linearly. Although the B_1 fields add linearly, the magnetization fields do not.

2.3.1.2 Selective Excitation

In selective excitation, a static z gradient $G_z z$ is applied during the RF pulse to select only spins in a desired "slice". Only spins where the resonant frequency matches the frequency of B_1 will be excited. Again, we assume T_1 and T_2 effects are negligible due to the short pulse duration. A circularly polarized RF pulse is applied at a frequency close to the Larmor frequency. Even with these simplifications, the Bloch equation can only be easily solved by making the small tip-angle approximation [98]. This approximation assumes that the system is initially at equilibrium (*i.e.*, the magnetization vector is completely in the longitudinal plane) and that the tip angle is small (less than 30 degrees). Under the small tip angle assumption, we can assume that $M_z \approxeq M_0$ and $dM_z/dt \approxeq 0$. After solving the decoupled differential equation, the expression for the transverse component after excitation is equal to the Fourier Transform of B_1. This relationship is [92]:

$$M(t, \vec{r}) = iM_0(\vec{r}){\rm B}_1^+(\vec{r})\, {\rm e}^{-\imath\omega(z)t} \int_0^t {\rm e}^{\imath\omega(z)s}\, \omega_1(s) ds, \tag{2.11}$$

where $\omega(z) = \gamma G_z z$ from which follows:

$$|M(\tau, z)| = M_0(\vec{r}){\rm B}_1^+(\vec{r})\mathcal{F}_{1D}\{\gamma b_1(t + \tau/2)\}|_{f=-(\gamma/2\pi)G_z z}. \tag{2.12}$$

If we have exact resonance (*i.e.*, either $z = 0$ or $G_z = 0$), then the same solution applies as in non-selective excitation - the tip angle is equal to the integral of the RF pulse. This can be expanded to include multiple coils, as well.

Because of the Fourier Transform relationship, finding the ideal RF pulse is difficult because both the RF pulse itself and the resultant slice profile are necessarily time limited. An infinite sinc pulse is impossible to create in practice, as is the ideal rectangular slice profile. In practice, truncated sincs or Gaussian pulses are used. This can create problems when an algorithm is based upon the ideal of an infinitely thin and/or rectangular achieved slice profile.

2.3.2 Signal Equation

After a portion of the volume has been excited, we must further understand the MR signal and how to create the appropriate gradients to obtain a spatially encoded signal for the final image.

Ideally, receiver coil(s) detect flux changes in transverse magnetization uniformly over the entire volume or ROI. (To combat this non-ideality, many models add the sensitivity pattern of the coils as a parameter [69, 113].) Each excited spin contributes to the signal. Therefore, the signal equation is equal to the volume integral of the transverse magnetization:

$$S_r(t) = \int_{vol} \mathrm{B}^{\text{receive}}(\vec{r}) M(\vec{r}, t) d\vec{r}. \tag{2.13}$$

We note here that this signal equation ignores constant factors and phase factors based on ignoring T2 decay. We will also include the coil sensitivities in this analysis. In the case where these are not appropriate assumptions, even this first signal equation might be called into question. Using (2.6), the signal equation is:

$$s_{\vec{r}}(t) = \int\int\int M_0(\vec{r}) \mathrm{B}^{\text{receive}}(\vec{r})\, \mathrm{e}^{-t/T_2(\vec{r})}\, \mathrm{e}^{-\imath\omega_0 t}\, \mathrm{e}^{-\imath\gamma \int_0^t \vec{G}(\tau)\cdot\vec{r} d\tau}\, dxdydz. \tag{2.14}$$

Again, we ignore the relaxation term. We look only at the envelope of this signal and assume no z gradient is applied. This yields the following equation:

$$s(t) = \int_x \int_y m(x, y) \mathrm{B}^{\text{receive}}(x, y)\, \mathrm{e}^{-\imath\gamma \int_0^t \vec{G}(\tau)\cdot\vec{r} d\tau}\, dxdy, \tag{2.15}$$

where $m(x, y)$ is the integral of the magnetization over the slice. It can be also written using the kspace notation (which will be explained in the next section) as:

$$s(t) = \int_x \int_y m(x, y) \mathrm{B}^{\text{receive}}(x, y) \, \mathrm{e}^{-\imath 2\pi(k_x(t)x + k_y(t)y)} \, dxdy, \tag{2.16}$$

where

$$k_x(t) = \gamma/2\pi \int_0^t G_x(\tau) d\tau \tag{2.17}$$

$$k_y(t) = \gamma/2\pi \int_0^t G_y(\tau) d\tau, \tag{2.18}$$

where G_x and G_y are the x and y gradients. This signal is detected by the receivers and via a Fourier Transform (also explained in the next section) to create our MR image $m(x, y)$.

2.3.3 Gradients

After excitation, gradients in the x and y direction are applied to spatially encode information into the MRI signal as shown in the previous equation. This equation clearly shows a Fourier relationship between the signal and the magnetization at kx and ky locations. These spatial frequency locations are usually referred to as kspace, where k is usually measured in cycles/cm. Thus, each time in the signal corresponds to a Fourier transform of kspace. This perspective greatly aids in designing trajectories.

As the gradients are applied, the spins are also simultaneously returning to equilibrium. This free-induction decay (FID) signal is “read-out” or measured by the coils. A sufficient amount of time (called TR or repetition time) is waited until the system returns to equilibrium and then another excitation cycle begins, different gradients are applied, and the signal is again read out.

The signal is typically largest at the center of kspace. The signal is read out here at what is referred to as the echo time. This type of echo is called a gradient echo and is the type of echo used in this thesis.

2.3.4 Multiple Transmit Coils (parallel excitation)

The severe problem of B_1^+ inhomogeneity in high fields ($\geq 3T$) precipitated the development of multiple transmit coils and parallel excitation [67, 108, 134, 135, 142, 143, 145, 148]. Ideally, each coil can be adjusted with phase and amplitude to try to compensate for the effects of B_1 field inhomogeneity. This led to the development of completely separate pulses for each coil. The trend toward using higher main field strengths with their subsequent benefits would be undermined without a strategy to compensate for B_1 inhomogeneity. Multiple transmit coils also have other possible benefits. RF pulses could be shortened in length or a larger space could be covered. A third possibility is decreasing the RF power required. Parallel excitation motivates the need for accurate and efficient B_1^+ maps.

2.3.5 Noise in MRI

Noise in the MR signal is additive Gaussian noise [83]. The noise is primarily thermal, the resistance coming both from the coil and body being imaged. Some noise is also produced by the pre-amplifier. However, through proper design of the coil and MR system, the major noise source is the imaging object. Because the DFT is a unitary transform, the final MRI also has Gaussian noise. When the kspace samples are uniform on a Cartesian grid, the Gaussian noise is white; other sampling methods produce colored noise. Because of complex components after the Fourier transform is taken, one usually look at the magnitude of the image. This will give a Rayleigh distribution in background regions of the image and a Rician distribution in the signal. Because the mean is usually much greater than the variance, these distributions can be approximated as Gaussian.

The signal to noise ratio (SNR) is affected by many factors in MRI. A general rule of thumb is that the SNR is proportional to the B_0 field strength if, as is common, the imaging object is the main source of resistance. However, this relationship is quite complex because other parameters in MR are also a function of B_0's magnitude. SNR is proportional to the square root of the total measurement time, whether by increasing the number of samples, the number of signal averages, or the length of the readout time. As a rule of thumb, increasing the spatial resolution by a factor reduces the SNR by that same factor.

2.4 MRI Field Inhomogeneity

In solving the Bloch equation as shown in Chapter II, field homogeneity is often assumed. However, due to the nature of objects being imaged as well as the difficulty in engineering perfect magnetic coils, fields are inhomogeneous. The sources of this inhomogeneity, its effects, and correction methods are explored in this section. As will be seen, these correction methods require a map of the inhomogeneous field. The estimation of these fields is the subject of this thesis.

2.4.1 Main Field (B_0) Inhomogeneity

As was seen in the Larmor equation (2.1), resonance frequency is directly related to the magnetic field strength. Thus, main field inhomogeneity causes different resonant frequencies at each spatial location. An inhomogeneous main magnet can be made more homogeneous via shimming. However, inhomogeneity can also arise from the specific morphology of the brain. Differences in the bulk magnetic susceptibility (BMS) of structures in the body cause macroscopic field inhomogeneity. The difference in BMS is highest in areas where air and tissue meet; for example, in the sinuses and ear canal, lungs, and the abdomen. There is an increased sensitivity to these problems at high B_0 field strengths. Inhomogeneity can also arise from chemical shift. Outer electrons shield the nucleus and slightly reduce the magnetic field experienced by the nucleus. This causes a small change in the resonant frequency as well. This chemical shift is experienced by fat and causes the fatty parts of an image to be shifted or blurred depending on the trajectory. Because the specific focus of this thesis is fMRI and fat suppression pulses are usually used, this cause of inhomogeneity is considered negligible and not further considered in this thesis.

2.4.1.1 Effects of Inhomogeneity

Depending on the trajectory, inhomogeneity causes different effects. The need for speed, especially in fMRI, requires use of trajectories which traverse most, if not all, of kspace in one shot, or excitation cycle. Unfortunately, these trajectories with especially long read out times exacerbate the problem of inhomogeneity.

Inhomogeneity affects the amplitude of the signal and causes signal loss [117]. Under field inhomogeneity, the object has a distribution of different resonant frequencies which gives the spins phase incoherence. When the contribution from each spin is added together, this dephasing causes a signal loss. This effect is referred to as T_2^* decay and causes a much faster decay in the transverse magnetization. (Sometimes, the reciprocal of T_2^* or R_2^* is used, such as in Section 4.2.4). With longer readout times, this problem becomes even more severe and results in signal loss. If the T_2^* decay is severe, the signal is weighted in k-space, creating blur in the final image.

Geometric distortions can also result. In trajectories, such as echo-planar, the resulting geometric distortion due to field inhomogeneity is a shift. However, spiral trajectories cause a blur in the resulting image which is harder to correct for in the image domain [66], though both trajectories can be corrected in the signal domain.

2.4.1.2 Correction methods

Given a field map of the inhomogeneity, these effects can be corrected for. One major correction method is conjugate phase methods, which attempt to compensate for the phase at each voxel (*e.g.*, [94]). These methods require a spatially smooth field map and do not perform well where this assumption breaks down. Iterative reconstruction techniques have also been developed, both for specific trajectories [52] and for more general situations

[114].

Field maps are also used in other MR applications. For example, in developing tailored RF pulses to compensate for signal loss due to inhomogeneity, an accurate fieldmap is required [140]. Because of the importance of accurate field map estimation for fMRI, we focus on this problem in Chapter IV.

2.4.2 Radio Frequency field Inhomogeneity

Inhomogeneity in the RF field, B_1, can be caused by many factors. High B_0 field strengths make the RF wavelength shorter. In addition, the tissue dielectric constant causes the RF wavelength to be even shorter. A shorter wavelength causes the RF field to interact with the subject even more, causing even more inhomogeneity. The distance from the transmit coil also can effect inhomogeneity. Inhomogeneity can be quite large at high fields; at 3T, inhomogeneity ranging from 30-50% has been found [20]. Surface coils only compound the problem and create even greater variation.

2.4.2.1 Effects of B_1^+ inhomogeneity

Inhomogeneity of the RF field (B_1^+) causes a nonuniform effect on spins; the net magnetization vector will be tipped at different angles depending on the particular value of B_1^+. This can make MR images very difficult to interpret due to spatially varying signal and intensity in the image. This can be seen as lighter and darker regions at higher B_0 levels (≥ 3T). In addition, the spin density will be measured incorrectly causing quantitative problems, for example in measuring brain volumes [145].

2.4.2.2 Correction Methods

There are several methods used to try to minimize B_1^+ inhomogeneity. These include coil design and special pulses, such as adiabatic, impulse 2D pulses, 3D MDEFT imaging and FLASH imaging [102]. However, correcting for B_1^+ inhomogeneity may still be needed after minimization strategies are used or in the case when these trajectories are not applicable. More recently, tailored RF pulses such as [102] have been proposed to reduce inhomogeneity; they require use of a B_1^+ map. A new method in parallel transmit excitation has been proposed using the transmit SENSE slice-select pulses [145] which also requires uses of such a map. Dynamically adjusting the RF power is another option which also requires use of a B_1 map. To apply these new methods that more comprehensively compensate for B_1 inhomogeneity, an accurate B_1^+ map (and one that additionally includes the phase) is required. We focus on this problem in Chapter V and Chapter VI.

CHAPTER III

Iterative Estimation Background

Creating a field map for either B_0 or B_1^+ requires an accurate, reliable estimator based on available measurements. Many common estimators are based on heuristic schemes and not on a statistical model. Other common estimators disregard signal noise and its properties. The solution of this dissertation uses statistical estimators to solve the field map problems. Therefore, we review various statistical estimators.

The first step in estimation requires creating a model for the data including the desired parameter and other unknown parameters and their statistics. Next, we use this model to create an estimator. Our goal is to estimate the field map from the MR data available (for example, from an initial scan, either for the machine or for each patient). The data is usually referred to as a vector $\boldsymbol{x}$, while the desired parameters (the field map) are θ. Based on a model, there are many choices for an estimator. Each estimator is based on a different cost function, a function which describes the cost of any particular estimate; for example, the cost might be the mean squared error or the cost may penalize rough images. Based on the given cost function, different estimators give different results.

One way to measure the effectiveness of an estimator is to look at its bias and variance. The bias of an estimator is the difference between the expected value of the parameter and the value of the parameter. Often, we desire an unbiased parameter, *i.e.*, the bias of the estimator is zero for each possible parameter. Ideally, we would also seek the estimator with the lowest variance. However, the mean squared error is equal to the variance plus the bias squared. Reducing the bias will increase the variance. Understanding this trade off is important in selecting a good estimator.

3.1 Bayesian Estimators

Bayesian estimators require more data than just the parameters and the available data. They also require a statistical distribution for the parameters called a prior distribution, $f(\theta)$. Unfortunately in imaging problems, this distribution is usually not known; when it can be obtained, it is often at great cost and time. These estimators minimize the average cost:

$$\mathcal{E}[c] = \int_{\Theta} \int_{X} c(\hat{\theta}, \theta) f(x|\theta) f(\theta) dx d\theta, \tag{3.1}$$

where c is the cost of an estimate based on the true value of θ. Different cost functions generate different estimators. A minimum mean squared error cost function yields the conditional mean estimator (CME). A minimum mean absolute error cost function yields the conditional median estimator (CmE). A minimum mean uniform error cost function yields the maximum a posterior estimator (MAP). One disadvantage of using these estimators is finding an appropriate prior.

3.2 ML Estimator

The Maximum Likelihood (ML) estimator is one of the most common statistical estimators in practice. This estimator maximizes the likelihood function $f(x|\theta)$ - the density function of the data given the parameter or $f(x;\theta)$ if θ is not random. It seeks the estimate which best matches the data based on the likelihood function. Maximizing this function can sometimes be difficult, but maximizing any monotone increasing function of the likelihood (for example, the log of the likelihood) also maximizes the likelihood. We usually express the estimator as:

$$\hat{\theta} = \arg\max_{\theta \in \Theta} \ln f(x|\theta). \tag{3.2}$$

The ML estimator has many desirable properties; it is asymptotically unbiased and Gaussian and is also transform invariant.

Although ML estimators are theoretically appealing, in practice, the estimators do not always have good performance. They are often sensitive to noise or are computationally expensive, for example, calculating the inverse of a large matrix. The performance declines significantly as the number of parameters approaches the number of values to be estimated.

3.3 Penalized-Likelihood Estimators

There are two major options to improve the results of an ML estimator. First, we can add more information (the prior distribution), which gives us Bayesian estimators. However, priors are difficult to find and usually do not reflect an "average" image. A second option is using penalized-likelihood (PL) estimators. These can be thought of as a Bayesian (MAP) estimator with a possibly improper prior. A penalized-likelihood estimator seeks an estimator which most closely matches the data (through the ML estimate) while also satisfying other criteria through a penalty. The expression is shown below:

$$\begin{aligned} \hat{\theta} &= \arg\min_{\theta \in \Theta} - \ln f(x|\theta) + \beta R(\theta) && (3.3) \\ \hat{\theta} &= \arg\min_{\theta \in \Theta} \Psi(\theta), && (3.4) \end{aligned}$$

where Ψ is the new cost function. $R(\theta)$ maps θ to a penalty based on some characteristic - usually data smoothness. When β is large, the resulting image will be very smooth, whereas when β is small, the estimate will be based more on the data and the image may be rough.

The user can choose this parameter independently. The most common roughness penalty in 1D is a quadratic penalty on the difference between neighboring pixels:

$$R(\vec{y}) = \sum_{n=2}^{N} (y_n - y_{n-1})^2, \tag{3.5}$$

where N is the number of pixels in an image. Quadratic penalties have better noise performance than an ML estimator, but blur the image. This is the fundamental noise-resolution trade off. With a PL estimator, the resolution can be quantified based on the choice of β, giving the user more control on where they operate on this continuum. A multi-dimensional quadratic penalty is similar to (3.5) but considers neighbors in each direction. Diagonal neighbors could be given less weight than horizontal or vertical neighbors. Non-quadratic estimators can be used to reduce noise and still not blur edges, but are more complicated to analyze. One common roughness penalty used in the literature is the total variation (TV) penalty, or an absolute value penalty *e.g.*, [7]. They are useful, but suffer from the disadvantage of not being differentiable.

3.4 Cramér-Rao Bound

The Cramér-Rao Bound (CRB) can be used on a statistical model to measure lower bounds for any unbiased estimator. The CRB shows a region of variance that can not be achieved by any unbiased estimator. While it is not specific to any particular estimator, we can better understand how good our estimator is in relation to the CRB. The matrix CRB is defined by:

$$\mathsf{Cov}_{\boldsymbol{\theta}}\left\{\hat{\boldsymbol{\theta}}\right\} \geq \mathsf{F}^{-1}(\boldsymbol{\theta})$$

where

$$\mathsf{F}(\boldsymbol{\theta}) = -\,\mathsf{E}\left[\nabla^2_{\boldsymbol{\theta}} \ln \mathsf{p}(\boldsymbol{Y}; \boldsymbol{\theta})\right]$$

is the Fisher information. For an unbiased estimator, this CRB gives a scalar bound for each estimator of each parameter (the values along the diagonal of the matrix), as well as showing bounds for the covariance between parameters. The Fisher information measures the average curvature of the log likelihood function by the true value of the parameter.

The CRB is applicable for an unbiased ML estimator. However, the regularization term in a PL estimator makes the estimator inherently biased and the CRB does not apply. A PL estimator can operate below the curve specified by the CRB because of its bias. Nevertheless, the CRB can give useful analysis for pixels where the SNR is high. For pixels where the SNR is low, on the other hand, the regularizer basically just interpolates those pixels and we are less interested in the noise properties.

PL estimators are complicated because they are defined implicitly in terms of the minimum of a cost function. This makes their mean and variance characteristics very difficult to analyze carefully. Some methods have been developed in these situations, but they deal with asymptotic relationships of the mean squared error. This has the characteristic that mean and variance are equally weighted, whereas in applications, the relative importance of mean and variance may differ. Some approximations do exist which look at moments, but they are not explored further in this report.

3.5 Spatial Resolution Analysis

As explained in Section 3.3, regularizing PL estimators create blur. To choose β, it is necessary to understand the spatial resolution properties of the estimator. Another reason to look at the spatial resolution is to try to achieve more uniform resolution by modifying the estimator itself. Here, by spatial resolution, we refer to the impulse response of the estimator. Although there are several ways to define the impulse response, all versions rely on the gradient of the estimator itself. Estimators which are defined implicitly (*e.g.*, PL estimators) are more complicated to analyze. We would like to know the impulse response of the estimator. Although several definitions of the impulse response are possible, the general form is similar. The impulse response is the gradient of the estimator (based on either the data or the mean data) times the gradient of the average data. Regardless of the definition chosen, we need an expression for the gradient of the estimator. We require a few set of conditions to find the gradient - the cost function must have a unique minimizer, be differentiable, and have an invertible Hessian (among other conditions). Then, the gradient is defined. PL estimators consist of a log-likelihood term $l(\theta, x)$ and a regularization term $R(\theta)$ as follows:

$$\Psi(\theta, x) = l(\theta, x) + R(\theta).$$

The gradient of this estimator is then defined as (after much simplification) [30]:

$$\nabla\hat{\theta}(x) = [\nabla^{[2,0]} l(\theta, x) + \nabla^2 R(\theta)]^{-1} [-\nabla^{[1,1]} l(\theta, x)]|_{\theta=\hat{\theta}(x)}, \tag{3.6}$$

where $\nabla^{[2,0]}$ is the derivative taken twice with regard to the first argument (here θ) and where $\nabla^{[1,1]}$ is the derivative taken once with regard to each argument.

In this report, spatial resolution analysis was performed as in [119] and [30] using a Taylor's series approximation and Parseval's relation and then minimizing the cost function by taking the gradient, setting it to zero, and solving. This is basically the same method as described above.

3.6 Minimization of Cost Function via Iterative Methods

After defining our model and choosing an estimator, we need to actually evaluate it. For the methods shown in this section, estimators are the extrema of a cost function. For some problems, an analytic formula for the extrema exits. However, for most cost functions, especially PL estimators which include a regularizer, this is not possible. Even for problems where an analytic solution exists, the solution is often not feasible numerically (*e.g.,* inverting a large matrix). Therefore, iterative methods which converge to a local minima (or maxima) must be used. This is a large mathematical and statistical topic with many algorithms to choose from. Mathematical packages such as Matlab often contain several built-in optimizers, such as Newton's method or the conjugate gradient method. For the joint B_1^+ , T_1 estimation in Chapter VI, we used one general purpose optimization method: preconditioned gradient descent (PGD), which is explained in Section 3.6.2. For the first two estimation problems in Chapter IV and Chapter V, these general purpose optimizers are not used, because we were able to develop monotonic optimizers based on the principles of optimization transfer. Optimization transfer is explained in Section 3.6.1. General purpose optimizers often converge faster than algorithms produced from optimization transfer, but for problems such as non-quadratic and non-convex problems, these optimizers are not always monotonic and guaranteed to converge.

3.6.1 Optimization Transfer

Optimization transfer consists of two major principles. First, we choose a surrogate function $\phi^{(n)}$. This function is normally a function with an analytical minimizer or one that is easy to find. Second, we minimize the surrogate. This minimum is not usually the global minimum, so we must repeat these steps until the algorithm converges. The key lies in choosing appropriate surrogate functions. They are usually designed so that: 1) The surrogate and the cost function have the same value at each iterative step, and 2) the surrogate function lies above the cost function. When both functions are differentiable, this implies that the tangents are also matched at each iterative step.

In this report, we use quadratic surrogates based on Huber's algorithm [60, p.184-5]. These have the benefit of having an analytic solution for the minimizer of the surrogate. For a quadratic surrogate, the following iteration will monotonically decrease the original cost function:

$$\theta^{(n+1)} = \theta^{(n)} - [\nabla^2 \phi^{(n)}]^{-1} \nabla \Phi(\theta^{(n)}. \tag{3.7}$$

However, unless $\phi^{(n)}$ is separable, this inverse is not computationally practical. Therefore, in this report, we use separable quadratic surrogates (SQS). This is explained in more detail in Appendix A applied specifically to the B_0 field map problem and in Appendix C applied specifically to the B_1 field map problem.

3.6.2 Preconditioned Gradient Descent: PGD

Gradient descent, or steepest descent, algorithms are a general optimization method where each iteration descends a step along the negative of the gradient of the cost function. In preconditioned gradient descent, the gradient of the cost function is first multiplied by a preconditioning matrix P and then descended a step size α along that direction,

$$\theta^{(n+1)} = \theta^{(n)} - \alpha P \nabla \Psi\left(\theta^{(n)}\right). \tag{3.8}$$

A preconditioner can give much faster convergence. Under certain conditions of the gradient and also the preconditioner (for example, the gradient satisfies a Lipschitz condition, true with a twice differentiable bounded cost function, and the preconditioner is a symmetric positive definite matrix), the algorithm can be shown to monotonically decrease the cost function. We can ensure descent and force monotonicity by reducing the step size α by half until the cost function decreases. This guarantees descent, but can come a costly number of evaluations of the cost function. This half-stepping method, as well as α selection is explained further in Section 6.5.2.

CHAPTER IV

Field Map B_0 Estimation

4.1 Introduction

MR [1] imaging techniques with long readout times, such as echo-planar imaging (EPI) and spiral scans, suffer from the effects of field inhomogeneity that cause blur and image distortion. To reduce these effects via field-corrected MR image reconstruction, *e.g.*, [93, 107, 114, 118], one must have available an accurate estimate of the field map. A common approach to measuring field maps is to acquire two scans with different echo times, and then to reconstruct the images (without field correction) from those two scans. The conventional method is then to compute their phase difference and divide by the echo time difference $\triangle_1$. This model makes no account for noise and creates field maps that are very noisy in voxels with low spin density. Section 4.2 first introduces this model and then reviews standard approaches for this problem. A limitation of the standard two-scan approach to field mapping is that selecting the echo-time-difference $\triangle_1$ involves a trade off: if $\triangle_1$ is too large, then undesirable phase wrapping will occur, but if $\triangle_1$ is too small, the variance of the field map is large. One way to reduce the variance while also avoiding phase unwrapping procedures is to acquire more than two scans, *e.g.*, one pair with a small echo time difference and a third scan with a larger echo time difference. By using multiple echo readouts, the scan times may remain reasonable, at least for the modest spatial reso-

---

[1] This section is based on [44]

lutions needed in fMRI. Therefore, we present a general model that accommodates more than two scans and describe a regularized least-squares field map estimation method using those scans. Section 4.3 shows the improvements both in the estimated field maps and the reconstructed images using multiple scans. This is shown first with simulated results in Section 4.3.1 and then using real MR data in Section 4.3.2.

4.2 Multiple Scan Fieldmap Estimation - Theory

4.2.1 Reconstructed Image Model

The usual approach to measuring field maps in MRI is to acquire two scans of the object with slightly different echo times, and then to reconstruct images $\boldsymbol{y}^0$ and $\boldsymbol{y}^1$ (without field correction) from those two scans, *e.g.*, [21, 65, 87]. We assume the following model for those undistorted reconstructed images is

$$\begin{aligned} y_j^0 &= f_j + \epsilon_j^0 \\ y_j^1 &= f_j \, \mathrm{e}^{\imath \omega_j \triangle_1} + \epsilon_j^1, \end{aligned} \tag{4.1}$$

where $\triangle_1$ denotes the echo-time difference, f_j denotes the underlying complex transverse magnetization in the jth voxel which is a function of the spin density, and ε_j denotes (complex) noise. The goal in field mapping is to estimate an (undistorted) field map, $\boldsymbol{\omega} = (\omega_1, \ldots, \omega_N)$, from $\boldsymbol{y}^0$ and $\boldsymbol{y}^1$, whereas $\boldsymbol{f} = (f_1, \ldots, f_N)$ is a nuisance parameter vector. This section reviews the standard approach for this problem, other approaches in the literature, and then describes a new and improved method.

4.2.2 Conventional Field Map Estimator

Based on (4.1), the usual field map estimator $\hat{\omega}_j$ uses the phase difference of the two images, computed as follows [47, 107]:

$$\hat{\omega}_j = \angle(y_j^{0*} y_j^1) / \triangle_1 \,. \tag{4.2}$$

This expression is a method-of-moments approach that would work perfectly in the absence of noise and phase wrapping, within voxels where $|f_j| > 0$. However, (4.2) can be very sensitive to noise in voxels where the image magnitude $|f_j|$ is small relative to the noise deviations. Furthermore, that estimate ignores our *a priori* knowledge that field maps tend to be smooth or piecewise smooth. Although one could try to smooth the above estimate using a low pass filter, usually many of the $\hat{\omega}_j$ values are severely corrupted so smoothing would further propagate such errors (see Fig. 4.2 top right). Instead, we propose below to integrate the smoothing into the estimation of $\boldsymbol{\omega}$ in the first place, rather than trying to "fix" the noise in $\hat{\boldsymbol{\omega}}$ by post processing.

4.2.3 Other Field Map Estimators

Although the conventional estimate (4.2) is most common, other methods for estimating field maps have appeared in the literature.

Different techniques have been proposed that incorporate field map acquisition with image acquisition ([87] for projection reconstruction and [88] for spiral scans). Chen *et al.* in [15] used multiple echos during EPI acquisition and used these distorted scans to create a final corrected undistorted image. Priest *et al.* in [100] used a two-shot EPI technique to obtain a field map for each image; this could prevent changes in the field map due to subject motion from being propagated through an entire fMRI time series.

Stand alone field map acquisition techniques have also been proposed. Windischberger *et al.* [132] used three echos and corrected for phase wrapping by classifying the degree of phase wrapping into seven categories. They then used linear regression to create a field map that is followed by median and Gaussian filtering. Reber *et al.* [101] used ten separate echo times and acquired distorted EPI images. They used a standard phase unwrapping technique of adding multiples of 2π and then spatially smoothed the image with a Gaussian filter. While these techniques both seek to use more echos to increase the accuracy of the field map, they have several disadvantages. Neither are based on a statistical model and, thus, do not consider any noise in developing their estimator. The filtering suggested by both techniques also adds additional blur. Aksit *et al.* [3] used three scans, the first two with a small echo time and no phase unwrapping and the third with a larger echo time. Two techniques were tried: 1) phase unwrapping by using the first two sets of data and 2) taking a Fourier transform to determine the EPI shift experienced. In phantom studies, using three scans yielded half to a third of the error of two scans. Because the estimator uses a linear fit, there is still error in voxels near phase discontinuities and along areas of large susceptibility differences.

An additional technique used to improve the conventional estimate is local (non-linear) fitting, *e.g.* [61, 106]. While this can improve the conventional estimate, we desire a more statistical approach.

Our technique is unique in that it uses a statistical model using multiple scans and operates without the constraint of linearity. By using a penalized-likelihood cost function, we can easily adjust the regularization parameter to control the amount of smoothing without any additional filtering step. By using a field map derived from the first two echos as the initialization for the iterative method (assuming the two echos are close enough together), no phase unwrapping is required. Our model also takes into account R_2^* decay, which was ignored in previous multiple echo techniques.

4.2.4 Multiple Scan Model

We now generalize the conventional model (4.1) to the case of multiple scans, *i.e.*, with more than one echo time difference. The reconstructed images are denoted here by $\boldsymbol{y}^0, \ldots, \boldsymbol{y}^L$, where L is the number of echo time differences. Because we are using multiple echo time differences, R_2^* decay may no longer be negligible and should be included in our model. Our model for these images is:

$$y_j^l = f_j \, \mathrm{e}^{\imath \omega_j \triangle_l} \, \mathrm{e}^{-R_j \triangle_l} + \varepsilon_j^l, \tag{4.3}$$

for $l = 0, \ldots, L$, where $\triangle_l$ denotes the echo time difference of the lth scan relative to the original scan *i.e.*, ($\triangle_0 = 0$), where j denotes the voxel number and where R_j denotes the value of R_2^* for the jth voxel. As in most field map estimation methods, this model assumes implicitly there is no motion between the scans. As in (4.1), f_j denotes the complex transverse magnetization and ε_j^l denotes the (complex) noise. If we choose the $\triangle_l$ values carefully, this data model allows for a scan that is free or largely free of phase wraps but which gives a phase difference lower in SNR, as well as scan(s) with wrapped phase but higher in SNR. Including the scan(s) with a larger echo time difference should help reduce noise in $\hat{\omega}_j$, whereas the wrap-free scan helps avoid the need for phase unwrapping tools.

4.2.5 Maximum-Likelihood Field Map Estimation

The conventional estimate (4.2) appears to disregard noise effects, so a natural alternative approach is to estimate $\boldsymbol{\omega}$ using a maximum likelihood (ML) method based on a statistical model for the measurements $\boldsymbol{y}$. In MR, the k-space measurements have zero-mean white gaussian complex noise [85], and we furthermore assume here that the additive noise values in $\boldsymbol{y}$ in (4.3) have independent gaussian distributions[2] with the same variance

---

[2] Independence in image space is an approximation. The noise values in k-space data are statistically independent, but reconstruction may produce correlations, especially in scans with non-Cartesian k-space imaging.

σ^2. Under these assumptions, the joint log likelihood for $\boldsymbol{f}$ and $\boldsymbol{\omega}$ given $\boldsymbol{y} = (y^0, \ldots, y^L)$ is

$$\begin{aligned} \log \mathsf{p}(\boldsymbol{y}; \boldsymbol{f}, \boldsymbol{\omega}) &= \sum_{l=0}^{L} \log \mathsf{p}\big(\boldsymbol{y}^l; \boldsymbol{f}, \boldsymbol{\omega}\big) \\ &\equiv \frac{-1}{2\sigma^2} \sum_{j=1}^{N} \sum_{l=0}^{L} \left| y_j^l - f_j \, \mathrm{e}^{\imath \omega_j \triangle_l} \, \mathrm{e}^{-R_j \triangle_l} \right|^2 , \end{aligned} \tag{4.4}$$

where "$\equiv$" denotes equality to within constants independent of $\boldsymbol{f}$ and $\boldsymbol{\omega}$. If the R_j values were known, the joint ML estimate of $\boldsymbol{f}$ and $\boldsymbol{\omega}$ could be solved by the following minimization problem:

$$\underset{\boldsymbol{\omega} \in \mathbb{R}^N, \boldsymbol{f} \in \mathbb{C}^N}{\arg\min} \sum_{j=1}^{N} \left\| \begin{bmatrix} y_j^0 \\ y_j^1 \\ \vdots \\ y_j^L \end{bmatrix} - \begin{bmatrix} 1 \\ \mathrm{e}^{\imath \omega_j \triangle_1} \, \mathrm{e}^{-R_j \triangle_1} \\ \vdots \\ \mathrm{e}^{\imath \omega_j \triangle_L} \, \mathrm{e}^{-R_j \triangle_L} \end{bmatrix} f_j \right\|^2 . \tag{4.5}$$

This problem is quadratic in f_j; minimizing over f_j yields the following ML estimate:

$$\hat{f}_j = \frac{\sum_{l=0}^{L} y_j^l \, \mathrm{e}^{-\imath \omega_j \triangle_l} \, \mathrm{e}^{-R_j \triangle_l}}{\sum_{l=0}^{L} \mathrm{e}^{-2 R_j \triangle_l}} . \tag{4.6}$$

Substituting this estimate back into the cost function (4.5) and simplifying considerably yields the following cost function used for ML estimation of $\boldsymbol{\omega}$:

$$\begin{aligned} \Psi_{\mathrm{ML}}(\boldsymbol{\omega}) \equiv & \sum_{j=1}^{N} \sum_{m=0}^{L} \sum_{n=0}^{L} \left| y_j^m y_j^n \right| \cdot w_j^{m,n} \cdot \\ & \big[1 - \cos\!\big(\angle y_j^n - \angle y_j^m - \omega_j (\triangle_n - \triangle_m) \big) \big] , \end{aligned} \tag{4.7}$$

where $w_j^{m,n}$ is a weighting factor that depends on R_2^* as follows:

$$w_j^{m,n} = \frac{\mathrm{e}^{-R_j (\triangle_m + \triangle_n)}}{\sum_{l=0}^{L} \mathrm{e}^{-2 R_j \triangle_l}} . \tag{4.8}$$

Similar weighting appeared in the weighted phase estimate proposed in [6] for angiography. The ML cost function $\Psi_{\mathrm{ML}}(\boldsymbol{\omega})$ is periodic, similar to cost functions used in phase unwrapping problems, *e.g.*, [76]. The cost function (4.7) appears to require either knowledge of or a good estimate of R_2^*. However, we note that:

$$\left|\mathsf{E}\left[y_j^m\right]\right| = |f_j| \left|\mathrm{e}^{-R_j \triangle_m}\right| ;$$

therefore, hereafter, we approximate $w_j^{m,n}$ as follows:

$$w_j^{m,n} \approx \frac{\left|y_j^m\right| \left|y_j^n\right|}{\sum_{l=0}^{L} \left|y_j^l\right|^2}. \tag{4.9}$$

This approximation does not require knowledge of R_2^* values.

There is no analytical solution for the minimizer, $\boldsymbol{\omega}$ in (4.7), except in the $L = 1$ case. Thus, iterative minimization methods are required, even for the ML estimator.

4.2.6 Special Case: $L = 1$ (Conventional Two Scans)

In the case where $L = 1$ usually $\triangle_1$ is chosen small enough that we can ignore R_2^* decay (*i.e.*, let $R_2^* = 0$) and the ML cost function in (4.7) simplifies to

$$\Psi_{\mathrm{ML}}(\boldsymbol{\omega}) \equiv \sum_{j=1}^{N} \left|y_j^0 y_j^1\right| \left[1 - \cos\left(\angle y_j^1 - \angle y_j^0 - \omega_j \triangle_1\right)\right] . \tag{4.10}$$

The ML estimate is not unique here due to the possibility of phase wrapping. But ignoring that issue, the ML estimate of $\boldsymbol{\omega}$ is $\hat{\omega}_j = (\angle y_j^1 - \angle y_j^0)/\triangle_1$, because $1 - \cos(t)$ has a minimum at zero. This ML estimate is simply the usual estimate (4.2) once again to within multiples of 2π. Thus the usual field mapping method (for $L = 1$) is in fact an ML estimator under the white gaussian noise model. The more general cost function (4.7) for the field map ML estimator for $L > 1$ is new to our knowledge.

4.2.7 Penalized-Likelihood Field Map Estimation

The ML estimator ignores our *a priori* knowledge that field maps tend to be spatially smooth functions due to the physical nature of main field inhomogeneity and susceptibility effects[3]. (We note that this assumption does not address the presence of signal from fat). A natural approach to incorporating this characteristic is to add a regularizing roughness penalty to the cost function. Here we regularize only the phase map $\boldsymbol{\omega}$ and not the magnetization map $\boldsymbol{f}$; we expect $\boldsymbol{f}$ to be far less smooth because it contains anatomical details. Such regularization is equivalent to replacing ML estimation with the following penalized-likelihood estimator:

$$(\hat{\boldsymbol{\omega}}, \hat{f}) = \arg\max_{\boldsymbol{\omega},\boldsymbol{f}} \sum_{l=0}^{L} \log \mathsf{p}\big(\boldsymbol{y}^l; \boldsymbol{f}\big) - \beta\, \mathsf{R}(\boldsymbol{\omega}),$$

where $\mathsf{R}(\boldsymbol{\omega})$ is a spatial roughness penalty (or log prior in a Bayesian MAP philosophy). Based on (4.6) and (4.7), after solving for $\boldsymbol{f}$ and substituting it back in, the resulting regularized cost function has the form

$$\Psi_{\mathrm{PL}}(\boldsymbol{\omega}) \triangleq \Psi_{\mathrm{ML}}(\boldsymbol{\omega}) + \beta\, \mathsf{R}(\boldsymbol{\omega}), \tag{4.11}$$

where we use the approximation (4.9) for $\Psi_{\mathrm{ML}}(\boldsymbol{\omega})$. This cost function automatically gives low weight to any voxels where the magnitude $\left|y_j^m y_j^n\right|$ is small. For such voxels, the regularization term will have the effect of smoothing or extrapolating the neighboring values. Thus, this approach avoids the phase "outlier" problem that plagues the usual estimate (4.2) in voxels with low signal magnitude. If $\boldsymbol{\omega}$ corresponds to a $N_1 \times N_2$ field map $\omega_{n,m}$, then a typical regularizing roughness penalty uses the second-order finite differences between

---

[3] There may be discontinuities at air/water boundaries. Even in this case, sharp boundaries can be problematic if there is motion between scans, further motivating the use of regularization.

horizontal and vertical neighboring voxel values as follows:

$$
\begin{aligned}
\mathsf{R}(\boldsymbol{\omega}) &= \sum_{n=1}^{N_1-1}\sum_{m=0}^{N_2-1}\psi(2\omega_{n,m}-\omega_{n-1,m}-\omega_{n+1,m}) \\
&+ \sum_{n=0}^{N_1-1}\sum_{m=1}^{N_2-1}\psi(2\omega_{n,m}-\omega_{n,m-1}-\omega_{n,m+1}), \qquad (4.12)
\end{aligned}
$$

where ψ is a convex "potential function." Here, we use the quadratic potential function, $\psi(t) = t^2/2$. In this paper, we used second-order differences for all results; we found that second-order finite differences are preferable to first-order differences because the resulting PSF tails decrease more rapidly even when the FWHM values are identical. A quadratic potential function has the advantage of being differentiable and easy to analyze, especially with Gaussian noise. Although quadratic regularization blurs edges, we assume the field map is smooth, so a more complicated potential function, such as using a Huber function [60], is not considered here.

Usually ψ is differentiable, so we can minimize the cost function $\Psi(\boldsymbol{\omega})$ either by conventional gradient descent methods or by optimization transfer methods [8, 63, 72]. In particular, in the usual case where $\dot{\psi}(t)\,/t$ is bounded by unity, then the following iteration is guaranteed to decrease $\Psi(\boldsymbol{\omega})$ monotonically:

$$
\boldsymbol{\omega}^{(n+1)} = \boldsymbol{\omega}^{(n)} - \mathsf{diag}\left\{\frac{1}{d_j + \beta\cdot c}\right\}\nabla\Psi(\boldsymbol{\omega}^{(n)}), \qquad (4.13)
$$

where ∇ is the gradient of the cost function,

$$
c \triangleq \begin{cases} 4, & \text{regularization with 1st-order differences} \\ 16, & \text{regularization with 2nd-order differences} \end{cases} \qquad (4.14)
$$

and

$$
d_j \triangleq \sum_{m=0}^{L}\sum_{n=0}^{L}\left|y_j^m y_j^n\right|\cdot w_j^{m,n}\cdot(\triangle_n - \triangle_m)^2, \qquad (4.15)
$$

using the approximation for w_j shown in (4.9). For examples in this paper, we used a similar minimization algorithm described in Appendix A because of its faster convergence properties.

To initialize $\boldsymbol{\omega}^{(0)}$, we used the regularized ML estimate (4.11) based on the first two sets of data $\boldsymbol{y}^0$ and $\boldsymbol{y}^1$. We choose the echo times to avoid phase wrapping between these sets of data (this same idea is used in [3] in their three-point method). Therefore, there is no need to apply phase unwrapping algorithms - the algorithm will converge to a local minimizer in the "basin" of the initial estimate [63].

In [37], we considered approximating the $1 - \cos$ term in (4.11) with its second-order Taylor series to create a penalized weighted least squares (PWLS) cost function. A simplified PWLS approach where the weights were thresholded was also considered. Those models ignore any phase wrap that may occur when evaluating (4.2). They also have increased error with little computational benefit. Therefore, those simplified methods are not explored further in this paper.

4.2.8 Spatial Resolution Analysis of Field Map Estimation

To use the regularized method (4.11) the user must select the regularization parameter β, which could seem tedious if one used trial-and-error methods. Fortunately, it is particularly simple to analyze the spatial resolution properties for this problem, using the methods in [35] for example. We make the second-order Taylor series approximation for this analysis. The local frequency response of the estimator using second-order finite differences at the jth voxel can be shown to be:

$$H(\Omega_X, \Omega_Y) \approx \frac{1}{1 + \frac{\beta}{d_j}(\Omega_X^2 + \Omega_Y^2)^p}, \tag{4.16}$$

where Ω_X and Ω_Y are the Discrete Space Fourier Transform (DSFT) frequency variables. and where $p = 1$ for regularization based on first-order differences and $p = 2$ for second-order finite differences as in (4.12). (See [119] for related analyses.) From (4.16) we see that the spatial resolution at each voxel depends on the data through d_j. In areas with small signal magnitudes, there will be more smoothing, as desired. The spatial resolution (4.16) also depends on the $\triangle_l$ values being used. Data from scans with larger $\triangle_l$ values have lower $\hat{\omega}_j$ variance (see (4.17) below), and will be smoothed less. However, data from these scans will also be affected by R_2^* decay through $w_j^{m,n}$ if the data is not scaled to compensate for this factor. To simplify selecting β, we normalize the data by the median of the square root of (4.15) using the approximation (4.9) for w_j. Normalizing by this factor allows us to create a standard β to FWHM table or graph (*e.g.*, Fig. 4.1). If this normalization were not applied, a similar figure would need to be calculated with each new data set (or at least with each new set of $\triangle_l$ values) or β would need to be chosen empirically. Normalizing based on the analytical result (4.16) enables us to use the same β for all scans.

We used the inverse 2D DSFT of (4.16) to compute the PSF $h[n, m]$ and tabulate its FWHM as a function of β, assuming the previous corrections were made and that the pixel j has $d_j = 1$. Fig. 4.1 shows this FWHM as a function of $\log_2(\beta)$, for both $p = 1$ and $p = 2$. The FWHM increases monotonically with β, as expected, although the “knees” in the curve are curious. Nevertheless, one can use this graph to select the appropriate β given the desired spatial resolution in the estimated field map. The resulting spatial resolution will be inherently nonuniform, with more smoothing in the regions with low magnitudes and vice versa. One could explore modified regularization methods [35] to make the resolution uniform, but in this application nonuniform resolution seems appropriate since the goals include “interpolating” across signal voids.

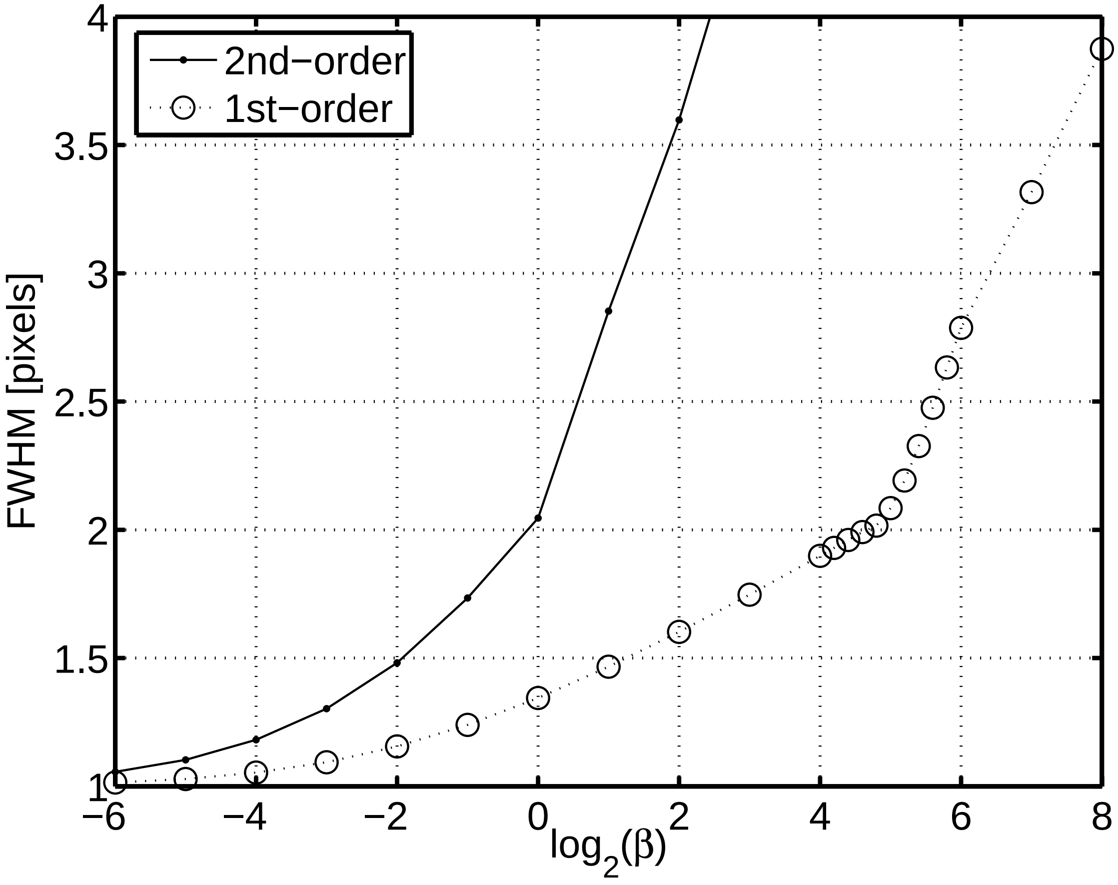

Figure 4.1: Angularly averaged FWHM of PSF. Shown for field map estimation as a function of $\log_2 \beta$ for $d_j = 1$ in (4.16).

4.2.9 Qualitative Example: $L = 1$

Fig. 4.2 shows an example of the data magnitude $\left|y_j^0\right|$ and the usual phase estimate based on $L = 1$ (4.2) which is very noisy. This is real data taken from a 3T MR scanner with $\triangle_1 = 2$ ms. The maximum value of $|\omega_j \cdot \triangle_1|$ is 1.61 radians in nonzero voxels, making the scan free of any phase wraps. Fig. 4.2 also shows the penalized-likelihood estimate based on (4.13) using two different values for β and using 150 iterations. Here, we can see the improvement from using a regularized estimator versus the conventional ML estimator. The effect of β on the smoothness of the estimate is also seen. The improvement seen is analyzed quantitatively in Section 4.3. Fig. 4.2 also shows the effective FWHM (in pixels) of the regularized algorithm based on (4.16) for both values of β. Most of the image has a FWHM corresponding to the chosen β based on Fig. 4.1. Areas of low magnitude have a much higher FWHM (such as the sinuses) and areas of high magnitude have the lowest FWHM.

4.2.10 Theoretical Improvements Over 2 Data Sets

Using more than two sets of data requires a longer data acquisition and also involves choosing the $\triangle_l$ values. Analyzing the theoretical improvements that may be attained by using multiple data sets can help determine when the increased acquisition time is warranted and can guide our choice of the $\triangle_l$ values. Therefore, we calculated the Cramér-Rao bound (CRB) for the model (4.3). This bound expresses the lowest achievable variance possible for an unbiased estimator based on a given model. Although a biased estimator (the penalized-likelihood estimator) is used in our implementation, the bound quantifies the maximal improvement possible based on the model and allows for a comparison on how close our implementation is to the ideal, unbiased case.

Because there are multiple unknown parameters in these models $\boldsymbol{\theta} = (\omega_j, |f_j|, \angle f_j)$,

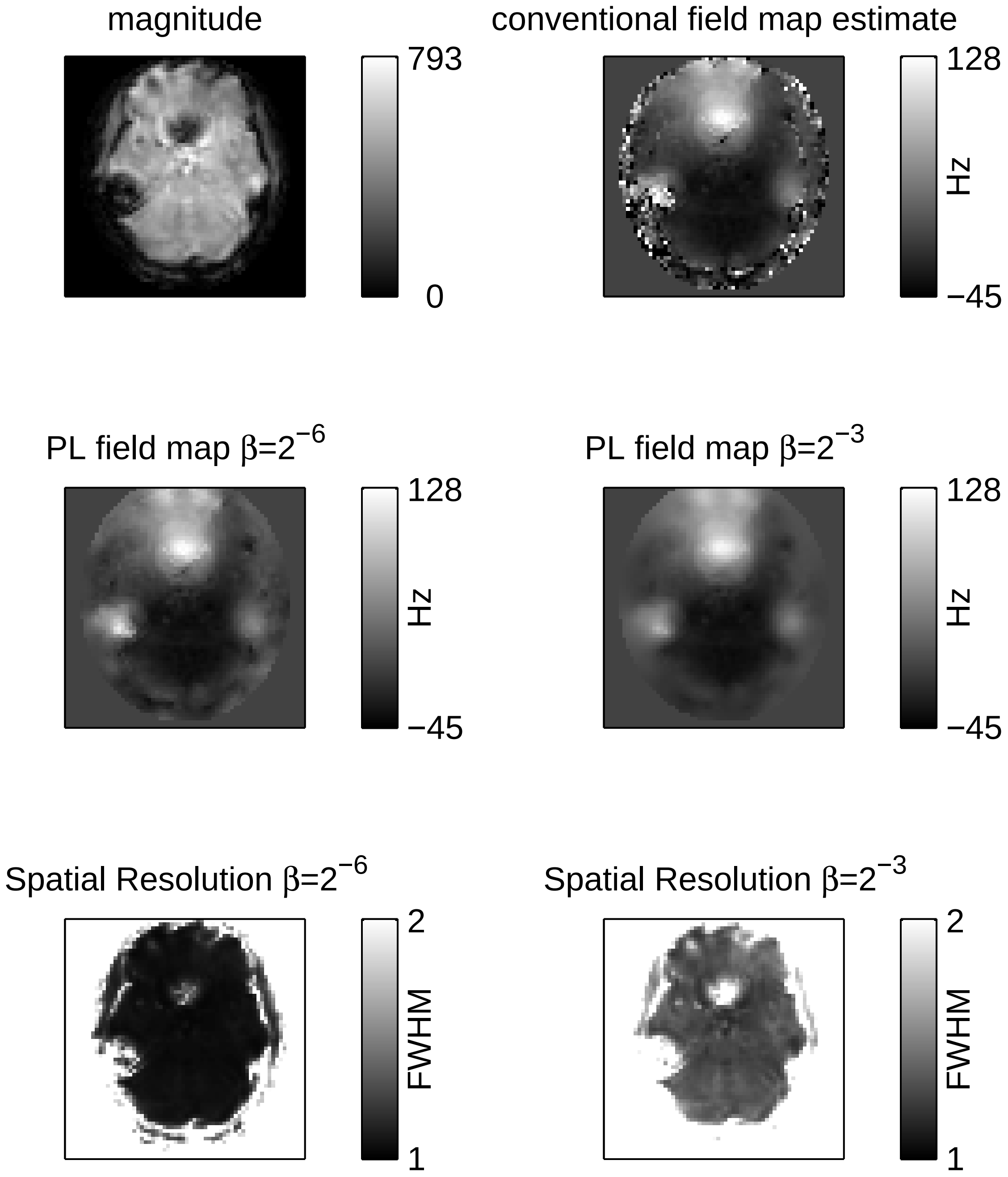

Figure 4.2: Field map estimate example. Top row: magnitude image $|y_j|$, conventional field map estimate(4.2). Middle row: (field map estimates): penalized-likelihood estimate using (4.13) with $\beta = 2^{-6}$ (left) and $\beta = 2^{-3}$ (right). Bottom row: Maps of the spatial resolution at each pixel measured by the FWHM for $\beta = 2^{-6}$ (left) and $\beta = 2^{-3}$ (right).

the multiple parameter CRB must be used. In that case, the matrix CRB is

$$\mathsf{Cov}_{\boldsymbol{\theta}}\left\{\hat{\boldsymbol{\theta}}\right\} \geq \mathbf{F}^{-1}(\boldsymbol{\theta})$$

where $\mathbf{F}(\boldsymbol{\theta}) = -\mathsf{E}[\nabla^2_{\boldsymbol{\theta}} \ln \mathsf{p}(\boldsymbol{Y};\boldsymbol{\theta})]$ is the Fisher information. Because f_j is a nuisance parameter, we focus on the CRB for the variance of ω_j, although the effect of f_j will be felt through the inversion of the Fisher matrix. For simplicity, we initially set R_2^* to 0 in the CRB derivations shown below.

Applying the CRB to the L echo-time difference model (4.3) yields, after considerable simplification, the expression:

$$\mathsf{Var}_L\{\hat{\omega}_j\} \geq \frac{\sigma^2}{(L+1)\,\triangle_1^2\,|f_j|^2\,\lambda_L}, \tag{4.17}$$

where, defining $\alpha_l = \triangle_l \,/\, \triangle_1$:

$$\lambda_L \triangleq \left(\frac{1}{L+1}\sum_{l=0}^{L}\alpha_l^2\right) - \left(\frac{1}{L+1}\sum_{l=0}^{L}\alpha_l\right)^2.$$

The variance reduces, in general, as L is increased. The expression for λ_L is the "variance" of $\{\alpha_0, \alpha_1, \cdots \alpha_L\}$, measuring the variance between the echo time differences. Increasing the variance (spread) of the $\triangle_l$ values will decrease the overall variance of the field map estimate.

For the $L = 1$ (2 sets of data) model, $\lambda_1 = 1/4$ and (4.17) simplifies to:

$$\mathrm{CRB}_1 \triangleq \frac{2\sigma^2}{\triangle_1^2\,|f_j|^2}.$$

As expected, the field map variance decreases when the signal strength $|f_j|$, or echo time difference $\triangle_1$, increase. For an unbiased estimator based on the model (4.3) with $L = 2$

(3 sets of data) one can show:

$$\mathrm{CRB}_2 \triangleq \frac{\mathrm{CRB}_1}{4/3(\alpha_2^2 - \alpha_2 + 1)}. \tag{4.18}$$

Interestingly, simply using three scans, but using $\triangle_2 = \triangle_1$ (or $\alpha_2 = 1$), would reduce the variance by only $4/3$.

From (4.18), increasing α_2 should decrease the variance for an unbiased estimator. Making α_2 arbitrarily large, however, is not advisable for many reasons. A larger α_2 creates more phase-wrapping. Eventually, the wrapping will lead to intra-voxel aliasing and the desired improvement would be unattainable. Another problem with large values of α_l is the effect on the MR pulse sequence length. A large α_2 also causes much more R_2^* decay in the signal as shown in (4.7). Choosing optimal $\triangle_l$ values requires some knowledge of R_2^* decay. This can be seen more clearly in the CRB bounds for the model (4.3) with R_2^* decay included. For the $L = 1$ model, one can show:

$$\mathsf{Var}_1\{\hat{\omega}_j\} \geq \mathrm{CRB}_1 \cdot \frac{1 + \mathrm{e}^{2R_j\triangle_1}}{2}. \tag{4.19}$$

For the $L = 2$ (3 sets of data) model:

$$\mathsf{Var}_2\{\hat{\omega}_j\} \geq \frac{\sigma^2}{\triangle_1^2 \, |f_j|^2} \frac{1 + \mathrm{e}^{-2R_j\triangle_1} + \mathrm{e}^{-2R_j\triangle_1\alpha_2}}{b}, \tag{4.20}$$

where

$$b \triangleq \mathrm{e}^{-2R_j\triangle_1} + \alpha_2^2 \, \mathrm{e}^{-2R_j\triangle_1\alpha_2} + (1 + \alpha_2^2 - 2\alpha_2) \, \mathrm{e}^{-2R_j\triangle_1(1+\alpha_2)}.$$

Using these expressions, we can optimize the $\triangle_l$ values, which will be inversely proportional to the value of R_2^*. In fact, for $L = 1$, one can show that the optimal choice is $\triangle_1^{\mathrm{opt}} = 1.11 \,/\, R_j$. Therefore, small values of α_l based on the amount of R_2^* decay expected should be used.

4.3 Experiments

4.3.1 Simulation: Comparison of $L = 1$ and $L = 2$ Methods

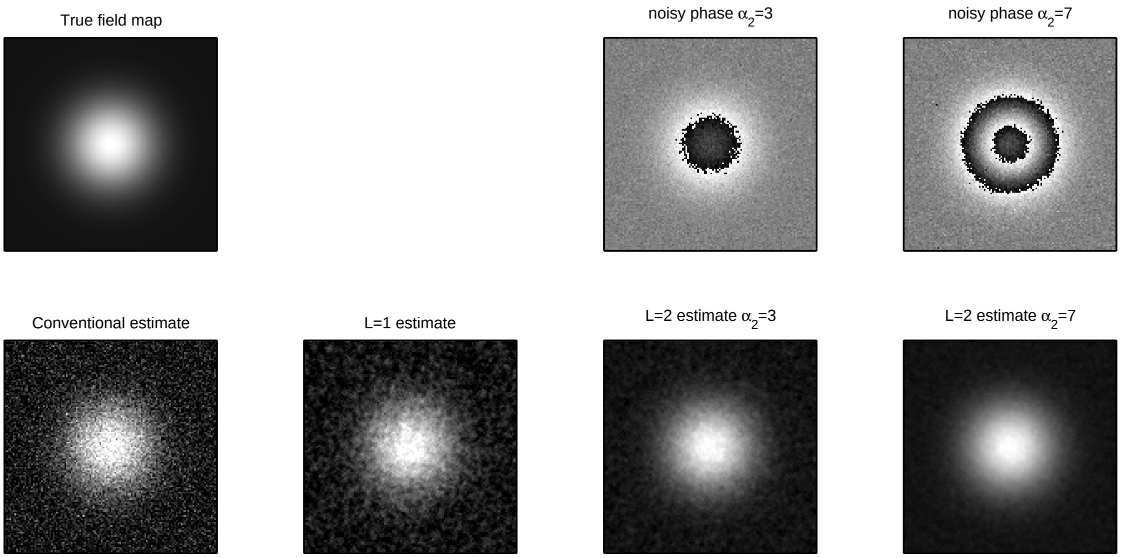

Figure 4.3: Field map Gaussian example. Top: "True" field map for Gaussian example in Hz; Noisy (SNR = 10dB) wrapped phase $\angle y_j^2$ with $\alpha_2 = 3$, Noisy (SNR = 10dB) wrapped phase with $\alpha_2 = 7$. Bottom: Conventional estimate for $L = 1$, PL estimates for $L = 1$, $L = 2$ with $\alpha_2 = 3$, and $L = 2$ with $\alpha_2 = 7$. All field maps and estimates are shown on a colormap of [-10 128] Hz. The wrapped phase images are shown on a colormap of [-π π].

We compared the $L = 1$ and $L = 2$ methods with two examples. First, we used a simulated Gaussian true field map (Fig. 4.3) with a magnitude map equal to unity at all points. Second, we simulated a brain example. For the magnitude, we used a simulated normal T1-weighted brain image [18, 70]. We generated a simple field map consisting of a 4.8 cm diameter sphere of air (centered around the nasal cavity) embedded in water using simple geometrical equations [51, 104], using a slice slightly above the sphere. Fig. 4.4 shows the field map and magnitude image $|f_j|$. We added complex Gaussian noise at many levels of SNR to the images. For this paper, we used the following definition of SNR:

$$\text{SNR} = 20 \log \frac{\|\boldsymbol{f}\|}{\|\boldsymbol{y}^0 - \boldsymbol{f}\|}. \tag{4.21}$$

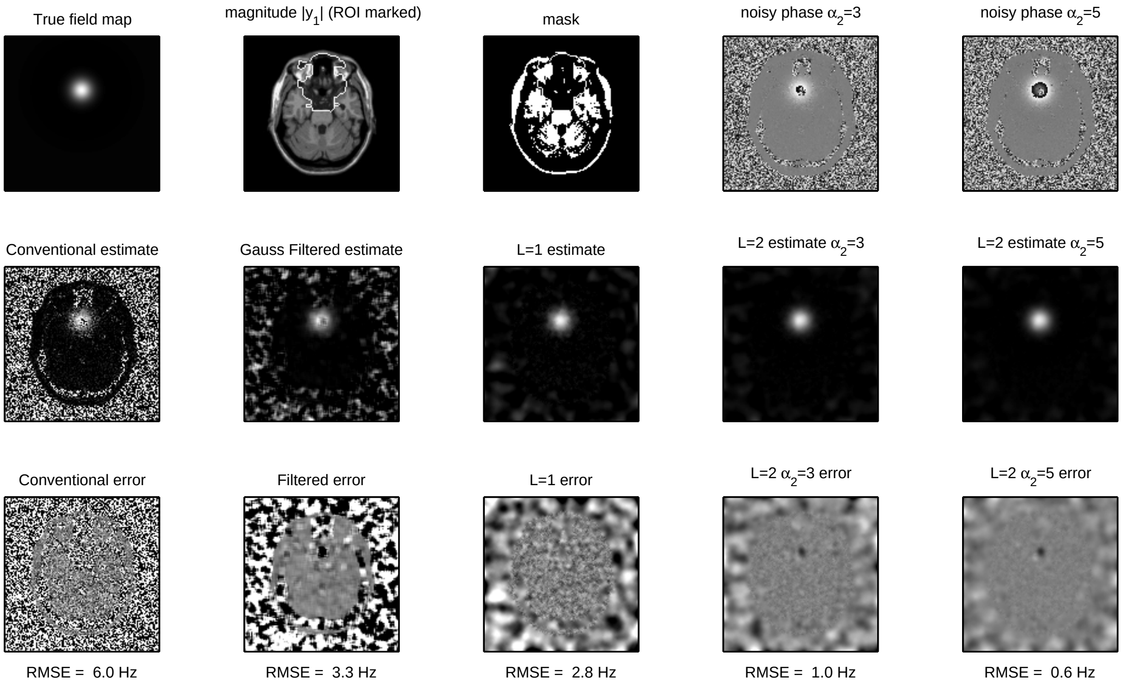

Figure 4.4: Field map brain example. Top: True field map and magnitude for brain example and mask, (SNR = 8.5dB) wrapped phase for $\alpha_2 = 3$ and $\alpha_2 = 5$ images. Center and Bottom: Conventional, Conventional convolved with a Gaussian filter, PL with 2 sets ($L = 1$), and PL with 3 sets ($L = 2$) for both $\alpha_2 = 3$ and $\alpha_2 = 5$ estimated field maps and their respective errors and RMSE. The wrapped phase images are shown on a colormap of [-π π]. All field maps and estimates are shown on a colormap of [-2 100] Hz. Field map errors are shown on a colormap of [-15 15] Hz.

The SNR remains consistent even when varying R_2^*, L, or α.

We used $\triangle_1 = 2$ msec for both cases. For the $L = 2$ case we also varied α_2 to produce several $\triangle_2$ values. We used a uniform value of $R_2^* = 20$ sec^{-1} in generating our simulations.

The field map was reconstructed using the penalized-likelihood method (4.11) using normalization as described in Section 4.2.8 for both $L = 1$ and $L = 2$. The algorithm (4.13) was run at each SNR level for the $L = 1$ case and for the $L = 2$ case of data with varying values of α_2 using 5 realizations. We ran 300 iterations of the algorithm, using $\beta = 2^{-3}$.

We also applied the conventional estimator to our data. To reduce the noise, we convolved the conventional estimate with Gaussian filters of varying widths ($\sigma = 0.0625, 0.1250, \ldots, 3.125$). We chose the "optimal" σ based on the minimum masked RMSE. Choosing the optimal σ using the true field map gives the conventional estimate an advantage in this example unavailable in practice.

The RMS error (in Hz) was computed between the "true" field map and the field map reconstructed using the PL method (4.11) and the conventional estimate. This RMSE was calculated in a masked region (pixels with magnitudes at least 20% of the maximum true magnitude).

Fig. 4.3 shows an example of the PL with $L = 1$ estimate compared to the PL with $L = 2$ estimate at $\alpha_2 = 3$ and $\alpha_2 = 7$ at an SNR of 10dB. Qualitatively, we can see improvements with increases in both L and α_2. Fig. 4.4 shows similar results for the brain example.

The largest errors in these field maps occur where the magnitude is smallest. The RMSE is much higher using only the conventional method. We also calculated the RMSE in the sinus region of the brain (the ROI is shown in Fig. 4.4). We chose this ROI because the low magnitude makes the field map difficult to estimate here although the field inhomogeneity is also greatest here. The RMSE in this ROI was 61.1 Hz for the conventional estimate, 11.6

Hz for the Gaussian filtered estimate, 3.4 Hz for the $L = 1$ regularized estimate, and 1.9 Hz for the $L = 2$ $\alpha_2 = 3$ regularized estimate and 1.7 Hz for the $L = 2$ $\alpha_2 = 5$ regularized estimate. Overall, the filtered conventional estimate performed similar to the PL method with $L = 1$ over the masked region, but had higher error in the ROI. The PL method with $L = 2$ showed a decreased error in both the masked region and the ROI. We would expect even higher improvement over any practical Gaussian filtered estimate because a suboptimal σ would be used. The proposed regularized estimators are more accurate in pixels with low magnitude. Adding additional scans ($L > 1$) makes the PL estimate even more accurate.

Fig. 4.5 shows the improvement (defined as the RMS error for PL estimate with $L = 1$ divided by the error for PL estimate with $L = 2$) gained by using an additional set of data for the Gaussian example. For comparison, we also plotted the predicted improvement, given by the square root of the ratio of the expressions (4.19) and (4.20). The experimental gains are actually higher than the improvements anticipated as shown by the dotted lines (the predicted improvement) for some SNR values. Because this is a ratio of RMSEs and the amount of bias can vary between $L = 1$ and $L = 2$, the unbiased CRB provides a benchmark of expected ratios rather than an exact upper limit. Also, recall that (4.19) and (4.20) considered R_2^* to be a known value when, in fact, R_2^* is unknown and approximated through (4.9). The RMSE is low (in voxels with large magnitudes) at high SNRs using either $L = 1$ or $L = 2$. At lower SNRs, however, including in voxels with low magnitudes, using $L = 2$ and higher values of α_2 greatly reduces RMS error. We repeated these simulations with $R_2^* = 0$ (results not shown) and the empirical improvement almost exactly matched (4.18).

Fig. 4.6 shows the improvement gained by using an additional set of data for the brain image. For a low SNR (for example 10 dB), the improvements are close to expected. The brain image has some areas where the magnitude is very low, making estimation using any method quite challenging. In addition, the field map phase itself is less smooth than in the

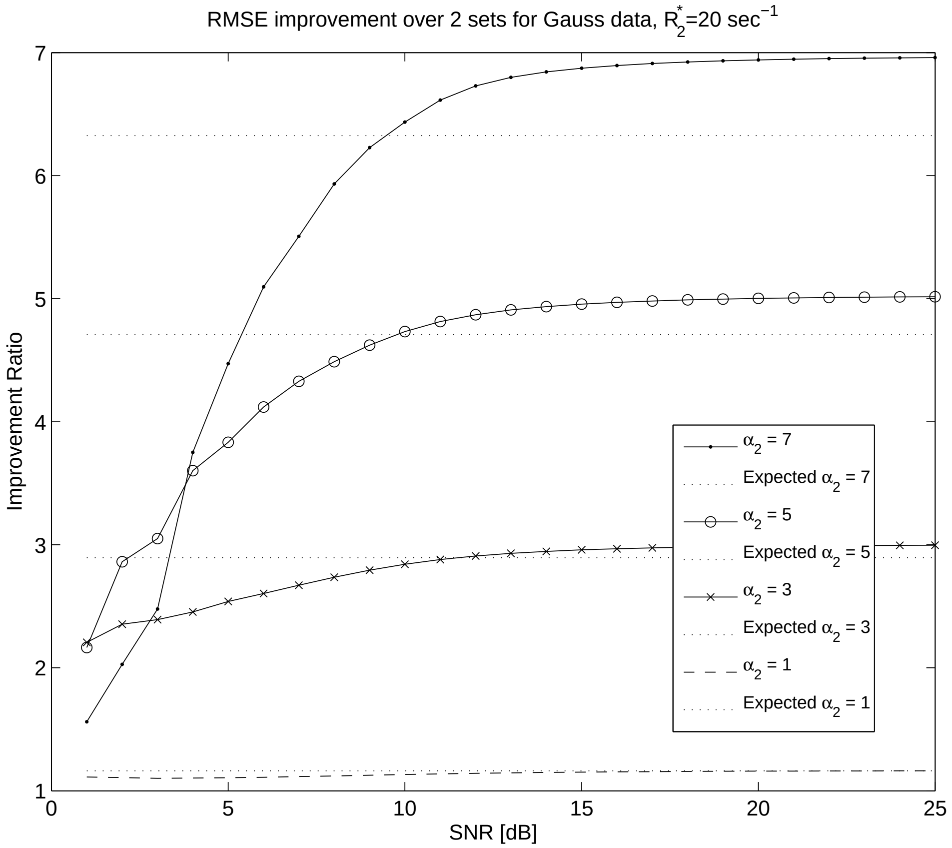

Figure 4.5: Improvement in the RMSE for the Gaussian example by using 3 data sets rather than 2 sets. Expected improvements shown by dotted lines.

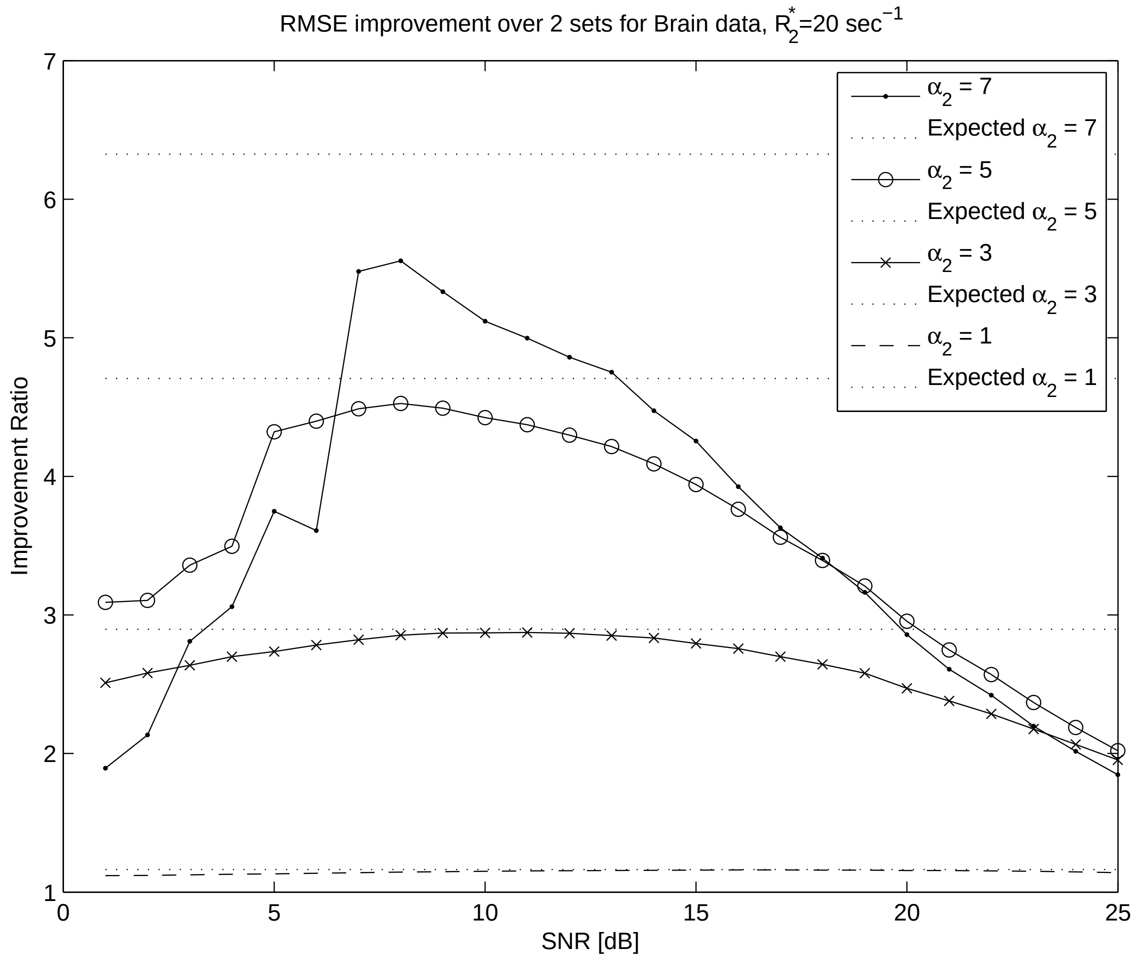

Figure 4.6: Improvement in the RMSE for the brain example by using 3 data sets rather than 2 sets. Expected improvements shown by dotted lines.

Gaussian case, making the estimation more difficult. For a higher SNR (for example 20 dB), the 3-set case still outperforms the 2-set case substantially but by less than predicted by (4.18).

The RMSE has components of both bias error and variance in it, as shown below:

$$\mathrm{RMSE(X)} = \sqrt{\mathsf{Var}\{X\} + \mathrm{bias}^2(X)}.$$

Therefore, we analyzed the bias and the standard deviation at a single representative SNR = 20 dB and at α_2 = 1, 2, $\ldots$7 using 500 iterations and 100 realizations for each factor. Fig. 4.7 compares the standard deviation for each α_2 relative to that at α_2 = 1 and the empirical improvements were compared to those predicted by the CRB (4.20) for the Gaussian example. As expected, the improvements in variance are very close to predicted. Here, the bias is also very low at all levels of SNR - explaining the improvement seen in RMSE in Fig. 4.7.

Fig. 4.8 shows the bias and standard deviation for a signle SNR = 20 for the brain example. The empirical variances were close to those expected. The bias, however, introduced in part by the regularization, was nearly constant (independent of α). So for large values of α_2, the bias begins to dominate the variance in RMSE calculations, explaining Fig. 4.6.

Overall, the variance reductions in both examples due to using three echo times were close to the results predicted by the CRB. For low values of α_2 (*i.e.*, five or less), the expected benefit using $L > 1$ holds even with a moderate value of R_2^*. The RMSE reductions are largest at lower SNRs. For phase estimation, the local SNR depends on the spin density of each voxel as seen in (4.17). Voxels with lower spin density effectively have lower SNR. It is precisely in these voxels where using 3 or more scans has the greatest benefit.

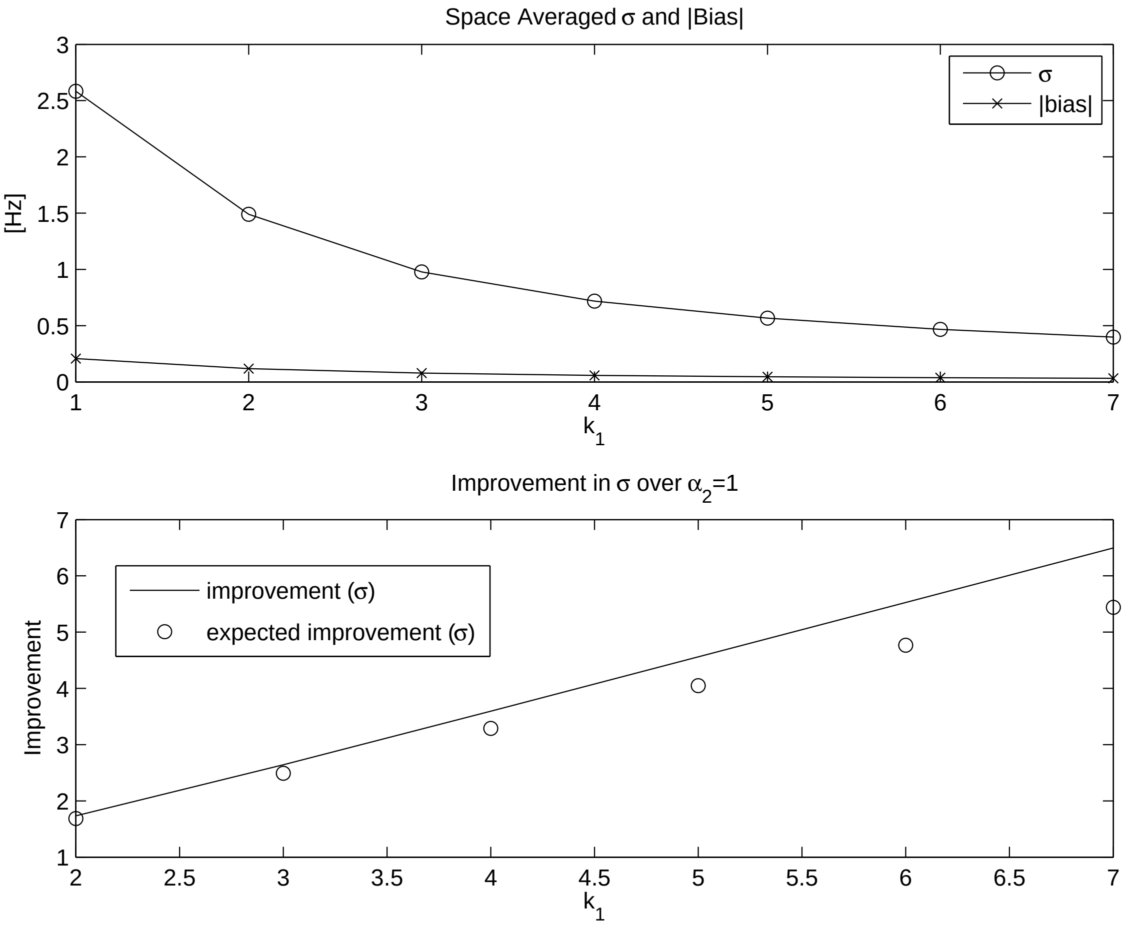

Figure 4.7: Bias and RMSE improvement for Gaussian example. Top: Space-averaged σ and absolute bias for several α_2 values; Bottom: RMSE improvement, empirical and expected, over α_2 = 1 for several α_2 values.

Table 4.1: Phantom NRMSE for two representative slices

Phantom NRMSE (%) for one realization								
	Slice One				Slice Three			
	Whole Image		Low Magnitude		Whole Image		Low Magnitude	
	μ	σ	μ	σ	μ	σ	μ	σ
No Field Map	31.1	-	4.8	-	20.4	-	2.9	-
Conventional	15.0	0.5	6.8	0.6	15.5	0.2	2.2	0.1
Gauss Filter	14.3	0.4	6.1	0.4	15.1	0.2	1.9	0.08
L=1	13.0	0.4	4.0	0.4	15.2	0.2	1.8	0.04
L=2 $\alpha_2 = 2$	13.1	0.4	4.1	0.4	14.8	0.1	1.8	0.03
L=2 $\alpha_2 = 5$	13.5	0.08	4.3	0.2	14.6	0.02	1.8	0.01
L=3	13.5	0.09	4.4	0.1	14.6	0.02	1.8	0.01

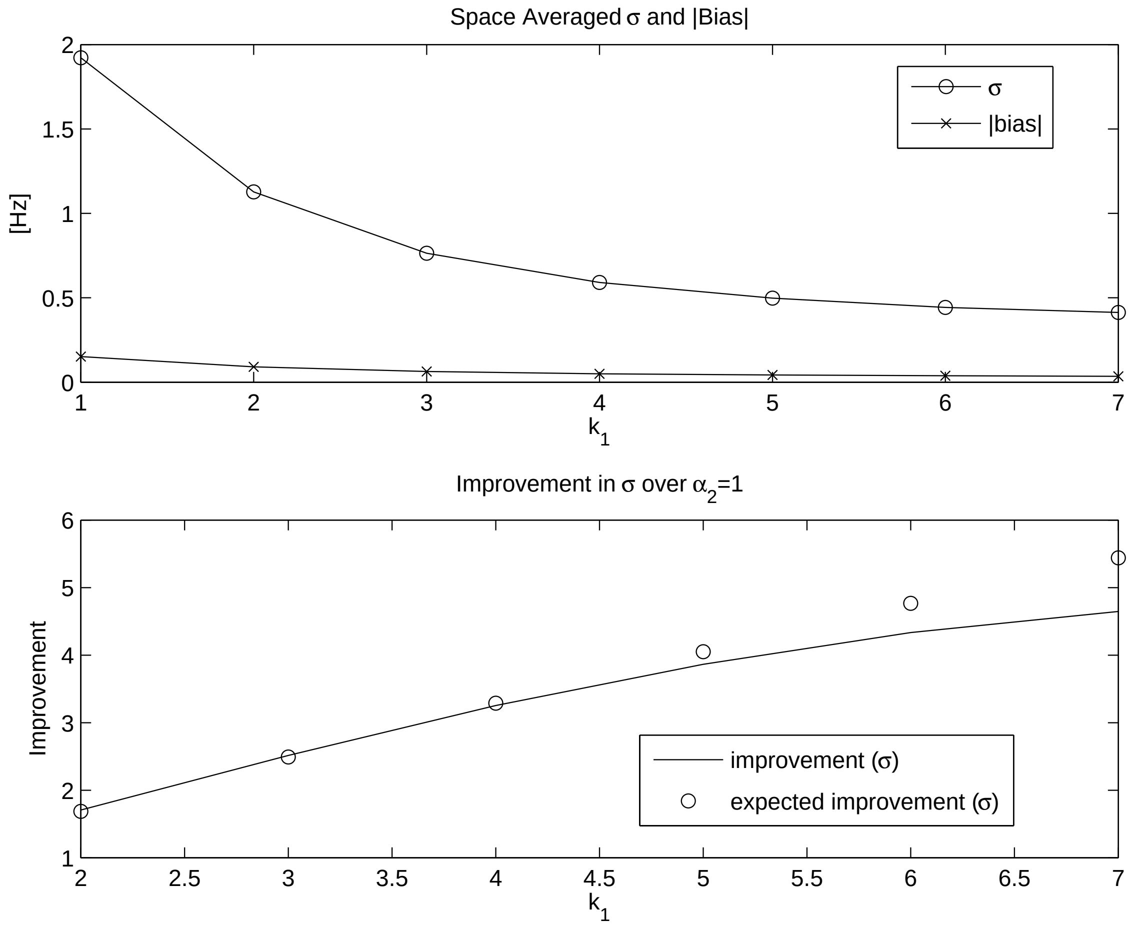

Space Averaged σ and |Bias|

Improvement in σ over α_2=1

Figure 4.8: Bias and RMSE improvement for brain example. Top: Space-averaged σ and absolute bias for several α_2 values; Bottom: RMSE improvement, empirical and expected, over α_2 = 1 for several α_2 values.

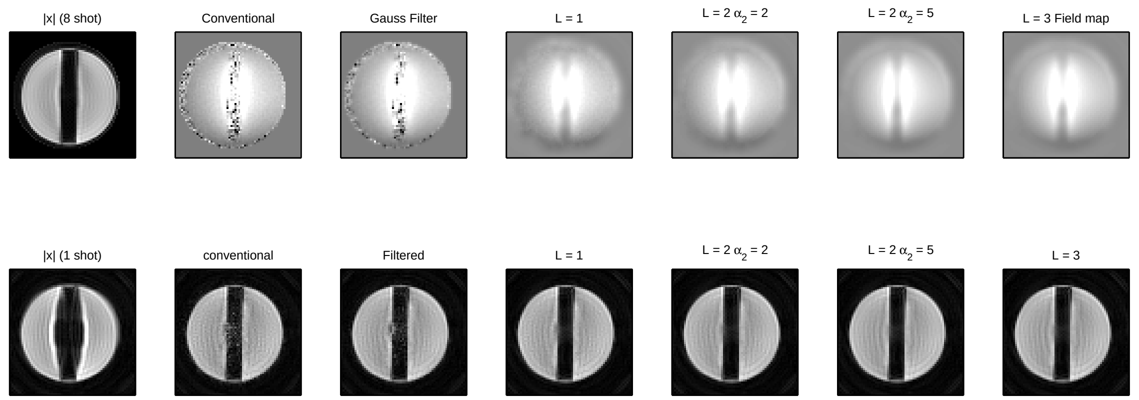

Figure 4.9: MR phantom data field map reconstructed using proposed method. First Slice - Top: Reconstructed 8-shot image, Conventional field map, Gaussian filtered field map, regularized field map L=1, regularized field map L=2; $\alpha_2 = 2$, regularized field map L=2 $\alpha_2 = 5$, regularized field map L=3. The field maps are displayed with a common color scale from -35 Hz to 50 Hz; Bottom: Reconstructed one-shot image with no field map and with each of the field maps above. The images are all on the same color scale. These are all from one representative realization.

4.3.2 MR phantom data: Application to Spiral Trajectories

To illustrate how improved field map estimation leads to improved reconstructed images, we used field maps produced by the conventional method (4.2) and produced by the PL method with three scans (4.11) to correct real spiral MR data for field inhomogeneities. We imaged a phantom with large field inhomogeneity. We used a spiral-out trajectory with a TE of 30 ms, TR of 2 sec, and a flip angle of 90 degrees. We took six slices spaced 5 cm apart over the 15 cm field of view. First, we collected data to create the field maps (using eight interleaves to minimize the effect of the field inhomogeneity) at the original 30 ms, as well as at 32 ms ($\triangle_1 = 2$ ms) and at 34 ms ($\triangle_2 = 4$ ms) and at 40 ms ($\triangle_2 = 10$ ms). We took ten realizations for each echo difference. We reconstructed iteratively the resulting 64×64 pixel images in a masked region using [36]. Then, we used these images to create (for each slice) a conventional field map (4.2), a conventional field map blurred with a Gaussian filter, a PL field map with $L = 1$, a PL field map with $L = 2$ and $\alpha_2 = 2$, a PL field map with $L = 2$ and $\alpha_2 = 5$, and a PL field map with $L = 3$, (4.11). We used $\beta = 2^{-6}$

for the regularized iterative algorithm and $\sigma = .5$ for the Gaussian filter approach, approximately matching the FWHM of the two approaches. Finally, we collected one-shot spiral out data with TE = 30 ms. This scan is thus much more affected by final inhomogeneity. We collected two realizations and then averaged them in k-space. We first reconstructed this data iteratively without a field map as in [36]. Uncorrelated field inhomogeneity causes a blurred image for spiral trajectories. Finally, we iteratively reconstructed this one-shot data with each of the field maps previously created as in [114].

Fig. 4.9 shows one representative slice. The regularized field maps are less noisy than the conventional one, especially in areas of low magnitude and along the edges. Fig. 4.9 illustrates the blur and distortion in the one-shot image reconstructed without a field map. The images reconstructed with a field map do not have this blur. Nevertheless, a noisy field map can cause error in the reconstructed image. For example, in Fig. 4.9, the image reconstructed with the conventional field map shows more artifacts than the eight-shot data or either of the images reconstructed with regularized field maps. Using the eight-shot data as “truth”, we computed the NRMSE of each image and Table 4.1 shows the mean and variance over the ten realizations. We include data from two representative slices to show a range of values, although slice three is not shown. In addition, we calculated the NRMSE in the one-shot reconstructed images in pixels where the magnitude is less than $.2$ times the maximum pixel value of the eight-shot reconstructed image to see if the regularized field maps reduce errors in areas of the image with low magnitude. This is also reported in Table 4.1. We use the norm of the eight-shot 30 ms image for normalization. The regularized iterative PL methods have a lower RMSE and much less variability than the other methods. Therefore, these regularized methods (especially with more than one echo time) give a very reliable estimate of the field map with little variability.

4.3.3 Application to EPI Trajectories

The search for more accurate field map estimation methods is motivated by fast MR imaging, such as echo-planar imaging (EPI) and spiral imaging used in fMRI. Because these methods use long readout times, B_o field inhomogeneities or magnetic susceptibilities become more pronounced. Without any correction for a non-uniform field, the resulting reconstructed images will have artifacts. Using field map correction will result in an improved MR image [32,74,75]. More accurate field maps, as produced using the methods in this paper, should further decreases the artifacts, resulting in an improved final MR image.

To illustrate how improved field map estimation leads to improved images that are reconstructed with field correction, we used field maps produced by the conventional method (4.2) and by two scans as well as three scans (4.11) using α_2 = 5 with $R_2^* = 20$ sec^{-1} with 150 iterations, to correct simulated EPI data for field map inhomogeneities. We used a readout length of 30ms with a matrix size of 64x64 for the simulations and used the iterative method for reconstruction explained in [114].

Fig. 4.10 has a simple field map of a square inside an oval using $\beta = 2^{-6}$. Here, RMSE was calculated in the oval region. This simpler field map makes visual analysis of the field maps and their errors easier to judge. Again, the conventional field map estimate has much more noise, especially in areas of low magnitude. The two scan field map has a much more accurate field map with lower overall RMSE. The three scan field map is also included here. The overall error is again much lower and the image is less noisy than the two-scan field maps.

We generated k-space data for an EPI trajectory using these simulated field maps and a magnitude with a grid phantom. Fig. 4.11 shows the results of the field map correction on the reconstructed image. With no field map correction, several shifts occur to the grid. Using the true field map for the field map correction creates the true image with a clean grid. The conventional field map, although an improvement over no field map correction, still has large artifacts at all locations where the magnitude is small. The images using the

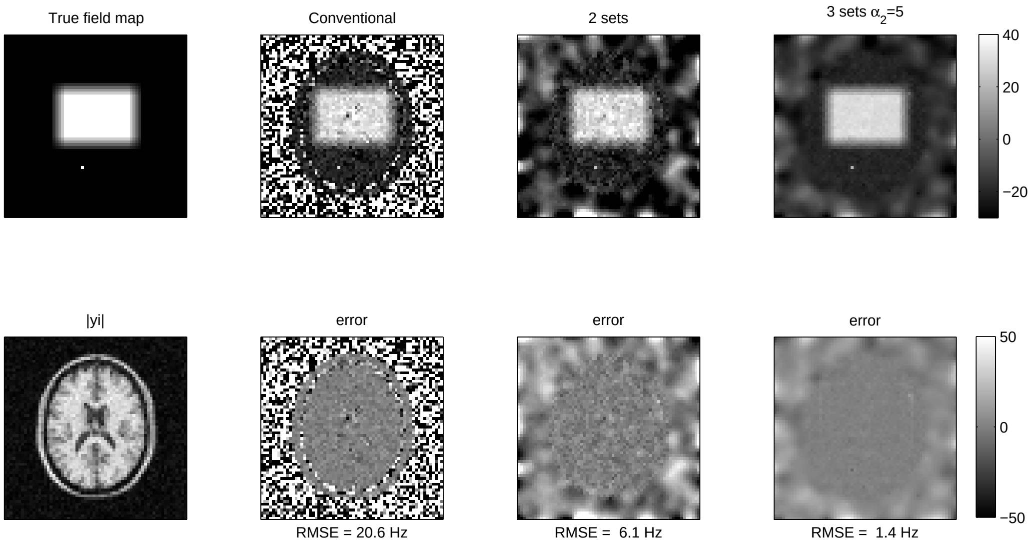

Figure 4.10: Simple field map to correct a simulated EPI trajectory. Top row: simple field map and estimated field map. Bottom row: brain image and field map error images.

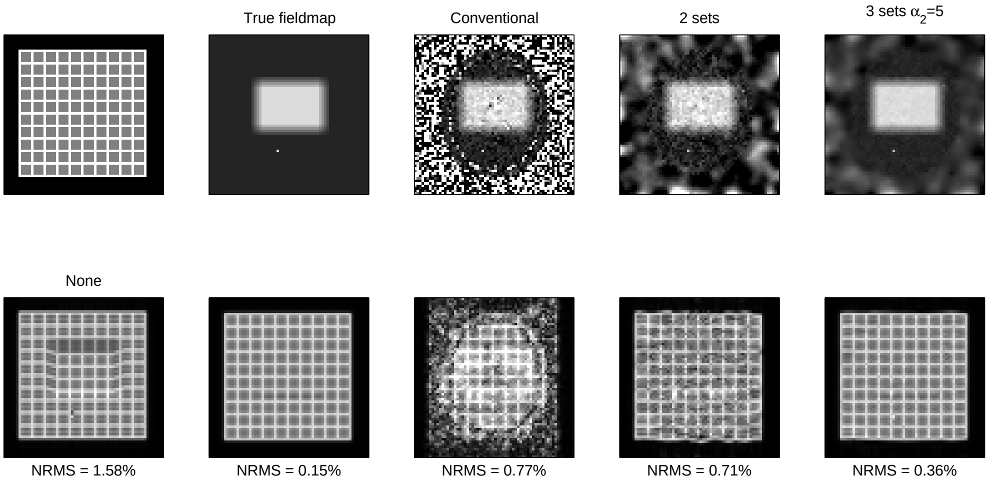

Figure 4.11: Grid phantom to show effects of proper field map correction. Top row: Grid phantom and estimated field maps from Fig. 4.10. Bottom row: Reconstructed images using no field map correction; correct field map; conventional estimate; 2 sets estimate; 3 sets estimate with α_2=5

two scan and the three scan field maps for the correction have less artifacts.

As can be seen in the reconstructed images, omitting corrections for magnetic field inhomogeneities dramatically affects the final image quality. Using a simple, conventional field map estimate corrects for some of the problems, but still introduces image artifacts, especially in areas of very low magnitude where field map errors begin to dominate. These images show the dramatic improvements made by an improved field map. Using the methods introduced in this paper to create more accurate field maps gives much more accurate reconstructed images.

4.3.4 Fieldmap estimation in k-space

The methods described above estimate the fieldmap from two or more *reconstructed* images. To work well, those images should be relatively free of artifacts, blur, and distortions, necessitating appropriate data acquisition types. For pulse sequences with long readout times, it may be more appropriate to estimate the fieldmap directly from the raw k-space data. A typical scenario is that we can collect two sets of k-space data, with slightly different echo times, from which we want to estimate the fieldmap $\boldsymbol{\omega}$ and the baseline magnetization $\boldsymbol{f}$. A reasonable model for the data is:

$$\mathsf{E}\left[y_i^{(l)}\right] = \int f(\vec{\mathrm{x}})\, \mathrm{e}^{-\imath\,\omega(\vec{\mathrm{x}})(t_i+\triangle_l)}\, \mathrm{e}^{-\imath 2\pi\vec{\nu}_i\cdot\vec{\mathrm{x}}}\, \mathrm{d}\vec{\mathrm{x}},\ l = 0, 1, \ldots L.$$

This is a joint estimation problem like that described in [115]. One can define a cost function in terms of $\boldsymbol{f}$ and $\boldsymbol{\omega}$, and then alternate between holding $\boldsymbol{\omega}$ fixed and minimizing over $\boldsymbol{f}$ (using the CG method) and then holding $\boldsymbol{f}$ fixed and minimizing over $\boldsymbol{\omega}$ (using steepest descent [115] or linearization [96] or optimization transfer methods akin to [33]). These k-space methods require considerably more computation than the image domain methods, so one should first apply an image-domain method to get a reasonable initial estimate of the fieldmap $\boldsymbol{\omega}$.

4.4 Discussion

We described a regularized method for field map estimation using two or more scans: the penalized-likelihood method (4.11). This method yields field maps that interpolate smoothly over regions with low spin density, thereby avoiding phase outliers that plague the conventional estimate (4.2). The method has been used with $L = 1$ (without full description) in [93, 115, 139].

Our analysis also shows that the conventional estimate (4.2) is in fact the ML estimate, a property that has previously gone unnoticed to our knowledge.

We also analyzed the spatial resolution properties of this method, leading to a practical procedure for choosing the regularization parameter to achieve a given desired spatial resolution.

We studied the CRB on the variance of the estimate for this method and found that our empirical simulation results for the PL method compared favorably, showing a reduction in the RMSE in comparison to using only two scans.

We collected real MR phantom data and created conventional and PL estimates of the field map which were used to reconstruct final images. The PL estimate reduces image artifacts caused by the field inhomogeneity and has a reduced RMSE, especially in areas of very low magnitude where the conventional estimate has many errors. Omitting or using a poor field map estimate for image reconstruction can dramatically affect the final image quality.

As noted in Section 4.2.4, our cost function assumes, as do most other field map estimation problems, that there is no motion between scans. While our analysis indicated that a larger L is better in terms of variance, motion could be a problem during the larger time required for L echo time differences. Practically, $L = 1$ or $L = 2$ are the most likely choices for L and here motion is less likely to be an issue. If a larger number of echo differences are desired, then the cost function could be further generalized to include a joint estimation of the field map and rigid motion parameters.

We have focused here on the case of a single receive coil. It is straightforward to generalize the method for phased array coils, *cf.* [80].

Although we did not estimate R_2^*, we used a simple weighting (4.9) in our algorithm to partially account for R_2^* decay; the improvements seen over estimation with two scans are still large, especially when using a small value of α_2.

While this method assumed the first two echo time differences were close enough to prevent phase wrapping, this method could, with proper intialization, extend to data with larger echo time differences and some phase wrapping. This is especially interesting at higher field strengths where wrapping still exists at low echo time differences.

Overall, this method has potential to be a reliable estimator for MR field maps, able to utilize many scans to produce a good estimate. The general penalized-likelihood approach in this work is also applicable to estimating other parametric maps in MRI, such as relaxation maps [46] and sensitivity maps [138]. It may also be useful for phase unwrapping problems with noisy data. In some cases, it may be preferable to use edge-preserving regularization in (4.12), such as the Huber potential function [141].

Ultimately, this method is a tool that may help answer the main question of field mapping: how to best allocate scan time to achieve the most accurate field map. The preliminary CRB analysis guides choice of echo times given a set number of scans. In future work, we wish to further explore the relationship between number of echoes, signal to noise ratio, and spatial resolution.

CHAPTER V

B_1^+ Map Estimation

5.1 Introduction

In [1] MRI, RF transmit coils produce non-uniform B_1 field strengths, creating varying tip angles over the field of view. In particular, as B_0 increases, the RF wavelength shortens, causing more B_1 inhomogeneity. Measured inhomogeneity ranges from 30-60% [20, 112, 120] at high field strengths ($B_0 \geq 3$T). In fact, B_1 is inherently inhomogeneous, both in magnitude and phase, because there is no solution to Maxwell's equations for a uniform RF field over a whole volume at high frequency [56]. Uncorrected, non-uniform tip angles cause spatially varying signal and contrast in the image. The field inhomogeneity can also degrade quantification, such as in measuring brain volumes [145].

A map of the B_1^+ field strength, called a B_1^+ map, is essential to many methods to help minimize and correct for this inhomogeneity. For example, tailored RF pulses such as [102, 111] require use of a B_1^+ map. Other techniques, such as myocardial perfusion imaging [59] also require a B_1^+ map. At high fields (≥ 3T), a B_1^+ map allows for proper pre-scan calibration [20]. In parallel transmit excitation (using a coil array), *e.g.*, [67, 108, 134, 135, 142, 143, 145, 148], one must have a map of the B_1^+ field strength and phase for RF pulse design.

A conventional approach to B_1^+ mapping is to collect two scans, one of which uses

---

[1] This section is based on several conference publications: [41–43].

twice the RF amplitude of the other, *e.g.*, [2, 12, 20, 127, 128]. Using the double angle formula, a standard method-of-moments estimator is used that ignores noise in the data. This estimator performs poorly in image regions with low spin density. This simple approach also does not allow for more than two angles nor does it account for more complicated physical factors such as slice selection effects.

We propose a new approach that incorporates multiple coils and multiple tip angles as well as accounts for noise in the model. This model also incorporates the RF excitation pulse envelope to account for slice selection effects. The iterative regularized estimator estimates the unknown complex B_1^+ map from multiple reconstructed images. The subsequent sections first review the standard approach for this problem, and then describe our new and improved method with examples of the improved B_1^+ maps.

5.2 B_1^+ Map Estimation: Theory

5.2.1 Conventional B_1^+ map

The double angle method (DAM), a conventional approach to B_1^+ mapping, uses two scans, one of which uses twice the RF amplitude of the other. A model for the reconstructed images is

$$\begin{aligned} y_{j1} &= f_j \sin(\alpha_j) + \varepsilon_{j1} \\ y_{j2} &= f_j \sin(2\alpha_j) + \varepsilon_{j2}, \end{aligned} \tag{5.1}$$

where y_{jl} denotes the complex image value in the jth voxel for the lth scan ($l = 1, 2$), f_j denotes the unknown object value and α_j is the unknown tip angle at the jth voxel. Estimating α_j is equivalent to estimating the B_1^+ field strength magnitude at the jth voxel.

Using the double angle formula:

$$\frac{\mathsf{E}[y_{j2}]}{\mathsf{E}[y_{j1}]} = \frac{\sin(2\alpha_j)}{\sin(\alpha_j)} = 2\cos(\alpha_j)\,.$$

The standard estimate of α_j is a method-of-moments estimator that ignores the noise in the data:

$$\hat{\alpha}_j = \arccos\left(\frac{1}{2}\left|\frac{y_{j2}}{y_{j1}}\right|\right). \tag{5.2}$$

This method has several limitations. First, it performs poorly in image regions with low spin density, *i.e.*, where y_{j1} is small. It suffers from 2π ambiguities if α_j is too large, yet it would be sensitive to noise if α_j is too small. Additionally, repeatibility for small α_j (under $20°$) is poor [112]. The solution to the added noise ignored by the model is usually low-pass filtering, which must be fine-tuned. Low pass filtering can corrupt neighbors of pixels with small α_j or f_j values. The estimator (5.2) also does not immediately generalize to the case where we acquire multiple scans to cover a larger range of tip angles, possibly even angles that are larger than 2π in some image regions. The estimate (5.2) also does not provide phase information and most methods do not incorporate any phase estimate.

Finally, the estimate (5.2) does not take into account any information about the excitation pulse, thus ignoring slice selection effects. The model shown in (5.1) assumes a linear relationship between the pulse amplitude and the flip angle. Such linearity holds for a non-selective pulses but is only an approximation for slice selective pulses. According to [110], the linear approximation is adequate for sinc pulses up to 140 degrees, but using a non-ideal pulse such as a Gaussian would decrease the accuracy even further. The effects of using a finite pulse also cause residual error, but are not accounted for in published methods. Different slice profiles affect the aboslute flip angle as well as the flip angle distributions throughout the sample [126].

The model (5.1) usually requires a very large TR so that f_j is the same for both y_{j1}

and y_{j2} (*i.e.*, the effects of both T_1 and T_2 relaxation are negligble). For an object with a known T_1 value or known T_1 map, one can generalize the model (5.1) to include the effects of T_1, *e.g.*, [143]. Some papers, such as [128], using the conventional model (5.1) suggest that shorter TR values can be used. Sequences have been suggested that can shorten scan time and enable rapid B_1^+ mapping, such as [20]. Some fast methods have been developed that concurrently estimate or correct the B_1 field, (*e.g.*, [24]) to circumvent the difficulty of a quick direct mapping. Some methods have been developed that are "T_1 oblivious" over the relevant range of T_1 values (*e.g.*, [39]) to circumvent needing T_1 information at all. All current B_1^+ mapping have disadvantages that need to be corrected (*e.g.*, flow artifacts, off-resonance, suceptibility effects), but most have low noise and low bias [81]. Because the proposed method is built around a very general cost function, it is also applicable to fast methods developed for the DAM.

Our proposed method seeks to map both the magnitude and phase of the B_1 field. This method uses a statistical cost function that incorporates noise and slice selection effects ignored by the conventional estimate. Including regularization into our cost function also circumvents the need for later filtering.

5.2.2 Signal model for multiple coils, multiple tip angles/coil combinations

Suppose there are K coils. We take M measurements by transmitting with different coil combinations and receiving from a common coil. (This method could be generalized to use multiple receive coils.) For each measurement, one or more coil(s) are driven simultaneously by the same RF signal $b_1(t)$ with possibly different known amplitude scaling factors α_{mk}, where $k = 1, \ldots, K$ denotes the coil number, $m = 1, \ldots, M$ denotes the measurement number, and $\boldsymbol{\alpha}$is a $M \times K$ array containing the scaling factors α_{mk}. For the problem to be tractable, we require that $M > K$. The complex coil patterns sum together due to linearity to make the total transmitted B_1 field. This general model encompasses the conventional model (5.1) if we let $K = 1$, $M = 2$, and

$$\boldsymbol{\alpha} = \begin{bmatrix} 1 \\ 2 \end{bmatrix}.$$

We model the resulting M reconstructed images as follows:

$$y_{jm} = f_j F \left(\sum_{k=1}^{K} \alpha_{mk} z_{jk} \right) + \varepsilon_{jm}, \tag{5.3}$$

for $m = 1, \ldots, M$ and $j = 1, \ldots, N$, where f_j denotes the underlying object transverse magnetization in the jth voxel (multiplied by the sensitivity of the receive coil) and ε_{jm} denotes zero-mean complex gaussian noise. The B_1^+ map, constrained to be real in the conventional model, is actually a complex quantity. z_{jk} denotes the unknown complex B_1^+ map that relates RF amplitude to tip angle at the jth voxel for the kth coil. When multiple coils are driven by the same signal $b_1(t)$ (with possibly different amplitudes), then the fields from those coils will superimpose and the complex coil patterns will add by linearity, hence the sum over k in (5.3). If the units of the amplitudes α_{mk} are gauss, then the units of z_{jk} will be radians per gauss. More typically, the units of α_{mk} are arbitrary, and all that is known is their relative values. In this case z_{jk} will have units such that the product of α_{mk} and z_{jk} has units of radians. This should suffice for RF pulse design.

The function F in (5.3) replaces the typical $\sin$ seen in the double angle formula and inherently incorporates slice selection effects. The function F is explained further in Appendix B.

The model (5.3) expands the one used in [41, 42] and includes both slice selection effects and linear transceive coil combinations. Recent B_1 mapping methods [10, 90] have introduced linear combinations of transmit coils. These methods have the advantage of using much smaller tip angles while still collecting enough signal to produce accurate results. The proposed method accomodates this matrix transmit technique with a comprehensive measurement model that also includes slice selection effects and accounts for the noise factors that are ignored by existing methods.

The goal is to estimate each B_1^+ map $\boldsymbol{z}_k \triangleq (z_{1k}, \ldots, z_{Nk})$ from the reconstructed images $\{y_{jm}\}$. The underlying magnetization $\boldsymbol{f} \triangleq (f_1, \ldots, f_N)$ is also unknown but is a nuisance parameter. We would like the estimator to work robustly even in image regions where f_j is small.

If f_j were allowed to be complex, then the model above would be non-identifiable so we take the approach of constraining $\boldsymbol{f}$ to be real.

We also note a single surface coil for receive will suffice, even when multiple transmit coils are used. In this case, $\boldsymbol{f}$ will be a product of the spin density and the receive coil sensitivity pattern.

Kerr *et al.* [68] considered a similar problem, except they assumed α_{mk} values are powers of two, F was the ideal sin relationship, and z was a real quantity. They did not use coil combinations, so each row of $\boldsymbol{\alpha}$ would correspond to an indicator function. They used the following cost function:

$$\sum_{j,m} \left(|y_{jm}| - |f_j| \sin(|\alpha_{mk} z_{jk}|)\right)^2 .$$

This cost function does not correspond to the complex gaussian statistical model for the data. They applied a general purpose minimization method from MATLAB. In particular for simplicity, for each voxel they used only the value of tip index for which the tip was closest to $\pi/2$. They also applied no regularization. In contrast, we use all the data at every voxel, with a statistically motivated cost function, and a minimization algorithm that is tailored to this problem. We allow arbitrary choices for the α_{mk} values, although powers of two may be a reasonable choice. We use the Bloch equation to accomodate real pulse sequences instead of assuming a perfect rectangular slice profile.

5.2.3 Regularized estimator

We propose to jointly estimate the B_1^+ maps $\boldsymbol{z} = (\boldsymbol{z}_1, \ldots, \boldsymbol{z}_K)$ and the object $\boldsymbol{f}$ by finding minimizers of the following penalized least squares cost function:

$$\begin{aligned} (\hat{\boldsymbol{z}}, \hat{\boldsymbol{f}}) &= \arg\min_{\boldsymbol{z},\boldsymbol{f}} \Psi(\boldsymbol{z}, \boldsymbol{f}), \\ \Psi(\boldsymbol{z}, \boldsymbol{f}) &= L(\boldsymbol{z}, \boldsymbol{f}) + \beta R(\boldsymbol{z}), \end{aligned} \tag{5.4}$$

where

$$L(\boldsymbol{z}, \boldsymbol{f}) = \sum_{j=1}^{N} \sum_{m=1}^{M} \frac{1}{2} \left| y_{jm} - f_j F\left(\sum_{k=1}^{K} \alpha_{mk} z_{jk} \right) \right|^2 \tag{5.5}$$

and

$$R(\boldsymbol{z}) = \sum_{k=1}^{K} \mathsf{R}(\boldsymbol{z}_k), \tag{5.6}$$

where $\mathsf{R}(\boldsymbol{z}_k)$ is regularizing roughness penalty function for the kth B_1^+ map and β is a regularized parameter that controls the smoothness of the estimate.

We use quadratic regularization for the maps $\boldsymbol{z}_k$ because B_1^+ maps are expected be spatially smooth, although edge-preserving regularization could be used if needed. However, we choose not to regularize the magnetization image $\boldsymbol{f}$ because it will contain detailed structural information.

There is no analytical solution for the minimizer of $\Psi(\boldsymbol{z}, \boldsymbol{f})$ over both parameters, so iterative methods are required. We consider an block alternating minimization approach in which we minimize Ψ by cycling over each parameter and minimizing with respect to one parameter vector while holding the other at its most recent value.

For a given estimate $\hat{\boldsymbol{z}}^{(n)}$ of $\boldsymbol{z}$ at the nth iteration, the minimizer of Ψ with respect to $\boldsymbol{f}$

is found analytically to be:

$$\hat{f}_j^{(n)} = \frac{\sum_{m=1}^{M} \text{real}\left\{ y_{jm}^* F(x_{jm}^{(n)}) \right\}}{\sum_{m=1}^{M} \left| F(x_{jm}^{(n)}) \right|^2}, \tag{5.7}$$

where we define the composite B_1^+ maps $\mathbf{x}_m$ as follows:

$$x_{jm} \triangleq \sum_{k=1}^{K} \alpha_{mk} \hat{z_{jk}}. \tag{5.8}$$

For given $\hat{\boldsymbol{f}}$ values, the problem of minimizing Ψ with respect to the complex B_1^+ map $\boldsymbol{z}_m$ appears nontrivial because of the nonlinearity of F. Therefore, we use an iterative algorithm of the following form:

$$\hat{\boldsymbol{z}}^{(n+1)} = \hat{\boldsymbol{z}}^{(n)} - D(\hat{\boldsymbol{z}}^{(n)}, \hat{\boldsymbol{f}}^{(n)}) \nabla_{\hat{\boldsymbol{z}}} \Psi \left(\hat{\boldsymbol{z}}^{(n)}, \hat{\boldsymbol{f}}^{(n)} \right),$$

where D is a diagonal matrix that is derived using quadratic majorizer principles [8] to ensure that the cost function Ψ is decreased each iteration. See Appendix C for details.

Variable projection is another possible approach (see [48, 54, 109]) where we substitute the linear solution of $\boldsymbol{f}$ (5.7) back into the cost function (5.4) and then find an estimator for $\boldsymbol{z}$. However, we found no simplifications in (5.4) in using (5.7); so we use alternating minimization. The cost function Ψ is nonconvex, so the alternating minimization algorithm described above will descend from the initial estimates to a local minimum [63]. Thus it is desirable to choose reasonable initial estimates. See Appendix E for details.

Regularized methods have the benefit of being able to choose a value for β based on quantitative analysis. In Appendix G, we analyze the spatial resolution of the regularized estimator (5.4). This analysis leads to a modified penalty function which achieves more uniform spatial resolution in regions with a constant f_j. We choose a value for β based on the desired FWHM of regularizer smoothing.

5.3 Experiments

5.3.1 Simulation Study

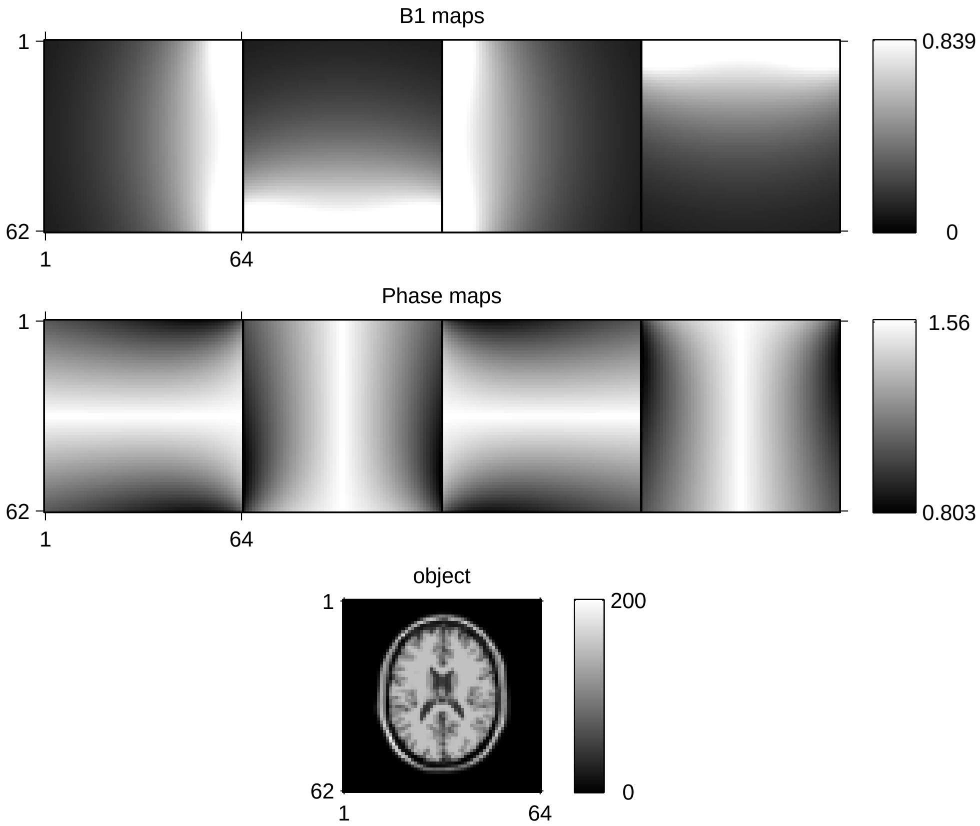

Figure 5.1: True B_1^+ magnitude and phase maps and object used in simulation.

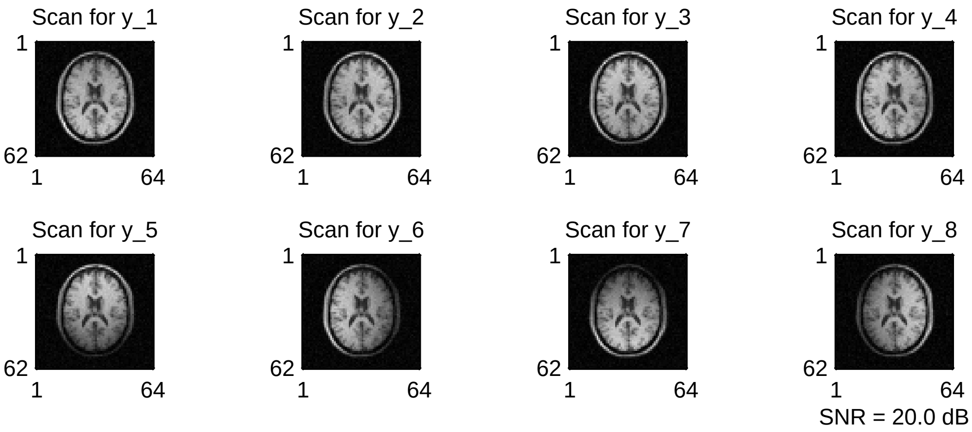

Figure 5.2: Simulated MR scans for leave-one-coil-out (LOO). Estimation with $M = 8$ measurements and with an SNR of 20dB.

To evaluate the regularized B_1^+ map estimation method described above, we performed a simulation study using the synthetic true maps shown in Fig. 5.1. For the object magnitude f_j, we used a simulated normal T1-weighted brain image [18, 70] for the truth. The B_1^+ maps were simulated based on equations for a magnetic field in a circular current loop [49, 129]. We simulated noisy reconstructed images for $K = 4$ different transmit coils using the model (5.3) and varying both the number of measurements ($M = 2K$ or $M = K + 1$), $\boldsymbol{\alpha}$, and the RF pulse (truncated gaussian and truncated sinc, see Appendix B for details). For our scaling matrix $\boldsymbol{\alpha}$, we used "one-coil-at-a-time" (OAAT) (*i.e.*, for $M = 2K$

$$\boldsymbol{\alpha}_{\text{OAAT}} = \begin{bmatrix} I_K \\ 2 \cdot I_K \end{bmatrix},$$

where I_K is a $K \times K$ identity matrix) and "leave-one-coil-out" (LOO) (*i.e.*, for $M = 2K$

$$\boldsymbol{\alpha}_{\text{LOO}} = \begin{bmatrix} 1_K - I_K \\ 2 \cdot 1_K - 2 \cdot I_K \end{bmatrix},$$

where 1_K is a $K \times K$ matrix of ones). There are many possible choices for $\boldsymbol{\alpha}$, but we focus on these two possible matrices as an illustration of the method. Both matrices are well-conditioned ($\kappa\left(\boldsymbol{\alpha}_{\text{OAAT}}\right) = 1$ and $\kappa\left(\boldsymbol{\alpha}_{\text{LOO}}\right) = 3$). All choices for $\boldsymbol{\alpha}$ in this paper meet the criteria of the modified DAM used in Appendix E in calculating $\boldsymbol{z}^{(0)}$. We just show images for the truncated sinc pulse as images from both excitation pulses look similar. We added complex gaussian noise such that the SNR, defined by $10\log_{10}(\|\boldsymbol{y}\|/\|\boldsymbol{y} - \mathsf{E}[\boldsymbol{y}]\|)$, was about 20 dB when $M = 2 \cdot K$ and about 30 dB when $M = K + 1$. Fig. 5.2 shows the data magnitude $|y_{jm}|$ scans for LOO at $M = 8$.

Fig. 5.3 and Fig. 5.4 show the initial estimates, regularized estimates and their respective errors using the methods described in Appendix E for the usual $M = 8$ case. Both the conventional DAM estimate for $|\boldsymbol{z}|$ and the method of moment estimate for $\angle \boldsymbol{z}$ are quite noisy. For the first pass through the algorithm, we ran 5 iterations and used $\beta_1 = 2^{-10}$

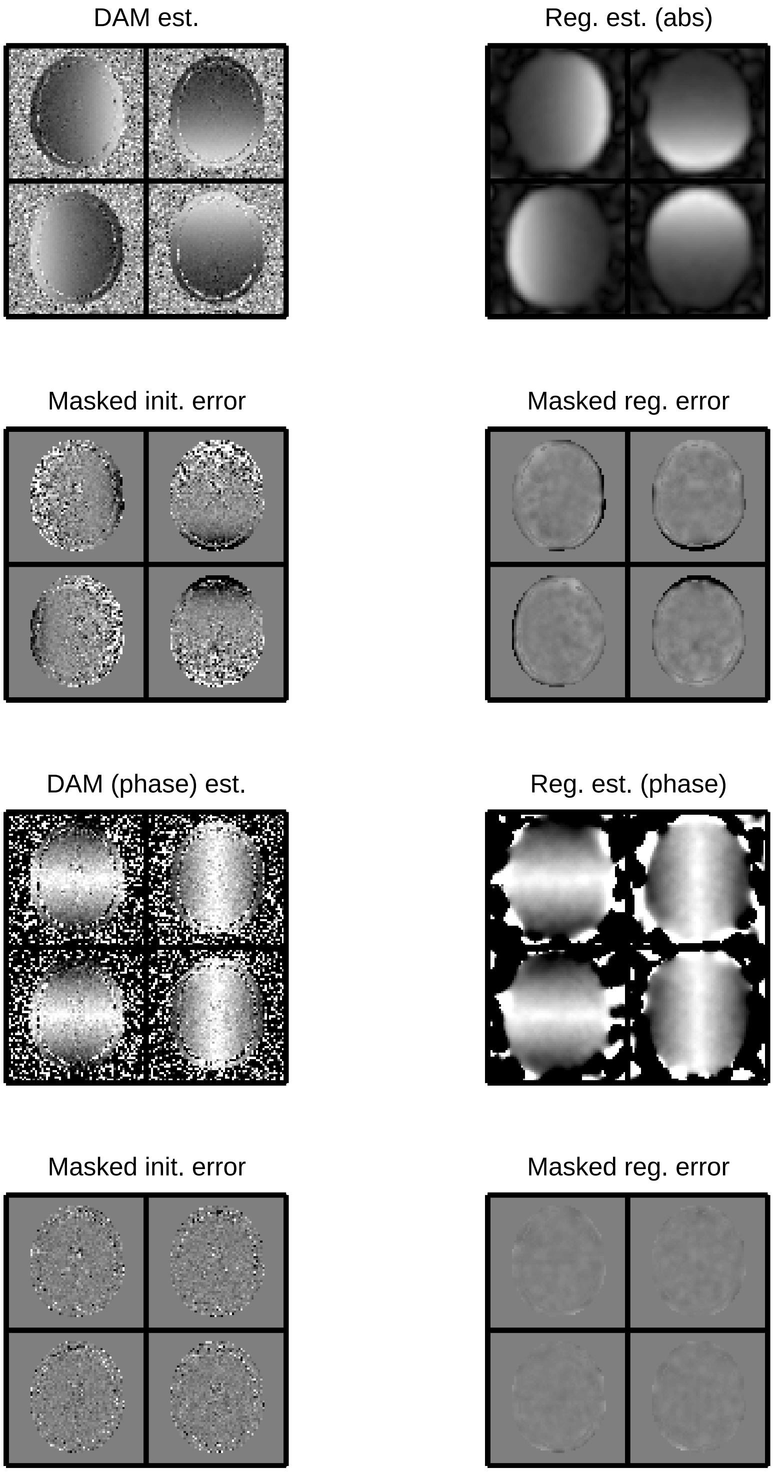

Figure 5.3: Figures for one coil at a time (OAAT). 500 iterations, M=8, SNR about 20 dB, $\beta = 2^{-1}$, Same figure colorbar as Fig. 5.1. Error colorbar is [-.07, .07] for $|\boldsymbol{z}|$ and $[-\pi/8, \pi/8]$ for $\angle \boldsymbol{z}$

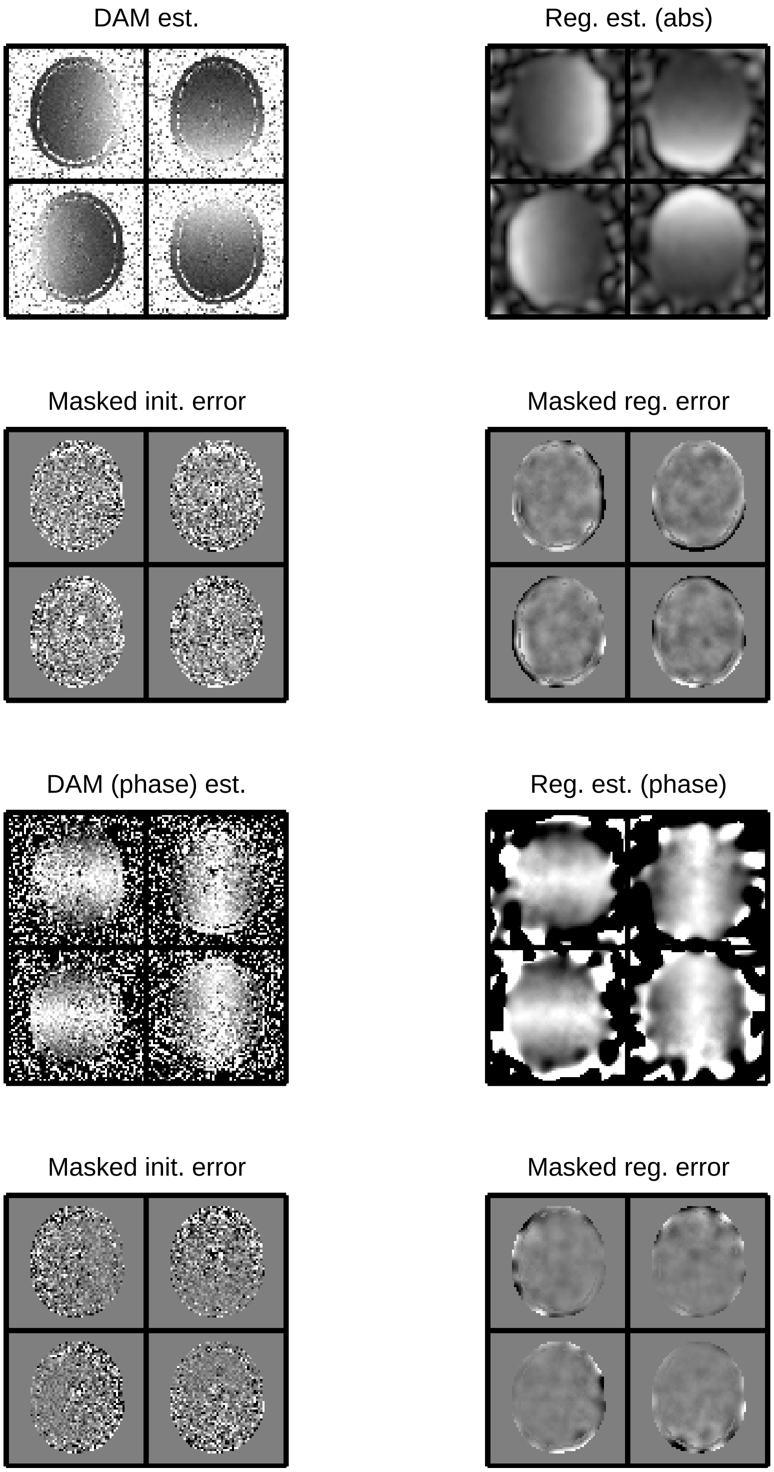

Figure 5.4: Figures for 3 coils at a time (LOO). 150 iterations, M=8, SNR about 20 dB, $\beta = 2^{-1}$, Same colorbar as Fig. 5.3.

and used the modified penalty as described in Appendix G. The data was also normalized by the median of the first pass estimate of the object as described in Appendix G. We ran the algorithm with 150 iterations, using $\beta = 2^{-1}$ and using the modified penalty (G.7). The algorithm, including the first pass, took 300 seconds to run on Matlab. Fewer iteration could be run (when $M = 2K$) to further speed up processing - all estimates have less than 10% NRMSE at 75 iterations, for example, which would almost halve the run time.

The reduced noise due to regularization and due to using all the scan data is evident. Fig. 5.3 shows the conventional estimate for the B_1^+ map. Not only is this image very noisy, but the B_1^+ map is not properly estimated in the large signal void of the skull. This is expected from the very low tip angles that are used here (about 20 degrees in the center for the first four scans and about 40 degrees in the center for the next four scans). We see some improvement in Fig. 5.4 even in the initial estimates because using three coils at a time brings the center tip to around 60 degrees for the first four scans and about 120 degrees for the next four scans, making the DAM much better conditioned and less prone to error. The proposed method improves over the initial estimate for both the OAAT and LOO cases. It smoothly interpolates across this signal void for a smooth B_1^+ map in the region of interest as seen in Fig. 5.3 and Fig. 5.4. Similarly, signal voids can be seen in the initial estimate of the phase map yet are smoothed appropriately in the final estimate.

We calculated the error of both the conventional and our new estimate for all four coils. We used a mask to include only those points where the signal value is non-negligible (*i.e.*, where $|f_j| > 0.1 \max(f_j)$). For error in the phase of the B_1^+ map, we looked at $\left|e^{i\boldsymbol{z}} - e^{i\hat{\boldsymbol{z}}}\right|$. The results are summarized in Table 5.1, where the errors are averaged over 20 realizations (the variance of the error over the realizations is very small, less than one percent). The error in the new regularized estimate for the B_1^+ magnitude is three to five times less than the error of the conventional estimate. OAAT has greater improvements due to the very poor DAM estimate at such low flip angles. The phase estimate and object estimate (not shown) are similarly good. This clearly shows the effects of less noise and interpolating

Table 5.1: Simulation NRMSE (%) for three selected excitation pulses averaged over 20 realizations

		$\|\boldsymbol{z}\|^{(0)}$	$\|\boldsymbol{z}\|^{(n)}$	$\angle \boldsymbol{z}^{(0)}$	$\angle \boldsymbol{z}^{(n)}$	SNR	# iters
Trunc. sinc pulse OAAT $M = 8$	$f_j > 0.1 \max f_j$	77.0	15.5	17.4	3.1	20	150
	Low Magnitude	143.2	19.3	63.8	2.7	20	150
Gaussian pulse OAAT $M = 8$	$f_j > 0.1 \max f_j$	78.3	16.4	16.0	3.1	20	150
	Low Magnitude	143.3	22.9	61.7	2.7	20	150
Ideal sinc pulse OAAT $M = 8$	$f_j > 0.1 \max f_j$	67.6	13.6	13.6	2.5	20	150
	Low Magnitude	134.8	18.0	57.1	2.3	20	150
Trunc. sinc pulse LOO $M = 8$	$f_j > 0.1 \max f_j$	17.4	4.9	28.5	6.7	20	150
	Low Magnitude	58.7	3.9	77.7	7.0	20	150
Gaussian pulse LOO $M = 8$	$f_j > 0.1 \max f_j$	26.8	8.3	29.1	5.5	20	150
	Low Magnitude	64.0	7.0	77.6	5.5	20	150
Ideal sinc pulse LOO $M = 8$	$f_j > 0.1 \max f_j$	14.1	3.9	24.2	5.4	20	150
	Low Magnitude	52.4	3.2	70.8	5.5	20	150

across the signal voids. Similarly, we looked at the error in the signal voids of the brain (the sinuses and skull) to see the improvement even more clearly. These results are also shown in Table 5.1 in the rows labeled “Low Magnitude”. The areas with low magnitude have much greater error (almost 2 times greater) than areas with higher signal magnitude in conventional estimators. Using the regularized estimator, the final error in pixels with low signal magnitude is similar to that of the other pixels, yielding an error six to fifteen times less that of the conventional error in low magnitude pixels. Thus, the regularized estimator makes impressive improvements, especially in the signal voids.

The flexibility of the signal model and regularized estimator introduced in this paper allows for less than the standard $M = 2K$ scans required by the DAM, for example. We require $M \geq K + 1$ to properly estimate both the K coil maps as well as the object. We initialize this method as described in Appendix E; this estimate is much worse for those coils which do not have a double angle initial estimate when we are using each coil sepa-

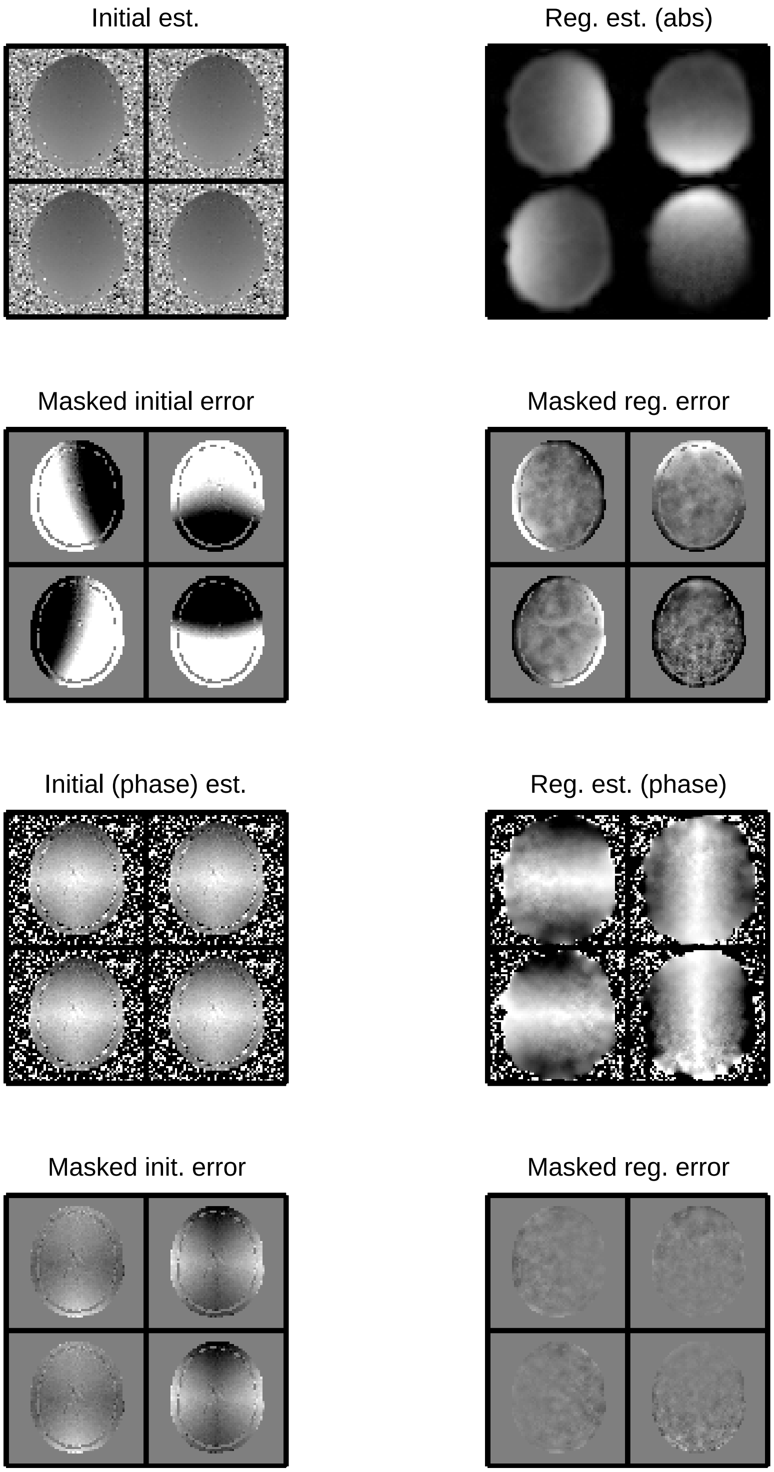

Figure 5.5: Figures for 3 coils at a time (LOO) with less measurements. 1000 iterations, M=5, SNR about 30 dB, $\beta = 2^{-4}$, Same colorbar as Fig. 5.3.

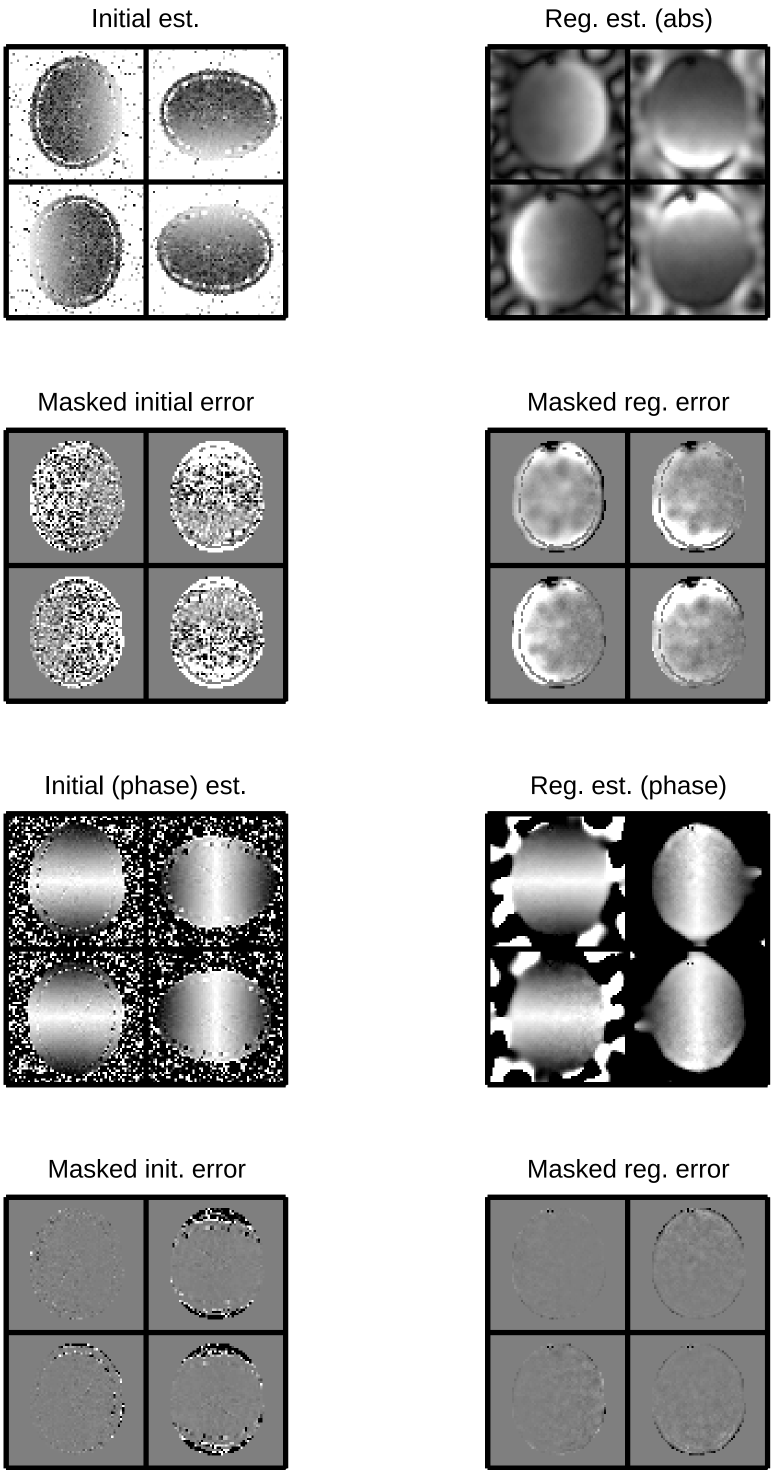

Initial est.

Reg. est. (abs)

Masked initial error

Masked reg. error

Initial (phase) est.

Reg. est. (phase)

Masked init. error

Masked reg. error

Figure 5.6: Figures for one coil at a time (OAAT) with less measurements. 200 iterations, M=5, SNR about 30 dB, $\beta = 2^{-4}$, rotate initial estimate from first coil for subsequent coils. Same colorbar as Fig. 5.3.

rately and the estimate is quite poor for all the coils when we use multiple coils at a time because we lack enough information to ascertain each coil's individual map. Even in these conditions, as long as the coils overlap enough to provide good coverage of the object, the estimator will provide a good solution. However, the regularized estimator takes many more iterations to converge to a good solution, the cost of having fewer scans. At low SNR, the object and B_1^+ estimates have more "holes" in them and the regularized estimator is especially prone to being caught in a local minima. This is especially problematic for OAAT-with less coil overlap, the initial estimate for $M = 5$ has many "holes" at an SNR less than 65 dB. Therefore, when using reduced number of scans, LOO is recommended, especially at low SNR. However, OAAT and LOO can be improved by using an increased number of scans ($M = 6$, for example) or by rotating the initial estimate for the coil (or coil combination) with two scans for the other coil (or combination) initial scans. Because the simulated coil maps used here are simply rotations of each other, this simple step gives good performance for even OAAT at an SNR of 30 dB with only 200 iterations (shown in Fig. 5.6). This is impressive considering that the algorithm performed very poorly at this low SNR without the initial coil rotation. Thus, using additional information or assumptions about the coil maps can lead to a significantly reduced number of scans.

The initial and final estimates for $M = 5$ LOO with 1000 iterations at an SNR of 30 is shown in Fig. 5.5 with $\beta = 2^{-4}$. We chose a slightly lower β for the low scan simulations to put more emphasis on the likelihood term (versus the penalty term). The initial magnitude and phase estimates are identical for each coil (as explained in Appendix E). The initial magnitude estimate is quite uniform across the object; as the algorithm iterates, the variation across the B_1^+ magnitude map for each individual coil is corrected and approaches a good, regularized solution. While there is still more high value error for the magnitude B_1^+ estimate, this can be further reduced using more iterations. The phase B_1^+ estimate is very good and reaches a good solution with low error quickly.

The results for $M = 5$ LOO, at an SNR of 30 at 250, 500, and 1000 iterations are compared to the conventional DAM method using $M = 8$ scans in Table 5.2. Note that the initial magnitude error with $M = 5$, which uses the DAM estimate for the first coil combination for all coil combinations, is not equal to the DAM magnitude error with $M = 8$. We use the MOM phase estimate (E.1) for the DAM $M = 8$ phase estimate. The DAM $M = 8$ at an SNR of 30 has a low error in high magnitude pixels (6%), but a much higher error in low magnitude pixels (32%). After 1000 iterations, we achieve a similar degree of error in low magnitude pixels (9%) and substantially reduce error in the low magnitude pixels (8%) giving a similar error rate in all pixels within the object mask. Phase error is lower for all number of iterations shown for the proposed method with $M = 5$ than for the MOM $M = 8$ estimator and is substantially lower in low magnitude pixels (by a factor of 10).

The OAAT coil combinations failed to provide good results with only 5 scans at an SNR of 30dB with the standard initialization. However, when we rotated the initial estimate for the first coil for the subsequent coils as explained above, the estimator provided good estimates with a much reduced number of iterations. Rotation of the oval brain shape caused more error along the edges of the oval, but overall the proposed method coped with the object shape irregularities quite well for OAAT (under the present implementation, the coil combinations used in LOO did not perform well with this rotation method). The final image using 200 iterations for this method is shown in Fig. 5.6 and error results in Table 5.2. OAAT has similar trends to LOO, but has significantly better results than the OAAT DAM $M = 8$ estimates. Because OAAT uses only one coil at a time, the achieved flip angles achieved are much lower and the OAAT DAM estimate has more initial error than that of LOO DAM $M = 8$ estimate. Therefore, the regularization of the proposed method substantially decreases the error, especially in low magnitude pixels.

Thus, using only 5 scans as opposed to the standard 8, produces similar (for LOO) or lower (for OAAT) NRMSE in high magnitude pixels and substantially lowered error in low magnitude pixels, albeit at the price of a high number of iterations. Optimization of

Table 5.2: Simulation NRMSE (%) for proposed method $M = 5$ versus conventional DAM method $M = 8$ averaged over 20 realizations (truncated sinc pulse with SNR=30dB)

		$\lvert\boldsymbol{z}\rvert^{(0)}$	$\lvert\boldsymbol{z}\rvert^{(n)}$	$\angle\boldsymbol{z}^{(0)}$	$\angle\boldsymbol{z}^{(n)}$	# of iters
LOO $M = 5$ proposed	$f_j > 0.1 \max f_j$	43.5	19.9	12.2	4.0	250
	Low Magnitude	49.4	22.8	25.7	4.8	250
	$f_j > 0.1 \max f_j$	43.5	13.2	12.2	3.8	500
	Low Magnitude	49.4	13.5	25.7	4.3	500
	$f_j > 0.1 \max f_j$	43.5	9.1	12.2	3.4	1000
	Low Magnitude	49.4	8.0	25.7	3.7	1000
LOO $M = 8$ DAM	$f_j > 0.1 \max f_j$		5.8		11.1	
	Low Magnitude		31.6		45.2	
OAAT $M = 5$ proposed	$f_j > 0.1 \max f_j$	80.5	17.3	35.5	8.4	50
	Low Magnitude	122.7	24.5	54.8	7.4	50
	$f_j > 0.1 \max f_j$	80.5	15.9	35.5	5.9	100
	Low Magnitude	122.7	24.5	54.8	3.3	100
	$f_j > 0.1 \max f_j$	80.5	14.6	35.5	4.9	200
	Low Magnitude	122.7	22.1	54.8	2.7	200
OAAT $M = 8$ DAM	$f_j > 0.1 \max f_j$		58.1		17.7	
	Low Magnitude		116.8		59.3	

this method (for example, improving the initial estimate based on information about the relative coil patterns as suggested above) may yield even greater improvements in reduced scan regularized estimation.

We tested the improvement seen by using the correct slice profile for estimation versus assuming an ideal sinc pulse profile. The results are summarized in Table 5.3. We see that using the correct slice profile gives slightly better error results for OAAT for the truncated sinc pulse (though curiously not for the gaussian pulse). This holds true for pixels with a high signal value as well for signal voids. We would not expect a very large difference for OAAT, because the flip angles are very small and the difference in F at these flip angles is also small. For LOO we see bigger relative differences, especially among the gaussian pulse. This is as we would expect, as the gaussian pulse differs greatly from the ideal sinc pulse at the flip angles seen in LOO. Thus, the improved slice profile is most advantageous at higher flip angles.

Table 5.3: Simulation NRMSE (%) using the correct slice profile for estimation versus using the conventional ideal pulse profile for estimation

Excitation pulse	Assumed pulse	$\boldsymbol{\alpha}$		$\lvert\boldsymbol{z}\rvert^{(0)}$	$\lvert\boldsymbol{z}\rvert^{(n)}$	$\angle\boldsymbol{z}^{(0)}$	$\angle\boldsymbol{z}^{(n)}$	SNR	# iters
Trunc sinc	Trunc sinc	OAAT $M = 8$	$f_j > 0.1 \max f_j$	77.0	15.5	17.4	3.1	20	150
Trunc sinc	Ideal sinc	OAAT $M = 8$	$f_j > 0.1 \max f_j$	77.0	16.7	17.4	2.7	20	150
Trunc sinc	Trunc sinc	OAAT $M = 8$	Low Mag	143.2	19.3	63.8	2.7	20	150
Trunc sinc	Ideal sinc	OAAT $M = 8$	Low Mag	143.2	21.0	63.9	2.6	20	150
Gaussian	Gaussian	OAAT $M = 8$	$f_j > 0.1 \max f_j$	78.3	16.4	16.0	3.1	20	150
Gaussian	Ideal sinc	OAAT $M = 8$	$f_j > 0.1 \max f_j$	78.3	10.8	16.0	2.8	20	150
Gaussian	Gaussian	OAAT $M = 8$	Low Mag	143.3	22.9	61.7	2.7	20	150
Gaussian	Ideal sinc	OAAT $M = 8$	Low Mag	143.3	12.0	63.7	2.7	20	150
Trunc sinc	Trun sinc	LOO $M = 8$	$f_j > 0.1 \max f_j$	17.4	4.9	28.5	6.7	20	150
Trunc sinc	Ideal sinc	LOO $M = 8$	$f_j > 0.1 \max f_j$	17.4	4.7	28.4	5.9	20	150
Trunc sinc	Trunc sinc	LOO $M = 8$	Low Mag	58.7	3.9	77.7	7.0	20	150
Trunc sinc	Ideal sinc	LOO $M = 8$	Low Mag	58.7	4.6	77.6	6.4	20	150
Gaussian	Gaussian	LOO $M = 8$	$f_j > 0.1 \max f_j$	26.8	8.3	29.1	5.5	20	150
Gaussian	Ideal sinc	LOO $M = 8$	$f_j > 0.1 \max f_j$	26.8	18.6	26.8	5.5	20	150
Gaussian	Gaussian	LOO $M = 8$	Low Mag	64.0	7.0	77.6	5.5	20	150
Gaussian	Ideal sinc	LOO $M = 8$	Low Mag	64.0	16.8	77.9	5.5	20	150

5.3.2 MRI Phantom Study

We also applied this algorithm to real MR data on a phantom scanned with coils positioned to create a B_1 map that was much larger on one side than on the other. We obtained images at eighteen nominal tip angles from 10 degrees to 180 degrees. Fig. 5.7 shows scans from the first three tip angles. Fig. 5.8 shows the results from the conventional estimate (5.2) (with tips at 30° and 60°) as well as using the proposed regularized estimator with three of the tip angles ($30^\circ, 60^\circ, 90^\circ$) and with all eighteen. The regularized estimates are much smoother than the conventional estimate. This matches our supposition that the phantom should have a smooth B_1 map. We see that even using just three images produces a much smoother image than the conventional estimate. We used the regularized estimate using all eighteen tip angles as ground "truth" and calculated the NRMSE of the regularized estimate using only three tip angles and the conventional estimate. The conventional magnitude estimate had a NRMSE of 29.9% compared to the regularized magnitude estimate with an error of 15.3%. Thus, using just one extra scan and the proposed regularized estimate reduces the magnitude estimate's error by almost half and also calculates a phase estimate with a NRMSE of 7.32%. Although both the real and the imaginary parts of $\boldsymbol{z}$ are smooth, the phase estimate had a small amount of phase wrapping which has been removed in Fig. 5.8 for display. Because (5.6) regularizes the complex object, or effectively the real and imaginary parts of $\boldsymbol{z}$, instead of the magnitude and phase of $\boldsymbol{z}$, a small amount of phase wrapping is possible in the final object. Simple phase unwrapping algorithms can be used as a final step after all iterations have been completed if a smooth phase map is desired.

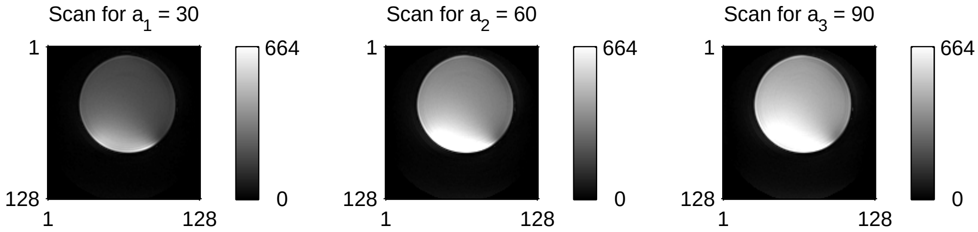

Figure 5.7: Three of the eighteen scans taken of the phantom. These scans show the varying contrast in the images due to the B_1 inhomogeneity.

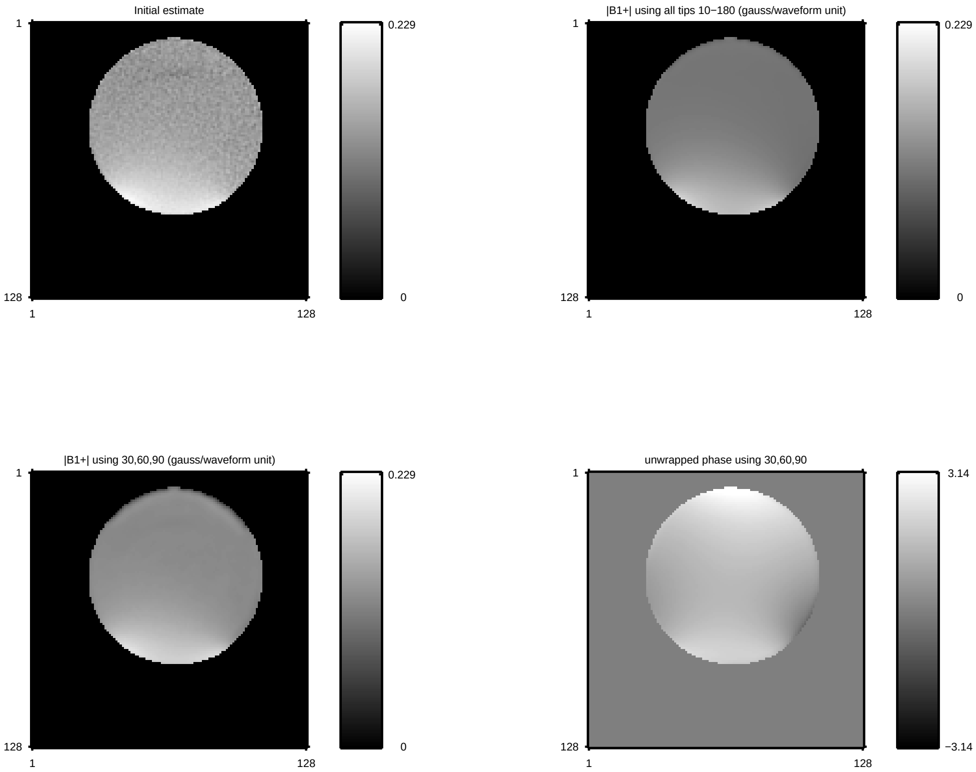

Figure 5.8: Estimation of the phantom using proposed method. Top: conventional estimate of B_1 using two images; regularized estimate of B_1 using all eighteen images; Bottom: regularized estimate of B_1 using three images; regularized estimate of the phase map.

5.4 Discussion

We have described a new regularized method for B_1^+ mapping that estimates both the B_1 magnitude and (relative) phase. This method allows for multiple coils allowing for easy use in designing pulse sequences for parallel excitation. This method yields B_1^+ maps that interpolate smoothly over regions with low spin density. This avoids noisy estimates in these regions as well as 2π ambiguities that plague the conventional estimate. The conventional estimate uses only two tip angles, while our method allows for any arbitrary selection of angles.

The simulation results show that the NRMSE of the new B_1 map is much less than that of the conventional estimate. These gains make this an appropriate method even when using only one coil and the standard two angles.

Although results showing the improvement made by using the correct slice profile in the model are still very preliminary, we expect that this improvement to the model will have a large effect at higher tip angles where F and sin have a larger discrepancy.

This model did not account for possible coil non-linearity or possible T_1 effects. We will explore these factors in future work.

Overall, the model and estimators explored in this paper make smoother, less noisy estimates while also allowing for the the use of multiple coils and tip angles to achieve an accurate B_1^+ and phase map for each coil.

CHAPTER VI

Joint B_1^+ , T_1 Map Estimation

6.1 Joint T_1 and B_1^+ Estimation: Motivation

The longitudinal relaxation time T_1 is a quantitative value of interest in MR. Fast, accurate, and precise mapping of T_1 has many applications: measuring the distribution of contrast agents to find tumors or assess organs [17, 84], perfusion imaging [27, 55], schizophrenia, epilepsy, multiple sclerosis, and Parkinson's diagnosis [73,123,131], quantifying myocardial blood flow [144], assessing lung function [64], preparing navigation and visualization tools for surgery [50], and, in combination with accurate maps of other parameters such as T_2 and spin density, artificially creating "on the fly" MR images with any desired contrast.

Moreover, T_1 and B_1^+ mapping are usually both unknown quantities in MR pulse sequences. Imaging sequences for the B_1^+ double angle estimation method, for example, require spin echo or gradient echo sequences with a long repetition time (TR $> 5T_1$) to remove any T_1 dependence from the acquired images. Fast and improved methods for the double angle method use scan time more efficiently [20, 110, 127]. Alternatively, image sequences which are accurate over a wide array of T_1 values have been developed [136]; these pulse sequences, however, may not give accurate phase information [89]. Simple techniques that are independent of T_1, such as finding the 180° null of the signal, do not work well at high B_0 signal strengths where B_1^+ mapping is even more crucial [28] and may not have good coverage over the entire volume. Ideally, B_1^+ estimation would be fast, simple, work at high signal strengths and give accurate magnitude and phase estimates. One possibility is to combine some sort of T_1 estimation into conventional B_1^+ estimation that incorporates signal dependence on T_1. Especially when B_1^+ maps are used in developing RF pulses, accurate B_1^+ maps that are robust to noise and less sensitive to T_1 effects are required. Small differences in the B_1^+ map can make a large difference in the final RF pulse design [82].

T_1 mapping is also adversely affected by B_1^+ inhomogeneity and non-ideal achieved slice profiles in many conventional pulse sequences. B_1^+ inhomogeneity and slice profile effects especially affect gradient echo and spin echo when using an acquisition with a short TR. At such a short TR, these methods are very sensitive to flip angle variations. Steady-state incoherent (SSI) imaging, a very popular fast imaging method that can be used in T_1 mapping, is especially sensitive; slice profile effects lead to an underestimation of T_1 and B_1^+ inhomogeneity causes large inaccuracies in uncorrected T_1 mapping [51]. Therefore, many T_1 mapping methods currently incorporate some form of B_1^+ mapping, though it is often a very crude flip angle correction and ignores slice profile effects entirely. Some other (and unfortunately, slower) methods of T_1 mapping also jointly estimate a flip angle map (for example, Look-Locker [79]) and are more insensitive to B_1^+ inhomogeneity. Ideally, the fast SSI T_1 mapping approach would also incorporate estimation of B_1^+ inhomogeneity and slice profile effects into the original problem formulation.

This chapter first considers current T_1 mapping methods in Section 6.2, including joint B_1^+ and T_1 estimators in Section 6.2.4. Limitations of these methods are explored in Section 6.3. Next, we do a Cramer Rao bound analysis of various mapping methods to choose an appropriate model in Section 6.4 with supplemental information Appendix G. Based on this analysis, we develop our joint B_1^+, T_1 estimator in Section 6.5 with supplemental information in Appendix I (cost function derivatives), Appendix J (model derivatives), Appendix K (initial estimates), Appendix L (spatial resolution analysis), and Appendix M (constrained T_1 estimation modifications). We performed simulation and phantom MR experiments in Section 6.6. Finally, we discuss the results and propose future work in Section 6.7.

6.2 Overview of Current T_1 Mapping Methods

Many different methods have been developed to estimate a T_1 map using very different imaging sequences and algorithms. In all of these methods, the relationship between T_1 and the imaging data obtained is complex and a simple explicit formula for T_1 can not be written. Most of the methods depend on transformations of the data which then use a linear or non-linear fit to several parameters which are simply related to T_1.

The simplest mapping method uses a ratio of two spin echo signal measurements with two separate repetition times (TR) using a saturation recovery pulse sequence [133]. The effect of T_2 is canceled in the ratio leaving a ratio of exponentials containing T_1. Obtaining an estimate of T_1 analytically from this ratio is not possible, so a look-up table is used. For some values of T_1 and TR, the relationship between the ratio and T_1 is quite linear; for other values, the relationship varies very slowly and good estimation of T_1 is impossible. Using principles of error propagation, reasonable values of TR can be calculated based on expected T_1 values and a good SNR can be ensured. Using only two points severely limits the accuracy of T_1 mapping, especially in the case where a wide spread of T_1 values is possible. Therefore, many methods have been developed which measure this curve at several points. This can be done for either spin echo or inversion recovery measurements. Because these methods all rely on exponential regrowth relationships, they have a similar relationship to SNR; the SNR is directly proportional to the dynamic range of the method. Because inversion recovery (IR) has the double the dynamic range of the spin echo, it also has a much better SNR. IR sequences are very slow, but faster implementations have been developed [9, 19, 103, 147].

The two most common methods currently used for T_1 mapping are the Look-Locker method and the SSI measurement with multiple flip angles.

6.2.1 Look-Locker imaging sequence

Look-Locker is based on the IR imaging method and its greater SNR but improves on the inherent inefficiency of the method, which requires a brief sampling time followed by a very long waiting time before the next repetition can begin. In Look-Locker, very small flip angles are applied several times during the recovery period, sampling the longitudinal magnetization. These pulses affect the recovery curve and give very different results than the IR imaging method. If the flip angles are very small, the sequence is similar to the IR sequence, but the method is then SNR-limited. This method has 3 parameters that are estimated using a least-squares fit. The major advantage of this method is the relative insensitivity to B_1^+ inhomogeneity; the method naturally incorporates estimation of a flip angle map. Some recent research into this pulse sequence has involved: jointly estimating T_1, T_2^*, and the proton density with flexible accuracy [130], optimization of number of inversion times and the appropriate TI values [95], multi-slice acquisitions incorporating the average flip angle and using smoothed flip angle maps [23] and modifying the sequence to work in cardiac imaging, where the cardiac cycle is shorter than T_1 [86].

6.2.2 SSI imaging sequence

Another common T_1 imaging method is based on SSI (steady-state incoherent) fast imaging. This method applies a spoiled gradient recalled-echo (SPGR) sequence consecutively acquired with many flip angles and is known as the variable flip angle (VFA) method. A spoiled FLASH (fast low angle shot) or driven equilibrium single pulse observation of T_1 (DESPOT1) acquisition is used. The SNR of this method is similar to the previously described methods but with a much shorter total acquisition time. However, this method is very sensitive to B_1^+ inhomogeneity and pulse profile effects.

We will derive the SSI model under the more general condition of a complex B_1^+ map with a phase angle of ϕ ($\phi = 0$ when the B_1^+ is real and all along the x' vector). The signal model is derived as follows (considering a single spin). The first pulse is applied at a tip angle of θ. After the pulse is applied (at time 0^+), the longitudinal magnetization is

$$M_z(0^+) = M_0 \cos(\theta),$$

where M_0 is the initial magnetization. The longitudinal magnetization then returns to the initial magnetization based on the T_1 relaxation constant for one spin as follows:

$$M_z(t) = M_0(1 - \exp\left(-\frac{t}{T_1}\right)) + M_z(0^+) \exp\left(-\frac{t}{T_1}\right).$$

The transverse magnetization after the θ pulse is

$$\begin{aligned} M_x(0^+) &= -M_0 \sin(\theta) \sin(\phi) \\ M_y(0^+) &= M_0 \sin(\theta) \cos(\phi) \\ M_\perp(0^+) &= M_0 \sin(\theta) \exp(i\phi), \end{aligned}$$

and decays back to 0 based on the T_2 relaxation constant for one spin as follows:

$$M_\perp(t) = M_\perp(0^+) \exp\left(-\frac{t}{T_2}\right).$$

Consecutive pulses are applied after a repetition time of T_R. At the end of each repetition time, the longitudinal magnetization for the spin is

$$M_z((n+1)T_R^-) = M_z(nT_R^+) \cos(\theta)\, E_1 + M_0(1 - E_1), \tag{6.1}$$

where

$$E_1 = \exp\left(-\frac{T_R}{T_1}\right). \tag{6.2}$$

In this derivation, we assume that the transverse magnetization decays to 0 before the beginning of the next RF pulse, or perfectly spoiled. A naturally spoiled sequence occurs when the repetition time is much longer than T_2. Otherwise, forced or external spoiling, to reduce the transverse magnetization to zero at the end of each pulse, is required. Similarly, the transverse magnetization is (assuming a perfectly spoiled signal)

$$\begin{aligned} M_\perp((n+1)T_R^-) &= M_\perp(nT_R^+)E_2 \\ &= M_z(nT_R^-)\sin(\theta)\exp(i\phi)\,E_2, \end{aligned} \tag{6.3}$$

where

$$E_2 = \exp\left(-\frac{T_E}{T_2}\right). \tag{6.4}$$

The sequence achieves steady-state when, for all subsequent pulses, at the end of each repetition time the longitudinal magnetization is the same and is equal to the equilibrium magnetization. Assuming a uniform tip angle, equilibrium is effectively achieved when the longitudinal magnetization changes by a very small percentage (*e.g.*, 1%) at the end subsequent pulses. Let N be the number of pulses applied before steady-state is (effectively) reached; N depends on the relative error allowed and on the parameters T_1 and T_R. After N pulses, the magnetization is then:

$$M_z(mT_R^-) \approx M_{ze}, \forall m \geq N,$$

where M_{ze} is the equilibrium magnetization. This magnetization can be found by setting $M_z((n+1)T_R^-)$ and $M_z(nT_R^-)$ in (6.1) equal to M_{ze} and then solving for M_{ze}. Then, the signal is measured at the end of the repetition time and, according to (6.3), the steady state signal is

$$S_i = M_0 E_2 \frac{(1 - E_1)\sin(\theta_i)\exp(i\phi)}{1 - E_1 \cos(\theta_i)}, \tag{6.5}$$

where θ_i is the ith flip angle. Using multiple flip angles and keeping TR constant, we can estimate both M_0 and T_1 using a non-linear least-squares fit. Alternatively, (6.5) can be transformed as follows:

$$\frac{S_i}{\sin(\theta_i)} = E_1 \frac{S_i}{\tan(\theta_i)} + M_0 E_2 \exp(i\phi)(1 - E_1). \tag{6.6}$$

Then, a transformation of the points (θ_i, S_i) into the coordinate plane $(\frac{S_i}{\tan(\theta_i)}, \frac{S_i}{\sin(\theta_i)})$ gives a line where the slope is E_1. Knowing E_1, we find T_1 using a least-squares fit.

Much work has been done using the SSI signal model. Recent research on the SSI image sequences is mostly in two veins - optimizing the flip angles and other parameters in the SSI sequence (usually in terms of precision and occasionally accuracy) [25, 38] and trying to correct for B_1 inhomogeneity, flip angle miscalibration, and/or pulse profile effects [16, 24, 97, 116, 121, 125], the dominant source of error in SSI T_1 estimation. Other research includes improving the estimation procedure: using weighting to improve linear least-squares estimation [14] and correcting for incomplete RF spoiling [99].

6.2.3 SSFP pulse sequence

The SSFP (steady state free precession) pulse sequence is related to the SSI as it is also a short T_R method using gradient echo imaging. Here, there is no spoiling and the signal adds coherently. The steady-state magnetization thus depends on both the longitudinal and transverse magnetization.

A non-spoiled signal is an attractive sequence for joint estimation because of the increased signal available (due to coherent build of signal) and not having to use (possibly incomplete) spoiling. However, the SSFP is a more complicated pulse sequence to analyze, especially the transient part of the signal and for any unbalanced pulse sequence. The SSFP is not a T_1 weighted sequence as is the SSI but is rather dependent on the ratio of T_1 to T_2 (Note, this can be seen in (6.7). Tissues with a high T_2 to T_1 ratio have a large signal). Imaging, therefore, shows high signal for CSF in the brain, but little contrast between GM and WM. In addition, the sequence is extremely dependent on B_0 off resonance, whether from the static field inhomogeneity to induced B_0 inhomogeneity due to the gradients. In fact, [51] motivates the derivation of the SSFP initially by discussing the off resonance, because two isochromats seeing different B_0 fields will indeed reach different steady state values. Therefore, this pulse sequence depends heavily on not only T_1, but also T_2 and B_0. B_1 dependence, on the other hand, seems to be much less than the SSI signal model.

The model can be simplified by assuming that the off-resonance is zero and looking at an extremely short T_R. In this simplified case, the SSFP or SSC (steady-state coherent) signal is [51]:

$$\begin{aligned} M &= \frac{M_0(1-E_1)\sin(\theta)}{1-E_1\cos(\theta) - E_2(E_1-\cos(\theta))} \\ &\approx \frac{M_0\sin(\theta)}{(\frac{T_1}{T_2}+1) - cos(\theta)\left(\frac{T_1}{T_2}-1\right)}, \end{aligned} \tag{6.7}$$

where $E_d = \exp(T_R/T_d)$.

There are a few examples in the literature where SSFP is used for T_1 quantification. First, [103] motivates using TrueFISP (a fully refocused SSFP) to avoid the problematic B_1^+ dependence on the SSI. While acknowledging that image banding could be a problem if B_1^+ inhomogeneity was too large (> 250 Hz), off resonance effects are otherwise ignored. They use the model (6.7). They claim that the TrueFISP recovery curve more closely mimics the mono-exponential curve of T_1 than the SSI model, which, therefore, underestimates T_1 (assuming no B_1^+ correction).

[26] uses the SSFP model to do rapid combined T_1 and T_2 mapping. They claim that T_1 mapping is best accomplished using the SSI signal model and that T_2 can then be quickly

mapped using the SSFP given that T_1 is already known. They present a linearization of the SSFP model similar to the linearization of the SSI model (6.6), which allows for simple estimation of both T_1 and T_2.

[105] uses the IR TrueFISP pulse to estimate the three major MR parameters: T_1, T_2, and spin density. They also ignore off resonance and acknowledge that this creates some error in their measurements (4% in T_1, 12% in M_0, and 20% in T_2 at an off resonance of $\pi/3$), but do not find this problematic, especially in their phantom and brain data. They claim this method gives good results with a tip angle between 30 and 70 degrees.

[45], however, questions whether IR-FISP can appropriately estimate T_1 and T_2 as in the papers above. They claim the pulse sequence and their subsequent results (simulations and in vivo scans) show a "very sensitive dependence on [the off-resonance], especially for smaller ratios of T_2 / T_1".

[77] interestingly uses the RAD-SSFP model and incorporates an approximate slice profile (uses a triangular function to approximate a single lobe sinc) to find improved results in estimating the T_1, T_2 ratio. This paper is unique in acknowledging slice profile effects in the SSFP sequence.

While SSFP does not require spoiling and has greater signal magnitude, SSFP depends strongly on a larger number of variables (T_1,T_2, and B_0) while having only a weak dependence on B_1, one of the desired estimated variables. Therefore, SSFP is a poor choice for joint T_1/B_1 estimation and will not be further considered in this thesis.

6.2.4 Overview of Current Joint T_1 and B_1 Estimation

Because SSI is so sensitive to B_1^+ inhomogeneity, many applications proposed in the literature use a crude estimate of B_1^+. Methods used to estimate B_1^+ (or, identically, flip angles) include: conventional double angle method [16], using the same SSI sequence with a very long repetition time on a phantom [97], and looking at the signal null [121] for a single pixel.

However, only a few methods claim to do combined estimation of both B_1^+ and T_1. These methods are explored here.

[28] maps the B_1^+ field using (6.5) ignoring the T_2 decay (as this scales the signal magnitude). While this method does not explicitly estimate T_1, the method is interesting in using the SSI signal model solely to measure B_1^+. θ in that equation is replaced by the nominal θ (as given to the scanner) multiplied by a flip angle scaling factor that varies based on position. This flip angle scaling factor, equivalent to B_1^+, is found by applying three flip angle close to 180° and looking for the signal null, which occurs irrespective to T_1. The images are first smoothed, based on the assumption that B_1^+ varies smoothly, to improve SNR. They use a 3D acquisition to avoid the problem of slice profile effects. Although the SSI method typically uses low flip angles, the authors found that the method works well for high flip angles as well, required in finding the signal null. A small variation in B_1^+ measured is found at very small T_R/T_1 due to poor SNR. This method fails with high off-resonance as a signal null is never found and the signal intensity no longer varies linearly with flip angle, though more flip angles could be used with a non-linear fit.

[116] presents a “joint” mapping method for contrast-enhanced abdominal MRI. The SSI model is the best approach because it is fast enough to allow dynamic quantization of contrast concentration. For B_1^+ mapping, a similar sequence, the actual flip angle sequence [89, 136] is used. This sequence uses two different repetition times consecutively and then repeats the entire sequence until steady state is reached. As in SSI, both T_1 and B_1^+ are tied together, but with small approximations, a formula for B_1^+ independent of T_1 can be found. Measurements from this sequence are used to correct the assumed flip angle required to estimate T_1. Although separate data has to be taken to solve for B_1^+, this method has the advantage of using very similar sequences that can be performed directly after each other; any non-idealities will be similar for the two sequences and motion artifacts will be negligible compared to methods which require radically different imaging procedures to compensate for B_1^+.

[57, 58] uses two RF pulse trains with the same flip angle α. The longitudinal magnetization after each pulse can be written in terms of a decay and a recovery component. Subtracting two identical pulse trains with different starting magnetization removes the common recovery component, leaving a post-subtraction signal which only contains a decay component. This method thus does not require steady-state and uses the transient pulse information. They develop two different methods, each of which uses two post-subtraction signals. The flip-angle priority (FAP) signals are identical, with the second having double the flip angle of the first. The slope of the regression line of the absolute ratio of the two signals is related to the flip angle and T_1 is found via curve-fitting. Relaxation-time priority (RTP) signals are identical with a common flip angle, but with different time coordinates. T_1 is found via regression and then the flip angle can be found via substitution. Flip angle maps were smoothed using a moving average, using an iterative method in RTP to get the final map.

[146] uses the SSI signal model but looks at the transient part of the signal before it reaches steady state. Ratios of the transient signal to the original signal are related to T_1 and B_1^+ and used to derive each. This method is extremely fast and can be easily combined with any fast readout, but has limited resolution for single shot and systematic error at low flip angles and low SNR.

More recently, [11] uses a similar approach to our proposed method, using multiple coil arrays to remove the need for large angles in exciting the B_1^+ field. A parametric model for both steady state spin warp and transient-state EPI data with two free parameters (B_1^+ and T_1) is used, while simultaneously incorporating B_0 inhomogeneity and some slice selection effects. The model is solved using least squares assuming no inhomogeneity effects and then iteratively refined with a separately obtained standard B_0 estimate. The method estimates relative phase and uses normalization by a reference image to eliminate all constant factors, such as $\boldsymbol{f}$. The focus of this method is on B_1^+, noting that the T_1 map is much less accurate than B_1^+ because the MR signal depends much less sensitively on relaxation than on the B_1^+ map.

[124] also uses a parametric method using the the standard SSI (FLASH method) to estimate both T_1 and $\boldsymbol{f}$, but assumes that B_1^+ is known. Like [11], the initial estimate is found via regression and then non-linear regression is used to find a more accurate solution under the natural constraints of the T_1 and $\boldsymbol{f}$. The need for at least three or four flip angles, in contrast to the standard two, to obtain accuracy is also discussed.

[122] generalizes the model for both the AFI (actual flip angle imaging) and SSI methods to create a new MTM model using multiple repetition times. This new model, which averages multiple measurements, can be solved either analytically or numerically using model fitting. The model has the benefit of giving accurate maps of both B_1^+ and T_1 when solved analytically, although the accuracy of the T_1 maps was not further analyzed because of the focus on B_1^+ maps. The Cramer Rao bound was also used to quickly determine optimal scan parameters.

[137] analyzes the importance of spoiling on measurement effects for both the AFI and the VFA methods for B_1^+ mapping (corrected for T_1). Because diffusion is critical in RF-spoiled sequences, the optimal angles and measurement of T_1 are strongly dependent on the strength of the spoiling. Spoiling is not considered in this thesis, but obviously is necessary to consider in the future work.

6.3 Limitations of Current Methods and Possible Solutions

6.3.1 B_1^+ inhomogeneity

As mentioned previously, B_1^+ inhomogeneity is the primary source of error in T_1 measurements and must be corrected for when using the SSI method. Some of the basic methods have been explained in the previous section. Almost all methods blur calculated B_1^+ maps to improve SNR without a solid understanding of the effect (*i.e.*, the FWHM of the blur, the effect on T_1 calculation). Additionally, many methods find a low-resolution B_1^+

map or one based on phantoms. Additionally, all methods estimate only the magnitude of the B_1^+ map and ignore the fact that it is a complex quantity. The ideal method would create an accurate, pixel-by-pixel, in-vivo complex B_1^+ map with high SNR without indiscriminant blurring and would not require a separate scan.

6.3.2 Slice profile effects, Bloch equation non-linearity, and flip angle miscalibration

Slice selective RF pulses would ideally have a rectangular shape, exciting only the spins in the desired slice, but this is not achievable in practice. Real slice profiles have varying flip angles over the slice. Because the measured signal in MRI integrates over the volume, the varying flip angles due to the slice profile can cause error in the accompanying T_1 measurements. In addition, spins do not behave linearly in the presence of an RF field; *i.e.*, doubling B_1^+ does not lead to twice the flip angle due to the non-linearity of the Bloch equation. While this approximation works well in the small-tip regime, using the Bloch equation to model the achieved flip angle across the slice profile is most accurate.

Flip angle variation and miscalibration can be particularly problematic in SSI imaging. The SSI signal, as a function of flip angle, passes through first a spin-density weighted and then a T_1 weighted area. Typically, two (or more) flip angles are chosen with the first maximizing the sensitivity and the second chosen small enough to be spin-density weighted and almost independent of T_1.

Some papers suggest using 3D imaging (which does not require slice-selective RF pulses) to bypass this effect *e.g.*, [28]. This must be done for all scans (including those to estimate other parameters) to mitigate the effect see [16]. Other papers, while noting the effect, claim it has little effect and make no modifications to their method *e.g.*, [116]. [57] minimizes the effect by dividing each slice into sub-slices, each with an expected uniform flip angle. [97] directly accounts for slice selection effects by integrating over the signal equation with respect to position and using the flip angle at each position as found using the achieved slice profile. [42] performs regularized B_1^+ map estimation incorporating slice-selection effects by using a Bloch-simulated signal model.

Flip angle miscalibration is a related issue. The nominal flip angle (the one input to the scanner) is often different than the real flip angle achieved in vivo. A flip angle factor is usually integrated when calculating the B_1 map, *e.g.*, [28] or the flip angle factor can be directly integrated into the model *e.g.*, [121].

The ideal method would inherently correct for slice selection, Bloch equation non-linearity, and flip angle miscalibration, without requiring any substantial increase in computation time.

6.3.3 Joint estimation and signal processing

Ideal joint estimation of two quantities would incorporate both variables into the same signal equation and account for appropriate noise. Most methods currently use a separate scan to find B_1, which can introduce motion artifacts and subtle differences between the two acquisitions that would influence the variables differently. Another possible problem with current methods is the order of estimation and the resulting error propagation. If the two variables depend on one another, an iterative approach to update each variable based on the other would provide the most accurate estimation of both.

Signal processing and estimation techniques used in current methods also lead to more errors. Most methods use ratios or subtraction. Ratios are inherently problematic, as the noise terms are usually left out of the signal equation. When the signal is small, the noise terms dominate and the ratio is unstable. Subtraction can also be problematic; noise is added to the signal and when the subtraction occurs, the signal may not be completely subtracted out, leaving a harder to analyze source of noise.

Another problem with current methods is using the signal equations to actually find B_1^+ and T_1. There are no closed form solutions for either variable using the SSI signal model without making many simplifying assumptions and approximations, *e.g.*, [53]. Many approximations, for example, by linearizing the exponential, are only valid in a small range and are inefficient because of the low signal SNR in that range. The main techniques use regression, least-squares, curve fitting, or error-propagation. The conventional technique involves transforming the data (6.6) and then performing a linear least-squares (LLS) fit on the transformed data. Because LLS minimizes residuals between the transformed data and the transformed predicted data based on the estimated variable, the fitting no longer matches the cost function and is suboptimal, resulting in a biased estimator with low accuracy. Using weighted least squares with careful choice of the weights transforms the residuals to match those of the original non-transformed cost function [14]. LLS gives an estimate of E_1 and conventional methods still must estimate T_1 in an additional step.

Ideally, the estimation techniques used would properly account for noise in the signal model and therefore, avoid problematic ratios and subtractions. Also, the technique would use the most accurate, unbiased methods available.

6.4 Model Selection: A CRB approach

Many[1] methods have been developed recently that jointly estimate both B_1^+ and T_1 (see Section 6.2.4). Making an informed choice between the wide variety of pulse sequences where relaxation effects and B_1^+ inhomogeneity feature prominently remains an open problem. Analysis of the accuracy and precision possible in B_1^+ and T_1 estimates and the inherent trade offs can aid this selection.

In this section, we first construct a general model for joint B_1^+, T_1 mapping. We then use the Cramér Rao Bound to analyze the lowest possible variance for unbiased joint estimation of B_1^+ and T_1 using several specific pulse sequences. We investigate the variance of both estimates over a range of B_1^+ and T_1 values. We also use this analysis to help optimize timing and flip angle parameters for each pulse sequence. This analysis extends the large body of research on optimization of parameters and precision for T_1 estimation (*e.g.*, [25, 26, 38]) to include joint B_1^+ and T_1 estimation. Joint estimation methods usually require a

---

[1] This section is partially based on [40].

higher resolution of one quantity (B_1^+ or T_1), often utilizing a map of the second quantity for greater accuracy in the initial mapping. For example, [116] concentrates on T_1 mapping while utilizing a B_1^+ map, while [11] concentrates on B_1^+ mapping but also estimates a lower-accuracy T_1 map. The trade offs and analysis from this section allows comparison of pulse sequences depending on the particular required accuracy for both B_1^+ and T_1.

6.4.1 General Joint Estimation Model for Model Selection

Most B_1^+ or T_1 mapping pulse sequences can be formulated using the following general model. Let the measured value of a single voxel for the ith scan be given by:

$$y_i = m_0 F\left(\frac{T_{Ri}}{T_1}, \alpha_i b\right) + \epsilon_i, \tag{6.8}$$

where m_0 is the nominal voxel magnetization dependent on T_E (the echo time) and T_2. T_1 is the longitudinal relaxation constant, b is the RF field strength at this voxel, T_{Ri} is the repetition time for a specific pulse sequence, and α_i is the relative amplitude of the RF pulse, where the product $\alpha_i b$ specifies the flip angle in a given voxel. The unitless function F describes the MRI scan signal value variation independent of T_E and T_2 based on the individual pulse sequence and scan parameters and is defined in Section 6.4.1 for three specific models. The full data $Y = (y_1, \cdots, y_N)$ consists of N scans where either T_{Ri} or α_i is varied. For example, for the double angle B_1^+ mapping method, $N = 2$ and $\alpha_2 = 2\alpha_1$ and $T_{R1} = T_{R2}$. ϵ_i is modeled as white, Gaussian noise. While magnitude images suffer from Rician noise, we model complex scans with complex Gaussian noise. We assume that $\sigma_{\epsilon_i} = \sigma_0 \forall i$.

The Cramér Rao Bound (CRB) expresses the lowest achievable variance possible for an unbiased estimator for a given model. Although practical estimators are often biased (*e.g.*, through smoothing or filtering the data or using approximations to the model), the bound quantifies the estimator variance and captures the coupling effects between the two unknown parameters. For simplicity, let $t \triangleq T_1$. Because $\boldsymbol{\theta} = (b, t)$, the multiple parameter CRB must be used. In that case, the matrix CRB is

$$\mathsf{Cov}_{\boldsymbol{\theta}}\left\{\hat{\boldsymbol{\theta}}\right\} \geq \boldsymbol{J}^{-1}(\boldsymbol{\theta}), \tag{6.9}$$

where the Fisher information matrix is

$$\boldsymbol{J}(\boldsymbol{\theta}) = \mathsf{E}\left[[\nabla_{\boldsymbol{\theta}} \ln \mathsf{p}(Y; \boldsymbol{\theta})][\nabla_{\boldsymbol{\theta}} \ln \mathsf{p}(Y; \boldsymbol{\theta})]^T\right]. \tag{6.10}$$

The Fisher information $\boldsymbol{J}$ is a 2×2 matrix with entries:

$$\begin{aligned} J_{11} &= \frac{1}{\sigma^2} \sum_i \left(\frac{\partial}{\partial b} \bar{y}_i\right)^2 \\ J_{12} &= J_{21} = \frac{1}{\sigma^2} \sum_i \left(\frac{\partial}{\partial b} \bar{y}_i\right)\left(\frac{\partial}{\partial t} \bar{y}_i\right) \\ J_{22} &= \frac{1}{\sigma^2} \sum_i \left(\frac{\partial}{\partial t} \bar{y}_i\right)^2, \end{aligned} \tag{6.11}$$

where $\bar{y}_i$ is the expected value of y_i. We define $\phi_i \triangleq \alpha_i b$ (tip angle) and $\gamma_i \triangleq \frac{T_{Ri}}{t}$. The derivatives of the general model (6.8) then are:

$$\begin{aligned} \frac{\partial}{\partial t} \bar{y}_i &= -M_0 \cdot \frac{T_{Ri}}{t^2} \cdot F^{01}(\phi_i, \gamma_i) \\ \frac{\partial}{\partial b} \bar{y}_i &= M_0 \cdot \alpha_i \cdot F^{10}(\phi_i, \gamma_i), \end{aligned} \tag{6.12}$$

where F^{10} and F^{01} denote partial derivatives with respect to the first and second arguments of F respectively. Then,

$$\begin{aligned} \sigma_b \triangleq \sqrt{CRB(b)} &= \sqrt{[\boldsymbol{J}^{-1}(\boldsymbol{\theta})]_{11}} \\ \sigma_t \triangleq \sqrt{CRB(t)} &= \sqrt{[\boldsymbol{J}^{-1}(\boldsymbol{\theta})]_{22}}. \end{aligned} \tag{6.13}$$

We also consider, for comparison purposes, the CRB for estimating B_1^+ with known T_1, given by $(1/\boldsymbol{J}_{11})$, and the CRB for estimating T_1 with known B_1^+, given by $(1/\boldsymbol{J}_{22})$, later in the analysis.

In this paper, we calculate the CRB for several specific models over a wide range of input parameters and optimize the scan parameters.

6.4.2 Specific Joint Estimation Models for Model Selection

For joint estimation model selection, we consider three main pulse sequences, with their corresponding models for F in (6.8). First, the SSI model [16] where

$$F_i^{\mathrm{SSI}} = \frac{(1 - e^{-\gamma_i}) \sin(\phi_i)}{1 - e^{-\gamma_i} \cos(\phi_i)}, \tag{6.14}$$

see (6.5) in Section 6.2.2 where the SSI method was introduced. This pulse sequence is used commonly for T_1 mapping by varying α_i although T_{Ri} can also be varied; this sequence also has been used successfully for solo B_1^+ mapping [28].

Second, we consider the Brunner-Pruessmann method (BP) used in [11] using a non-selective, spoiled prepulse with a varying flip angle (ϕ_i) followed by a slice excitation with a flip angle βb. As in [11], we set $\Delta = .05$ ms and $\beta b = 20^\circ$ to reduce the number of parameters to optimize. We define: $\eta \triangleq \frac{\Delta}{t}$. We also ignore any B_0 inhomogeneity and use the following model:

$$F_i^{\mathrm{BP}} \;=\; \cos(\phi_i) \sin(\beta b) \, \frac{\cos(\phi_i)\, e^{-\eta}(1 - e^{-\gamma_i - \eta)}) + 1 - e^{-\eta}}{1 - \cos(\phi_i) \cos(\beta b)\, e^{-\gamma_i}}. \tag{6.15}$$

Third, we consider pulse sequence used in the Actual Flip Angle (AFI) method [136]. When this pulse sequence is used in B_1^+ mapping, usually approximations and ratios are used to remove T_1 dependence in the final B_1^+ estimator. However, the signal depends on both B_1^+ and T_1 and is a candidate for joint estimation. This model differs from the previous two in that two repetition times, T_{R1} and T_{R2}, are used simultaneously in steady state and thus appear in both equations F_1^{AFI} and F_2^{AFI} as shown below:

$$\begin{aligned} F_{2i-1}^{AFI} &= \sin(\phi_i)\,\frac{1-e^{-\gamma_2}+(1-e^{-\gamma_1})e^{-\gamma_2}\cos(\phi_i)}{1-e^{-\gamma_1-\gamma_2}\cos^2(\phi_i)} \\ F_{2i}^{AFI} &= \sin(\phi_i)\,\frac{1-e^{-\gamma_1}+(1-e^{-\gamma_2})e^{-\gamma_1}\cos(\phi_i)}{1-e^{-\gamma_1-\gamma_2}\cos^2(\phi_i)}. \end{aligned} \tag{6.16}$$

This model is more difficult to generalize to $N > 2$, but using an even number of scans is one possibility.

6.4.3 Model Selection Method and Results

To compare the models using the CRB, we derived the CRB using implicit differentiation in MATLAB. Explicit differentiation can speed results but can become complicated for more complex expressions such as (6.15). F^{01} and F^{10} for the SSI and AFI models are included in Section G. The complexity of the derivatives does not immediately show any clear advantage to either model.

To enable fair comparison of models using different imaging time, consider that a scan repeated N times gives a standard deviation $\sigma_0/\sqrt{N}$. Therefore, we report $\tilde{\sigma}_b \triangleq \sigma_b \sqrt{\sum_i T_{Ri}}\ \frac{m_0}{\sigma}$ (compare [26]), defined as the TR Compensated Deviation (TRCD). To make optimization feasible over a very large parameter space, we constrain the search space by requiring that $\alpha_i = i\Delta_\alpha$ for the SSI (6.14) and BP (6.15) models. For the AFI model, we keep T_{R1} and T_{R2} constant and set $\alpha_{2i-1} = \alpha_{2i} = i\Delta_\alpha$. Therefore, we optimize over only 4-5 parameters regardless of the number of scans: $(\Delta_\alpha, T_{Ri}, b, t)$.

The ideal model will have a low $\tilde{\sigma}_b$ and $\tilde{\sigma}_t$ and also be relatively insensitive to variation in B_1^+ and T_1. There is a trade off between optimizing both TRCD values; therefore, we optimize a scalar valued function

$$f(\Delta_\alpha, T_R, b, T_1) = \tilde{\sigma}_b(\Delta_\alpha, T_R, b, T_1) + \tilde{\sigma}_t(\Delta_\alpha, T_R, b, T_1)$$

to consider the effect of both TRCDs. (We also tried f as a product of $\tilde{\sigma}_b$ and $\tilde{\sigma}_t$ with similar results). We seek scan parameters (tip angles and repetition times) whose TRCDs have low variation over a wide range of T_1 and B_1^+ values. We perform a min-max optimization; we *minimize* over the set of scan parameters the worst-case (*i.e.*, *maximum*) $f(\cdot)$ over the range of B_1^+ and T_1 values. This is expressed mathematically as optimizing the following equation:

$$(\Delta_\alpha^{\text{opt}}, T_R^{\text{opt}}) = \underset{(\Delta_\alpha, T_R)}{\arg\min} \max_{(b,t)} f(\Delta_\alpha, T_R, b, t). \tag{6.17}$$

We first find the TRCD over a large parameter space defined by the maximum tip angle $\Delta_\alpha \cdot N \in [\pi/4, 9\pi/4]$, $T_R \in [.1, 3]$, $t \in [.2, 1.2]$, and $b \in [.5, 2]$; these denote the "search" range. Typical values of T_1 for various tissues are: 250 ms for fat, 600 ms for white matter (WM), 900 ms for muscle, 950 ms for gray matter (GM), 1200 ms for blood, and 4500 ms for cerebrospinal fluid (CSF) [51], so this range covers most expected physiological values of T_1. This range also allows for a factor of four amplitude difference in B_1 values. We perform the optimization in (6.17). The optimal values for our choice of f are shown in Table 6.1.

To analyze the trade off between $\tilde{\sigma}_b$ and $\tilde{\sigma}_t$, we also find the worst case TRCD values over the range of B_1^+ and T_1. We define

$$\begin{aligned} \tilde{\sigma}_b^{\max}(\Delta_\alpha, T_R) &\triangleq \max_{(b,t)} \tilde{\sigma}_b(\Delta_\alpha, T_R, b, t), \\ \tilde{\sigma}_t^{\max}(\Delta_\alpha, T_R) &\triangleq \max_{(b,t)} \tilde{\sigma}_t(\Delta_\alpha, T_R, b, t). \end{aligned}$$

We then plot, for each $\tilde{\sigma}_b^{\max}$, the lowest achievable $\tilde{\sigma}_t^{\max}$ over all Δ_α and T_R values in the range defined above. These plots are shown in Fig. 6.4 ($N = 2$) and Fig. 6.5 ($N = 8$).

Next, using the optimal parameters $\Delta_\alpha^{\text{opt}}$ and T_{Ri}^{opt} (6.17), we calculate the TRCD over a larger range of B_1^+ (keeping the range of T_1 the same): $b \in [.25, .4]$; this is the "display" range. Now, we can see how robust the optimized parameters are when B_1^+ and T_1 are outside the original search range. We plot, for each B_1^+ value in the display range, the maximum $\tilde{\sigma}$ over the T_1 search range on one set of graphs (*e.g.*, $\tilde{\sigma}_b$ in plot B and $\tilde{\sigma}_t$ in plot D); and also for each T_1 value in the display range, the maximum $\tilde{\sigma}$ over the B_1^+ search range on another set of graphs (*e.g.*, $\tilde{\sigma}_b$ in plot A and $\tilde{\sigma}_t$ in plot C). The graphs are shown in Fig. 6.1, Fig. 6.2, and Fig. 6.3.

Table 6.1: Optimized scan parameters based on (6.17)

Model	N	Δ_α or α (radians)	Δ_{T_R} or T_{R1} (sec)	T_{R2} (sec)
SSI	2	1.1781	0.68	-
SSI	4	1.3744	0.68	-
SSI	8	0.8836	0.68	-
AFI	2	1.0996	0.245	0.10
AFI	4	1.3352	0.825	0.10
AFI	8	1.0603	0.68	0.10
BP	2	2.2776	0.825	-
BP	4	0.9818	0.535	-
BP	8	0.8836	0.825	-

6.4.4 Model Selection Discussion

In this analysis, we consider two main questions: 1) What is the trade off between $\tilde{\sigma}_b$ and $\tilde{\sigma}_t$? and 2) How robust are the optimal parameters found in (6.17)?

Fig. 6.4 and Fig. 6.5 show the trade off between $\tilde{\sigma}_b^{\max}$ and $\tilde{\sigma}_t^{\max}$. Improved accuracy in estimating B_1^+ decreases T_1 accuracy. Therefore, in scan parameter optimization, a function of both TRCDs is required. The SSI and AFI method have the lowest achievable worst case TRCD (the BP method is outside Fig. 6.4). Clearly, the SSI method has the best performance for $N = 2$; both the AFI and SSI method perform well for $N = 8$, with the AFI method having a slight advantage.

The optimal parameters robustness varies both on the method and the number of scans (see Figures (6.1), (6.2), and (6.3). TRCD, for all methods, is lowest when T_1 is small (plots A and C), but is more robust to the value of B_1^+ (plots B and D). This is especially

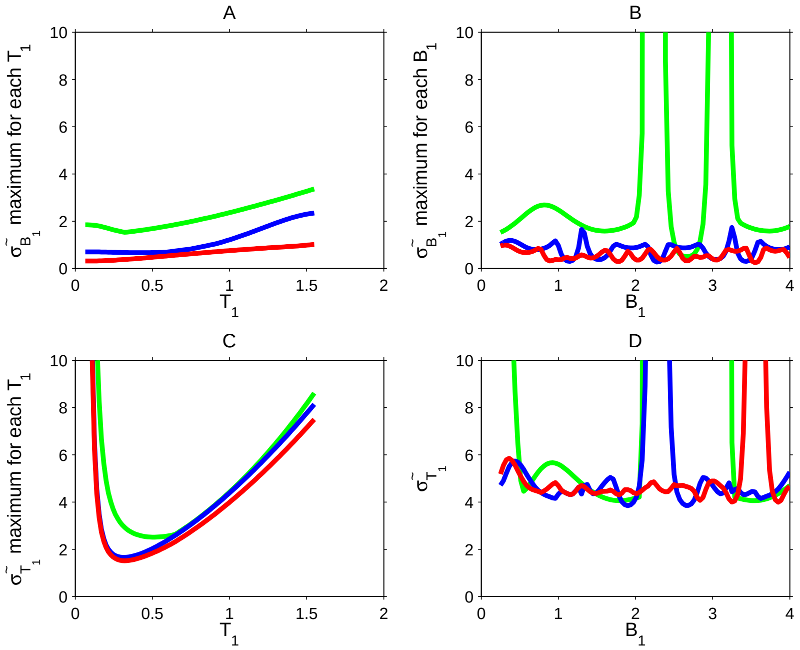

Figure 6.1: Robustness of the SSI model at the optimal parameters. $N = 2$ (green), 4 (blue), 8 (red). We plot, at the optimal parameters in Table 6.1, the maximum $\tilde{\sigma}_b$ for each T_1 over B_1^+ values in the search range (A), the maximum $\tilde{\sigma}_b$ for each B_1^+ over T_1 values in the search range (B), the maximum $\tilde{\sigma}_t$ for each B_1^+ over T_1 values in the search range (C), and the maximum $\tilde{\sigma}_t$ for each T_1 over B_1^+ values in the search range (D).

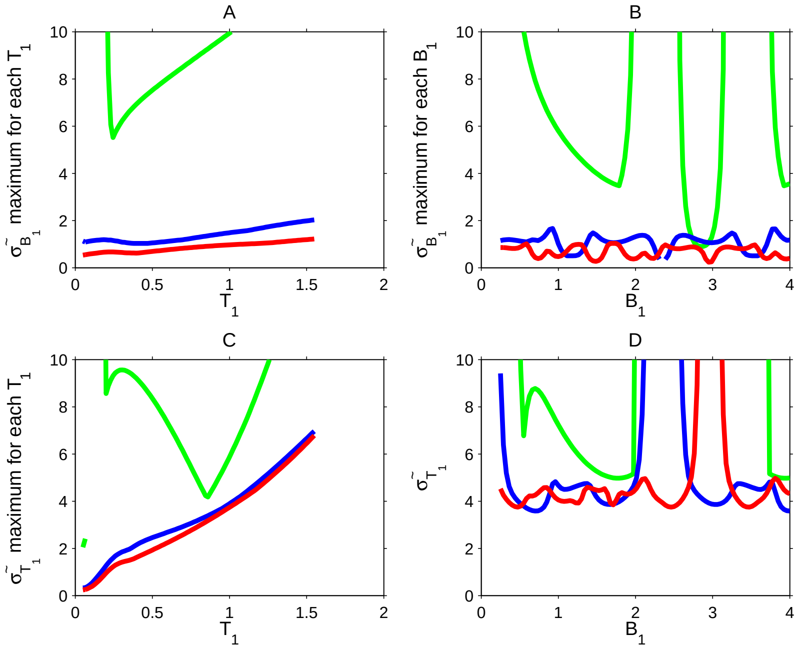

Figure 6.2: Robustness of the AFI model at the optimal parameters. Compare Fig. 6.1.

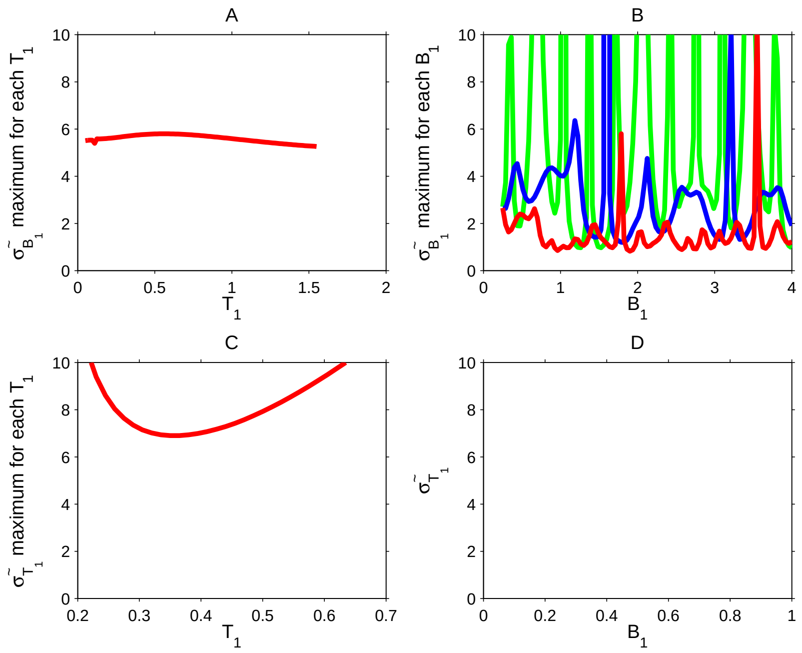

Figure 6.3: Robustness of the BP model at the optimal parameters. Compare Fig. 6.1.

true for $\tilde{\sigma}_t$. For all methods, $N = 4, 8$ performs much better than $N = 2$, especially for the AFI method. Using four or eight scans, both the SSI and AFI method are relatively insensitive to specific values of B_1^+ and T_1 and are appropriate to use for joint estimation, though SSI has the lowest TRCD values consistently. The BP method has relatively high TRCD values, even when $N = 8$, and $\tilde{\sigma}_b$ is especially sensitive to the value of B_1^+, so this method as implemented will have high variance for unbiased B_1^+ estimation.

After analyzing the CRB for joint estimation of B_1^+ and T_1, the SSI method has both the lowest worst case estimator variances and is the least sensitive to B_1^+ and T_1 values. The AFI method is also relatively insensitive to B_1^+ and T_1 values, but, overall, has higher estimator variances. The Brunner model, as modeled here, has poor performance, although this may be improved by further optimizing other scan parameters in the model. Although the results are not shown here, we also tried using the SSI model and varying T_R, but had very poor results. We note that this optimization does neglect SAR constraints which may be a problem when using a large tip angle and a short repetition time.

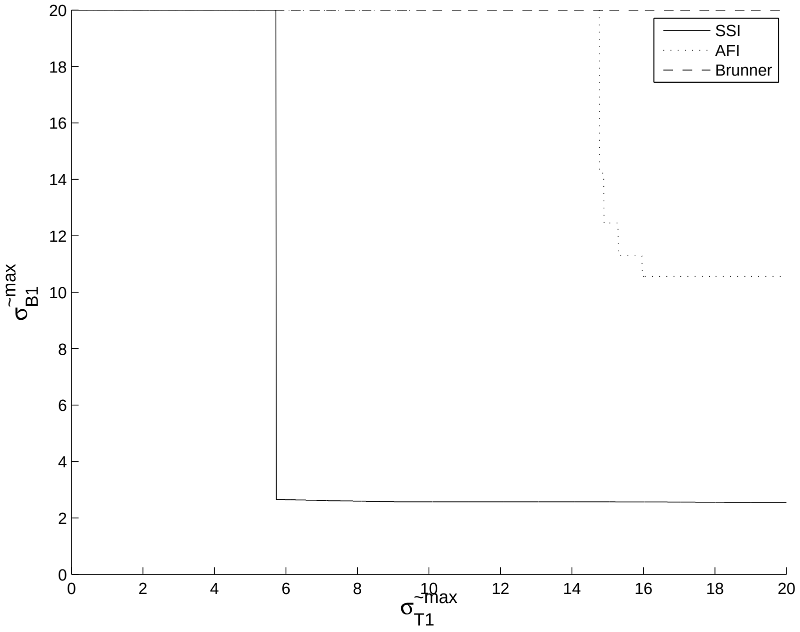

Figure 6.4: Minimum achievable $\tilde{\sigma}_b^{\max}$ for a maximum $\tilde{\sigma}_t^{\max}$ for two scans.

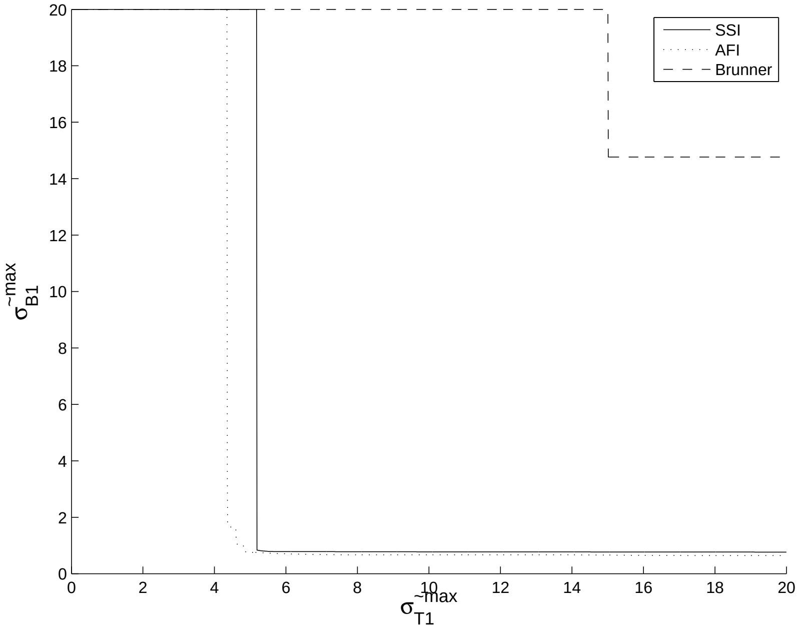

Figure 6.5: Minimum achievable $\tilde{\sigma}_b^{\max}$ for a maximum $\tilde{\sigma}_t^{\max}$ for eight scans.

6.4.5 CRB Extension: Joint estimation Versus Estimation With Only One Unknown Variable

We now consider the "cost" of joint estimation, *i.e.*, how much higher the CRB for estimating B_1^+ is for joint estimation of B_1^+, T_1 compared to estimating B_1^+ with known T_1, given by $(1/\boldsymbol{J}_{11})$, as well as how much higher the CRB for estimation T_1 is for joint estimation of B_1^+/T_1 compared to estimating T_1 with known B_1^+, given by $(1/\boldsymbol{J}_{22})$. We make graphs similar to Fig. 6.1 with three plots for each method, one each for $N = 2$, $N = 4$, and $N = 8$. Each plot shows $\tilde{\sigma}$ for joint estimation as a solid line and $\tilde{\sigma}$ for estimating one unknown variable as a dotted line. We use the same optimal values found previously in computing the graphs. These graphs are shown in Fig. 6.6, Fig. 6.7, Fig. 6.8, Fig. 6.9, Fig. 6.10, Fig. 6.11, Fig. 6.12, Fig. 6.13, and Fig. 6.14.

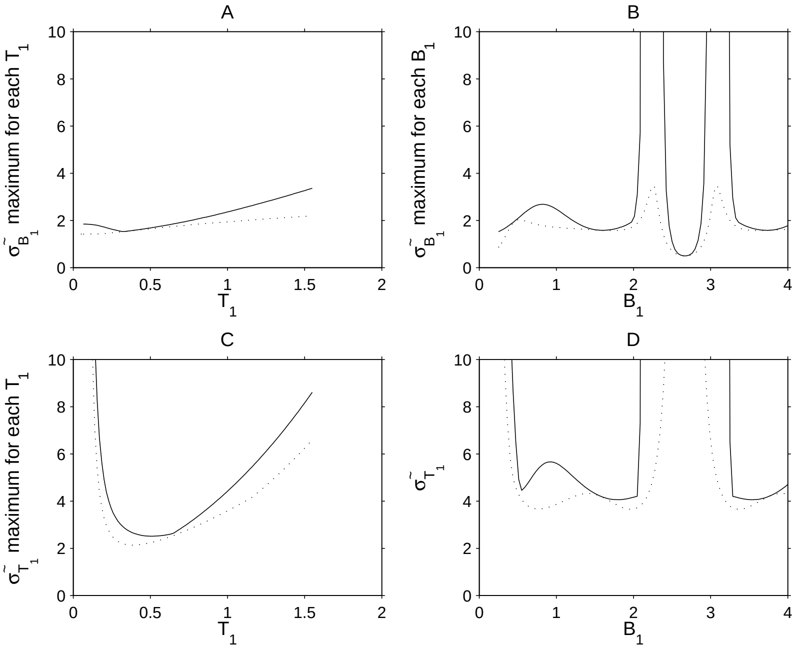

Figure 6.6: Cost of joint estimation for the SSI model $N = 2$. Compare Fig. 6.1. $\tilde{\sigma}$ for joint estimation is shown with a solid line and $\tilde{\sigma}$ for estimation of one unknown variable is shown with a dotted line.

As expected, $\tilde{\sigma}$ for joint estimation is higher than $\tilde{\sigma}$ for estimating just one unknown variable in every case. The biggest difference is seen in the AFI method for $N = 2$.

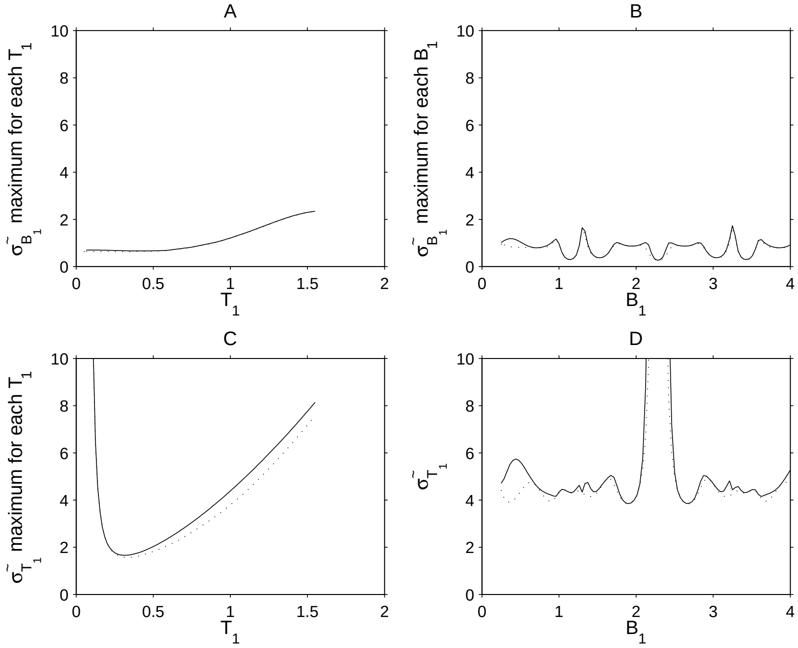

Figure 6.7: SSI model $N = 4$, compare Fig. 6.6.

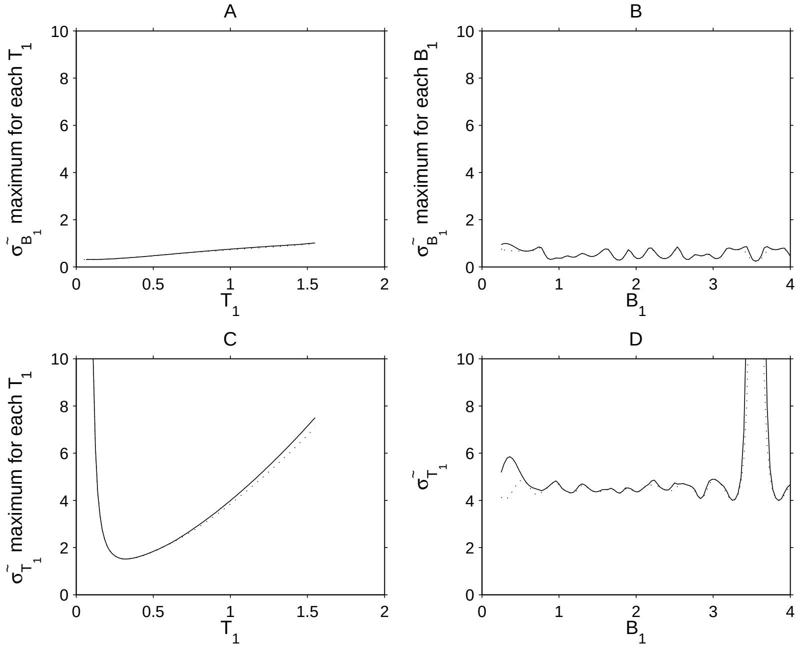

Figure 6.8: SSI model $N = 8$, compare Fig. 6.6.

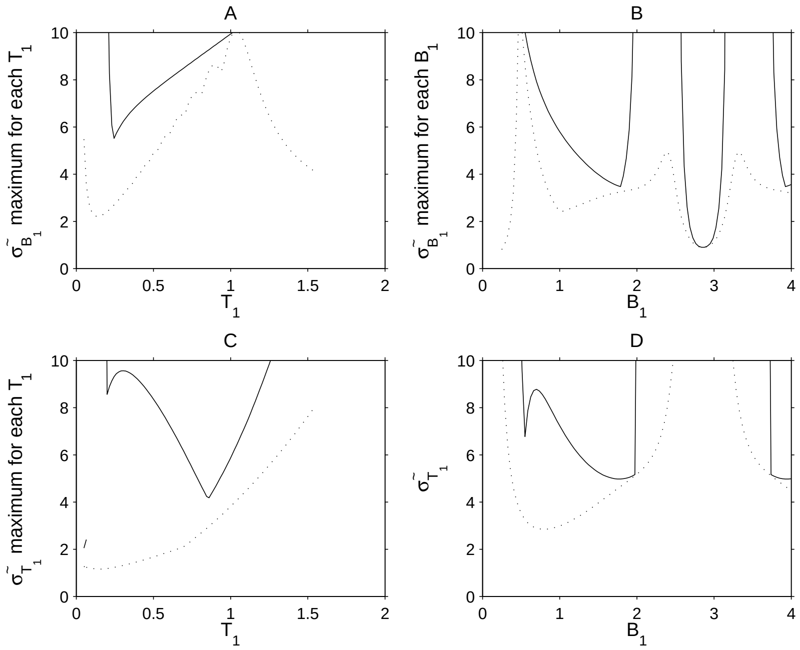

Figure 6.9: AFI model $N = 2$, compare Fig. 6.6.

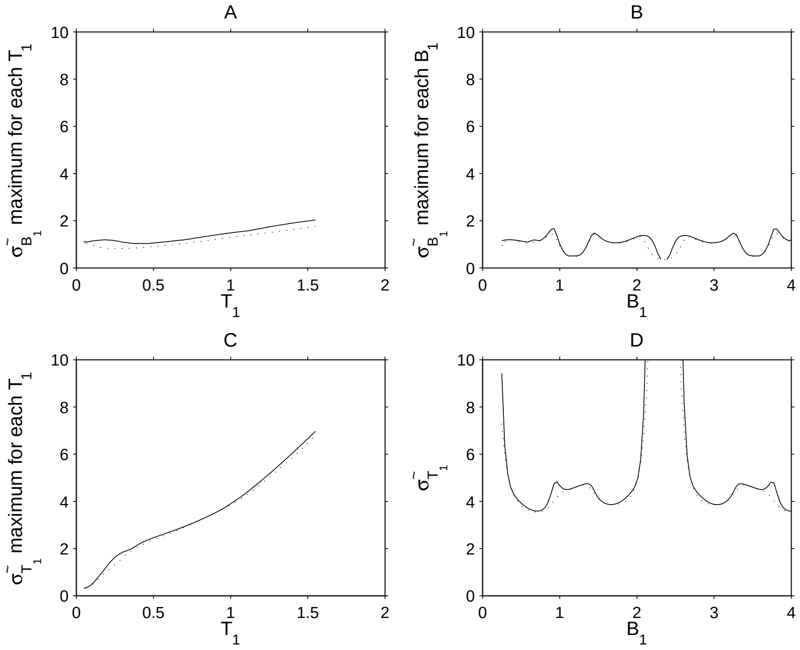

Figure 6.10: AFI model $N = 4$, compare Fig. 6.6.

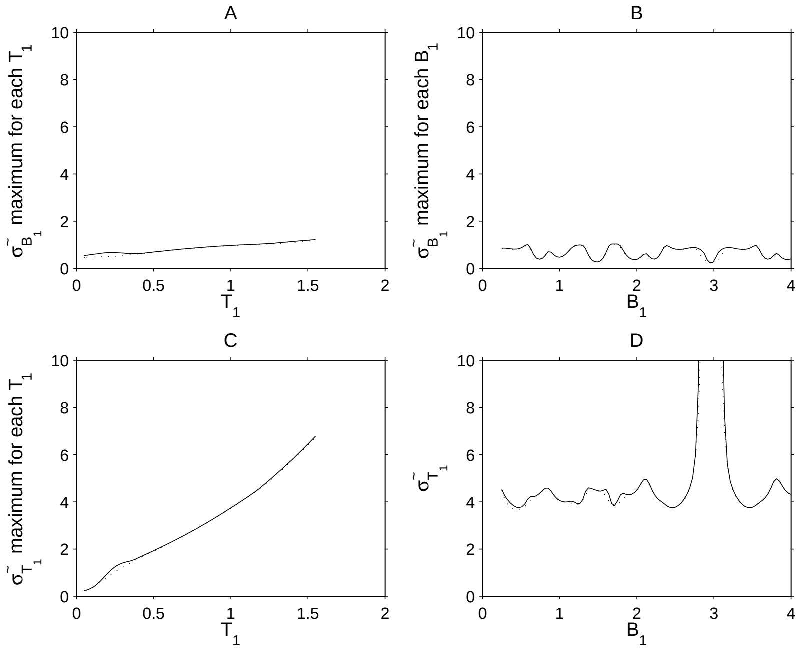

Figure 6.11: AFI model $N = 8$, compare Fig. 6.6.

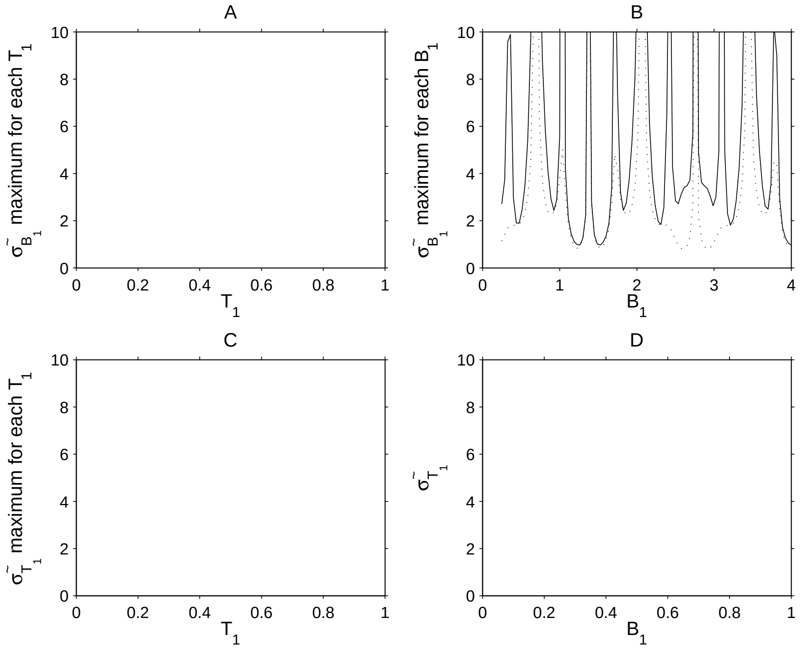

Figure 6.12: BP model $N = 2$, compare Fig. 6.6.

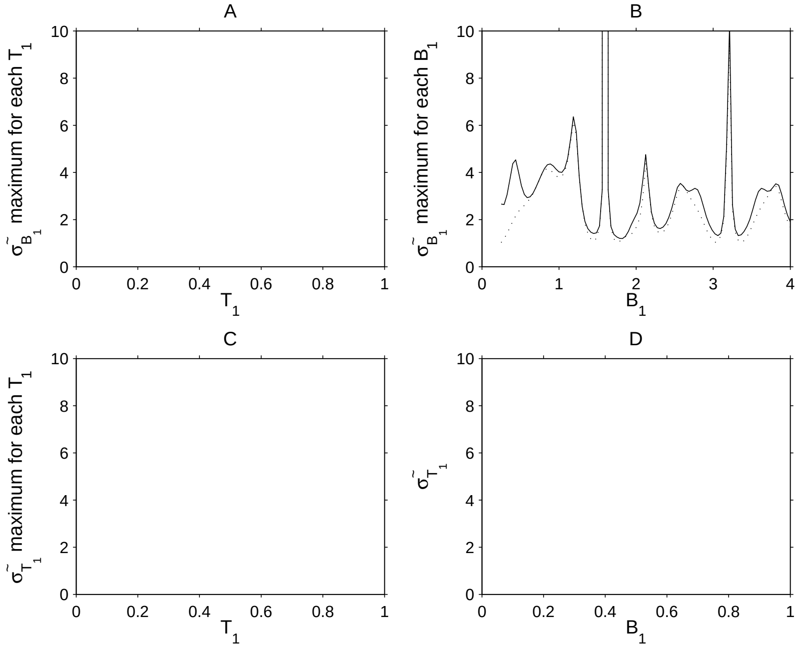

Figure 6.13: BP model $N = 4$, compare Fig. 6.6. Some CRB values exceeded the axis range.

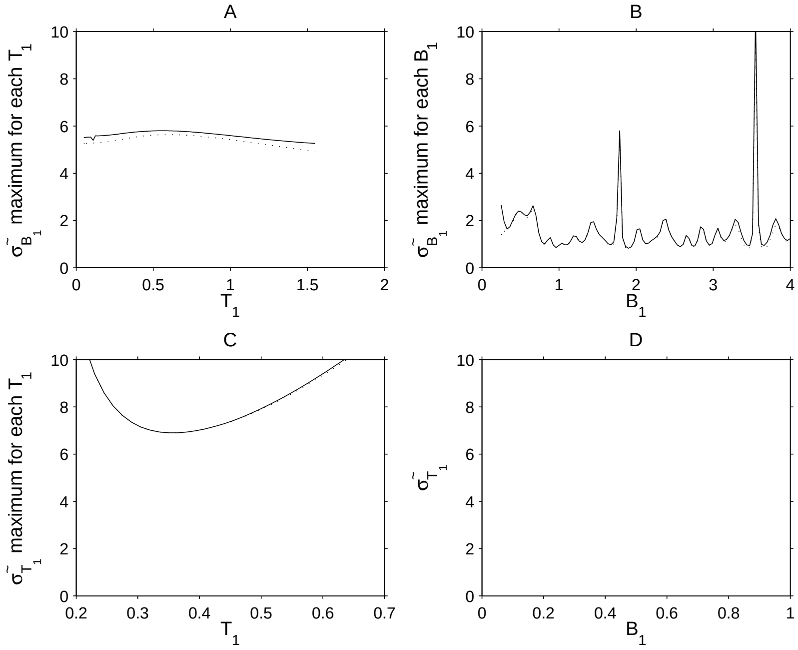

Figure 6.14: BP model $N = 8$, compare Fig. 6.6.

6.4.6 CRB Extension: Limitation of the Maximum Allowed TR

What happens to the optimal results when the maximum allowed T_R is limited? How does this effect the minimum achieved $\tilde{\sigma}_b$ and $\tilde{\sigma}_t$?

Here set the lower T_R search bound quite low to .01 and let the upper T_R search bound vary from .2 to 1.2. We looked at using two scans. As previously, (6.17) was minimized to give the optimal parameters. In Fig. 6.15, we plotted both $\tilde{\sigma}_b$ and $\tilde{\sigma}_t$ as a function of the upper T_R limit.

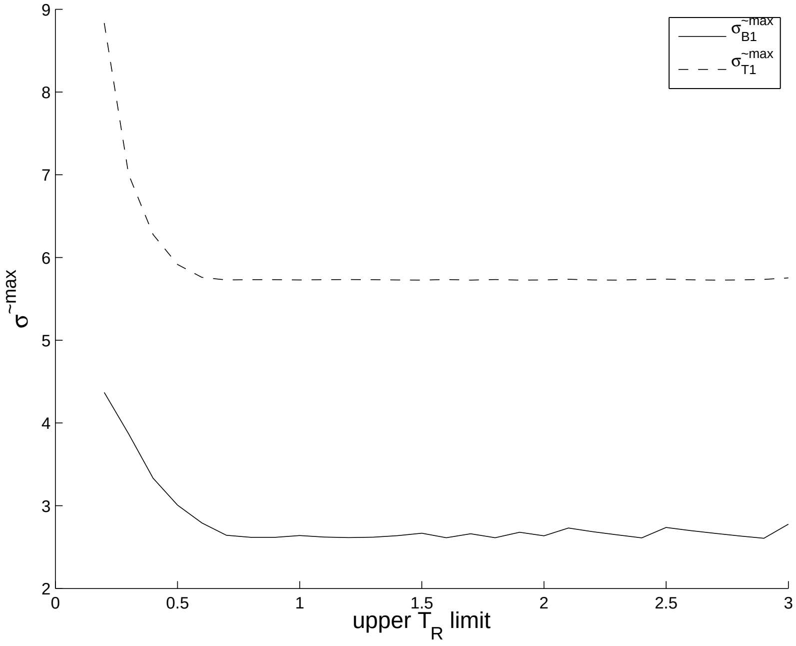

Figure 6.15: $\tilde{\sigma}_b$ and $\tilde{\sigma}_t$ as a function of upper T_R limit.

6.4.7 CRB Extension: Effect of ΔB_0

The previous analysis neglected the effect of B_0 in the models (6.14), (6.15), and (6.16). However, in the presence of magnetic field inhomogeneity, there is no closed form solution to the Bloch equation for an arbitrary RF pulse [78]. Therefore, to test the effect of B_0 inhomogeneity, we focused on the SSI model.

We simulated the model using a Bloch simulator in MATLAB and calculated numerical derivatives from the equilibrium signal values. The CRB from the simulator for $\Delta_{B_0} = 0$ matched the CRB when calculated with implicit or explicit differentiation as before. We set $B_0 = 1.5$ and let $\Delta_{B_0} = [0, 125, 250, 375, 500]$ Hz. We assumed a hard pulse (no slice selection effects). For the SSI pulse, the number of pulses needed to achieve a relative error err is given by:

$$n_{equ.} = \left[-\frac{T_1}{2T_R} ln(err) - \frac{1}{2} \right],$$

where $[\cdot]$ is the ceiling operator. We set $err = 0.001$ and repeated the pulse the larger of 5 or $n_{equ.}$ times. We originally did this analysis for $N = 2$, but the results are similar for $N > 2$.

We used the optimal design parameters found in Table 6.1. Then, we calculated a similar graph to Fig. 6.1. Here, in Fig. 6.16, each line corresponds to a different value of Δ_{B_0}. Clearly, we can see that the effect of B_0 inhomogeneity is very small and does not overly effect the results of the previous analysis at the optimal parameters. Only when the variance $\tilde{\sigma}$ becomes very large is the difference between the different amounts of magnetic field inhomogeneity even seen.

6.4.8 CRB Extension: Possible Application to Multiple Coils

This analysis focuses only on a single coil, single voxel model. With multiple coils, we theorize the possible effect on the effective combined B_1^+ map would be a smaller B_1^+ range over the object. Therefore, we performed a similar analysis but constrained $b \in [.81.2]$.

The optimal parameters using the smaller B_1^+ range are shown in Table 6.2. For the SSI method, the optimal parameters are similar, but the optimal parameters are quite different for the BP method.

The graphs similar to Fig. 6.1 are reproduced below in Fig. 6.17, Fig. 6.18, and Fig. 6.19.

The SSI model performs similarly, with slightly better results as does the AFI and we

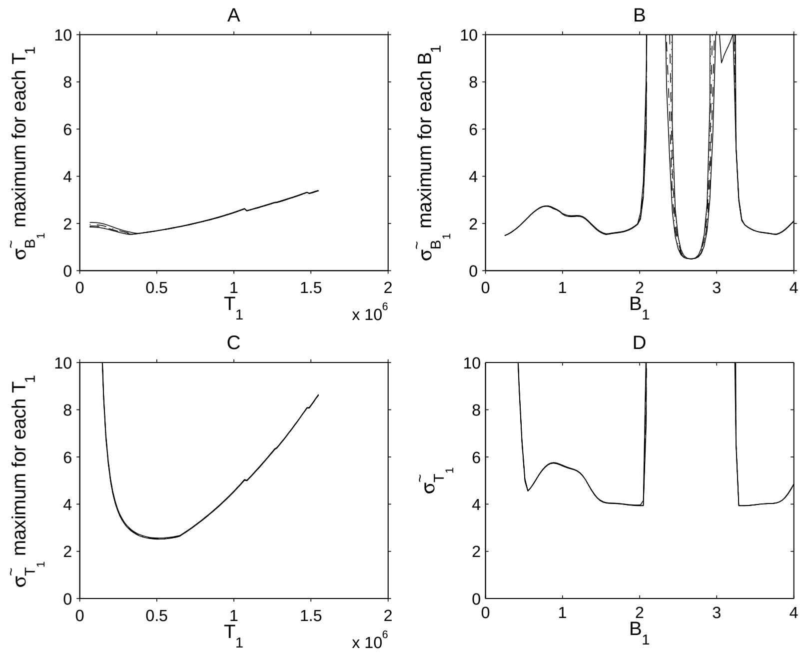

Figure 6.16: Magnetic field inhomogeneity effect on SSI model. $N = 2$, compare Fig. 6.1. Each line corresponds to a different level of magnetic field inhomogeneity from 0 to 500 Hz when $B_0 = 1.5$ T.

can see large improvements with the BP method.

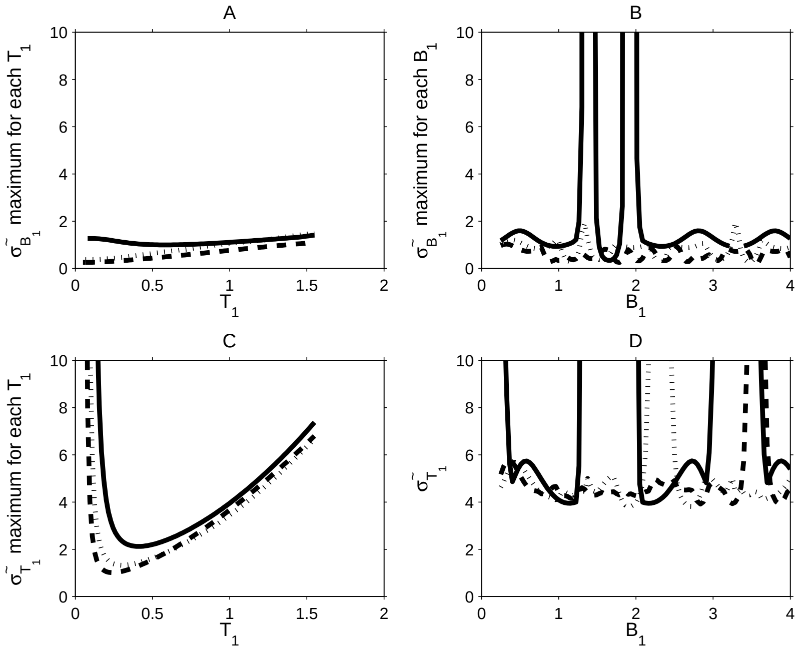

Figure 6.17: Application to multiple coils for the SSI model. $N = 2$ (solid line), 4 (dotted line), 8 (dashed line). We plot, at the optimal parameters in Table 6.1, the maximum $\tilde{\sigma}_b$ for each T_1 over B_1^+ values in the search range (A), the maximum $\tilde{\sigma}_b$ for each B_1^+ over T_1 values in the search range (B), the maximum $\tilde{\sigma}_t$ for each B_1^+ over T_1 values in the search range (C), and the maximum $\tilde{\sigma}_t$ for each T_1 over B_1^+ values in the search range (D).

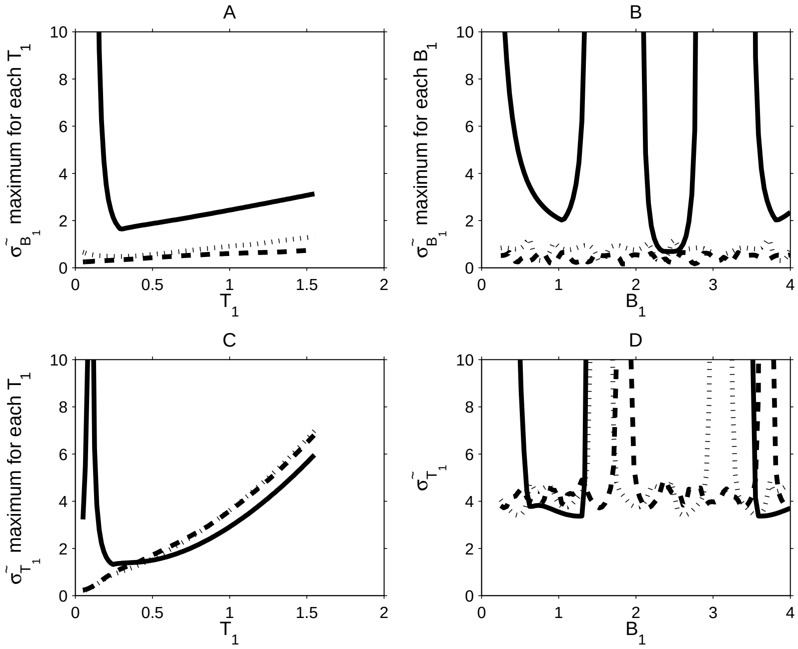

Figure 6.18: Application to multiple coils for the AFI model. Compare Fig. 6.1.

Table 6.2: Optimized scan parameters based on (6.17) with small B_1^+ range

Model	N	Δ_α or α (radians)	Δ_{T_R} or T_{R1} (sec)	T_{R2} (sec)
SSI	2	1.9006	0.82	-
SSI	4	1.3587	0.61	-
SSI	8	0.8836	0.52	-
AFI	2	0.6441	0.67	0.10
AFI	4	1.0132	0.61	0.10
AFI	8	0.8522	0.64	0.10
BP	2	0.3927	0.825	-
BP	4	0.1963	0.535	-
BP	8	0.0982	0.825	-

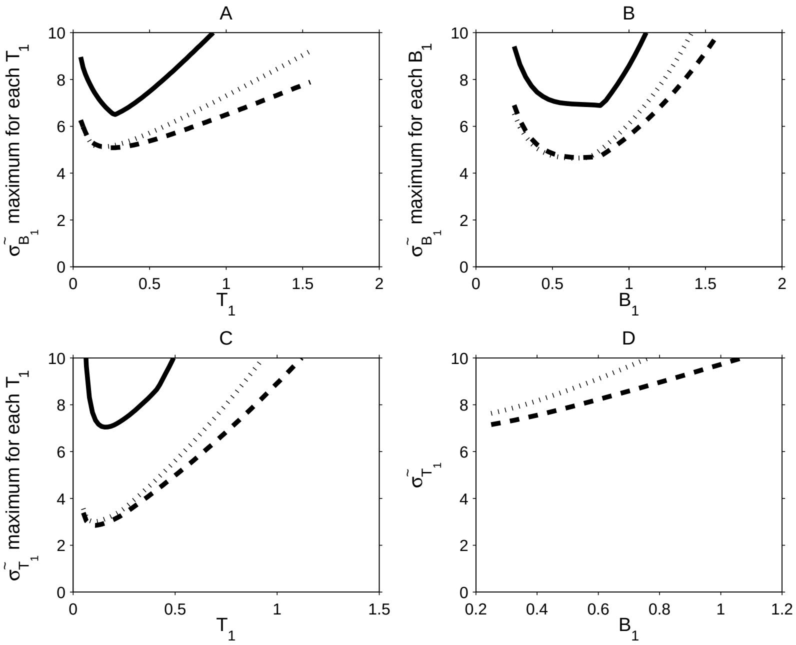

Figure 6.19: Application to multiple coils for the BP model. Compare Fig. 6.1.

6.5 Joint B_1^+,T_1 estimation: Theory

6.5.1 Signal model for multiple coils, multiple tip angles/coil combinations and/or multiple TRs

Suppose there are K coils. We take M measurements by transmitting with different coil combinations and receiving from a common coil. (This method could be generalized to use multiple receive coils.) For each measurement, one or more coil(s) are driven simultaneously by the same RF signal $b_1(t)$ with possibly different known amplitude scaling factors α_{mk}, where k denotes the coil number, $m = 1, \ldots, M$ denotes the measurement number, and $\boldsymbol{\alpha}$ is a $M \times K$ array containing the scaling factors α_{mk}. For the problem to be tractable, we require that $M > K + 2$. The complex coil patterns sum together due to linearity to make the total transmitted B_1^+ field. This general model encompasses the conventional model if we let $K = 1$, $M = 2$, and

$$\boldsymbol{\alpha} = \begin{bmatrix} 1 \\ 2 \end{bmatrix}.$$

We model the resulting M reconstructed images as follows:

$$y_{jm} = f_j F\left(\sum_{k=1}^{K} \alpha_{mk} z_{jk}, T_j, \Delta_j^{B_0}, \mathrm{TR}_m\right) + \varepsilon_{jm}, \tag{6.18}$$

for $m = 1, \ldots, M$ and $j = 1, \ldots, N$, where f_j denotes the underlying object transverse magnetization in the jth voxel (multiplied by the sensitivity of the receive coil) and ε_{jm} denotes zero-mean complex gaussian noise. TR_m is the repetition time of the pulse sequence. Δ^{B_0} is the offset in the B_0 field; we assume this is known (see [44], for example). $\boldsymbol{T}$ is the T_1 map over the object.

The B_1^+ map, constrained to be real in the conventional model, is actually a complex quantity. z_{jk} denotes the unknown complex B_1^+ map that relates RF amplitude to tip angle and phase at the jth voxel for the kth coil. When multiple coils are driven by the same signal $b_1(t)$ (with possibly different amplitudes), then the fields from those coils will superimpose and the complex coil patterns will add by linearity, hence the sum over k in (6.18). If the units of the amplitudes α_{mk} are gauss, then the units of z_{jk} will be radians per gauss. More typically, the units of α_{mk} are arbitrary, and all that is known is their relative values. In this case z_{jk} will have units such that the product of α_{mk} and z_{jk} has units of radians. This should suffice for RF pulse design. We would like to use as few coil combinations as possible, while still being able to estimate each coil pattern z_{jk} accurately.

The function F in (6.18) is a generalization of the SSI method that inherently incorporates slice selection effects. The function F is explained further in Section 6.5.3. We will not show explicitly F's dependence on Δ^{B_0} and TR because these are known constants with respect to this model.

The model (6.18) expands the one used in [41,42] (where TR was infinity) and includes both slice selection effects and linear transceive coil combinations. By jointly estimating T_1 and B_1^+, the SSI signal model allows for shorter TR values to be used

Recent B_1 mapping methods [10, 90] have introduced linear combinations of transmit coils. These methods have the advantage of using much smaller tip angles while still collecting enough signal to produce accurate results. The proposed method accommodates this matrix transmit technique with a comprehensive measurement model that also can include slice selection effects and accounts for the noise factors that are often ignored by existing methods.

The goal is to estimate each B_1^+ map $\boldsymbol{z}_k \triangleq (z_{1k}, \ldots, z_{Nk})$ and the T_1 map $\boldsymbol{T} \triangleq (T_1, \ldots, T_N)$ from the reconstructed images $\{y_{jm}\}$. The underlying magnetization $\boldsymbol{f} \triangleq (f_1, \ldots, f_N)$ is also unknown but is a nuisance parameter. We would like the estimator to work robustly even in image regions where f_j is small.

If f_j were allowed to be complex, then the model above would be non-identifiable because we could add phase to $\boldsymbol{f}$ and subtract the same phase from each $\boldsymbol{z}_k$ and $\mathsf{E}[y_{jkl}]$

would remain unchanged. We take the approach of constraining $\boldsymbol{f}$ to be real. This reduces the ambiguity to a sign change of $\boldsymbol{f}$ and a corresponding π phase shift in each phase map. This does have the disadvantage of assigning any object phase (from δB_0, for example) into the phase of the B_1^+ maps, which may influence the smoothness of the B_1^+ maps. Another solution that also makes the problem identifiable assumes that the first coil's phase map is zero and then all the other phase map values would be relative phases, in which case f can be complex.

We also note a single surface coil for receive will suffice, even when multiple transmit coils are used. In this case, $\boldsymbol{f}$ will be a product of the spin density and the receive coil sensitivity pattern and $\boldsymbol{z}$ will include a constant (over k) phase offset from the receive coil.

6.5.2 Regularized estimator

We propose to jointly estimate the B_1^+ maps $\boldsymbol{z} = (\boldsymbol{z}_1, \ldots, \boldsymbol{z}_K)$, the T_1 map $\boldsymbol{T}$, and the object $\boldsymbol{f}$ by finding minimizers of the following penalized least squares cost function:

$$\begin{aligned} (\hat{\boldsymbol{z}}, \hat{\boldsymbol{T}}, \hat{\boldsymbol{f}}) &= \arg\min_{\boldsymbol{z}, \boldsymbol{T}, \boldsymbol{f}} \Psi(\boldsymbol{z}, \boldsymbol{T}, \boldsymbol{f}), \\ \Psi(\boldsymbol{z}, \boldsymbol{T}, \boldsymbol{f}, \mathrm{TR}\,) &= L(\boldsymbol{z}, \boldsymbol{T}, \boldsymbol{f}) + \beta_{\boldsymbol{z}} R(\boldsymbol{z}) + \beta_{\boldsymbol{T}} R(\boldsymbol{T}) + \beta_f R(\boldsymbol{f}), \end{aligned} \tag{6.19}$$

where

$$L(\boldsymbol{z}, \boldsymbol{T}, \boldsymbol{f}) = \sum_{j=1}^{N} \sum_{m=1}^{M} \frac{1}{2} \left| y_{jm} - f_j F\left(\sum_{k=1}^{K} \alpha_{mk} z_{jk}, \boldsymbol{T} \right) \right|^2 \tag{6.20}$$

and

$$R(\boldsymbol{z}) = \sum_{k=1}^{K} \mathsf{R}(\boldsymbol{z}_k), \tag{6.21}$$

where $\mathsf{R}(\boldsymbol{z}_k)$ is regularizing roughness penalty function for the kth B_1^+ map. Each β is a regularization parameter that controls the smoothness of the estimate. Because one may desire different amounts of smoothing for each map, we label each parameter: $\beta_{\boldsymbol{z}}, \beta_{\boldsymbol{T}}, \beta_{f}$. However, each parameter is user-chosen based on the desired amount of smoothing (explained in Appendix L) and is not a function of any variable. Spatial resolution analysis aids in selection of each β.

We use quadratic regularization for the maps $\boldsymbol{z}_k$ because B_1^+ maps are expected be spatially smooth, although edge-preserving regularization could be used if needed. We note that although there seems to be plausible reasons why a particular B_1^+ map might not be smooth, in the literature, B_1^+ maps are always very smooth. This is true, even in cases such as cancer where there is a large deviation from the normal brain, presumably because the main cause of RF inhomogeneity, even in abnormal subjects, is due to air/water susceptibility as the RF waves propagate [13]. We use edge-preserving regularization for both T_1 (and, if desired, $\boldsymbol{f}$), because they contain detailed structural information, along with a relatively small β to preserve detail.

There is no analytical solution for the minimizer of $\Psi(\boldsymbol{z}, \boldsymbol{T}, \boldsymbol{f})$ over all parameters, so iterative methods are required.

Minimization with respect to $\boldsymbol{z}$ and $\boldsymbol{T}$ is nontrivial due to the non-linearity of F. Possible minimization approaches include quadratic majorizer principles (see Section 3.6.1), or variable projection (see Section 5.2.3), or generalized optimization methods. We choose to use the gradient descent method specified below. Derivatives for the gradient descent method are described in detail in Appendix I and Appendix J.

We use a preconditioned gradient descent method. There are many possibilities for updating all the variables. We can use either a simultaneous update for all variables or a block alternating minimization approach. With a simultaneous update for all variables, let $\boldsymbol{v} = \begin{bmatrix} \boldsymbol{z} & \boldsymbol{T} & \boldsymbol{f} \end{bmatrix}$, and then

$$\boldsymbol{v}^{(n+1)} = \boldsymbol{v}^{(n)} + \alpha_n \boldsymbol{d}^{(n)}, \tag{6.22}$$

where $\boldsymbol{d}$ is the search direction given by the gradient of the cost function with respect to each variable, letting the preconditioning matrix equal the identity matrix in this paper (see Section I for the derivatives).

Ideally, by an exact line search $\alpha_n = \arg\min_\alpha \Psi\left(\boldsymbol{v}^{(n)} + \alpha\, \boldsymbol{d}^{(n)}\right)$. In practice, we choose α using Newton's method as follows [30]:

$$\begin{aligned}
\Psi(\alpha) &= \Psi\big(\boldsymbol{v}^{(n)} + \alpha \boldsymbol{d}^{(n)}\big) \\
\dot{\Psi}(\alpha) &= \nabla\, \Psi\left(\boldsymbol{v}^{(n)} + \alpha \boldsymbol{d}^{(n)}\right) \boldsymbol{d}^{(n)} \\
\ddot{\Psi}(\alpha) &= \left(\boldsymbol{d}^{(n)}\right)' \nabla^2\, \Psi\left(\boldsymbol{v}^{(n)} + \alpha \boldsymbol{d}^{(n)}\right) \boldsymbol{d}^{(n)} \\
&\approx 1/\epsilon \left(\dot{\Psi}(\alpha+\epsilon) - \dot{\Psi}(\alpha)\right),
\end{aligned}$$

and finally, we let

$$\begin{aligned}
\alpha_n &= -\frac{\dot{\Psi}(0)}{\ddot{\Psi}(0)} \\
&\approx \frac{\left|-\nabla\, \Psi\big(\boldsymbol{v}^{(n)}\big)\, \boldsymbol{d}^{(n)}\right|}{\left|\frac{1}{\epsilon}\left(\nabla\, \Psi\left(\boldsymbol{v}^{(n)} + \epsilon \boldsymbol{d}^{(n)}\right) \boldsymbol{d}^{(n)} - \nabla\, \Psi\left(\boldsymbol{v}^{(n)}\right) \boldsymbol{d}^{(n)}\right)\right|}.
\end{aligned} \tag{6.23}$$

This still requires care in choosing ϵ. Here, we let

$$\epsilon = \frac{\max|\boldsymbol{v}|}{\max|\boldsymbol{d}|} * .01,$$

where $.01$ was chosen empirically. Then, to force monotonicity, following [71], we set $\alpha = \alpha/2$ until $\Psi\left(\boldsymbol{v}^{(n)} + \alpha_n \boldsymbol{d}^{(n)}\right) \leq \Psi\left(\boldsymbol{v}^{(n)}\right)$.

We note that for a given estimate $\hat{\boldsymbol{z}}^{(n)}$ of $\boldsymbol{z}$ and $\hat{\boldsymbol{T}}^{(n)}$ of $\boldsymbol{T}$ at the nth iteration, the minimizer of Ψ with respect to $\boldsymbol{f}$, assuming no regularization of $\boldsymbol{f}$, is found analytically to be:

$$\hat{f}_j^{(n)} = \frac{\sum_{m=1}^{M} \operatorname{real}\left\{y_{jm}^* F(\hat{x}_{jm}^{(n)}, T_j^{(n)})\right\}}{\sum_{m=1}^{M} \left|F(\hat{x}_{jm}^{(n)}, T_j^{(n)})\right|^2}, \tag{6.24}$$

where we define the composite B_1^+ maps $\mathbf{x}_m$ as follows:

$$x_{jm} \triangleq \sum_{k=1}^{K} \alpha_{mk} z_{jk}. \tag{6.25}$$

In this thesis, we choose to use an alternating minimization approach in each step, alternating which variable we minimize in $\boldsymbol{v}$ as in (6.22) while holding the other variables constant. We use this method because we do not regularize the object and also because the step size in PGD minimization scales appropriately for each variable. Simultaneous gradient descent appeared to converge slower; however, we anticipate that with a suitable diagonal preconditioner, this method would also be acceptable. In Section 6.6.1 and Section 6.6.2, we used a set number of iterations that gave good qualitative results; ideally, we would use stopping rules based on, for example, percent change in the iterative estimates.

We note that T_1 has a constraint that $\boldsymbol{T} > 0$. We modify the alternating PGD minimization to perform constrained minimization by performing a variable transformation as explained in Appendix M.

The cost function Ψ is non-convex, so the alternating minimization algorithm described above will descend from the initial estimates to a local minimum [63]. Thus it is essential to choose reasonable initial estimates. See Appendix K for details.

Regularized methods have the benefit of being able to choose a value for β based on quantitative analysis. In Appendix L, we analyze the spatial resolution of the regularized estimator (6.19). This analysis leads to a modified penalty function that achieves more uniform spatial resolution in regions with a constant f_j. We choose a value for each β based on the desired FWHM of regularizer smoothing.

6.5.3 F and Slice Selection Effects

In (6.18), F is a function that can incorporate both the type of pulse sequence being used as well as slice selection effects by using a Bloch equation simulator.

After considering an appropriate coordinate rotation, we can express the function F by the following equation:

$$F(z,t) = \mathrm{e}^{\imath \angle z} H(|z|,t). \tag{6.26}$$

Tabulating F would require storing a look-up table with a complex input, while H has a real input and we can store a lower dimensional table. H can be complex, depending on the input RF pulse We conjecture that most symmetric RF pulses will have a real H; this model is general enough to include other pulses, including non-symmetric ones. Both H and F are potentially complex. Therefore, we tabulate H and use (6.26) in our estimation algorithm. During our Bloch simulation, we can also vary T_1 values and B_0 offset values to create a more accurate table that incorporates a larger number of effects, albeit with longer computation time.

Assuming no slice selection effects (*i.e.*, the (unachievable) infinite sinc pulse is used, or 3D imaging) and no B_0 offset, we use the SSI model for F in this paper [16] where

$$H_i^{\mathrm{SSI}}(\phi,t) = \frac{(1-e^{-\gamma_i})\sin(\phi_i)}{1-e^{-\gamma_i}\cos(\phi_i)}, \tag{6.27}$$

where $\gamma = \mathrm{TR}/t$.

In the case of slice selection effects or B_0 offsets (Δ^{B_0}), we tabulate H by evaluating the Bloch equation using a RF pulse and varying its amplitude; *i.e.*, we use

$$b_1(v) = \frac{\theta}{\gamma \int_0^{\Upsilon} p(s)ds} p(v), \tag{6.28}$$

where Υ is the pulse length and $p(v)$ is the RF pulse shape and we vary the amplitude θ T_1, and the B_0 offset to create the three-dimensional table. In the case of non-selective excitation, or in the small-tip angle regime with exactly on resonance excitation, θ would be the excitation tip angle times the B_1^+ map. The table H is calculated once for each RF pulse: for convenience, we normalize H to a maximum value of 1.

In future work, we hope to investigate other common pulses such as those ((B.3),(B.4)) in Appendix B.

We note that one could use a different excitation pulse for each measurement, in which case F would be F_m. For simplicity, we assume the same RF pulse is used for each measurement and suppress the subscript m. We let the subscript R denote the real part and I denote the imaginary part of the quantity. For example, let F_{R} denote the real part of F and let F_{I} denote the imaginary part of F so

$$F = F_{\mathrm{R}} + iF_{\mathrm{I}}.$$

Fig. 6.20, Fig. 6.21, and Fig. 6.22 each show a graph of $H_{\mathrm{R}}(\theta, \boldsymbol{T})$ keeping either $\boldsymbol{T}$ or θ constant for the idealized pulse. The (null) imaginary part is not shown for the example symmetric pulses. Fig. 6.23 shows the derivative of $H_{\mathrm{R}}(\theta, \boldsymbol{T})$ with respect to θ. Fig. 6.24 and Fig. 6.25 show the derivative of $H_{\mathrm{R}}(\theta, \boldsymbol{T})$ with respect to $\boldsymbol{T}$.

6.6 Joint B_1^+,T_1 Experiments

6.6.1 Simulations

To evaluate the regularized B_1^+ and T_1 map estimation method described above, we performed a simulation study using synthetic true maps shown in Fig. 6.26. For the object magnitude f_j and T_1, we used a simulated normal brain anatomical model with each voxel classified into one of 11 different classes [4, 5] For T_1 truth, we generate an image using the classified model and typical T_1 values for each class type. For f_j truth, we generated a proton density image weighted by T_2^*, again using the typical PD and T_2^* values for each class. To use smaller images for truth, we resized these images using bicubic interpolation and anti-aliasing. The B_1^+ maps were simulated based on equations for a magnetic field in a circular current loop [49, 129].

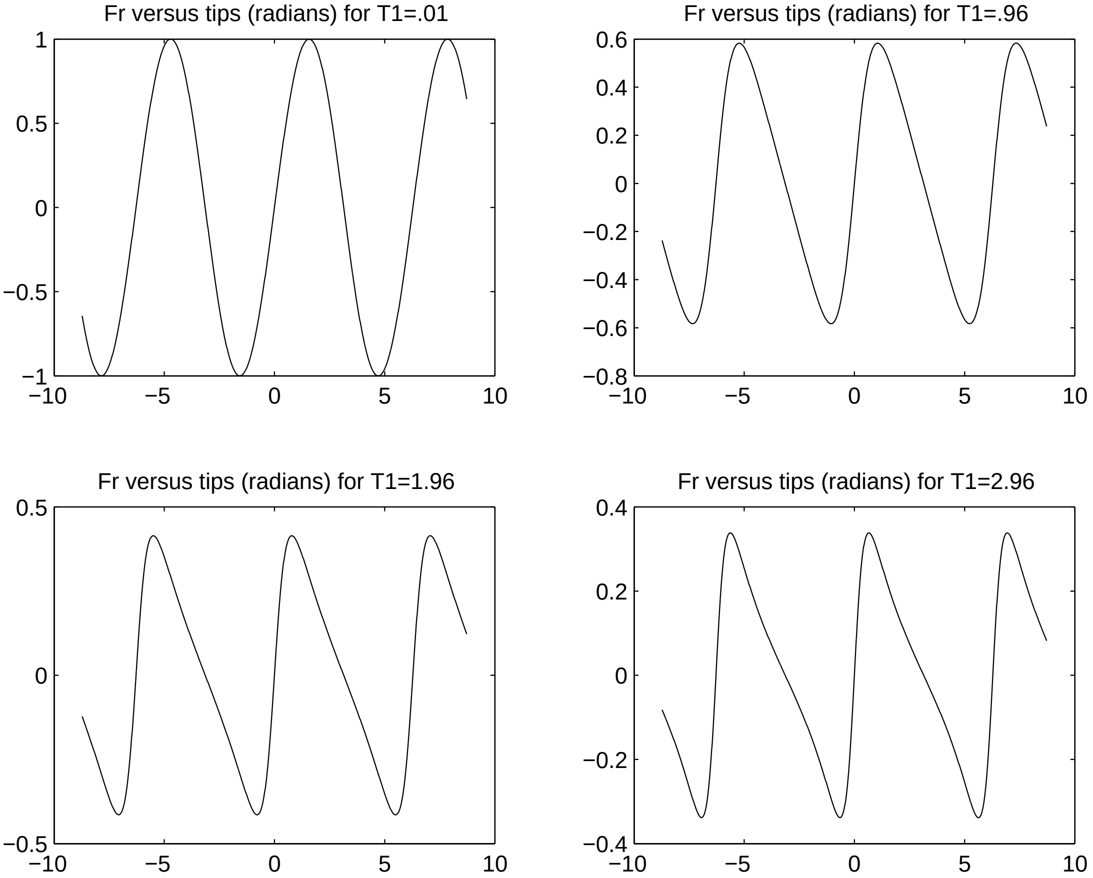

Figure 6.20: Graph of $H_{\mathrm{R}}(\theta, \boldsymbol{T})$ for an idealized infinite sinc pulse holding T_1 constant. We let T_1 equal $\begin{bmatrix}0.01 & 0.96 & 1.96 & 2.96\end{bmatrix}$ and vary θ along the horizontal axis.

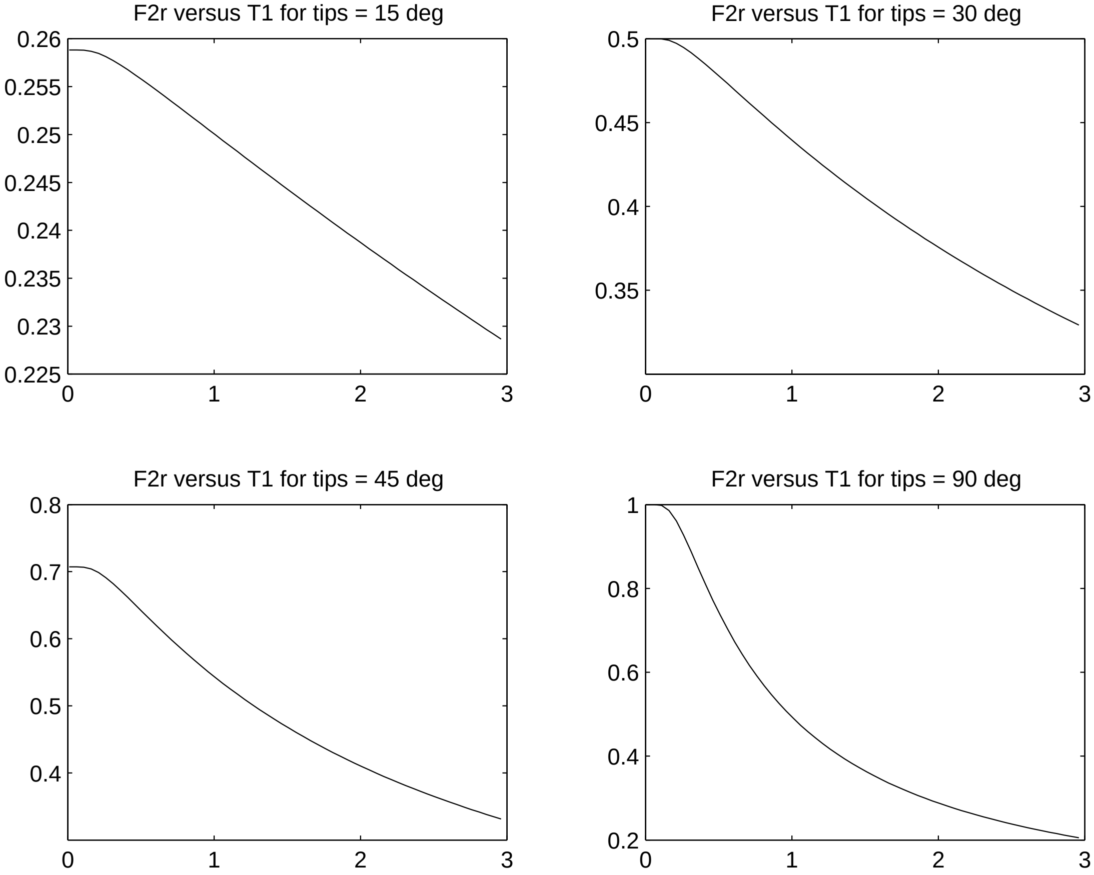

Figure 6.21: Graph of $H_{\mathrm{R}}(\theta, \boldsymbol{T})$ for an idealized infinite sinc pulse holding θ constant. We let θ equal $\begin{bmatrix} 15 & 30 & 45 & 90 \end{bmatrix}$ and vary $\boldsymbol{T}$ along the horizontal axis.

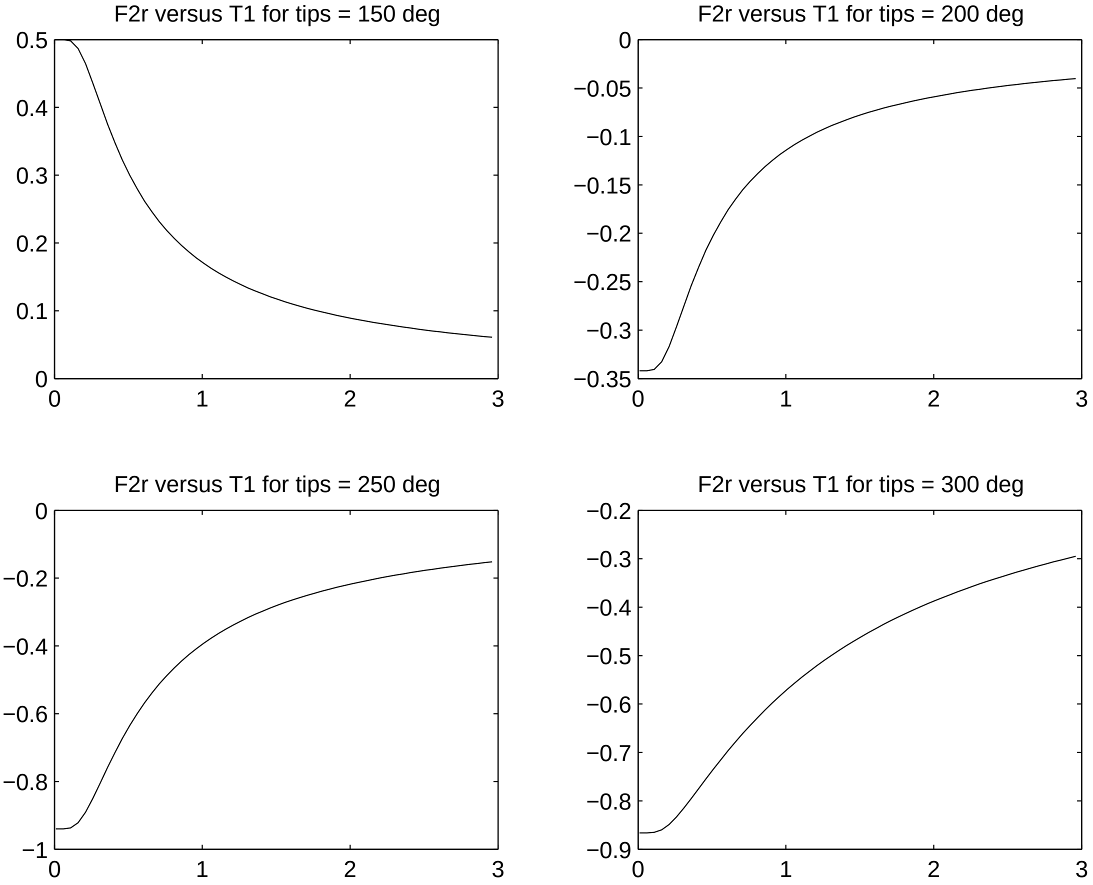

Figure 6.22: Graph of $H_{\mathrm{R}}(\theta, \boldsymbol{T})$ for an idealized infinite sinc pulse holding T_1 constant. We let θ equal $\begin{bmatrix}150 & 200 & 250 & 300\end{bmatrix}$ and vary $\boldsymbol{T}$ along the horizontal axis.

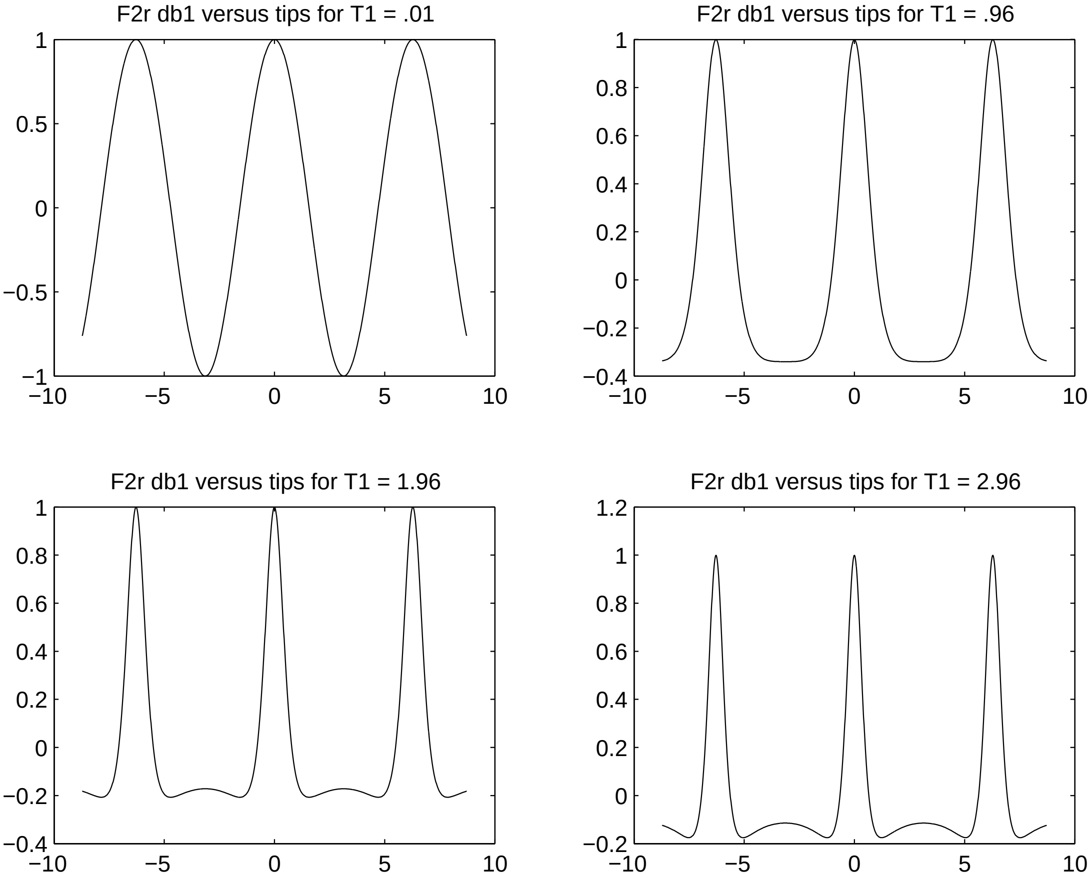

Figure 6.23: Graph of the first derivative of $H_{\mathrm{R}}(\theta, \boldsymbol{T})$ with respect to θ for an idealized infinite sinc pulse. We hold T_1 constant $\begin{bmatrix}0.01 & 0.96 & 1.96 & 2.96\end{bmatrix}$ and vary θ along the horizontal axis.

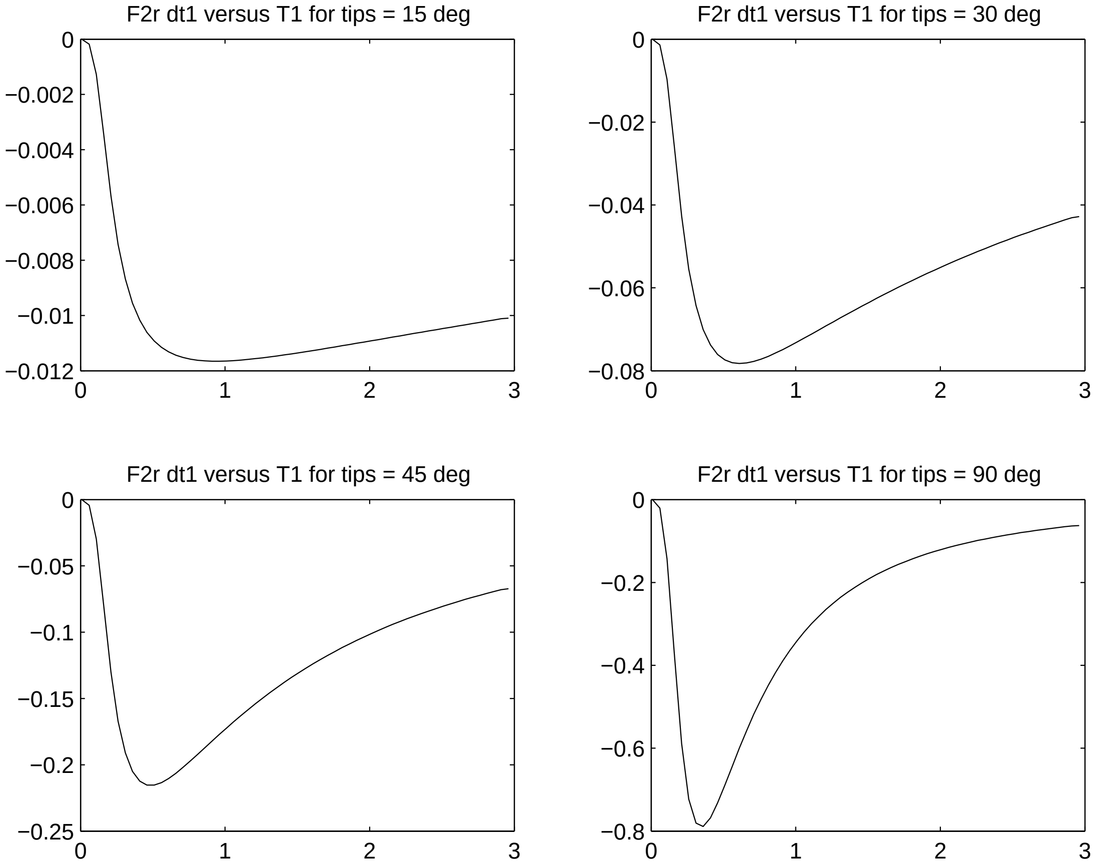

Figure 6.24: Graph of the first derivative of $H_{\mathrm{R}}(\theta, \boldsymbol{T})$ with respect to $\boldsymbol{T}$ for an idealized infinite sinc pulse. We hold θ constant $\begin{bmatrix}15 & 30 & 45 & 90\end{bmatrix}$ and vary $\boldsymbol{T}$ along the horizontal axis.

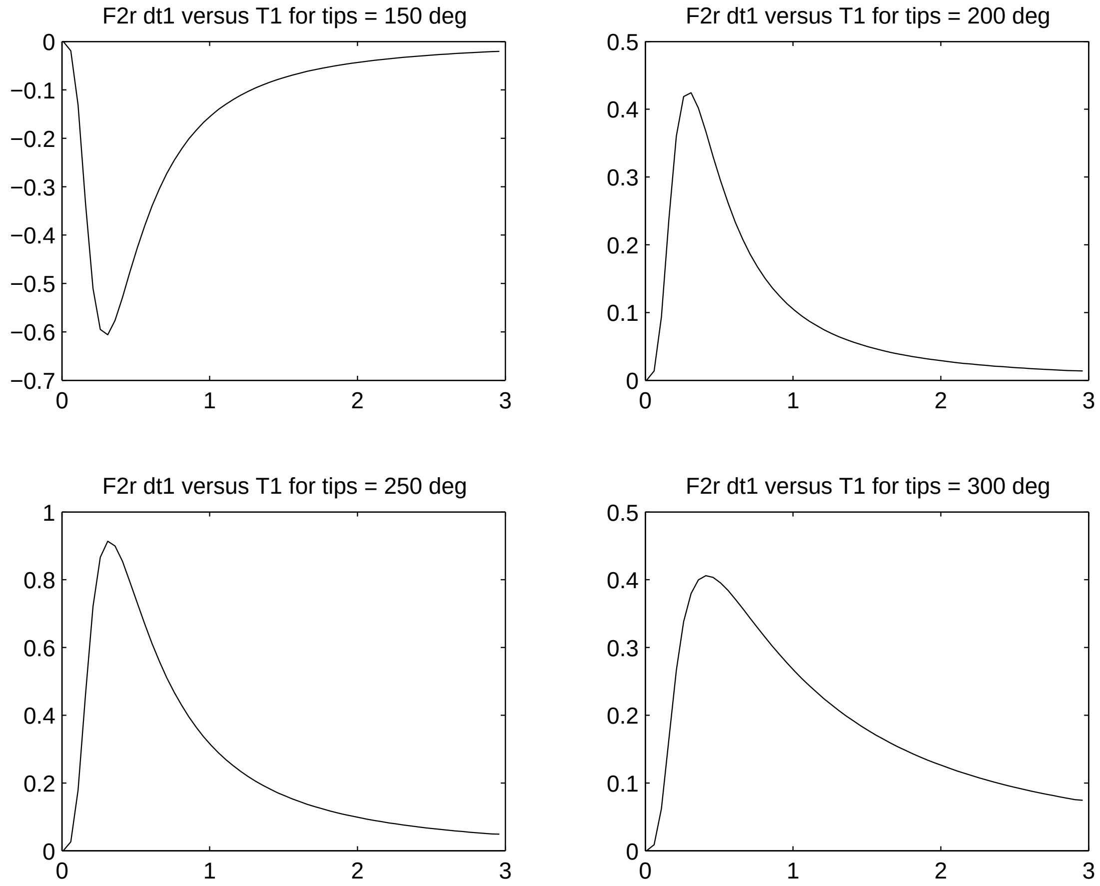

Figure 6.25: Graph of the first derivative of $H_{\mathrm{R}}(\theta, \boldsymbol{T})$ with respect to $\boldsymbol{T}$ for an idealized infinite sinc pulse. We hold θ constant $\begin{bmatrix}150 & 200 & 250 & 300\end{bmatrix}$ and vary $\boldsymbol{T}$ along the horizontal axis.

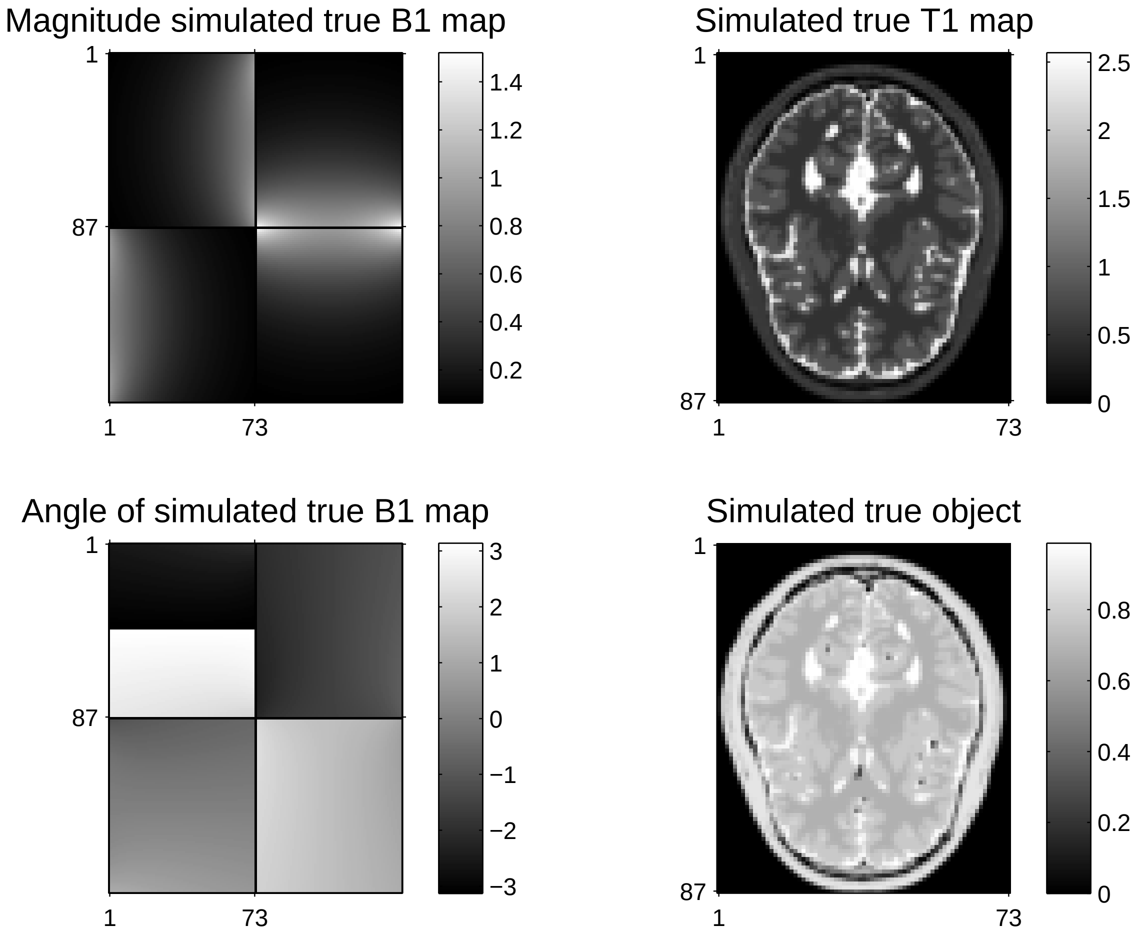
Magnitude simulated true B1 map

Simulated true T1 map

Angle of simulated true B1 map

Simulated true object

Figure 6.26: True simulated maps.

We simulated noisy reconstructed images for $K = 4$ different transmit coils using the model (6.18). We assumed an ideal sinc RF pulse. For our scaling matrix $\boldsymbol{\alpha}$, we used both "one-coil-at-a-time" (OAAT) (*i.e.*, for $M = 3K$

$$\boldsymbol{\alpha}_{\text{OAAT}} = \alpha \cdot \begin{bmatrix} I_K \\ 2 \cdot I_K \\ 3 \cdot I_K \end{bmatrix}, \tag{6.29}$$

where I_k is a $K \times K$ identity matrix) and "leave-one-coil-out" (LOO) (*i.e.*, for $M = 3K$

$$\boldsymbol{\alpha}_{\text{LOO}} = \begin{bmatrix} \alpha 1_K - \alpha I_K \\ 2\alpha \cdot 1_K - 2 \cdot I_K \\ 3\alpha \cdot 1_K - 3 \cdot I_K \end{bmatrix}, \tag{6.30}$$

where 1_K is a $K \times K$ matrix of ones). There are many possible choices for $\boldsymbol{\alpha}$ but we focus on these two possible matrices to illustrate the method. Both matrices are well-conditioned ($\kappa\left(\boldsymbol{\alpha}_{\text{OAAT}}\right) = 1$ and $\kappa\left(\boldsymbol{\alpha}_{\text{LOO}}\right) = 3$). In [91], these two different coil combinations are analyzed with respect to the AFI model, but the results apply to all types of B_1^+ mapping. They found that the LOO method has significantly better map quality than the OAAT, which has strong noise. LOO balances the trade off between noise, especially at low flip angles, and the complementarity of multiple coil maps and can reduce mapping error by an order of magnitude.

We added complex gaussian noise such that the SNR, $10 \log_{10}(\|\boldsymbol{y}\| / \|\boldsymbol{y} - \mathsf{E}[\boldsymbol{y}]\|)$, was either about 60 or 30 dB. Some of these images are shown in Fig. 6.27.

We used either 12 or 16 measurements. For 12 measurements, we repeated each coil combination three times at α, 2α, and 3α (see (6.29) and (6.30)), allowing us to use the triple angle initialization explained in Appendix K. We also compared the method with 16 total measurements, which also included 4α. We fixed $\text{TR} = 0.68$ s and $\alpha = 1.3744$ based on the analysis in Section 6.4 for the SSI model with $N = 4$. We used 50 iterations

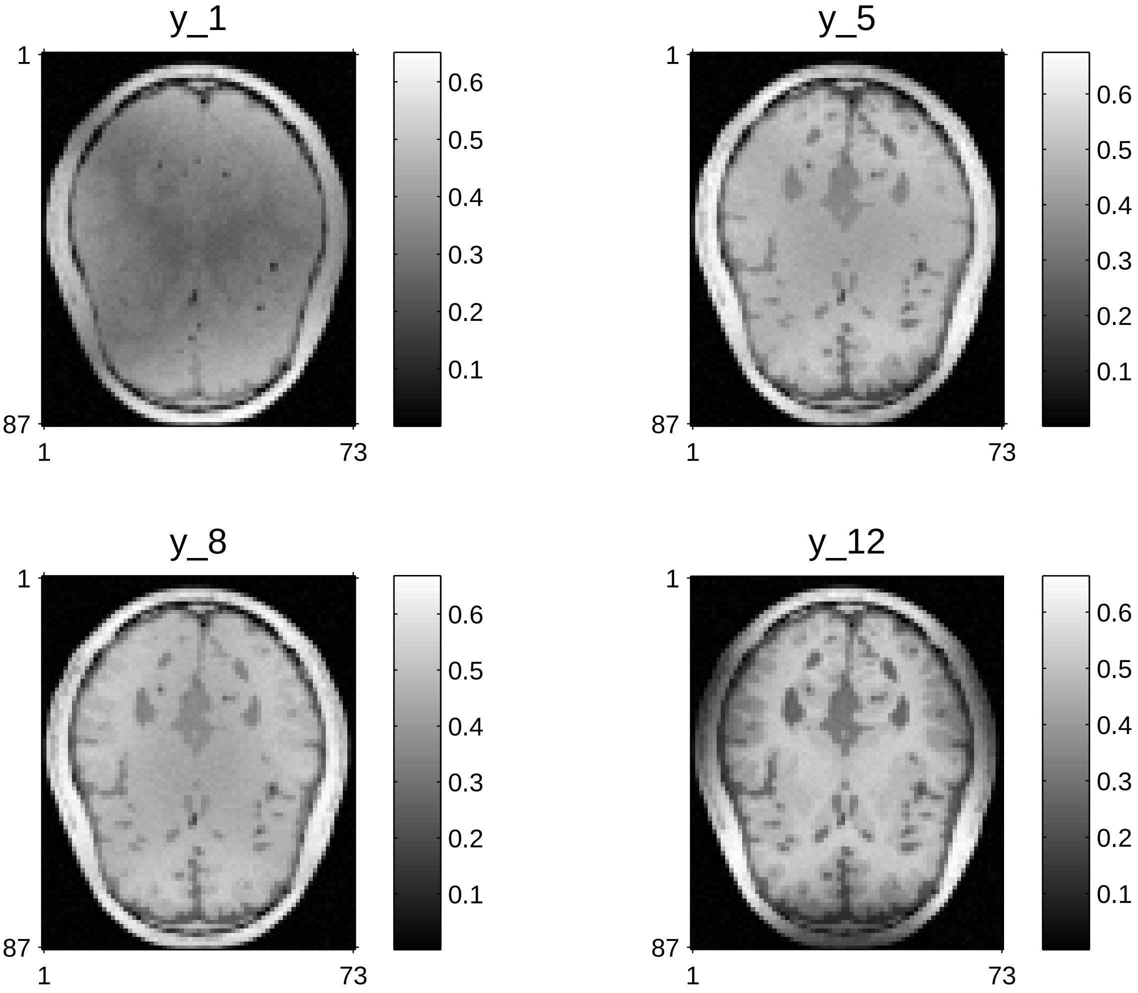

Figure 6.27: Simulated noisy images. For the 1st, 5th, 8th, and 12th measurements (corresponding to the respective rows in (6.30)). We used 4 coils and leave-one-coil-out with an SNR of 60 dB.

(alternating which variable to minimize) with 15 internal PGD iterations to show the full extent of the estimator, although for cases of high SNR, this is excessive. Masked NRMSE (reported in Table 6.3) for the joint B_1^+, T_1 estimation is compared to estimating only B_1^+ using the regularization estimation explained in Chapter V, referring to this estimator as the "previous" estimate. That method ignores T_1 effects, as if $T_R = \infty$. We note that the initial T_1 estimate here is the conventional T_1 estimate for the SSI method described in Section 6.2.2.

First, we compared at a high SNR of 60 dB the OAAT method (shown in Fig. 6.28, Fig. 6.29, Fig. 6.30, and Fig. 6.31) and LOO method (shown in Fig. 6.32. Fig. 6.33, Fig. 6.34, and Fig. 6.35.) We note, in regards to the SNR, some current T_1 mapping papers report SNRs ranging from 100 - 200 dB in the brain [14] and start to see significant bias at about 60 dB [16], though these methods use a much lower TR ($TR < 10$ ms). We used only 12 measurements because both methods perform well, with the most notable error in the T_1 map in OAAT in Fig. 6.30. We still see some small drop-out in the T_1 map for LOO Fig. 6.34, though the T_1 map is definitely improved.

We also compared these methods when used at a lower SNR of 30 dB. Here, the OAAT method struggled with only 12 measurements (figures not shown), so we used 16 measurements. Even at 16 measurements, the noise necessitated using the previous method with a small number of iterations as the initial guess. The final $\boldsymbol{f}$ (see Fig. 6.39) and T_1 (see Fig. 6.38) strongly underestimate the interior of the brain which causes some corruption of the B_1^+ magnitude maps (see Fig. 6.36). Clearly, using LOO improves all estimates, shown in Fig. 6.40, Fig. 6.41, Fig. 6.42, and Fig. 6.43. There is still some overestimation of T_1 along the skull, but overall the estimates perform well at the lower SNR and with only 12 measurements.

The LOO method works reasonably well at smaller SNRs (results for 20 dB shown in Table 6.3, figures not shown).

Overall, the simulation results shows that the proposed method works well, especially

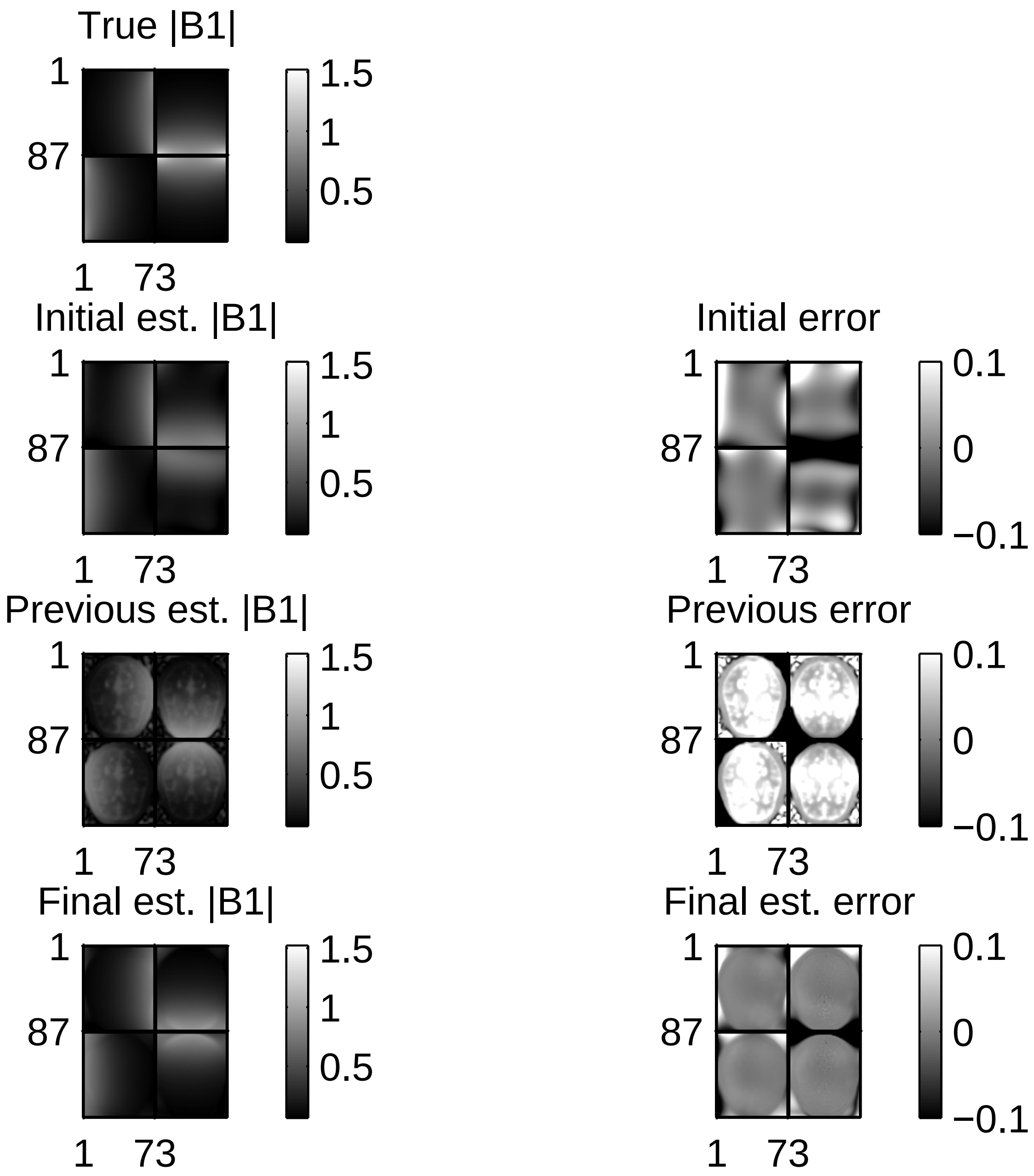

Figure 6.28: Magnitude B_1^+ maps for OAAT at 60 dB with 12 measurements. $|z|$, 50 iterations with 15 internal PGD iterations, 12 measurements, 4 coils, "one at a time", SNR around 60 dB, B_1^+ map regularization parameter is 2^{-3}, T_1 map regularization parameter is 2^{-5}. No object regularization.

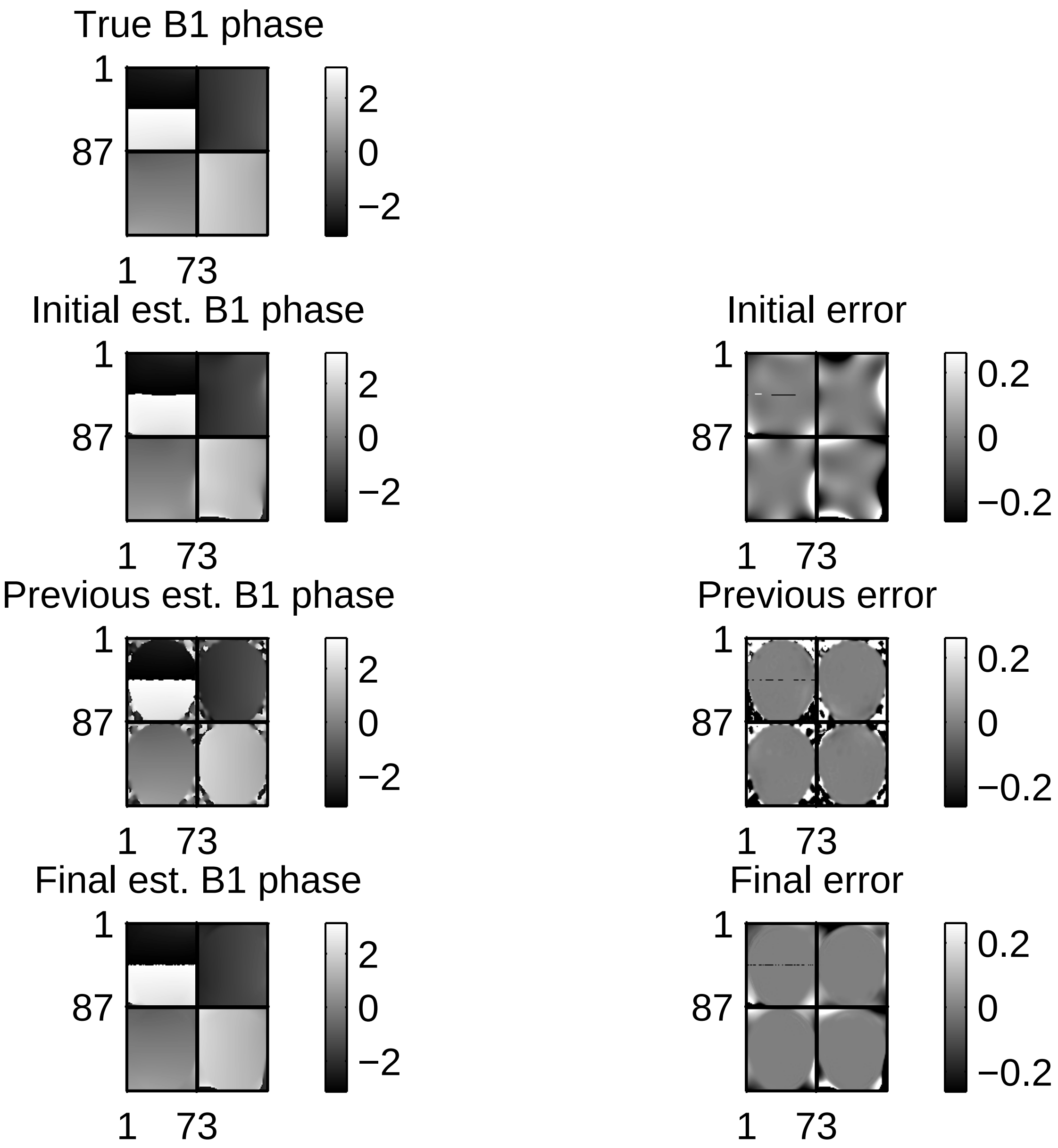

Figure 6.29: Phase B_1^+ maps for OAAT at 60 dB with 12 measurements. Compare Fig. 6.28.

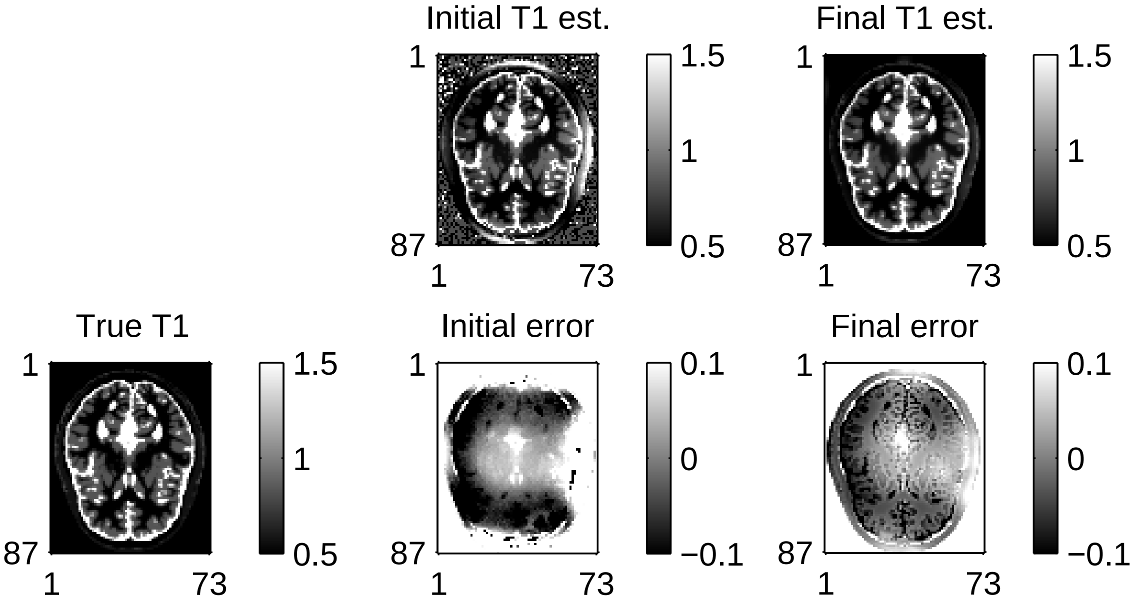

Figure 6.30: T_1 maps for OAAT at 60 dB with 12 measurements. Compare Fig. 6.28.

using the LOO method or when using a larger number of measurements. Areas closer to the skull tend to have some bias, especially in OAAT methods, but the B_1^+ maps are consistently accurate at lower TR values in comparison to the previous method.

We chose our values for α based on our analysis in Section 6.4. However, we wished to see if that analysis, based on the CRB, translated to our final implementation of our joint B_1^+, T_1 estimator. These preliminary results took the simulated true maps (with all four coils) and generated simulated data (16 measurements with “leave-one-out”) with an SNR of approximately 30 dB. The first set of results, summarized in Table 6.4, kept α constant and varied TR. Each set of parameters was only estimated once, so the results are not statistically significant; however, the variance in the NRMSE is not large for these maps and we can try to extrapolate from the table’s trends. Similarly, the second set of results, summarized in Table 6.5, kept TR constant and varied α (by keeping the “leave-one-out” and fixing the $\alpha_{2*j} = 2\alpha_{1*j}$ and $\alpha_{3*j} = 3\alpha_{1*j}$ and $\alpha_{4*j} = 4\alpha_{1*j}$ for $j = 1, 2, 3, 4$).

We see from Table 6.4, that using TR values around the “optimal” TR of .68 ms gave the lowest error for the B_1^+ maps, though a wide range of TR values gave very good B_1^+

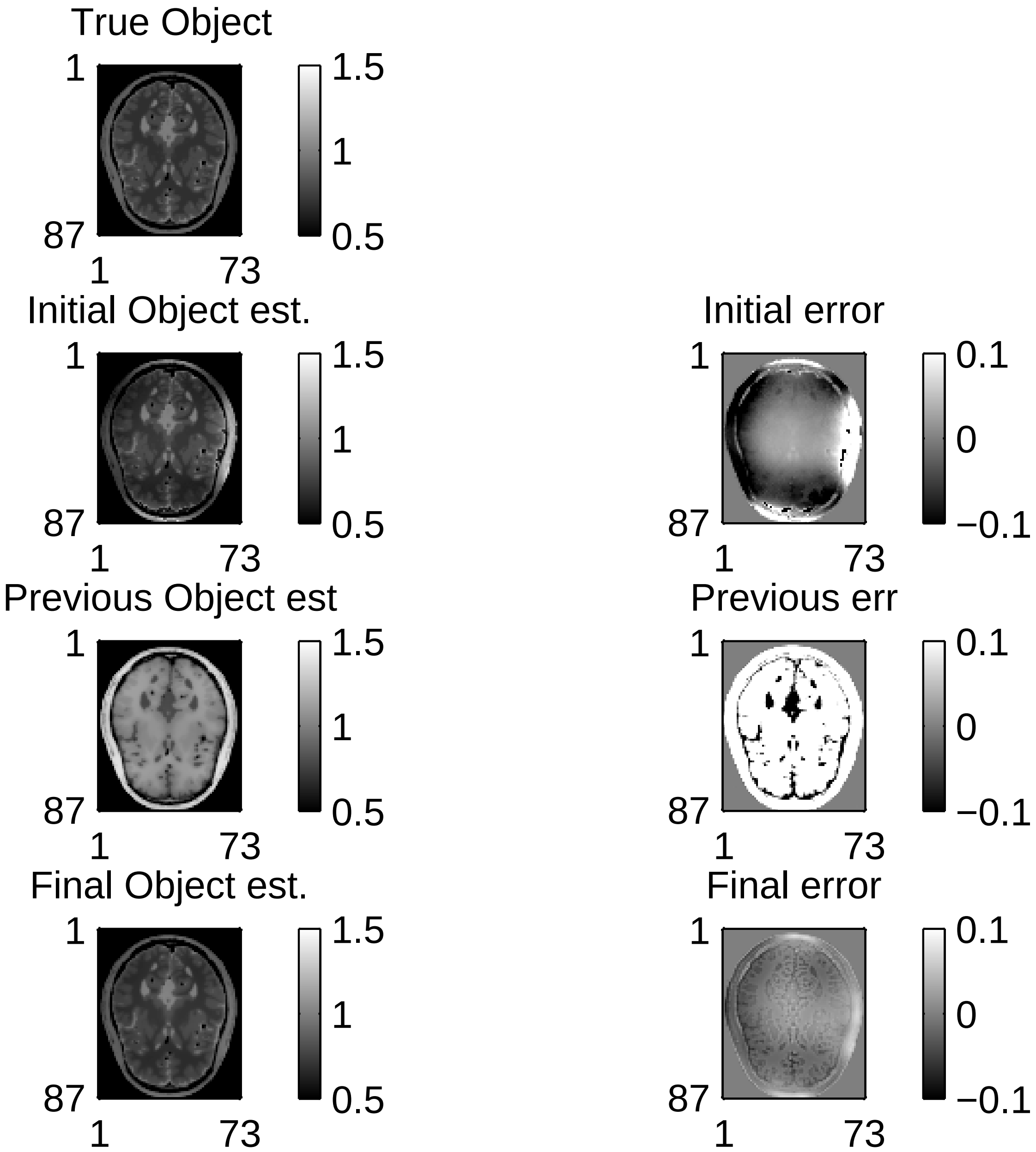

Figure 6.31: $\boldsymbol{f}$ estimates for OAAT at 60 dB with 12 measurements. Compare Fig. 6.28.

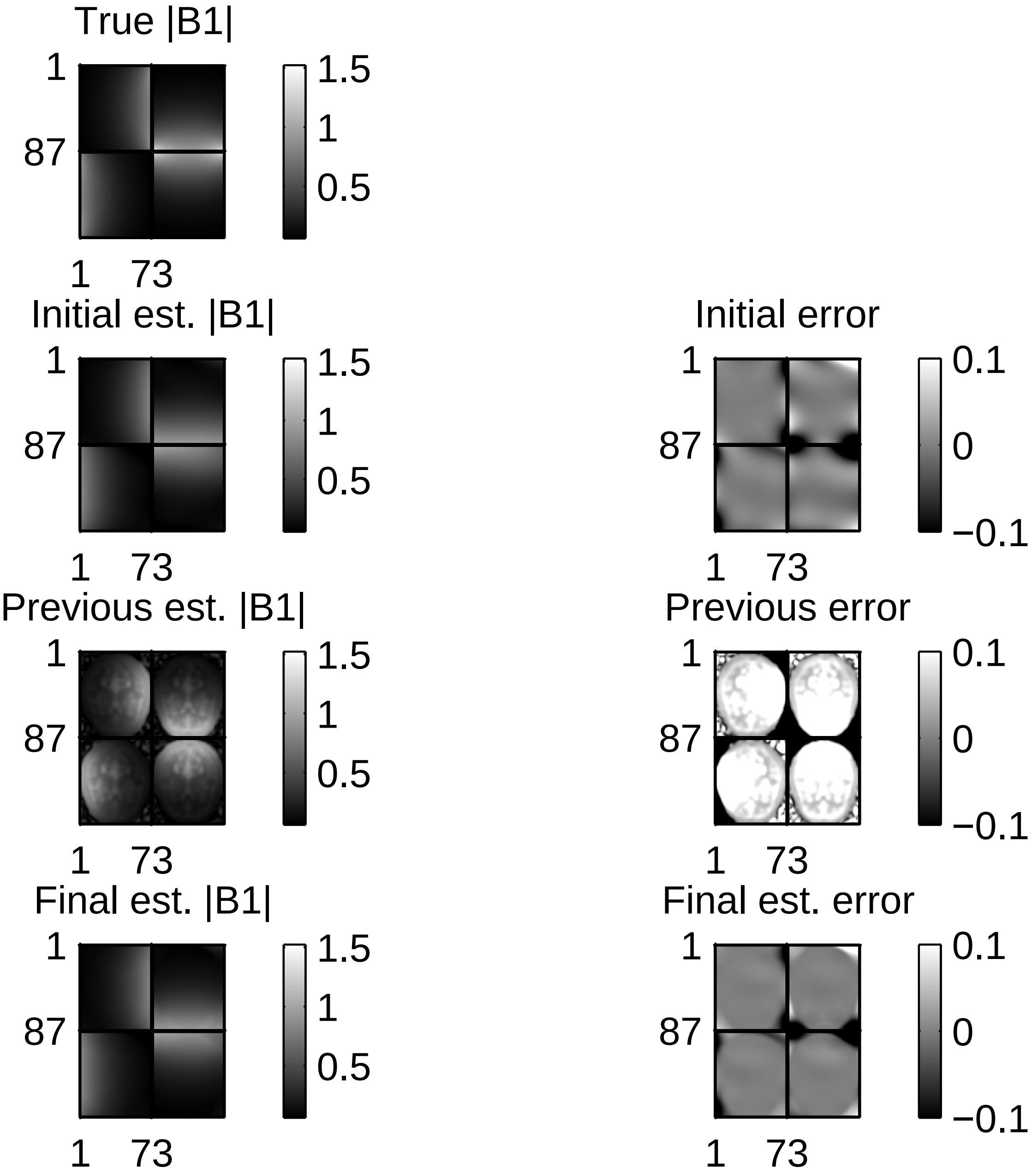

Figure 6.32: Magnitude B_1^+ maps for LOO at 60 dB with 12 measurements. $|z|$, 50 iterations with 15 internal PGD iterations, 12 measurements, 4 coils, “leave one out”, SNR around 60 dB, B_1^+ map regularization parameter is 2^{-3}, T_1 map regularization parameter is 2^{-5}. No object regularization.

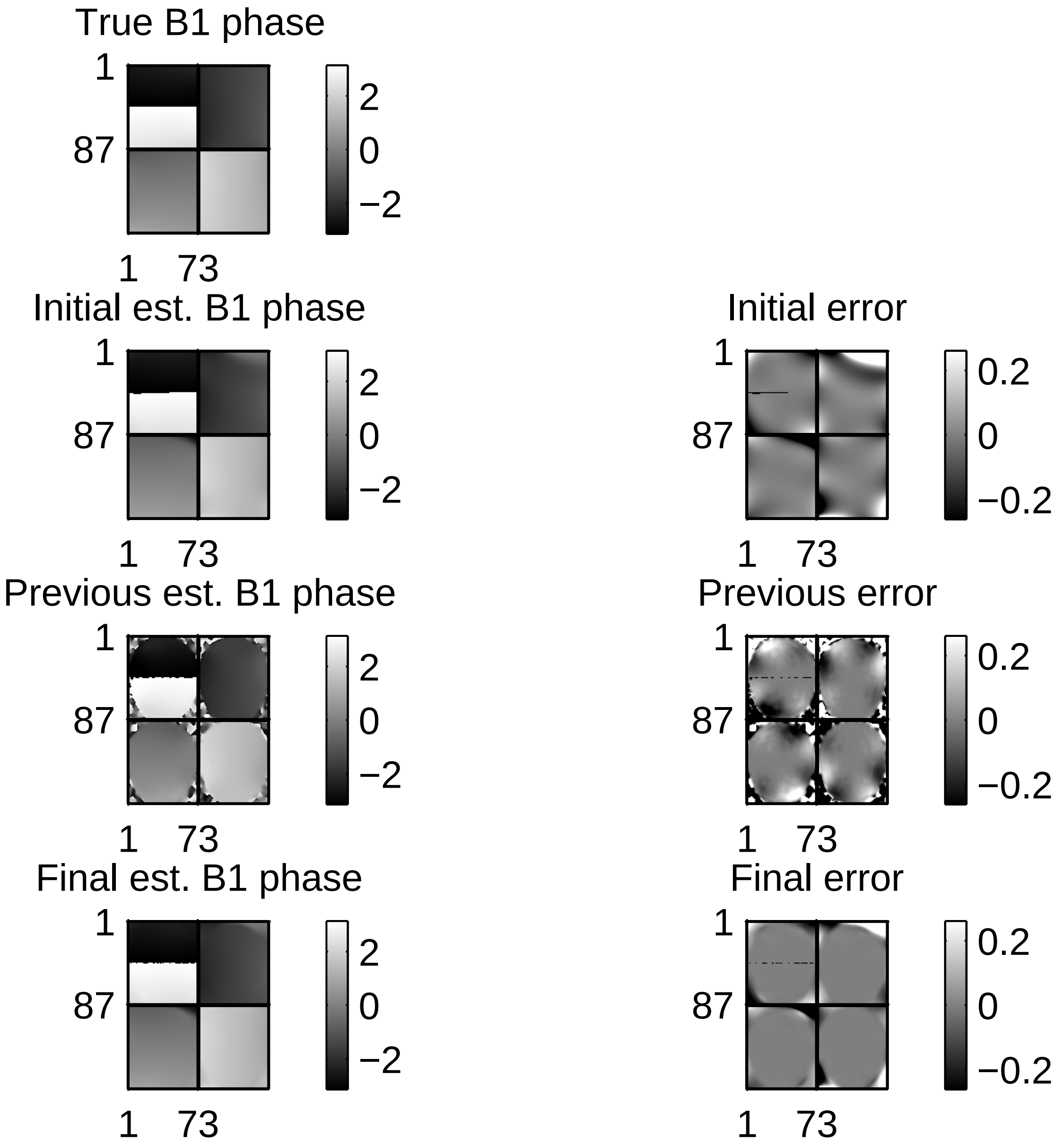

Figure 6.33: Phase B_1^+ maps for LOO at 60 dB with 12 measurements. Compare Fig. 6.32.

Table 6.3: Masked NRMSE for simulated images for different $\boldsymbol{\alpha}$, numbers of measurements, and SNR

			mag B_1^+			$\angle B_1^+$			T_1		$\boldsymbol{f}$		
Coil config	SNR	M	prev	init	final	prev	init	final	init	final	prev	init	final
OAAT	60	12	0.28	0.12	0.02	0.17	0.20	0.16	0.36	0.11	0.41	0.13	0.03
LOO	60	12	0.39	0.37	0.015	0.18	0.18	0.14	0.13	0.10	0.37	0.02	0.02
OAAT	30	12	0.29	0.74	0.72	0.18	0.54	0.22	0.59	0.66	0.43	0.30	0.25
OAAT	30	16	0.23	0.51	0.20	0.18	0.27	0.23	0.91	0.44	0.45	0.43	0.19
LOO	30	12	0.39	0.13	0.06	0.22	0.49	0.15	0.29	0.19	0.37	0.09	0.07
LOO	20	12	0.39	0.18	0.11	0.29	0.39	0.19	0.44	0.35	0.36	0.15	0.14
LOO	20	16	0.31	0.22	0.08	0.28	0.78	0.22	0.48	0.32	0.45	0.16	0.12

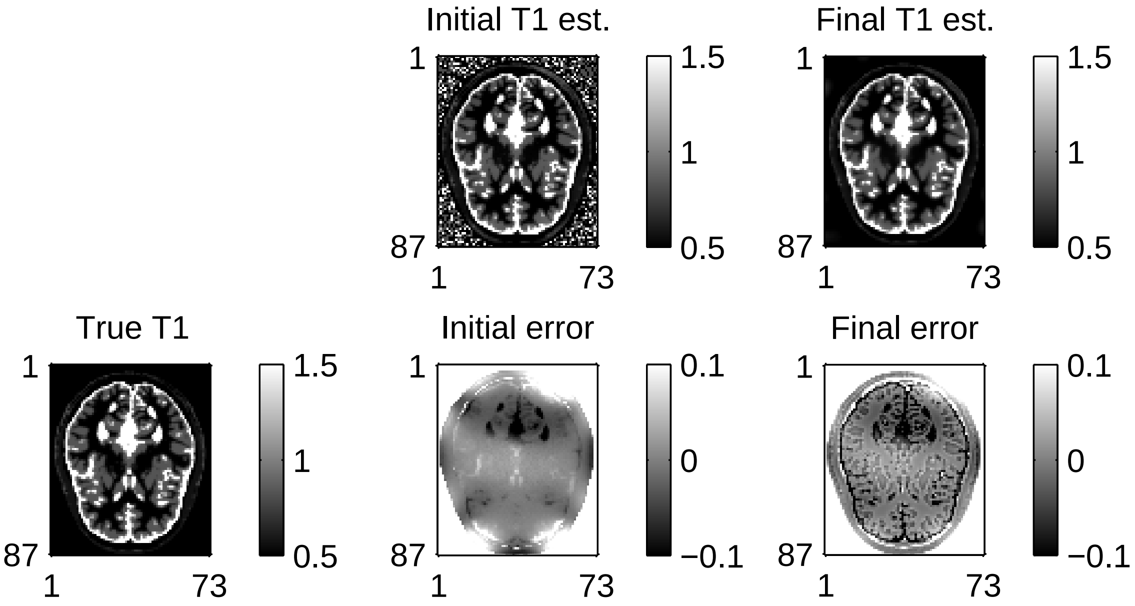

Figure 6.34: T_1 maps for LOO at 60 dB with 12 measurements. Compare Fig. 6.32.

map estimates. Estimates of T_1 were more variable and would require more data to be conclusive, though a slightly longer TR seems to give better results. This greater variability (and greater difficulty in measuring T_1) is suggested by our previous analysis, especially in Fig. 6.1 where higher T_1 values are more difficult to estimate. We can clearly see this in Fig. 6.34 where the high T_1 values at the center of the brain are underestimated. The high error at very low TR is predicted by Fig. 6.15. From Table 6.5, we see that using α values around the "optimal" α of 1.3744 give the lowest errors for estimating all maps. Very large or very small α values cause a much greater error. Assuming a B_1^+ range around 1, small α values do not cover a wide enough range of tips to successfully estimate B_1^+ and T_1. The initialization was important for this study and using the previous estimate of B_1^+ only for the initialization strongly improved results when a very small or very large values of α was chosen.

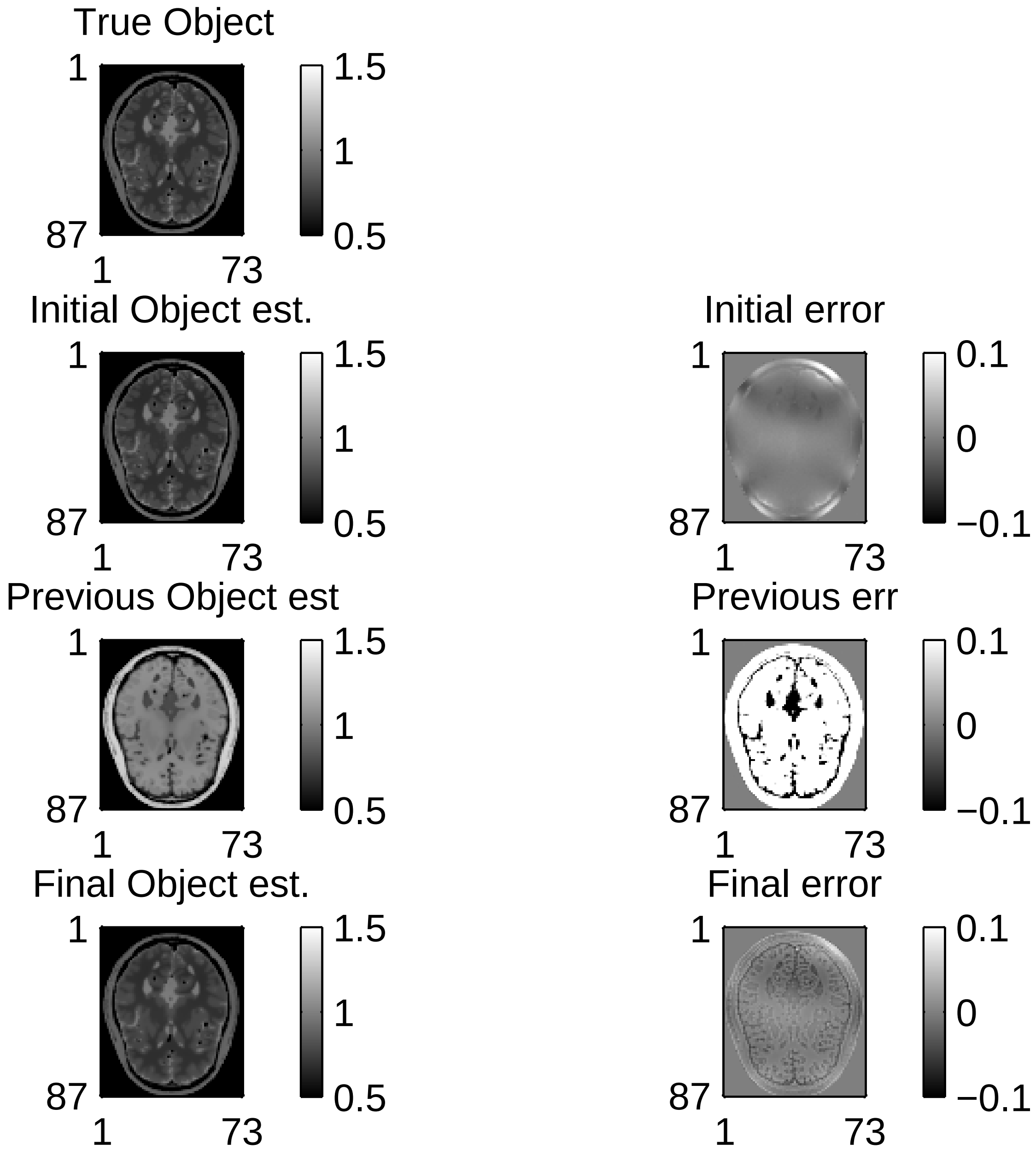
True Object

Initial Object est.

Initial error

Previous Object est

Previous err

Final Object est.

Final error

Figure 6.35: *f* estimates for LOO at 60 dB with 12 measurements. Compare Fig. 6.32.

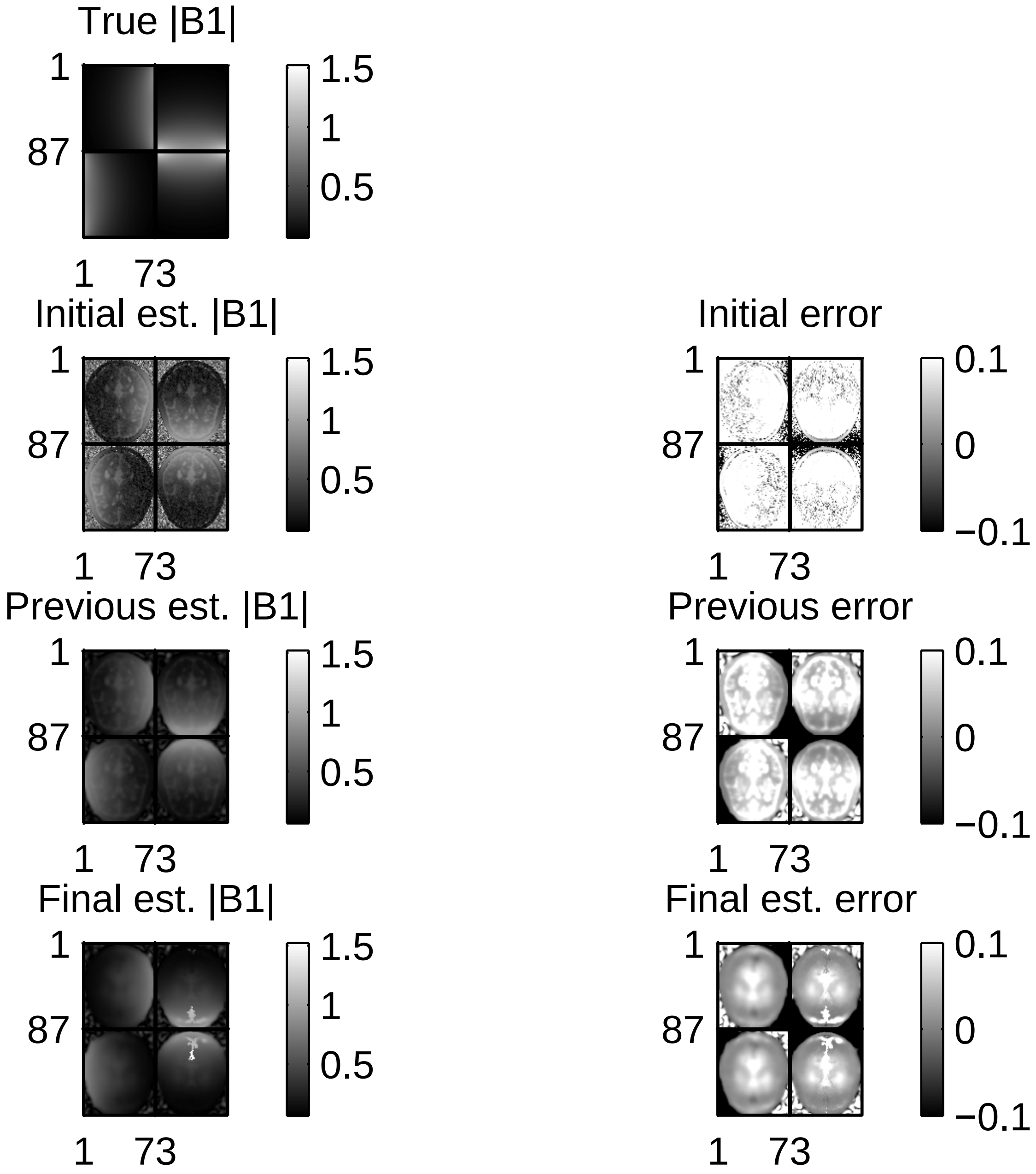

Figure 6.36: Magnitude B_1^+ maps for OAAT at 30 dB with 16 measurements. $|z|$, 50 iterations with 15 internal PGD iterations, 16 measurements, 4 coils, "one at a time", SNR around 30 dB, B_1^+ map regularization parameter is 2^{-3}, T_1 map regularization parameter is 2^{-5}. No object regularization.

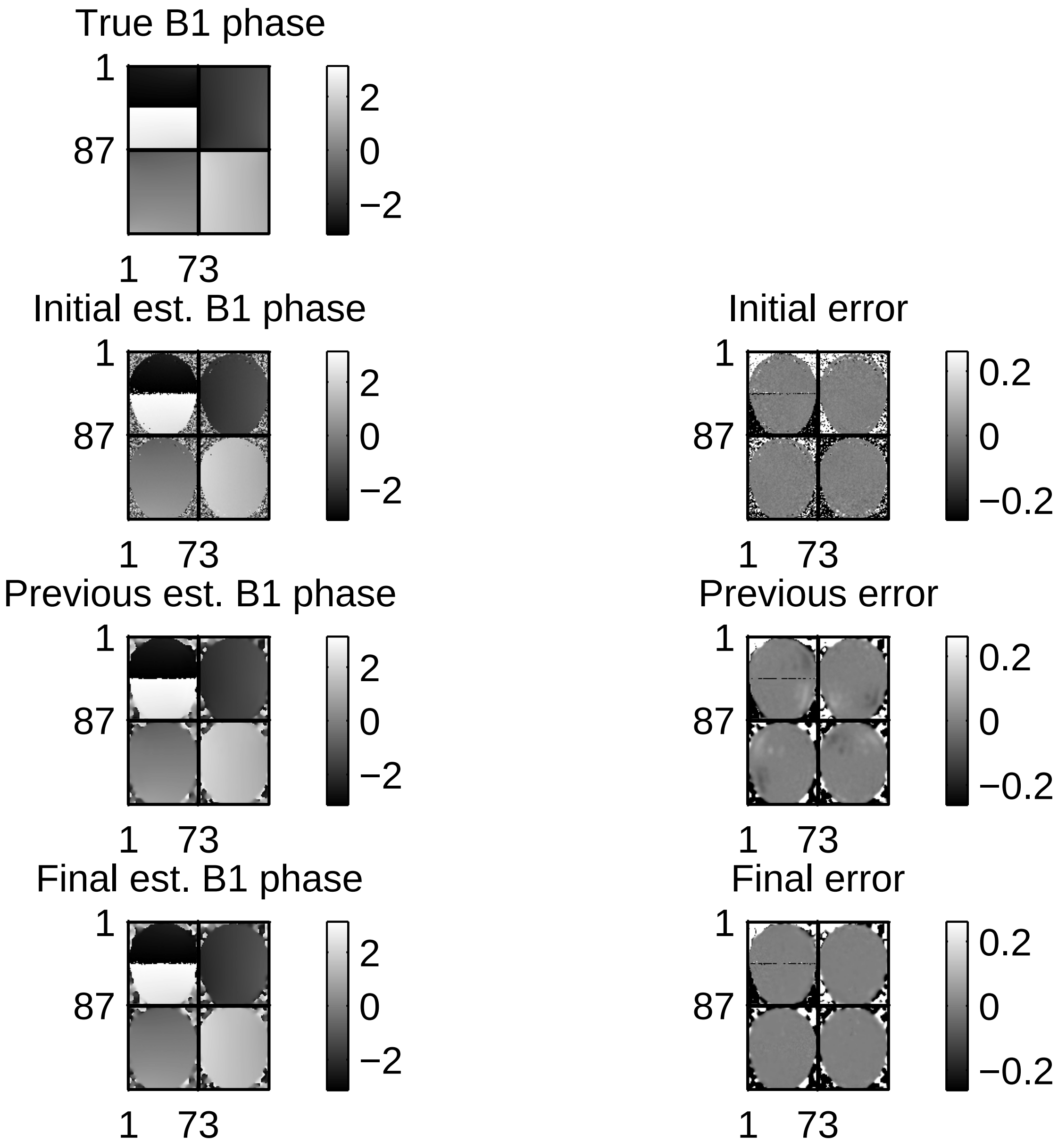

Figure 6.37: Phase B_1^+ maps for OAAT at 30 dB with 16 measurements. Compare Fig. 6.36.

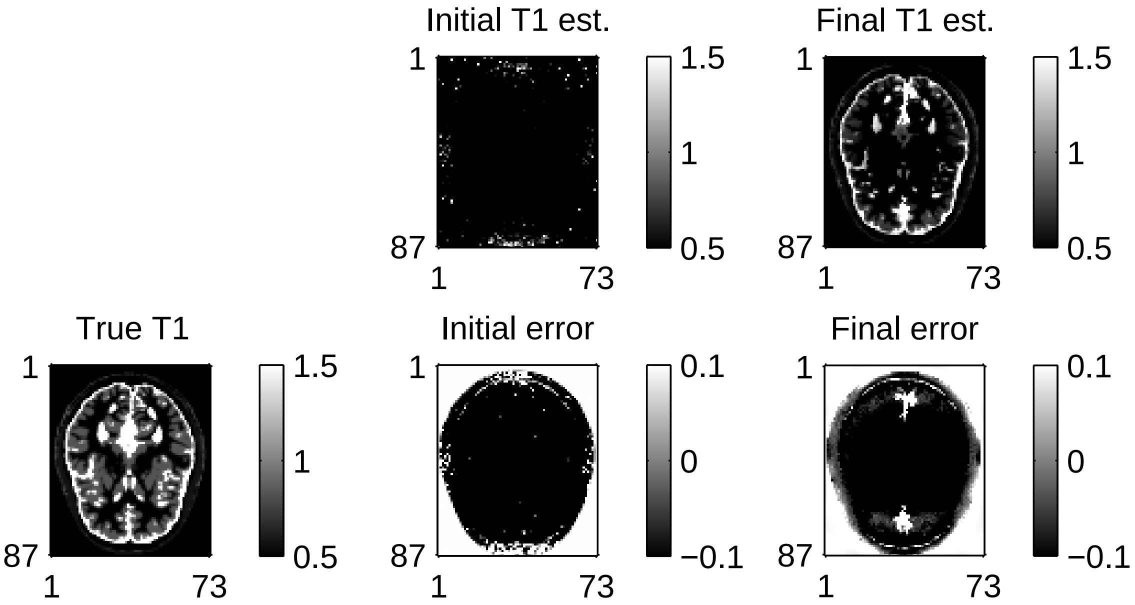

Figure 6.38: T_1 maps for OAAT at 30 dB with 16 measurements. Compare Fig. 6.36.

Table 6.4: Changes in NRMS with a change of TR, 1 estimate, 4 coils, 16 measurements, 30 iterations with 10 PGD iterations, SNR = 30 dB, $\alpha = 1.38 \cdot [1234]$

TR value	$\lvert b\rvert$ joint	$\lvert b\rvert$ previous	$\angle b$ joint	$\angle b$ previous	$\boldsymbol{T}$ joint	$\boldsymbol{f}$ joint	$\boldsymbol{f}$ previous
0.001	0.38	1.30	0.57	0.42	0.91	0.88	1.07
0.010	0.14	1.24	0.37	0.42	0.78	0.65	1.16
0.016	0.04	1.20	0.17	0.42	0.70	0.59	1.25
0.031	0.03	1.12	0.15	0.42	0.57	0.38	1.42
0.046	0.02	1.05	0.17	0.42	0.48	0.28	1.53
0.061	0.03	0.99	0.15	0.42	0.45	0.25	1.58
0.076	0.03	0.93	0.17	0.38	0.40	0.21	1.59
0.100	0.03	0.77	0.16	0.31	0.35	0.18	1.53
0.160	0.04	0.68	0.16	0.19	0.29	0.14	1.23
0.3	0.04	0.52	0.16	0.17	0.19	0.09	0.73
0.5	0.06	0.41	0.16	0.23	0.25	0.14	0.43
0.7	0.02	0.32	0.17	0.22	0.12	0.05	0.38
0.9	0.04	0.26	0.18	0.25	0.16	0.07	0.36
1.1	0.06	0.22	0.16	0.21	0.24	0.10	0.35
1.3	0.03	0.18	0.17	0.24	0.14	0.05	0.34
1.5	0.03	0.16	0.14	0.24	0.19	0.06	0.34
1.7	0.04	0.14	0.19	0.24	0.29	0.08	0.33

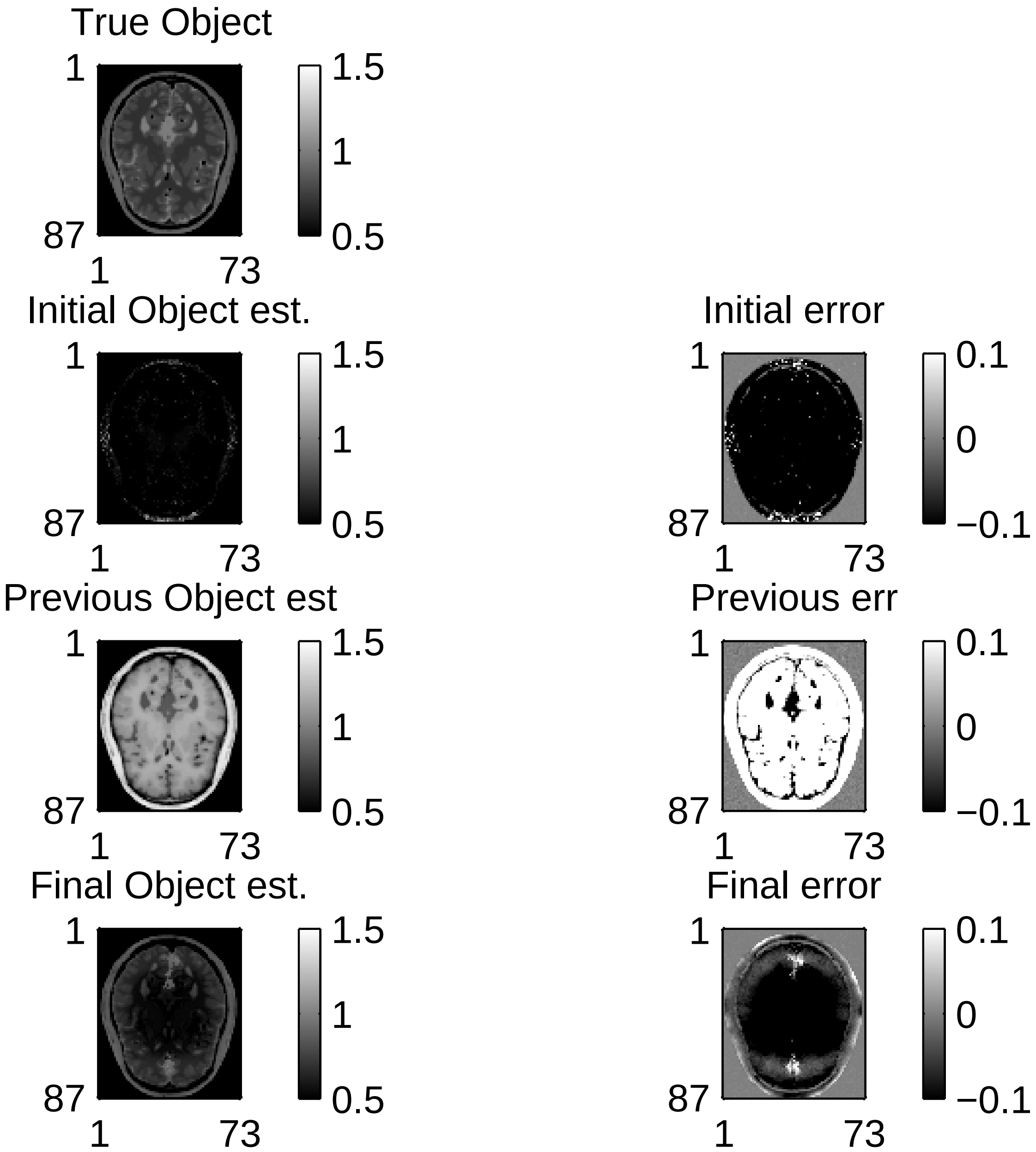

Figure 6.39: $\boldsymbol{f}$ estimates for OAAT at 30 dB with 16 measurements. Compare Fig. 6.36.

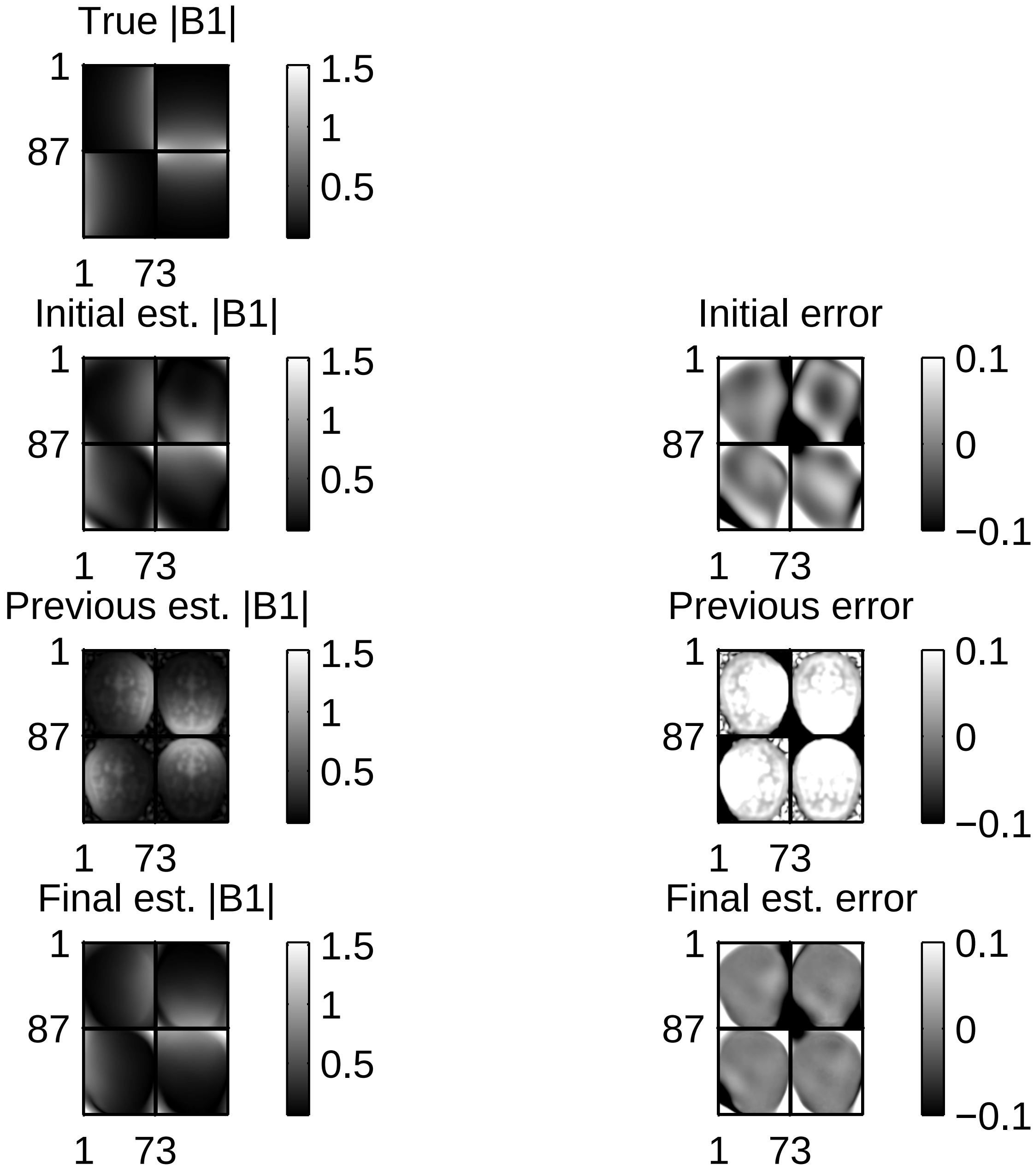

Figure 6.40: Magnitude B_1^+ maps for LOO at 30 dB with 12 measurements. $|z|$, 50 iterations with 15 internal PGD iterations, 12 measurements, 4 coils, “leave one out”, SNR around 30 dB, B_1^+ map regularization parameter is 2^{-3}, T_1 map regularization parameter is 2^{-5}. No object regularization.

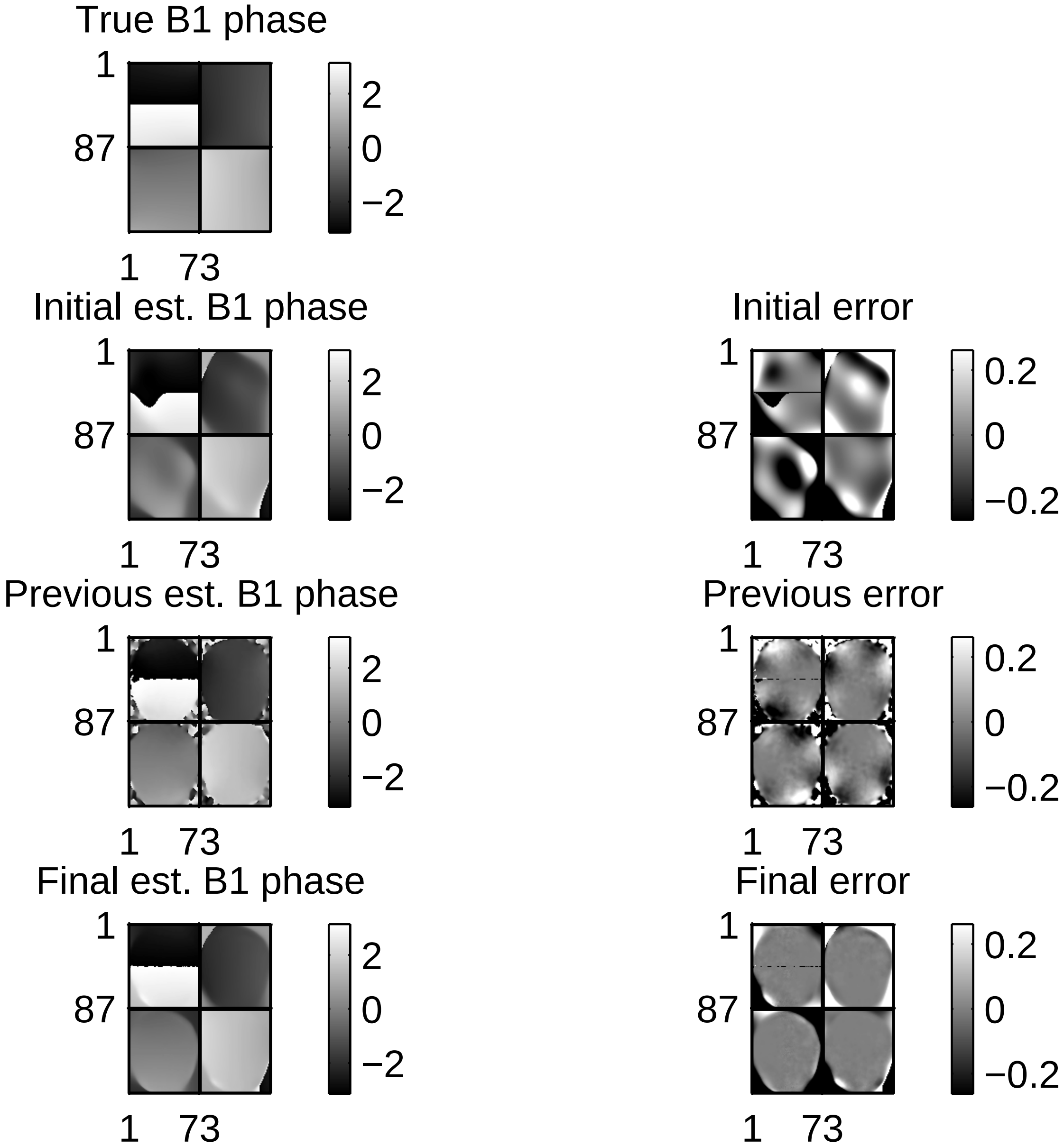

Figure 6.41: Phase B_1^+ maps for LOO at 30 dB with 12 measurements. Compare Fig. 6.40.

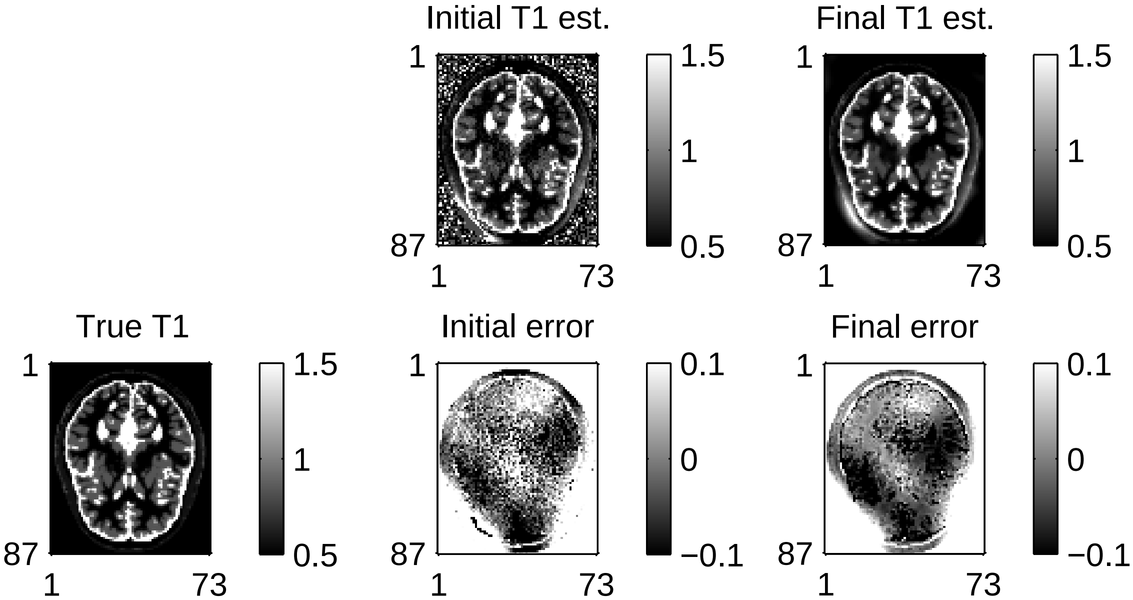

Figure 6.42: T_1 maps for LOO at 30 dB with 12 measurements. Compare Fig. 6.40.

Table 6.5: Changes in NRMS with a change of α, only 1 total scan each, 4 coils, 16 measurements, 15 iterations with 5 PGD iterations, SNR = 30 dB, TR = .68s

α	$\lvert b\rvert$ joint	$\lvert b\rvert$ previous	$\angle b$ joint	$\angle b$ previous	$\boldsymbol{T}$ joint	$\boldsymbol{f}$ joint	$\boldsymbol{f}$ previous
0.2	2.31	2.39	0.41	0.61	0.88	0.67	0.56
0.3778	1.04	1.12	0.35	0.53	0.89	0.49	0.48
0.5556	0.70	0.79	0.39	0.45	0.87	0.42	0.42
0.7333	0.52	0.65	0.35	0.37	0.87	0.38	0.39
0.9111	0.44	0.56	0.35	0.33	0.88	0.36	0.38
1	0.21	0.53	0.27	0.31	0.47	0.22	0.38
1.0889	0.16	0.48	0.28	0.29	0.46	0.21	0.39
1.2667	0.06	0.42	0.24	0.25	0.22	0.07	0.39
1.4444	0.02	0.36	0.18	0.23	0.13	0.03	0.42
1.6222	0.05	0.31	0.21	0.21	0.22	0.07	0.47
1.8	0.09	0.27	0.33	0.19	0.34	0.12	0.52
2	0.08	0.23	0.33	0.21	0.39	0.21	0.48
3	0.49	0.11	0.86	0.21	0.77	0.54	0.48
4	2.16	0.14	1.11	0.24	1.02	1.07	0.43

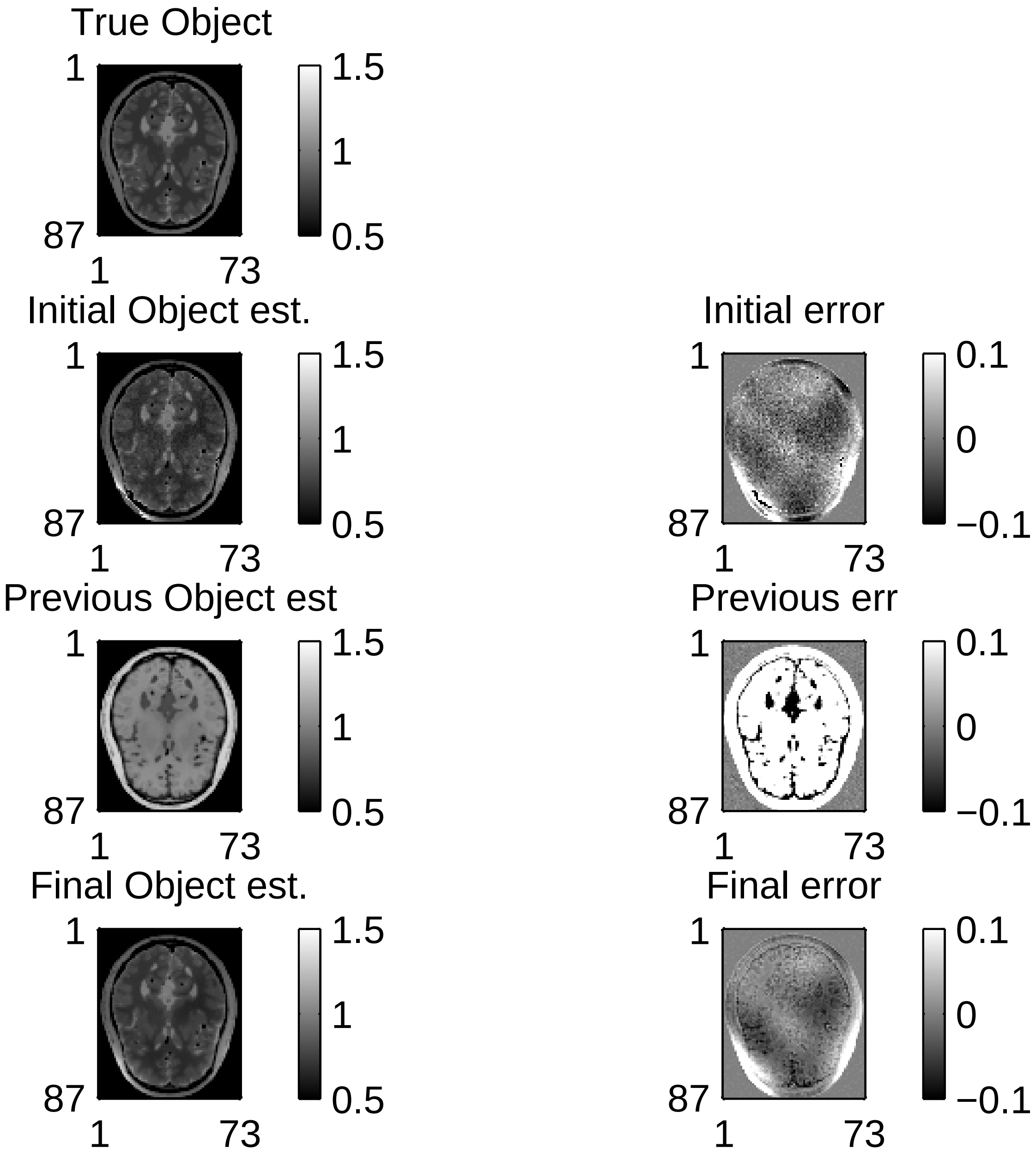

Figure 6.43: f estimates for LOO at 30 dB with 12 measurements. Compare Fig. 6.40.

6.6.2 Phantom Real MR Images

Phantom real MR data was taken using a four coil setup. The phantom has a stated true $\boldsymbol{T} = 1$s which we measured with an inversion recovery curve to $\boldsymbol{T} = 1.095$s. For this setup, varying TR was more reliable than varying the flip angle. Therefore, first one coil was turned on and complex image measurements recorded over the field of view for a wide range of TR values $\begin{bmatrix} 20 & 40 & 60 & 80 & 100 & 120 & 160 & 200 & 300 & 500 \\ 1000 & 2000 & & & & & & & & \end{bmatrix}$ ms. Next, the other three coils were turned on separately and complex measurements recorded with TR$=2000$ ms. Samples of this data are shown in Fig. 6.44.

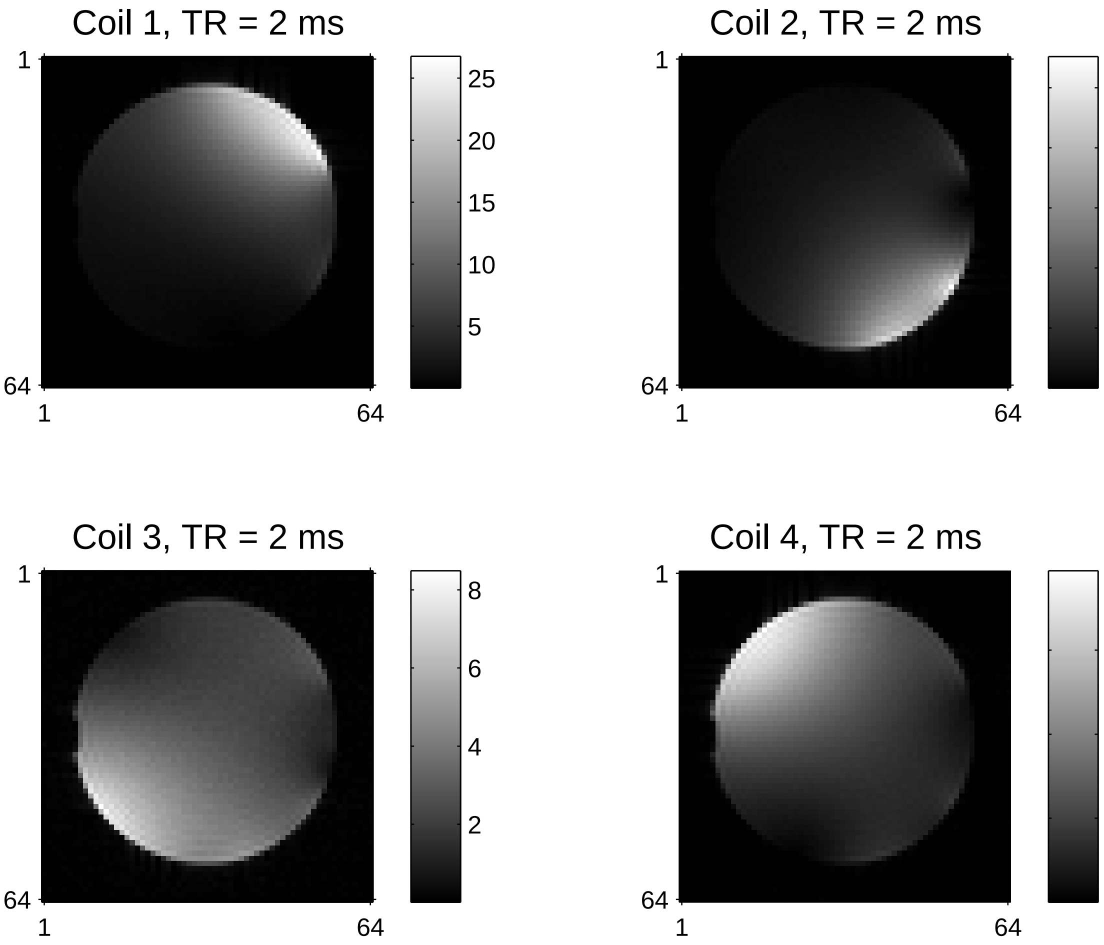

Figure 6.44: $|\boldsymbol{y}|$ transmitting individually for each of the four coils with TR = 2000 ms.

The initial procedure described in Appendix K. These initial estimates are shown in

Fig. 6.45.

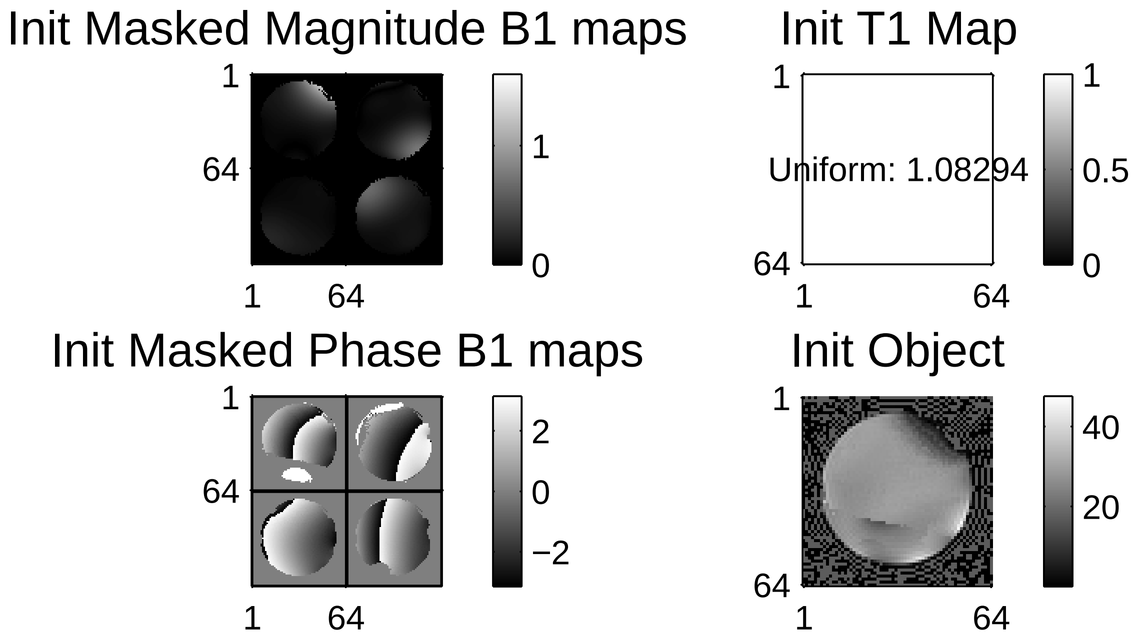

Figure 6.45: Initial phantom estimates.

Using these initial estimates and all the data, we ran the proposed joint B_1^+, T_1 estimator with 30 iterations with 15 iterations of the preconditioned gradient descent method algorithm using alternating minimization. We regularized the B_1^+ map with $\beta = 2^{-3}$ and also regularized the T_1 map with edge preserving regularization and $\beta = 2^{-6}$. We performed no object regularization. The final regularized images are shown in Fig. 6.46. We also ran the algorithm using no regularization to compare model fit with final unregularized images shown in Fig. 6.47.

Using these initial values, we measured model fit. We compared the measured magnitude data and compared that to the expected magnitude value using these initial values and also using a final estimate using our proposed algorithm with no regularization. For a few select pixels, graphs of the actual and estimated data (both the initial B1 estimate and also the final regularized estimate) are shown in the graphs below from Fig. 6.48 to Fig. 6.51. We repeated this graphs assuming that both T_1 and $\boldsymbol{f}$ are roughly constant and showing our calculated initial B_1^+ along the x-axis. These are shown in Fig. 6.52 to Fig. 6.56. Overall,

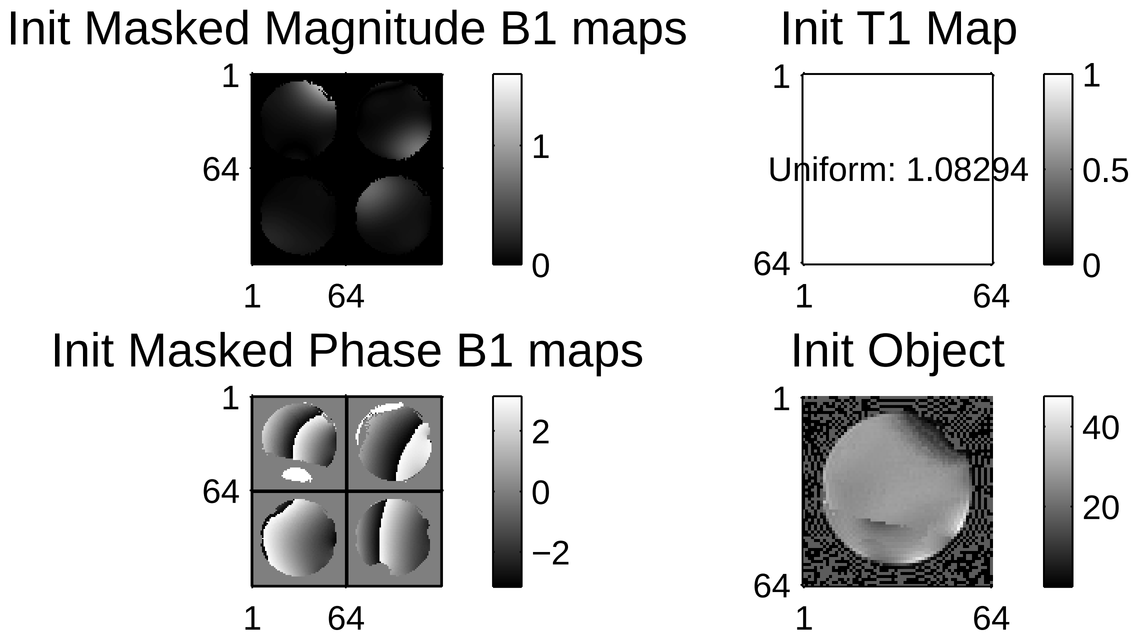

Figure 6.46: Final phantom regularized estimates.

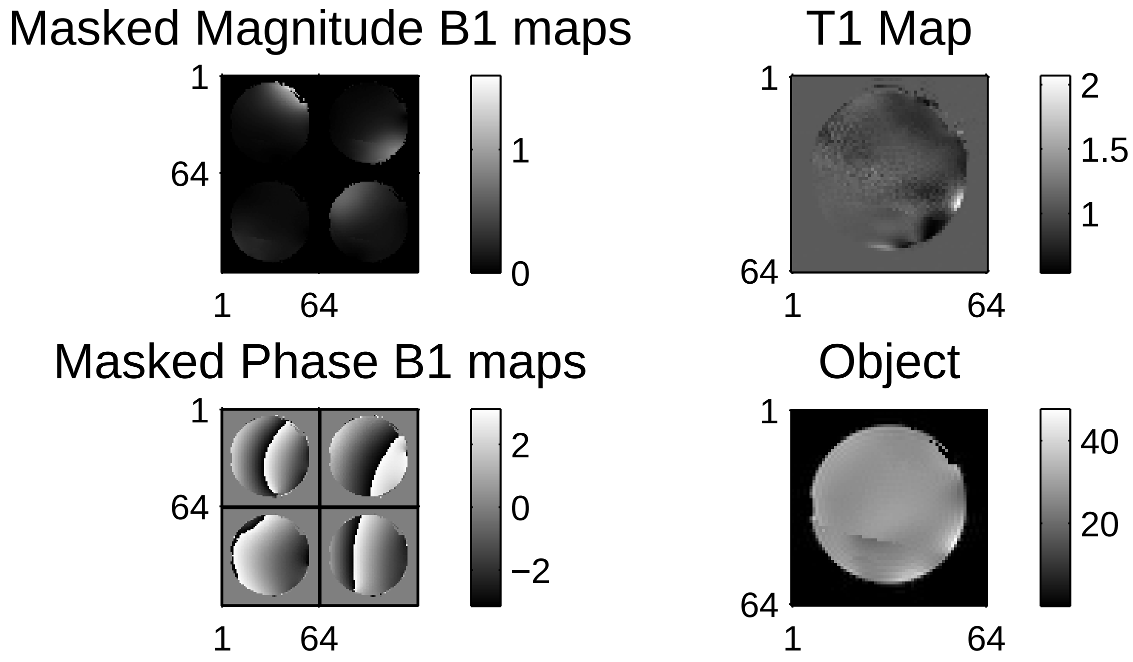

Figure 6.47: Final phantom unregularized estimate.

the fit is very good and shows improvement over the initial estimate, especially at very low B_1^+ map values.

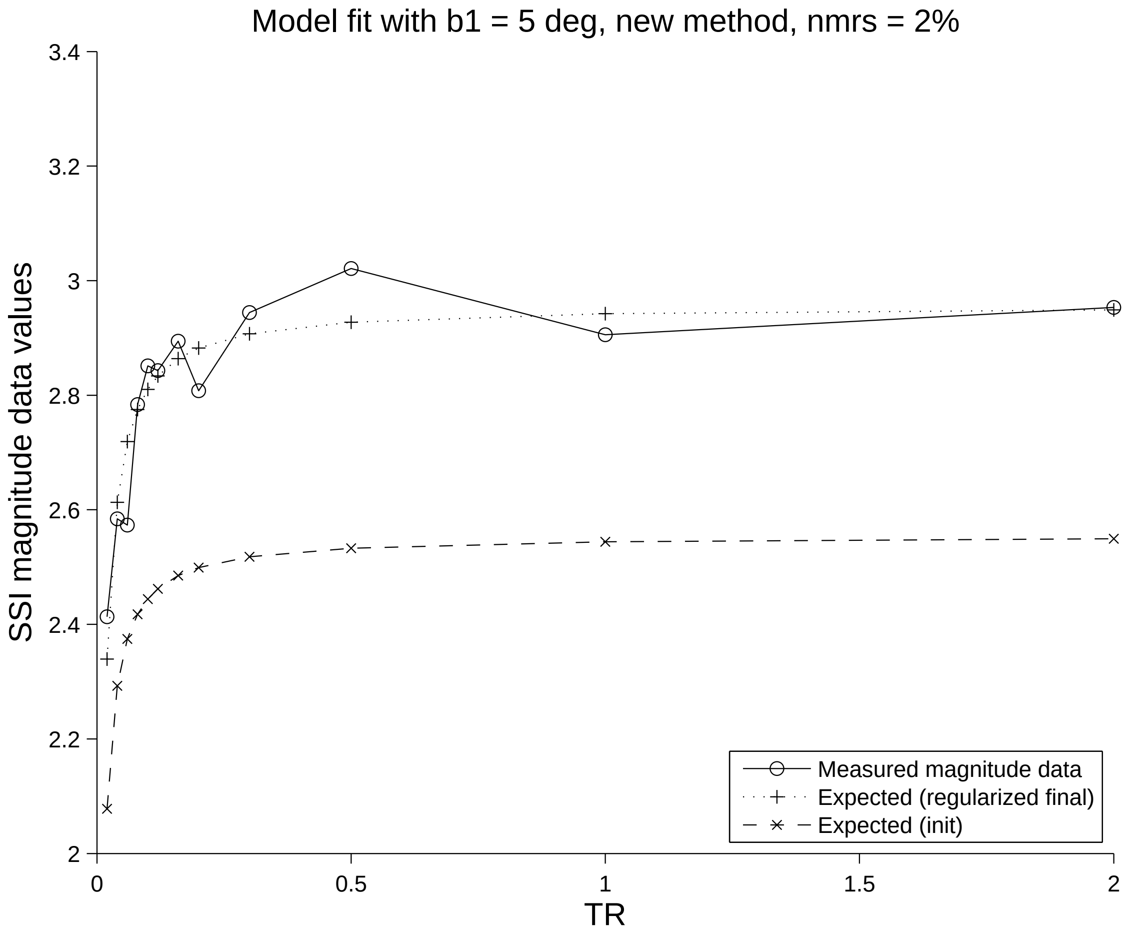

Figure 6.48: Phantom model fit, $\theta = 5$ degrees, where $\theta = \alpha b$

We also ran a second phantom study. Our first phantom study only used one coil at a time and is comparable to the “one-at-a-time” simulation studies. The second phantom study used several coils at a time and is more comparable to the “leave-one-out” simulation studies. Thus, we would expect better performance from the second phantom study.

In the second phantom study, all four coils were first turned on and data was taken at $TR = \begin{bmatrix} 50 & 100 & 500 & 2000 \end{bmatrix}$ ms. Then, three of the four coils were turned on and data was collected at the same TR values. This was repeated for each of the 4 three-coil combinations. The same general procedure was performed above with slight modifications. Again, the initial B_1^+ map was estimated by minimizing the cost, but here, we estimated the (complex) composite coil map. First, we used the estimated composite coils map as

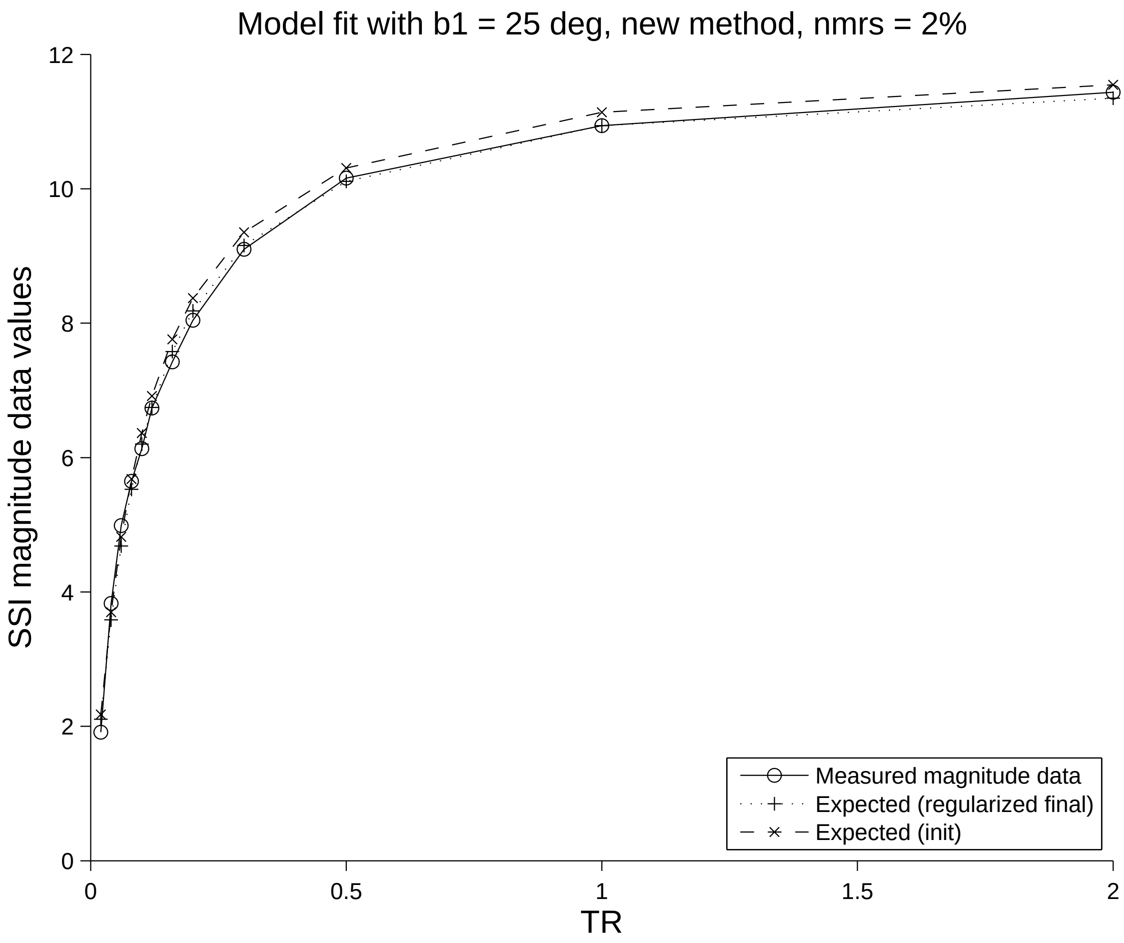

Figure 6.49: Phantom model fit, $\theta = 25$ degrees, where $\theta = \alpha b$

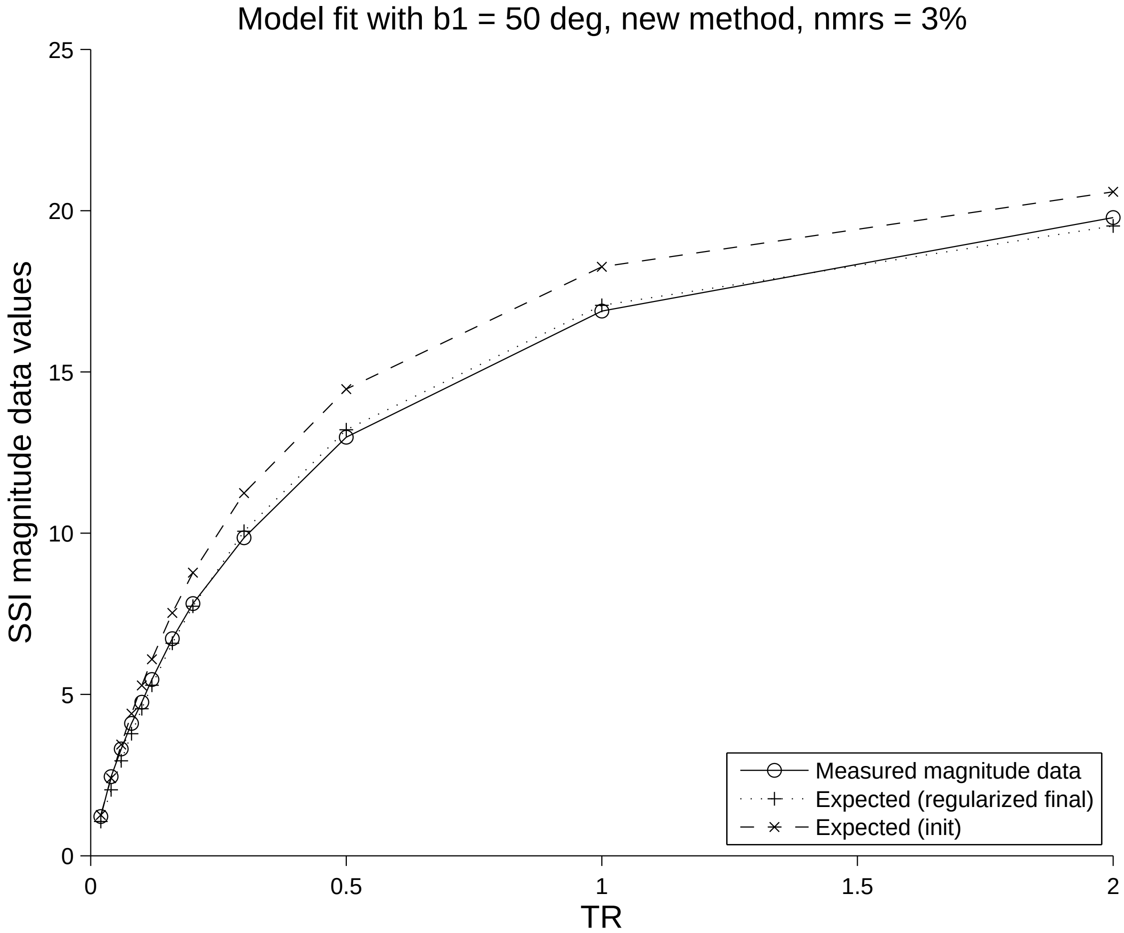

Figure 6.50: Phantom model fit, $\theta = 50$ degrees, where $\theta = \alpha b$

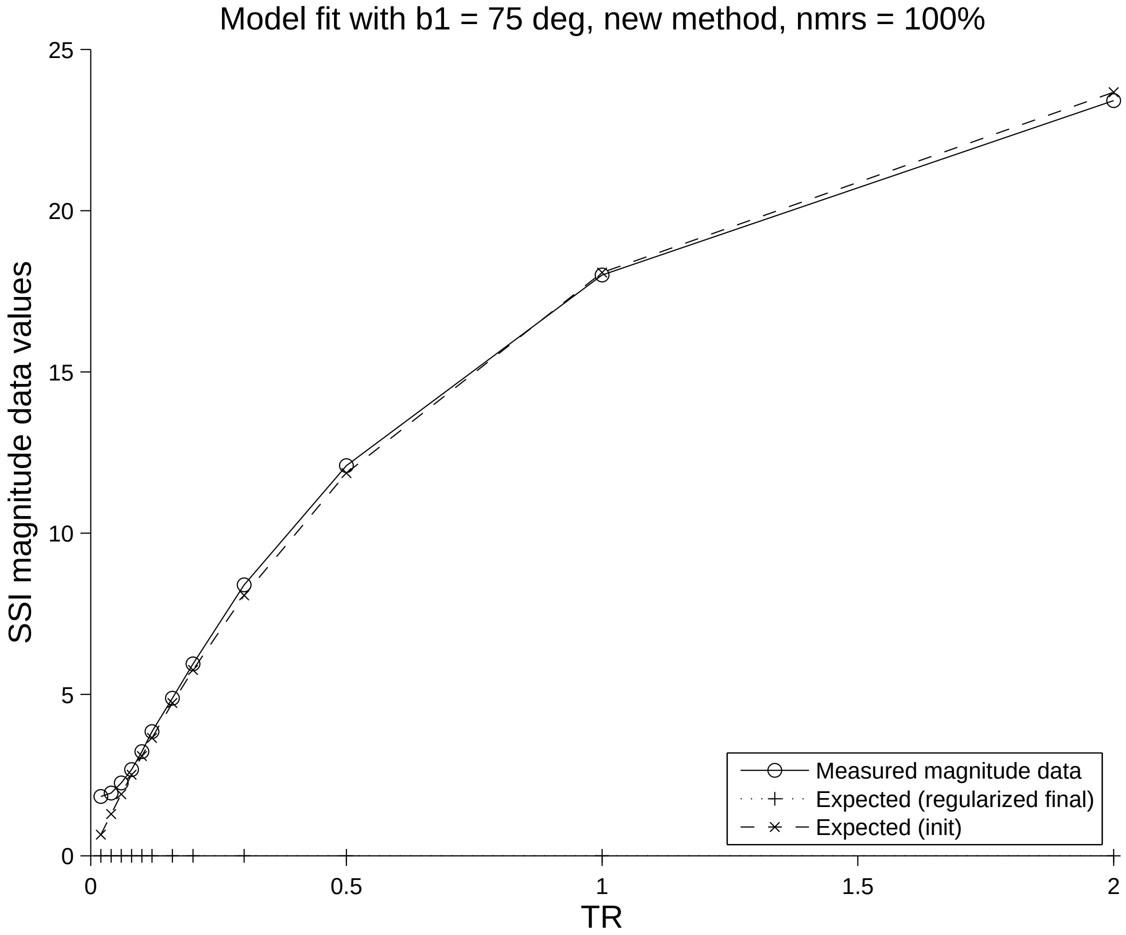

Figure 6.51: Phantom model fit, $\theta = 75$ degrees, where $\theta = \alpha b$

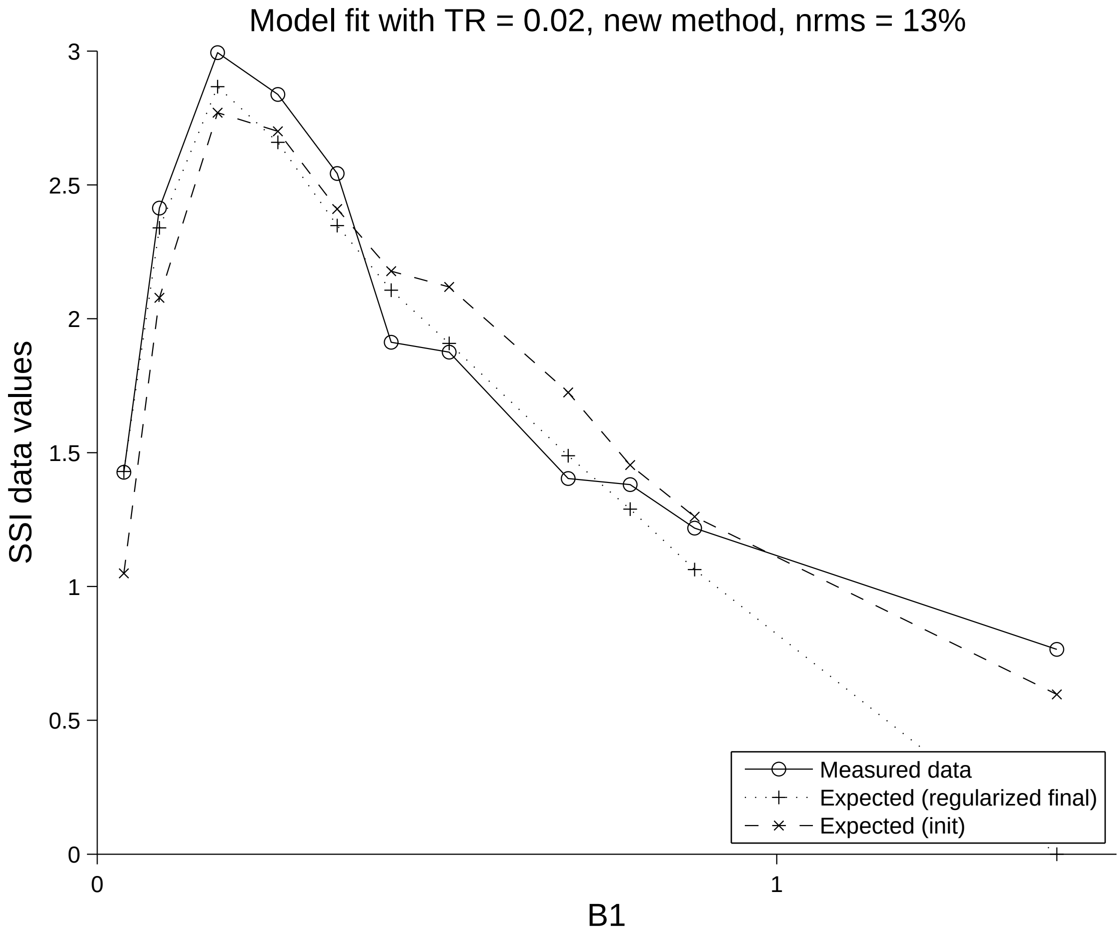

Figure 6.52: Phantom model fit with respect to b1, TR = 20 ms

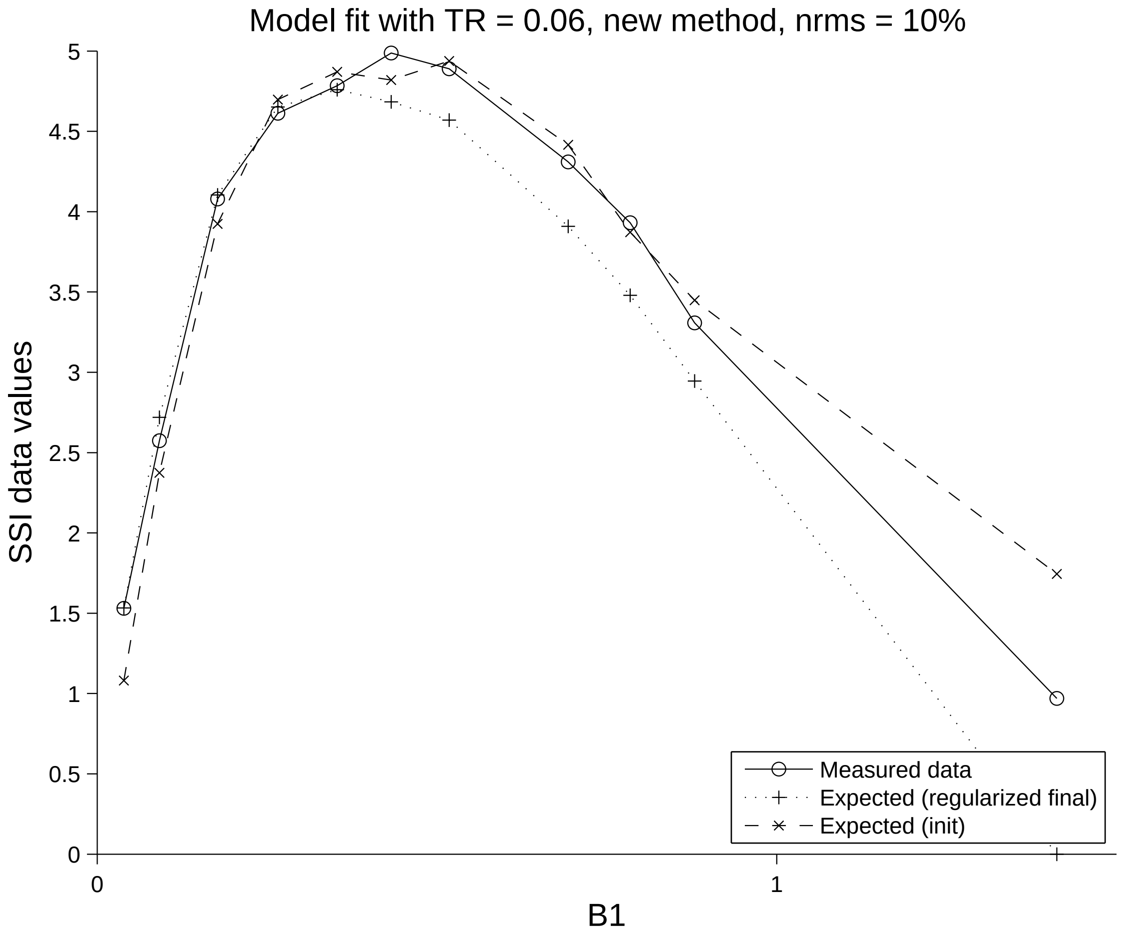

Figure 6.53: Phantom model fit with respect to b1, TR = 60 ms

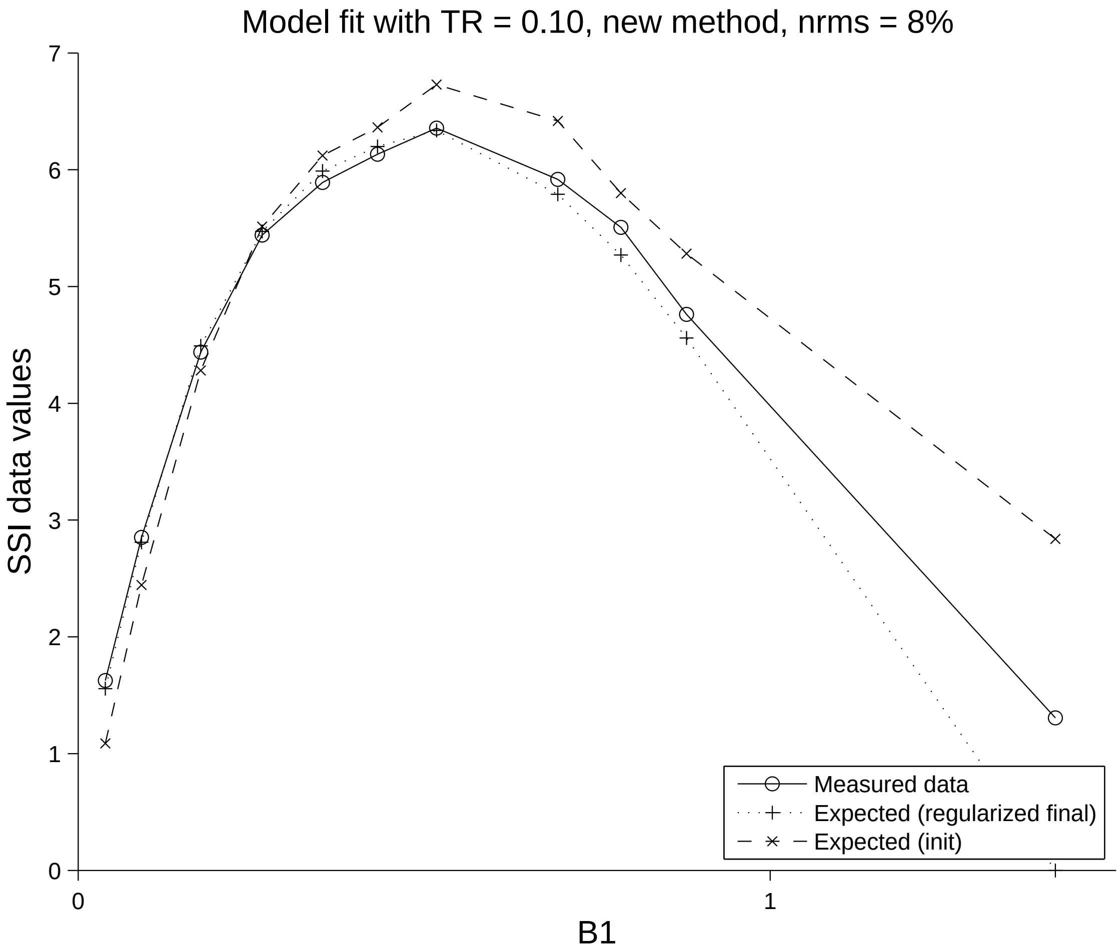

Figure 6.54: Phantom model fit with respect to b1, TR = 100 ms

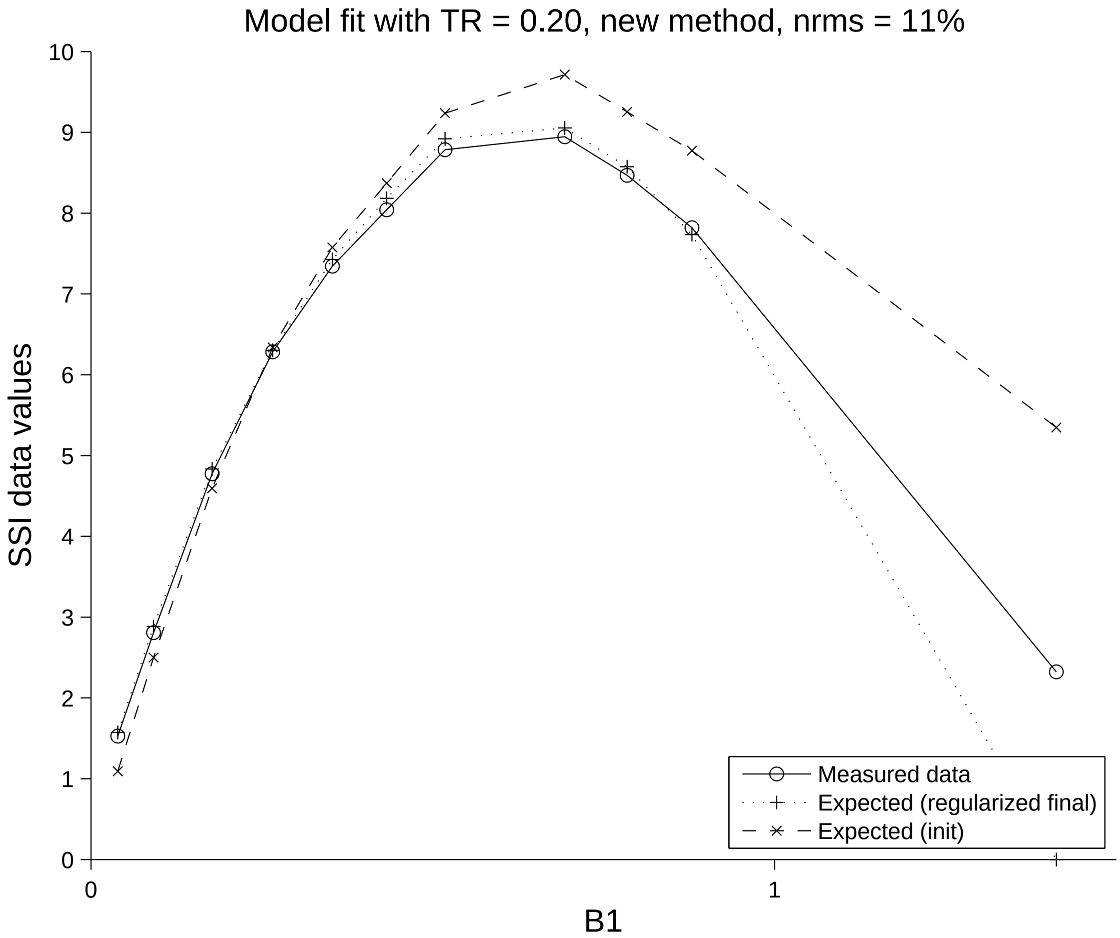

Figure 6.55: Phantom model fit with respect to b1, TR = 200 ms

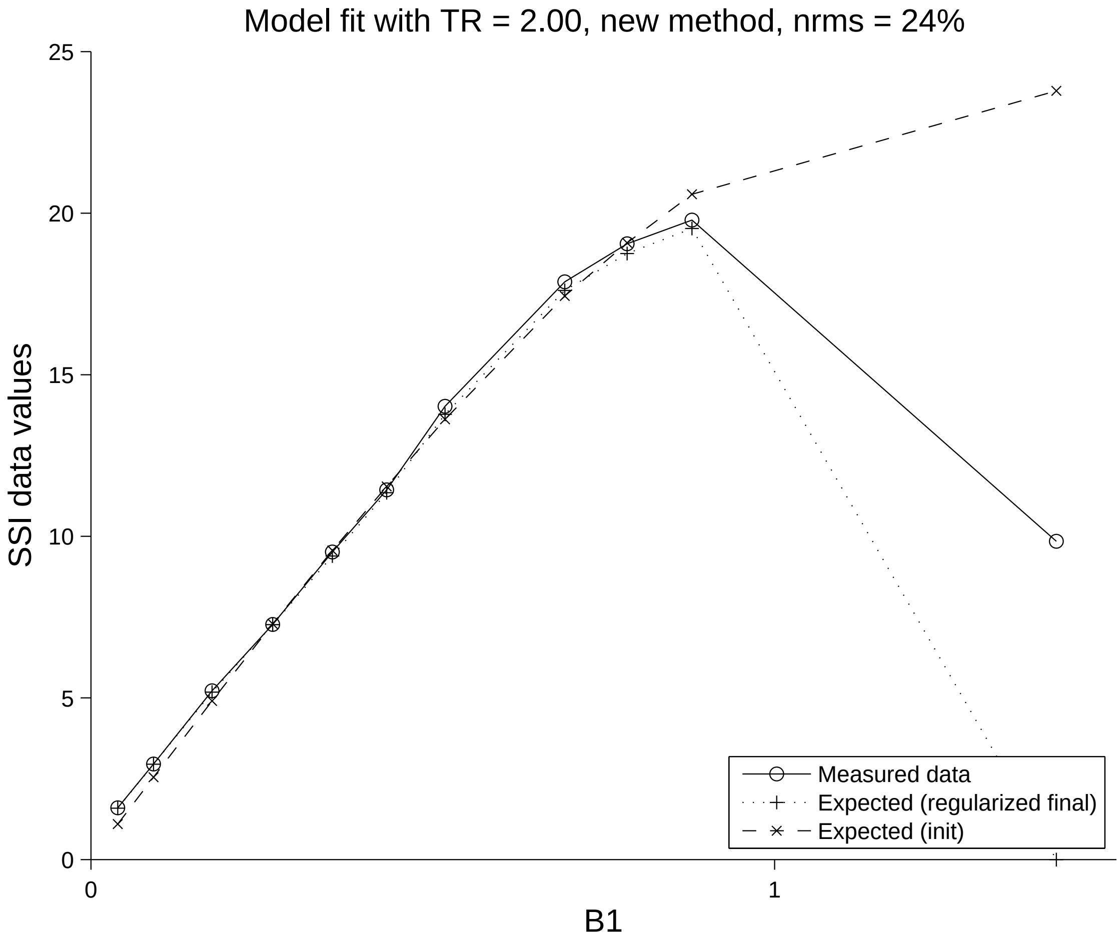

Figure 6.56: Phantom model fit with respect to b1, TR = 2000 ms

an initial estimate for our regularized estimator. These are shown in Fig. 6.58. Next, we kept the T_1 and $\boldsymbol{f}$ constant and estimated (via our regularized estimator) the individual coil maps to be our initial estimates for the algorithm. These are shown in Fig. 6.59. Finally, we ran the regularized algorithm with these initial estimates. This final step only resulted in small changes from the previous two-step procedure and is possibly unnecessary. The final estimate is shown in Fig. 6.60. The magnitude data with all coils turned on is shown in Fig. 6.57. The initial estimates are shown in Fig. 6.59.

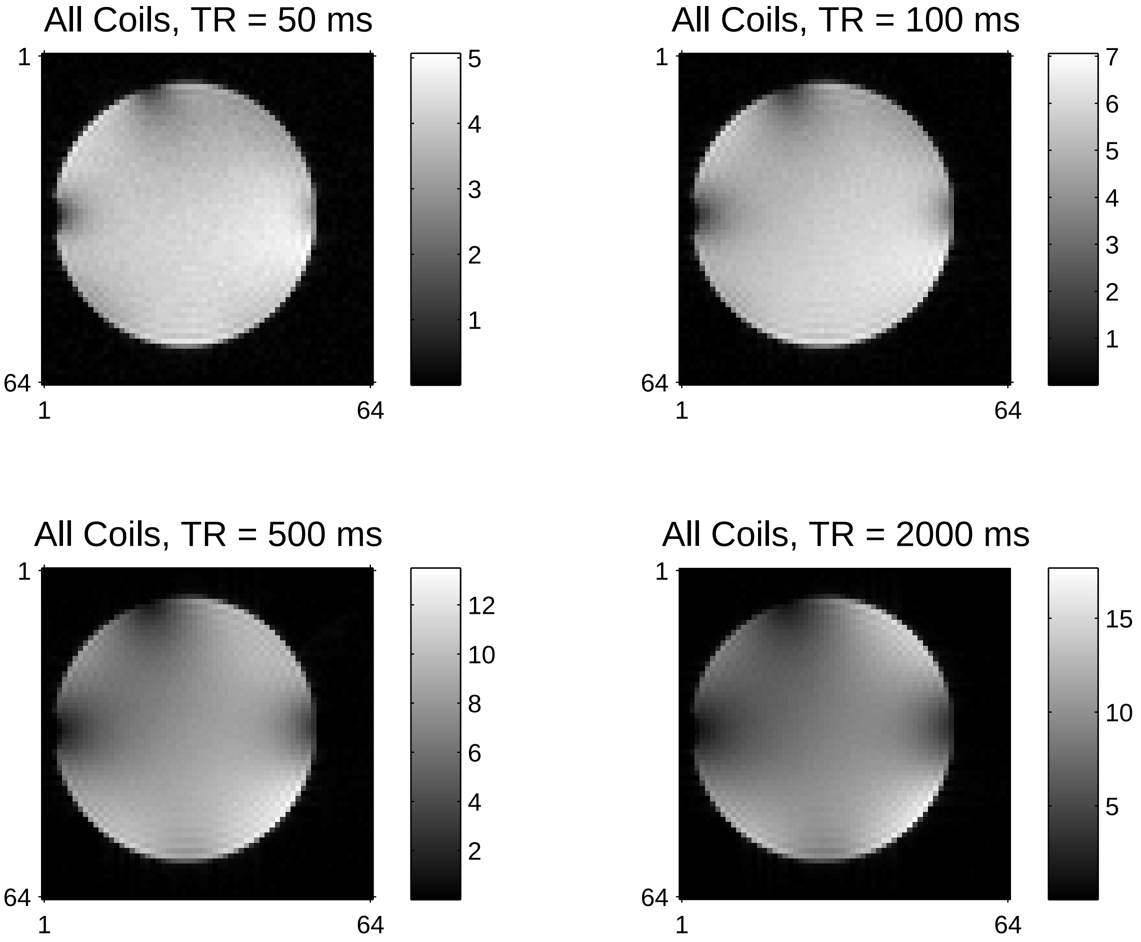

Figure 6.57: Phantom magnitude data with all four coils turned on at four repetition times.

Using these values, we measured model fit. We compared the measured magnitude data and compared that to the expected magnitude value using these initial values and also using a final estimate using our proposed algorithm. For a few select pixels, graphs of

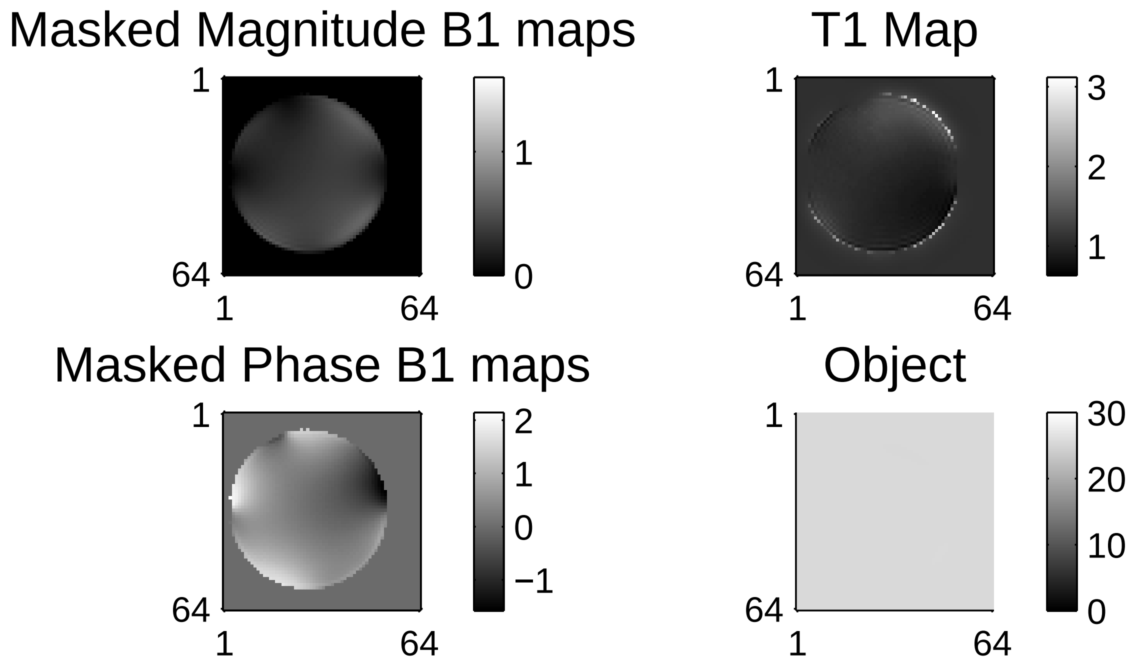

Figure 6.58: Phantom: Regularized estimates for all coils turned on.

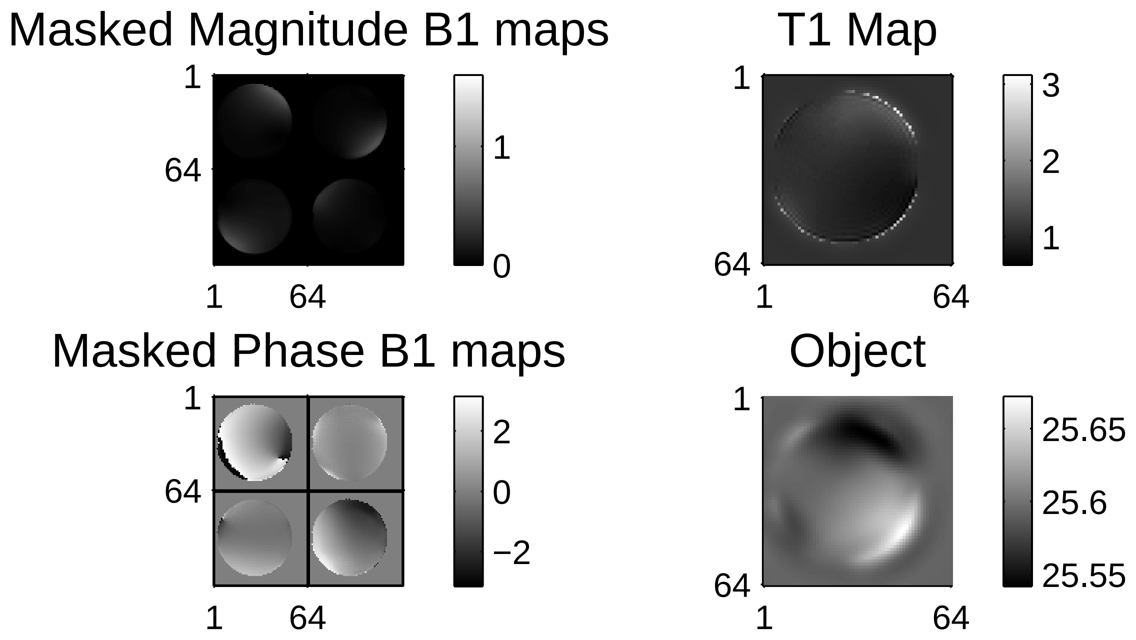

Figure 6.59: Phantom: estimate for individual coil maps.

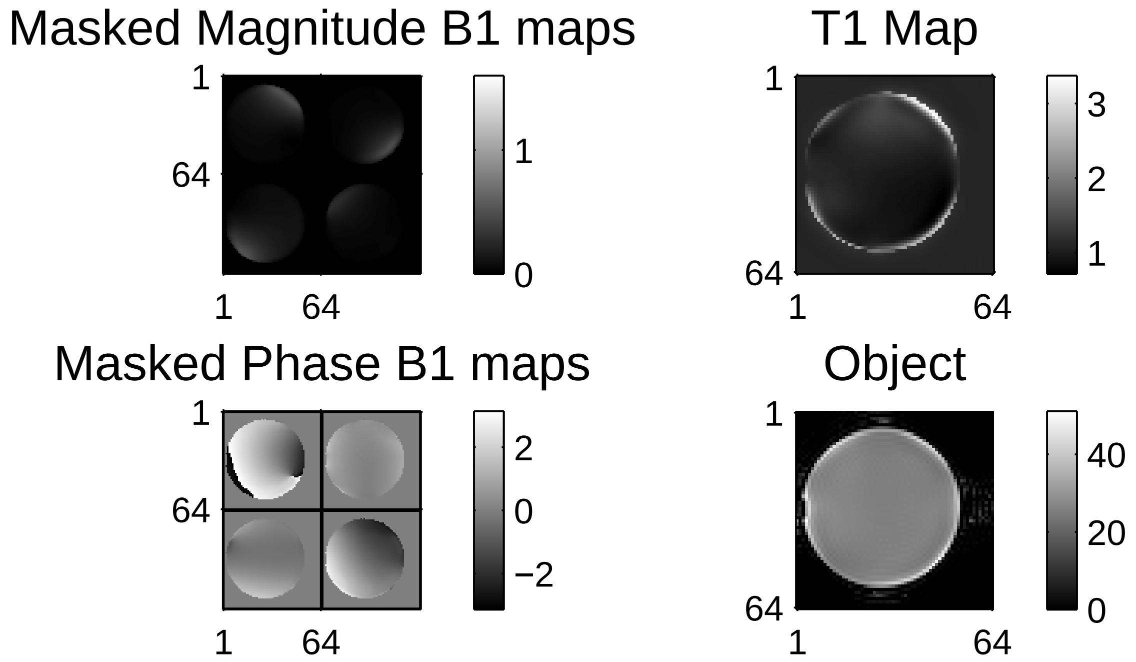

Figure 6.60: Final regularized estimates using all data for the second phantom experiment. Using 20 iterations with 5 internal PGD iterations. Regularization parameter for B_1^+ map is 2^{-2} and for the T_1 and $\boldsymbol{f}$ map is 2^{-2}.

the actual and estimated data (both the initial B1 estimate and also the final regularized estimate) are shown in the graphs below from Fig. 6.61 to Fig. 6.66. Overall, the fit is very good and shows improvement over the initial estimate. From the images, we can still see some possible residual model mismatch. The regularization in the object appears to give some residual error along the edge of the T_1 map. However, the B_1^+ maps (the parameter of interest) in Fig. 6.60 are smooth and match the data well, thus, achieving our goal.

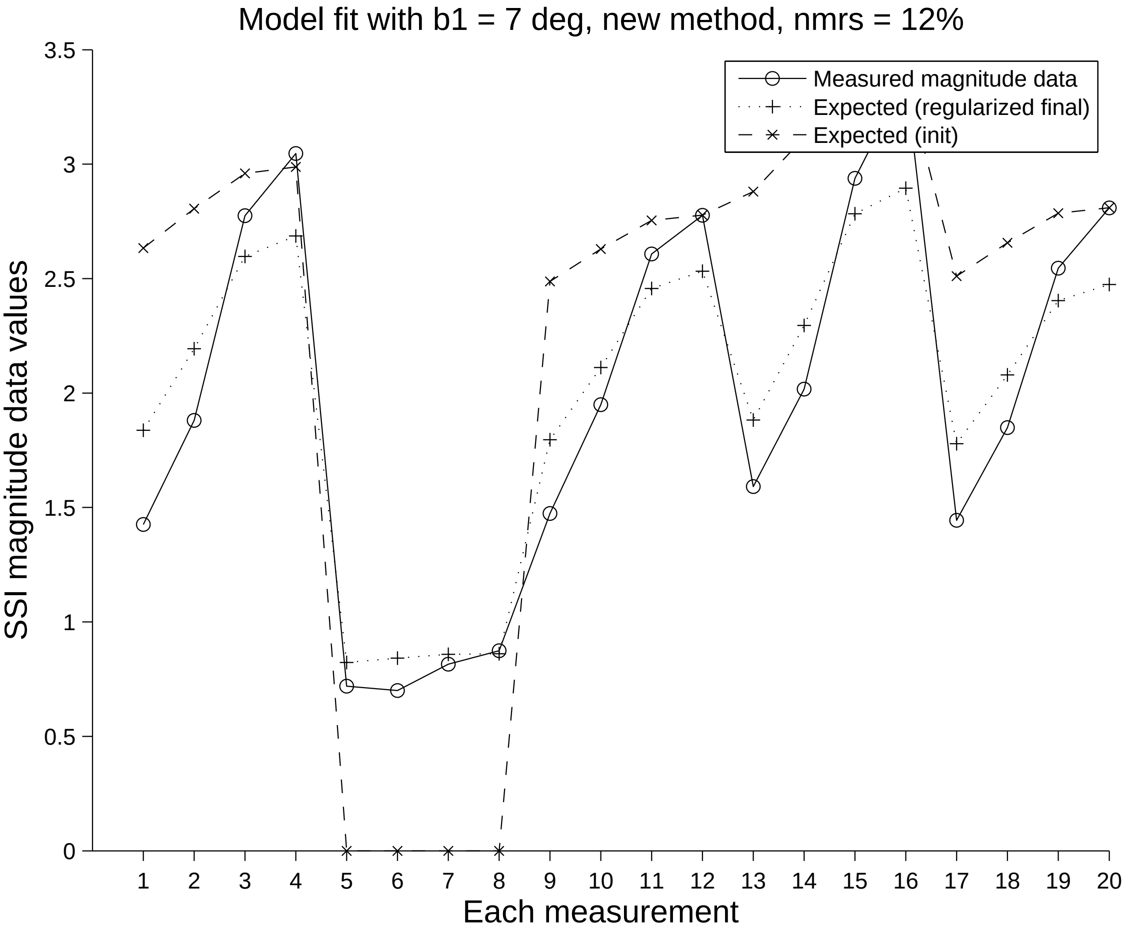

Figure 6.61: Phantom model fit, $\theta = 7$ degrees, where $\theta = \alpha b$

This section shows the feasibility of estimating real MR data and also varying the repetition time versus the tips angles for the SSI data. In the CRB analysis Section 6.4, keeping a constant tip angle while varying TR had a much higher variance than the other methods. Indeed, looking at Fig. 6.21 and Fig. 6.22, we can see that H varies slowly with T_1 (and re-

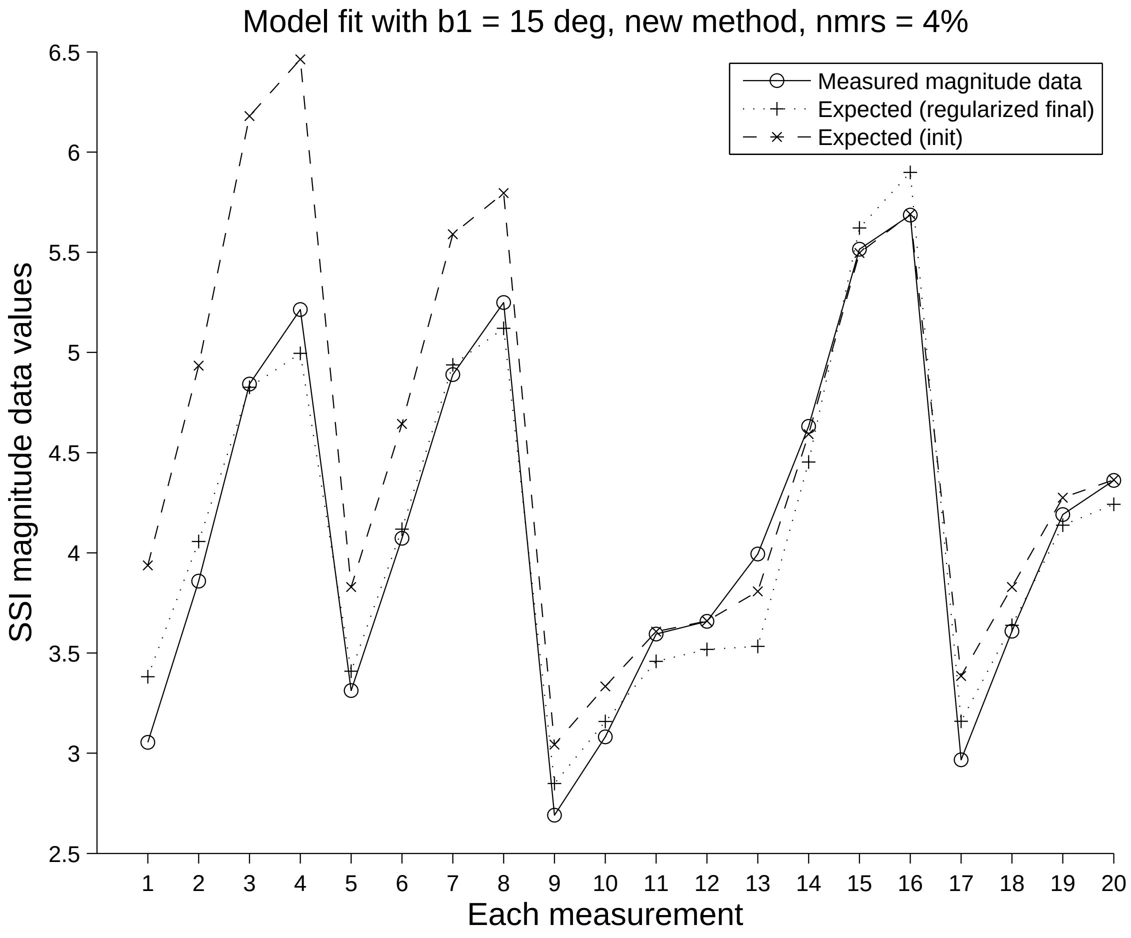

Figure 6.62: Phantom model fit, $\theta = 15$ degrees, where $\theta = \alpha b$

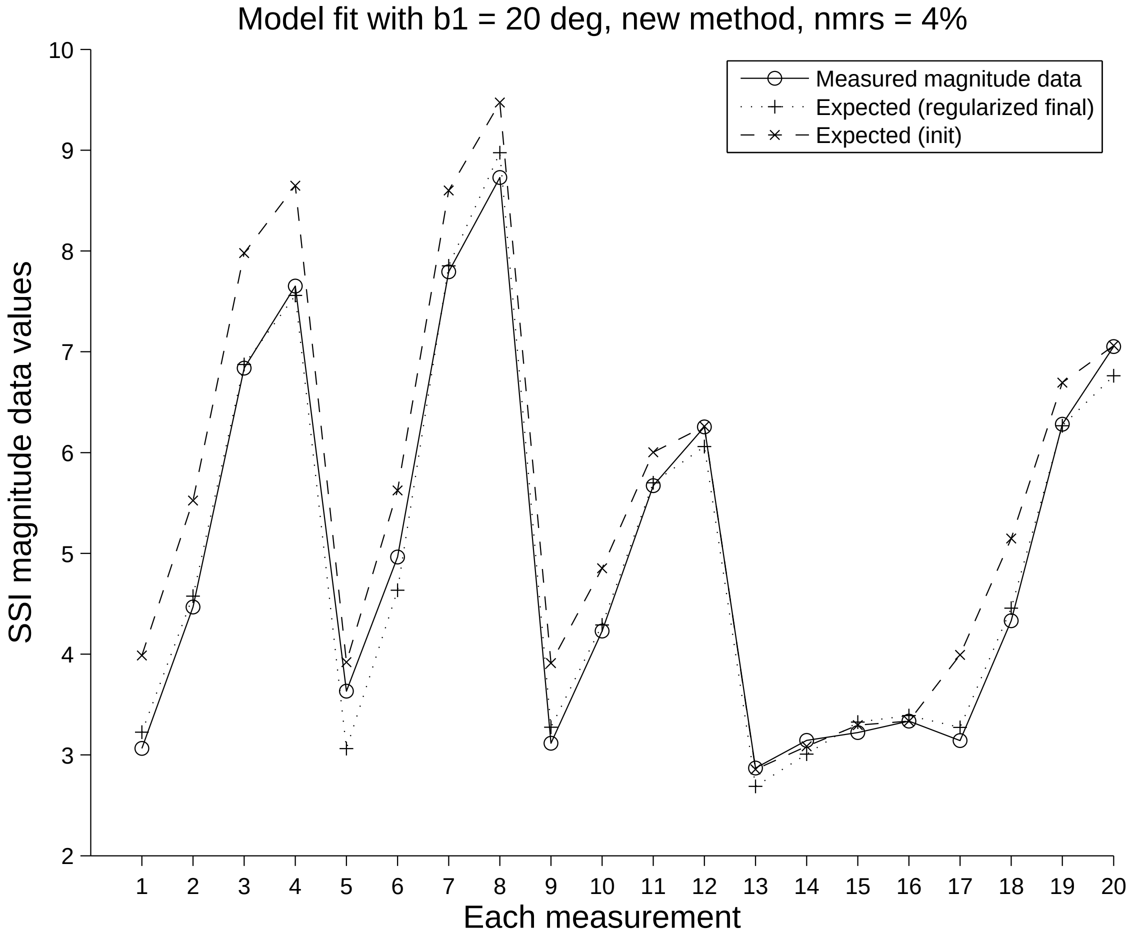

Figure 6.63: Phantom model fit, $\theta = 20$ degrees, where $\theta = \alpha b$

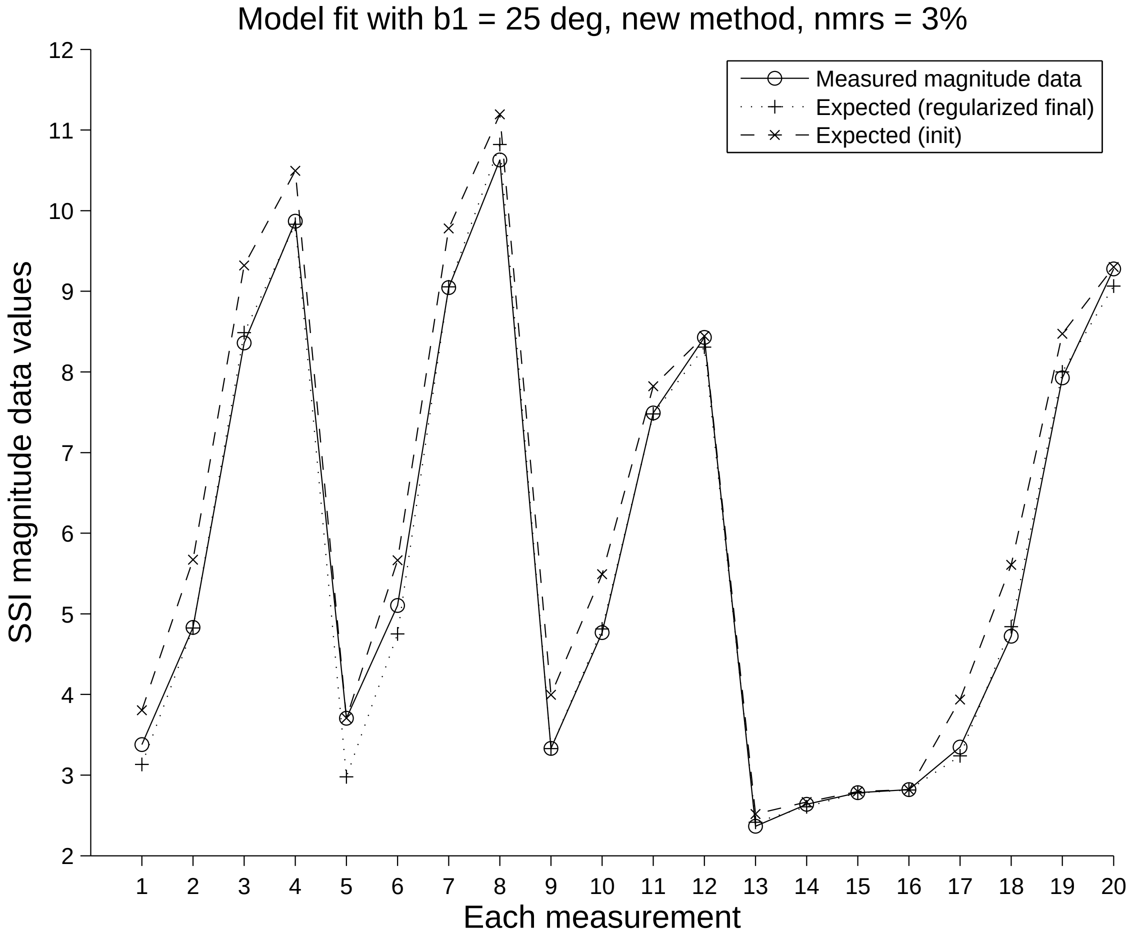

Figure 6.64: Phantom model fit, $\theta = 25$ degrees, where $\theta = \alpha b$

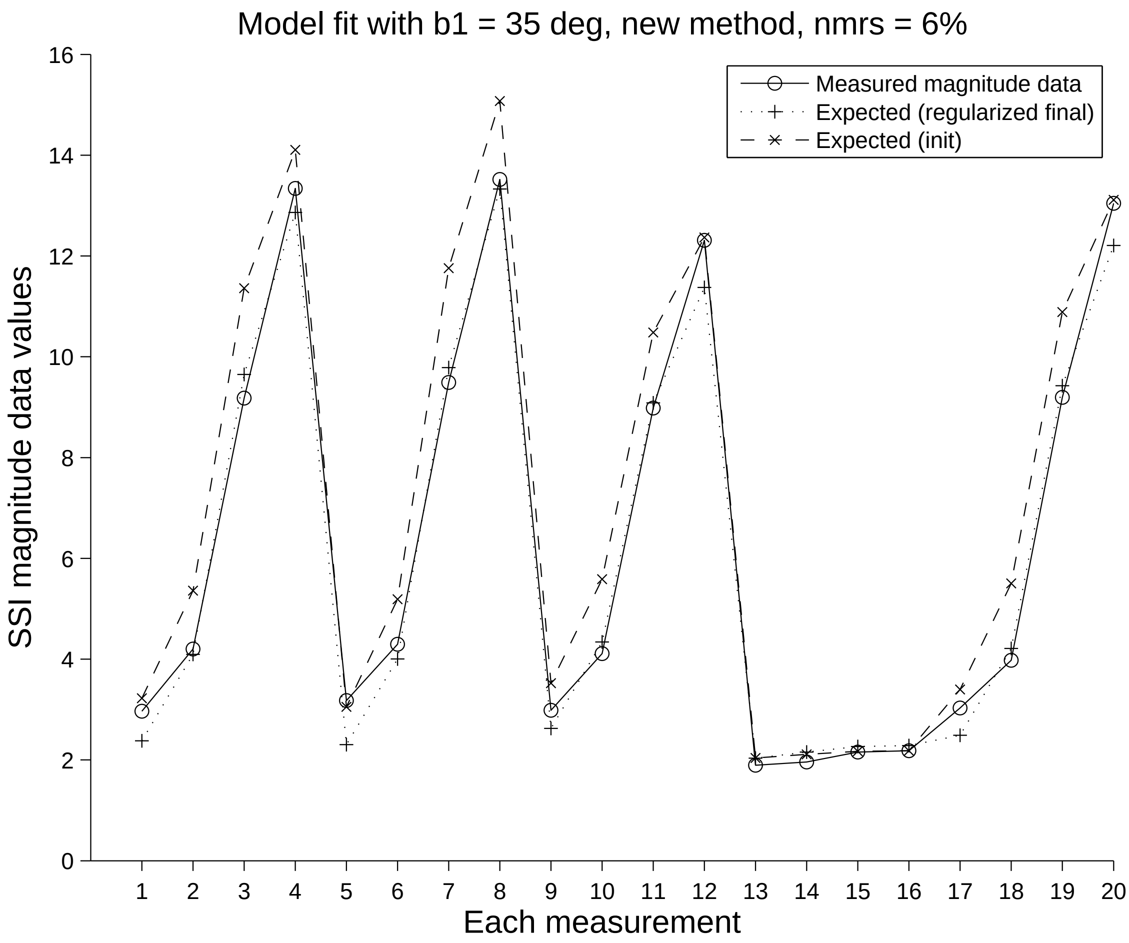

Figure 6.65: Phantom model fit, $\theta = 35$ degrees, where $\theta = \alpha b$

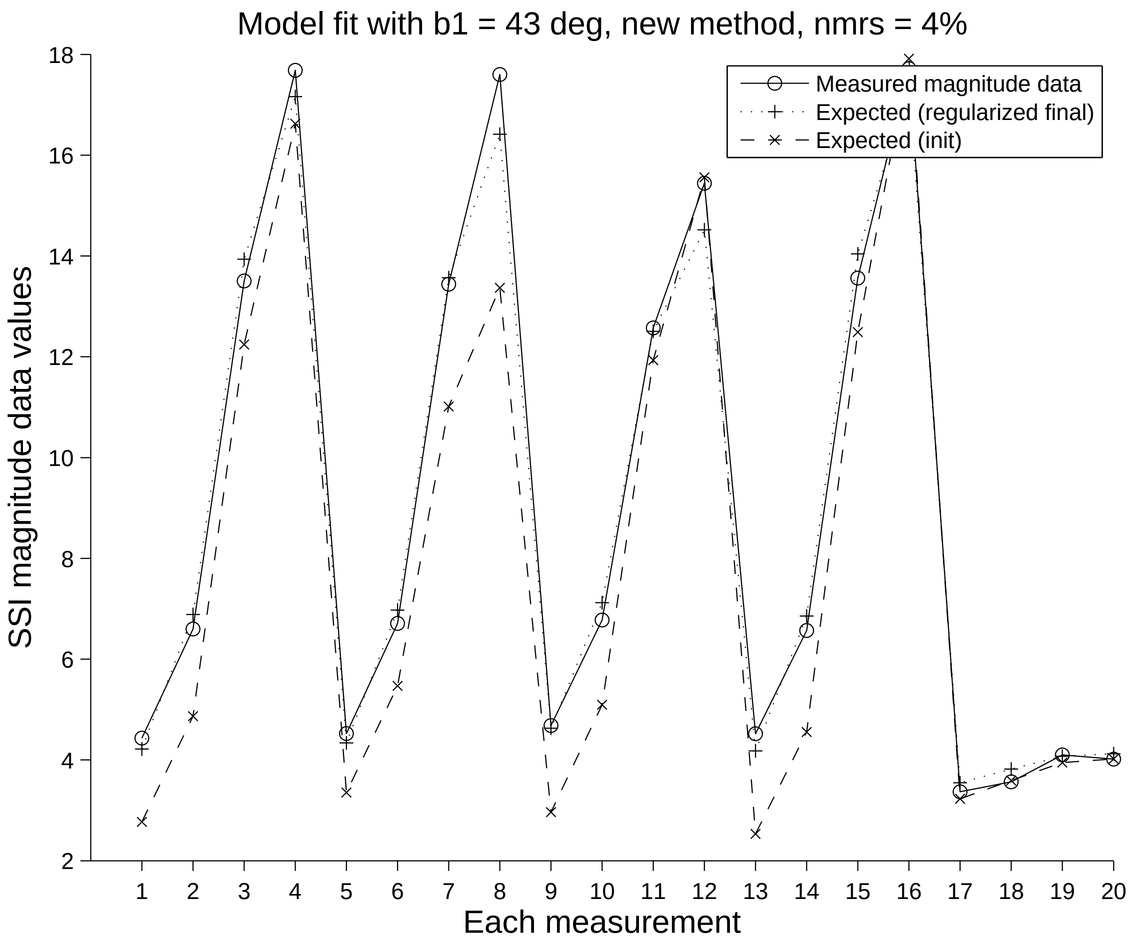

Figure 6.66: Phantom model fit, $\theta = 43$ degrees, where $\theta = \alpha b$

ciprocally, keeping T_1 constant and varying TR), especially at low flip angles. Variation in TR does not contain as much information as variation in tip angle (compare the differences in the magnitude data in Fig. 6.57 where all measurements are quite similar to Fig. 6.27 where each measurement has greater variation depending on T_1 values). Thus, we expect that phantom MR studies while varying tip angle will have lower error and better final estimates.

6.7 Joint B_1^+, T_1 estimation: Discussion

We have described a new regularized method for joint B_1^+ and T_1 mapping. Incorporating a T_1 estimate allows for decreased required repetition times while still estimating the B_1^+ magnitude and phase for multiple coils, especially for use in pulse sequence design. The B_1^+ maps interpolates smoothly in areas with low spin density with a user-chosen desired FWHM. This method allows for an arbitrary selection of both tip angles and repetition times, although careful selection of these aids the selection of an initial estimate.

This method is strongly based on our previous regularized method for B_1^+ mapping Chapter V and is an extension that allows for shorter repetition values. While not investigated in regards to joint estimation, this new method also allows for incorporation of B_0 inhomogeneity and correct slice profile.

The simulation results show that the NRMSE of the new joint B_1^+ estimates are less than those of our previous estimator, due to incorporation of T_1 effects.

In future work, we hope to investigate using different slice profiles and their subsequent effects on the final estimates. We anticipate that addition of slice profile effects will show a greater decrease in NRMSE compared to conventional estimators. We plan to implement estimating phase map differences among the coils to circumvent possible object phase that may contribute to less smoothness in the true B_1^+ maps. We plan to further investigate the optimal selection of tip angles and repetition times to minimize scan time while achieving a low NRMSE. We plan to further investigate the spatial resolution, especially for the object, and with multiple coils.

The model and estimators in this paper provide smooth, less noisy estimates that incorporate T_1 effects and greater repetition times selection that allow for a possibly shorter scan time and concurrent T_1 estimation.

CHAPTER VII

Conclusion and Future Work

Due to the high field strength and temporal requirements in modern MRI, field maps of the main field B_0 and of the radio frequency field B_1 are required for pulse design and image correction. Many current estimators for these fields are heuristic and not based on a comprehensive statistical model. This thesis proposed three new penalized-likelihood estimators based on statistical models. The field map estimator uses multiple scans and shows an empirical improvement with an improvement in RMSE over the conventional or penalized-likelihood estimator with only two scans. The B_1 estimator uses a model that accounts for a multiple coil design and includes slice-selection effects and allows for any number of arbitrary tip angles, an improvement over the double angle conventional estimator. The estimator additionally estimates both the magnitude and phase. The joint B_1^+, T_1 estimator accounts for a multiple coil design and allows for any number of arbitrary tip angles and repetition times while estimating the magnitude and phase for each coil and a T_1 map. Simulation and MRI studies show the reduced noise and (for the simulation) reduced RMSE when using each new PL estimator over the conventional estimator. Using PL estimators and a statistical model yields better results than just using conventional estimators. These estimators make smoother, less noisy estimates for B_0 and B_1 and T_1 maps for use in pulse design and image correction.

Ultimately, each of these methods is a tool that can only help answer the true question of mapping: the best use of scan time to create the most accurate map. While the preliminary CRB analyses in Section 4.2.10 and in Section 6.4 help guide the user to fortuitous selections of imaging parameters (the echo time in field map estimation or the repetition times and tip angles in joint B_1^+, T_1 mapping), neither finds the ideal use of scan time for estimating certain parameters. Indeed, most estimation in the literature balances between short scan time and accuracy in estimates, often using approximations that allow for shortened scan time at the cost of accuracy.

This is a complex problem. In B_1^+ mapping, for example, the long repetition times required by the regularized B_1^+ estimator in Chapter V may steer a user toward the joint B_1^+, T_1 estimator in Chapter VI. 3D imaging, however, has other drawbacks, such as increased motion artifacts. Using 2D imaging, a long TR with a single shot allows for many interleaved slices and may not cost much more time when compared to 3D imaging. This is especially interesting when slice selection effects are incorporated in the B_1^+ model, minimizing some of the negative effects of 2D imaging. In this case, the added complexity of the B_1^+, T_1 estimator (especially, when incorporating slice selection effects and the larger look-up table required with the addition of another variable) may not be necessary, especially when the T_1 estimate itself may be a nuisance parameter. A long single shot, of course, may bring susceptibility into the data, necessitating the use of field map estimation. 2D imaging also suffers more from through plane blood flow and in flow artifacts [81]. The joint B_1^+, T_1 estimator, on the other hand, has the advantage of allowing the user to vary either the tip angles or the repetition times. This is useful, especially in experimental setups where the repetition time can be picked with accuracy and there is possible non-linearity of tip angles. Choosing the best estimator to use for the most accurate B_1^+ maps is a complex problem with many different considerations.

In future work, we hope to further investigate the issue of optimal parameters and scan time in regards to B_1^+ mapping. Ideally, a large simulation and phantom study would compare 2D and 3D methods in regards to their accuracy and scan time. While we have compared our methods to the conventional B_1^+ estimator, a more thorough comparison would look at more time-efficient B_1^+ mapping procedures as well as "T_1" oblivious B_1^+ mapping procedures (*e.g.*, [39]) as well as compare to the more recent joint B_1^+ and T_1 estimators (*e.g.*, [11] or [124]). This would further elucidate the improvements in our regularized model-based estimators. Further investigation in the joint B_1^+/T_1 estimator of slice selection effects is also important; these effects are likely to be even greater at the shorter repetition times used in this estimator. We also hope to improve our estimators by estimating the phase difference between the coils, further guaranteeing a smooth B_1^+ map in these estimators. Further, studying the minimum number of measurements required for joint B_1^+, T_1 estimation would help reduce the required scan and estimation time.

Another item for future work is possible multi-scale estimation for the B_1^+, T_1 estimation. Because the B_1^+ maps are quite smooth, a much lower resolution map would still be acceptable while using a higher resolution T_1 and $\boldsymbol{f}$ which contain anatomical information. This is especially useful in positioning the estimator towards T_1 mapping with inherent B_1^+ correction.

Another item for future work is considering the effect of fat with its different resonance frequency. While fat suppression pulses are one possibility mentioned in the thesis, these do not always perform well, especially in areas outside the brain, such as the neck. One option is reformulating the model with the object as combination of fat and water (each with their own resonant frequency), with the percentage of fat estimated as an additional unknown parameter.

This thesis contributes three new penalized-likelihood estimators to the field of MR parameter mapping. Each signal model incorporates important physical effects such as R_2^* (for field mapping), slice selection and susceptibility effects (for B_1^+ mapping) and longitudinal relaxation effects (for joint B_1^+, T_1 mapping). The subsequent estimators smooth in areas of low data magnitude in a controlled manner by a user-selected β value that corresponds to a desired FWHM. The associated Cramer Rao bound analyses aid the user in selecting imaging parameters to give highest estimator accuracy. These estimators are a tool in the constant search for fast, high-fidelity parameter estimators to aid in improved pulse design and imaging.

APPENDICES

APPENDIX A

B_0 Minimization Algorithms

To minimize the cost function (4.11) developed in this paper, we would like a method that will decrease it monotonically. The simple minimization algorithm shown in (4.13) is guaranteed to decrease $\Psi(\boldsymbol{\omega})$ monotonically; the proof that ensures monotonicity uses the fact that the second derivative of $1 - \cos t$ is bounded above by unity. This algorithm will converge to a local minimizer of $\Psi(\boldsymbol{\omega})$ within the "basin" that contains the initial estimate [62].

However, this simple minimization algorithm shown in (4.13) is only one possible option to minimize the cost function given in (4.11). In our implementation, we used an optimization transfer approach to refine the iterative algorithm [8, 62]. First express (4.11) as shown below:

$$\Psi(\boldsymbol{\omega}) \triangleq \sum_{j=1}^{N} \sum_{m=0}^{L} \sum_{l=0}^{L} \varphi_{jml}(\omega_j) + \beta \, \mathsf{R}(\boldsymbol{\omega}), \tag{A.1}$$

where we define

$$\varphi_{jml}(\omega) \triangleq \left| y_j^m y_j^l \right| w_j^{m,l} \varphi \left(\omega(\triangle_l - \triangle_m) + \angle y_j^m - \angle y_j^l \right)$$

with

$$\varphi(t) \triangleq 1 - \cos(t)\,.$$

To minimize this cost function, we adopt an optimization transfer approach, for which we need a surrogate function for $\varphi(s)$. In particular, we use the following parabola surrogate for φ:

$$\varphi(t) \leq q(t;s) \triangleq \varphi(s) + \dot{\varphi}(s)(t-s) + \frac{1}{2}\kappa_{\varphi}(\{s\}_{2\pi})(t-s)^2$$

where $\{s\}_{2\pi}$ denotes the principle value of s. Huber stated that parabola surrogate functions (which he called a comparison function) exist for φ that satisfy Huber's conditions [60, p.184-5]; the functions must be differentiable, symmetric, and have curvatures ($\kappa_{\varphi}(s)$) that are bounded and monotone non-increasing for $s > 0$. For $|s| \leq \pi$, $\varphi(s)$ shown above satisfies Huber's conditions. We note

$$\dot{\varphi}(s) = \sin(s)$$

and

$$\kappa_{\varphi}(s) \triangleq \frac{\dot{\varphi}(s)}{s} = \frac{\sin(s)}{s}.$$

Replacing $\phi(t)$ with $q(t;s)$, in the expression for $\phi_{jml}(\omega)$ above yields a quadratic surrogate function for $\phi_{jml}(\omega)$. We must pick an appropriate value of s when defining this surrogate, and the appropriate value is when the argument of ϕ is evaluated at $\omega = \omega^{(n)}$, *i.e.*,

$$s = s_r^{(n)} \triangleq (\omega_j^{(n)}\,|\triangle_l - \triangle_m| + \angle y_j^m - \angle y_j^l) \bmod \pi.$$

Making this substitution initially yields a lengthy expression for the surrogate, which we denote as $q_{jml}^{(n)}(\omega_j)$. However, after some simplification, one can show that the surrogate function simplifies to:

$$\begin{aligned} q_{jml}^{(n)}(\omega) &\triangleq \varphi_{jml}(\omega_j^{(n)}) + \dot{\varphi}_{jml}(\omega_j^{(n)}) \left(\omega - \omega_j^{(n)}\right) \\ &+ \frac{1}{2}\kappa_{\varphi,jml}(s_r^{(n)}) \left(\omega - \omega_j^{(n)}\right)^2, \end{aligned}$$

where its curvature is given by

$$\kappa_{\varphi,jml}(s) \triangleq \frac{\dot{\varphi}_{jml}(s)}{s} = \left|y_j^m y_j^l\right| w_j^{m,l} (\triangle_l - \triangle_m)^2 \frac{\sin(s)}{s}.$$

Substituting this curvature $\kappa_\varphi(s)$ into the expression for $\varphi_{jml}(\omega)$ gives us the following curvature for the parabola surrogate

$$\kappa_{\varphi,jml}(s) \triangleq \frac{\dot{\varphi}_{jml}(s)}{s} = \left|y_j^m y_j^l\right| w_j^{m,l} (\triangle_l - \triangle_m)^2 \frac{\sin(s)}{s},$$

which is bounded as $s \to 0$ and decreasing as $|s|$ increases. For values of $|s| > \pi$, we exploit the periodicity of φ and find an integer k such that $|s - k2\pi| \leq \pi$, *i.e.*, the principal value of the phase s. Fig. A.1 shows φ and parabola surrogates for several values of s. When s is an even multiple of π, the curvature κ_φ is the maximum curvature of φ. When s is an odd multiple of π, the curvature κ_φ is zero, and $\dot{\varphi}$ is also zero, so the surrogate function is a constant.

Aggregating such surrogates leads to the following surrogate function for the cost function $\Psi(\boldsymbol{\omega})$:

$$\phi^{(n)}(\mathbf{x}) \triangleq \sum_{j=1}^{N} \sum_{m=0}^{L} \sum_{l=0}^{L} q_{jml}^{(n)}(\omega_j) + \beta\,\mathsf{R}(\mathbf{x})$$

where

$$\begin{aligned} q_{jml}^{(n)}(\omega) &\triangleq \varphi_{jml}(\omega_j^{(n)}) + \dot{\varphi}_{jml}(\omega_j^{(n)})(\omega - \omega_j^{(n)}) \\ &+ \frac{1}{2}\kappa_{\varphi,jml}(s_r^{(n)})(\omega - \omega_j^{(n)})^2, \end{aligned}$$

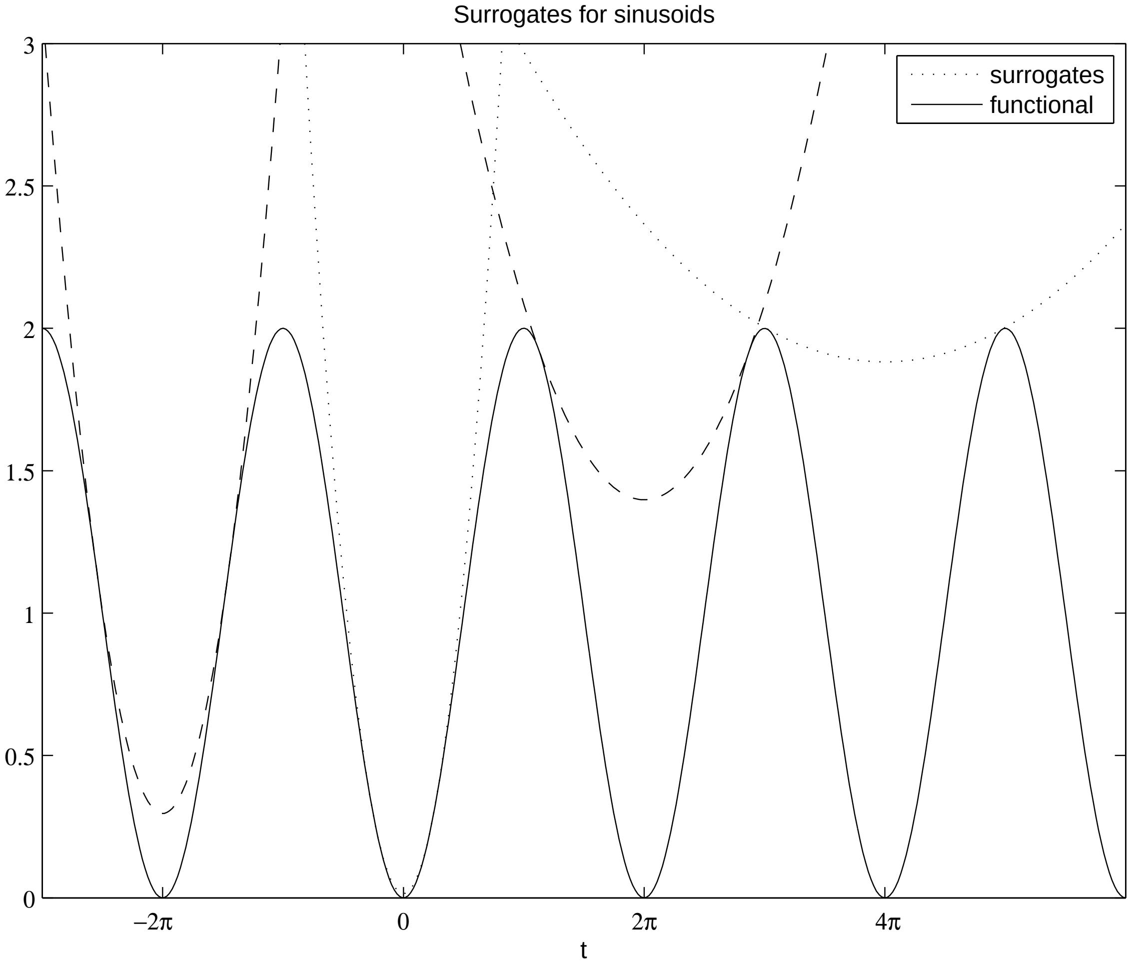

Figure A.1: Illustration of $\varphi(t)$ and quadratic surrogates for several values of s.

and where

$$s_r^{(n)} \triangleq (\omega_j^{(n)} \, |\triangle_l - \triangle_m| + \angle y_j^m - \angle y_j^l) \bmod \pi \in [-\pi, \pi].$$

If the roughness penalty $\mathsf{R}(\mathbf{x})$ is a quadratic function, which is the natural choice for smooth phase maps, then the surrogate $\phi^{(n)}$ above is a quadratic function that can be minimized easily by any classical method such as the conjugate gradient algorithm.

In our implementation, we used a separable quadratic surrogate algorithm to minimize this cost function [1]. Then, the following iteration, similar to that of (4.13), is guaranteed to decrease $\Psi(\boldsymbol{\omega})$ monotonically:

$$\boldsymbol{\omega}^{(n+1)} = \boldsymbol{\omega}^{(n)} - \mathsf{diag}\left\{ \frac{1}{\tilde{d}_j^{(n)} + \beta \cdot c} \right\} \nabla \Psi(\boldsymbol{\omega}^{(n)}), \tag{A.2}$$

where c was defined in (4.14) and where

$$\tilde{d}_j^{(n)} = \sum_{m=0}^{L} \sum_{l=0}^{L} \kappa_{\varphi,jml}(s_r^{(n)}).$$

The advantage of (A.2) over (4.13) is that $\tilde{d}_j^{(n)} \leq d_j$ in (4.15), so (A.2) will converge faster [31].

APPENDIX B

B_1: F and Slice Selection Effects

In (5.3), F is a sinusoidal-like function tabulated using a Bloch equation simulator, thus incorporating MR effects beyond the simplified sin model. Therefore, F can also have a complex output, depending on the input RF pulse. We conjecture that most symmetric RF pulses will have a real output; this model is general enough to include other pulses, including non-symmetric ones.

After considering an appropriate coordinate rotation, we can express the function F by the following equation:

$$F(z) = \mathrm{e}^{\imath \angle z} H(|z|). \tag{B.1}$$

Tabulating F would require storing a look-up table with a complex input, while H has a real input and we need store only a one-dimensional table. Both H and F have complex outputs. Therefore, we tabulate H and use (B.1) in our estimation algorithm.

We tabulate H by evaluating the Bloch equation using a RF pulse and varying its amplitude; *i.e.*, we use

$$b_1(t) = \frac{\theta}{\gamma \int_0^T p(s) ds} p(t), \tag{B.2}$$

where T is the pulse length and $p(t)$ is the RF pulse shape and we vary the amplitude θ to create the one-dimensional table. In the case of non-selective excitation, or in the small-tip angle regime with exactly on resonance excitation, θ would be the excitation tip angle times the B_1^+ map. The table H is calculated once for each RF pulse: for convenience, we normalize H to a maximum value of 1. We investigated two common pulses further in this paper: a truncated Gaussian pulse:

$$p(t) = \mathrm{e}^{-(8t/\tau)^2/\sqrt{2\pi}}\,\mathrm{rect}(t/\tau), \tag{B.3}$$

and a truncated sinc pulse:

$$p(t) = \mathrm{sinc}(8t/\tau)[.54 + .46\cos(2\pi t/\tau)], \tag{B.4}$$

for $t/\tau \in [-\frac{1}{2}, \frac{1}{2}]$. If the (unachievable) infinite sinc RF pulse were used, then $H(\theta)$ would simplify to $\sin(\theta)$. Thus, the conventional model (5.1) implicitly assumes a perfect rectangular slice profile. If this profile were used, (5.3) would be similar to the model in [41]. Because we use the Bloch equation to tabulate H, our model (5.3) accounts for slice selection effects.

We note that one could use a different excitation pulse for each measurement, in which case F would be F_m. For simplicity, we assume the same RF pulse is used for each measurement and suppress the subscript m. We let the subscript R denote the real part and I denote the imaginary part of the quantity. For example, let F_{R} denote the real part of F and let F_{I} denote the imaginary part of F so

$$F = F_{\mathrm{R}} + iF_{\mathrm{I}}.$$

Fig. B.1 shows a graph of $H_{\mathrm{R}}(\theta)$ for the Gaussian (B.3) and the truncated sinc pulse (B.4). The idealized model $\sin(\theta)$ is also shown for comparison. For both pulses, the function is only approximately sinusoidal. Integrated across the slice, the imaginary part almost completely cancels out for symmetric pulses, leaving only a very small imaginary part. Therefore, the imaginary part is not shown for the example symmetric pulses. Fig. B.2 shows a graph of the derivative of $H_{\mathrm{R}}(\theta)$ as well as $\cos(\theta)$ (the derivative of the idealized model) for comparison.

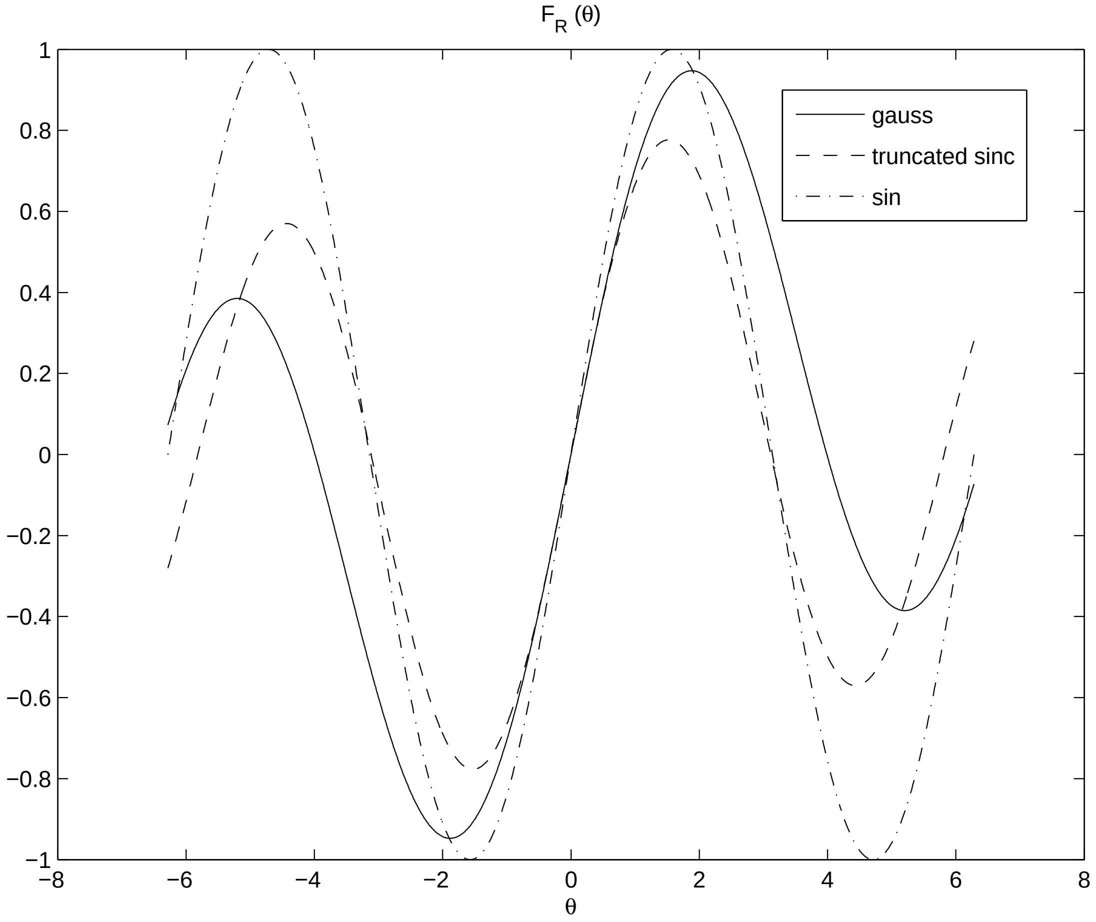

Figure B.1: Graph of $H_{\mathrm{R}}(\theta)$ for a Gaussian and truncated sinc pulse.

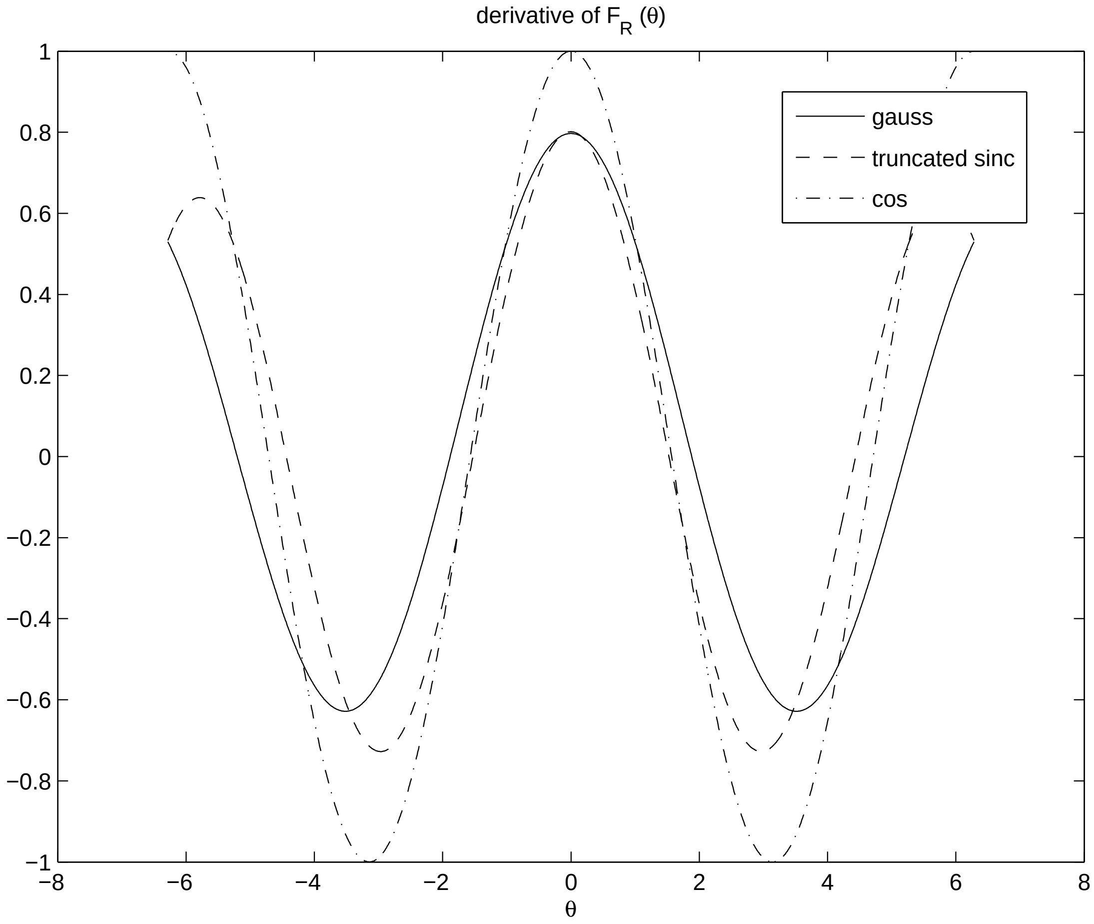

Figure B.2: Graph of the derivative of $H_{\mathrm{R}}(\theta)$ for a Gaussian and truncated sinc pulse.

APPENDIX C

B_1: Derivation of cost function gradients and separable surrogates

This section first considers a simplified version of the B_1^+ map cost function and its gradient. Any gradient-based algorithm uses the first derivative of the cost function. Next, we apply the results to our cost function (5.4). Then, we develop a quadratic surrogate for our cost function. Finally, we perform the additional step to create a separable quadratic surrogate (SQS) for (5.4) and present the final algorithm used for this paper. The equations in this section rely heavily on derivatives of the function F which are derived (in terms of derivatives of H) in Appendix D.

First, consider a simple (one voxel, one measurement) version of (5.5). We can rewrite (5.5) as follows:

$$\begin{aligned} \tilde{L}(\boldsymbol{z}, f) &= l\left(y, f, \mathrm{real}\left\{\sum_{k=1}^{K} \alpha_k z_k\right\}, \mathrm{imag}\left\{\sum_{k=1}^{K} \alpha_k z_k\right\}\right) \\ l(y, f, a, b) &\triangleq \frac{1}{2}\left|y - fG(a,b)\right|^2 \\ G(a,b) &\triangleq F(a+ib) = G_R(a,b) + iG_I(a,b), \end{aligned} \tag{C.1}$$

where $\boldsymbol{z} = (z_1, \ldots, z_K)$.

We simplify $l(\cdot)$ by ignoring terms independent of the unknown variables a or b (and recalling that f is constrained to be real):

$$\begin{aligned} l(y, f, a, b) \ &\triangleq \ - \operatorname{real}\{y\} \operatorname{real}\{fG(a,b)\} \\ &\quad - \operatorname{imag}\{y\} \operatorname{imag}\{fG(a,b)\} \\ &\quad + \frac{1}{2} |f|^2 |G(a,b)|^2 . \end{aligned} \tag{C.2}$$

$$\begin{aligned} l(y, f, a, b) \ &\equiv \ -y_R f G_R(a,b) - y_I f G_I(a,b) \\ &\quad + \frac{1}{2} f^2 |G(a,b)|^2 . \end{aligned} \tag{C.3}$$

The derivative of l with respect to the unknown variable a is:

$$\begin{aligned} \frac{\partial}{\partial a} l \ &= \ -y_R f \frac{\partial}{\partial a} G_R(a,b) - y_I f \frac{\partial}{\partial a} G_I(a,b) \\ &\quad + f^2 G_R(a,b) \frac{\partial}{\partial a} G_R(a,b) \\ &\quad + f^2 G_I(a,b) \frac{\partial}{\partial a} G_I(a,b) \\ &= \ -f(y_R - fG_R(a,b)) \frac{\partial}{\partial a} G_R(a,b) \\ &\quad - f(y_I - fG_I(a,b)) \frac{\partial}{\partial a} G_I(a,b) \\ &= \ -f(y_R - fG_R(a,b)) \frac{\partial}{\partial a} G_R(a,b) \\ &\quad + if(y_I - fG(a,b)_I) i \frac{\partial}{\partial a} G_I(a,b) \\ &= \ -f \operatorname{real}\left\{ (y - fG(a,b))^* \frac{\partial}{\partial a} G(a,b) \right\} . \end{aligned} \tag{C.4}$$

Similarly, the derivative with respect to b is:

$$\begin{aligned}
\frac{\partial}{\partial b} l &= -y_R f \frac{\partial}{\partial a} G_R(a,b) - y_I f \frac{\partial}{\partial b} G_I(a,b) \\
&\quad + |f|^2 \, G_R(a,b) \frac{\partial}{\partial b} G_R(a,b) \\
&\quad + |f|^2 \, G_I(a,b) \frac{\partial}{\partial b} G_I(a,b) \\
&= -f \, \mathrm{real} \left\{ (y - fG(a,b))^* \frac{\partial}{\partial b} G(a,b) \right\}.
\end{aligned} \tag{C.5}$$

The second derivatives are:

$$\begin{aligned}
\frac{\partial^2}{\partial a^2} l &= -f(y_R - fG_R(a,b)) \frac{\partial^2}{\partial a^2} G_R(a,b) \\
&\quad - f(y_I - fG_I(a,b)) \frac{\partial^2}{\partial a^2} G_I(a,b) \\
&\quad + f^2 \left(\left(\frac{\partial}{\partial a} G_R(a,b) \right)^2 + \left(\frac{\partial}{\partial a} G_I(a,b) \right)^2 \right) \\
&= -f \, \mathrm{real} \left\{ (y - fG(a,b))^* \frac{\partial^2}{\partial a^2} G(a,b) \right\} \\
&\quad + f^2 \left(\left(\frac{\partial}{\partial a} G_R(a,b) \right)^2 + \left(\frac{\partial}{\partial a} G_I(a,b) \right)^2 \right).
\end{aligned} \tag{C.6}$$

$$\begin{aligned}
\frac{\partial^2}{\partial b^2} l &= -f(y_R - fG_R(a,b)) \frac{\partial^2}{\partial b^2} G_R(a,b) \\
&\quad + f^2 (\frac{\partial}{\partial b} G_R(a,b))^2 \\
&\quad - f(y_I - fG_I(a,b)) \frac{\partial^2}{\partial b^2} G_I(a,b) \\
&\quad + f^2 \left(\frac{\partial}{\partial b} G_I(a,b) \right)^2 \\
&= -f \, \mathrm{real} \left\{ (y - fG(a,b))^* \, \frac{\partial^2}{\partial b^2} G(a,b) \right\} \\
&\quad + f^2 \left(\frac{\partial}{\partial b} G_R(a,b) \right)^2 \\
&\quad + f^2 \left(\frac{\partial}{\partial b} G_I(a,b) \right)^2,
\end{aligned} \tag{C.7}$$

$$
\begin{aligned}
\frac{\partial}{\partial a}\frac{\partial}{\partial b}l &= -f(y_R - fG_R(a,b))\frac{\partial}{\partial a}\frac{\partial}{\partial b}G_R(a,b) \\
&\quad +f^2(\frac{\partial}{\partial a}G_R(a,b))(\frac{\partial}{\partial b}G_R(a,b)) \\
&\quad -f(y_I - fG_I(a,b))\frac{\partial}{\partial a}\frac{\partial}{\partial b}G_I(a,b) \\
&\quad +f^2(\frac{\partial}{\partial a}G_I(a,b))(\frac{\partial}{\partial b}G_I(a,b)) \\
&= -f\,\mathrm{real}\left\{(y - fG(a,b))^*\frac{\partial}{\partial a}\frac{\partial}{\partial b}G(a,b)\right\} \\
&\quad +f^2(\frac{\partial}{\partial a}G_R(a,b))(\frac{\partial}{\partial b}G_R(a,b)) \\
&\quad +f^2(\frac{\partial}{\partial a}G_I(a,b))(\frac{\partial}{\partial b}G_I(a,g)). \qquad \text{(C.8)}
\end{aligned}
$$

Using these derivatives, we want to derive a quadratic surrogates for our simplified likelihood function $l(a,b)$ [8]. A quadratic majorizing surrogate approximates our cost function locally while always lying above the original function and, as a quadratic, can be trivially minimized. Let $v = (a,b)$ and define

$$l(v) \triangleq l(|y|/f, 1, a, b) \cdot f^2.$$

Then, we form our quadratic surrogate around the point $u = (a^{(n)}, b^{(n)})$, our current estimate of a and b, where the derivative of the surrogate matches the derivative of the simplified cost function (using (C.4) and (C.5)) and we use the maximum possible curvature c_1 (defined below). The quadratic surrogate for l is:

$$
\begin{aligned}
q(y,f,v,u) &\triangleq l(u) + \nabla l(u)\cdot(v-u) + \frac{c_1(y)}{2}\left\|v-u\right\|^2 \\
&\geq l(v) \quad \forall v, u, \qquad \text{(C.9)}
\end{aligned}
$$

where

$$\begin{aligned} c_1(y) &= \max_{v \in R^2} \left\| \nabla^2 l(v) \right\|_F \\ &= f^2 \max_{a,b} \left\| \nabla^2 l(|y|/f, 1, a, b) \right\|_F \\ &= f^2 c(|y|/f), \end{aligned} \tag{C.10}$$

where $\|\cdot\|_F$ is the Frobenius norm and the norm uses (C.6), (C.7), and (C.8). We numerically evaluated (C.10) for the RF pulse shapes used in this paper. We found $c(0) = \sqrt{2} \cdot h_R^2(0)$. For the profiles used in this paper, $c(y)$ is nearly piece-wise linear and depends only on $|y|$. For y close to 0, $c(y) = c(0)$. For larger y, $c(y)$ depends linearly on $|y|$. We numerically tabulated the function $c(y)$ for use in the algorithm.

We apply these results to the (multi-voxel, multi-measurement) likelihood (5.5) to form a quadratic surrogate. We rewrite (5.5) using our previous notation:

$$\begin{aligned} L(\boldsymbol{z}, \boldsymbol{f}) &= \sum_{j=1}^{N} \sum_{m=1}^{M} \frac{1}{2} \left| y_{jm} - f_j F\left(\sum_{k=1}^{K} \alpha_{mk} z_{jk} \right) \right|^2 \\ &= \sum_{j=1}^{N} \sum_{m=1}^{M} l(y_{jm}, f_j, \mathrm{real}\{[\boldsymbol{\alpha} \boldsymbol{z}_j]_m\}, \\ &\quad \mathrm{imag}\{[\boldsymbol{\alpha} \boldsymbol{z}_j]_m\}). \end{aligned} \tag{C.11}$$

This is an additively separable cost function; therefore, the quadratic surrogate for (5.5) is a sum of the quadratic surrogate q for each l, which we derived in (C.9). We define

$$\begin{aligned} v_{jm} &\triangleq (\mathrm{real}\{[\boldsymbol{\alpha} \boldsymbol{z}_j]_m\}, \mathrm{imag}\{[\boldsymbol{\alpha} \boldsymbol{z}_j]_m\}) \\ u_{jm} &\triangleq \left(\mathrm{real}\left\{[\boldsymbol{\alpha} \boldsymbol{z}_j^{(n)}]_m\right\}, \mathrm{imag}\left\{[\boldsymbol{\alpha} \boldsymbol{z}_j^{(n)}]_m\right\}\right), \end{aligned}$$

and $\boldsymbol{v}_m = (v_{1m}, \ldots v_{1N})$, $\boldsymbol{v} = (\boldsymbol{v}_1, \ldots \boldsymbol{v}_M)$, $\boldsymbol{u}_m = (u_{1m}, \ldots u_{1N})$, $\boldsymbol{u} = (\boldsymbol{u}_1, \ldots \boldsymbol{u}_M)$, and

$\tilde{\boldsymbol{z}} = (\mathrm{real}\{\boldsymbol{z}\}, \mathrm{imag}\{\boldsymbol{z}\})$. Let

$$\begin{aligned}
Q_L(\boldsymbol{z}; \boldsymbol{z}^{(n)}) &\triangleq \sum_{j=1}^{N}\sum_{m=1}^{M} q\left(y_{jm}, f_j^{(n)}, v_{jm}, u_{jm}\right) \\
&\equiv \sum_{j=1}^{N}\sum_{m=1}^{M} l(u_{jm}) + \nabla l(u_{jm}) \cdot (v_{jm} - u_{jm}) \\
&\quad + \frac{c_1(y_{jm})}{2} \left\| v_{jm} - u_{jm} \right\|^2 \\
&= \sum_{j=1}^{N} L\left(\tilde{\boldsymbol{z}}_j{}^{(n)}, f_j^{(n)}\right) \\
&\quad + \nabla L\left(\tilde{\boldsymbol{z}}_j{}^{(n)}, f_j^{(n)}\right)\left(\tilde{\boldsymbol{z}}_j - \tilde{\boldsymbol{z}}_j{}^{(n)}\right) \\
&\quad + \frac{1}{2}\left(\tilde{\boldsymbol{z}}_j - \tilde{\boldsymbol{z}}_j{}^{(n)}\right)' \boldsymbol{\alpha}' W_j^{(n)} \boldsymbol{\alpha} \left(\tilde{\boldsymbol{z}}_j - \tilde{\boldsymbol{z}}_j{}^{(n)}\right),
\end{aligned} \tag{C.12}$$

where the $2M \otimes 2M$ curvature matrix is

$$W_j^{(n)} = \mathsf{diag}\left\{c_{jm}^{(n)}\right\} \otimes I_2,$$

where $\otimes$ denotes the Kronecker product, I_2 is the 2×2 identity matrix and

$$c_{jm}^{(n)} = \left(f_j^{(n)}\right)^2 c\left(\frac{|y_{jm}|}{f_j^{(n)}}\right).$$

The gradient $\nabla L(\tilde{\boldsymbol{z}}^{(n)}, f^{(n)})$ can be calculated using (C.4) and (C.5) taking care to properly account for α_{mk} factors using the chain rule.

Q_L is quadratic, but not separable due to the matrix product $\boldsymbol{\alpha}' W_j^{(n)} \boldsymbol{\alpha}$. Generally, this matrix product is too large to compute, but here the matrices are small and constant and could be pre-computed and minimized, with conjugate gradient for example. However, when the surrogate for the regularization surrogates are added to the total surrogate, this matrix product is no longer small or static and can not feasibly be inverted.

Therefore, we continue the derivation to find a *separable quadratic surrogate*. We use steps similar to [22]. We first note that we can write

$$\begin{aligned}[\boldsymbol{\alpha}\boldsymbol{z}_j]_m &= \sum_{k=1}^{K} \alpha_{mk} z_{jk} \\ &= \sum_{k=1}^{K} \pi_{mk} \left(\frac{\alpha_{mk}}{\pi_{mk}} \left(z_{jk} - z_{jk}^{(n)} \right) + \left[\boldsymbol{\alpha}\boldsymbol{z}_j^{(n)} \right]_m \right),\end{aligned}$$

if $\sum_{k=1}^{K} \pi_{mk} = 1$ and $\pi_{mk} = 0 \iff \alpha_{mk} = 0$. Then, (if $\pi_{mk} > 0 \; \forall m, k$)

$$\begin{aligned} q\left(y_{jm}, f_j^{(n)}, v_{jm}, u_{jm} \right) \leq \sum_{k=1}^{K} \pi_{mk} \\ q\Bigg(y_{jm}, f_j^{(n)}, \frac{\alpha_{mk}}{\pi_{mk}} \left(\tilde{z}_{jk} - \tilde{z}_{jk}^{(n)} \right) + u_{jm}, u_{jm} \Bigg).\end{aligned}$$

Finally, combining all these steps, we find the separable quadratic surrogate for our likelihood cost function.

$$\begin{aligned} Q_{L-SQS} &= \sum_{j=1}^{N} \sum_{m=1}^{M} \sum_{k=1}^{K} \pi_{mk} \\ & \quad q\left(y_{jm}, f_j^{(n)}, \frac{\alpha_{mk}}{\pi_{mk}} \left(\tilde{z}_{jk} - \tilde{z}_{jk}^{(n)} \right) + u_{jm}, u_{jm} \right) \\ &= L\left(\tilde{\boldsymbol{z}}^{(n)}, f^{(n)} \right) + \nabla L\left(\tilde{\boldsymbol{z}}^{(n)}, f^{(n)} \right) \left(\tilde{\boldsymbol{z}} - \tilde{\boldsymbol{z}}^{(n)} \right) \\ & \quad + \frac{1}{2} \left(\tilde{\boldsymbol{z}} - \tilde{\boldsymbol{z}}^{(n)} \right)' \tilde{W}^{(n)} \left(\tilde{\boldsymbol{z}} - \tilde{\boldsymbol{z}}^{(n)} \right), \end{aligned} \tag{C.13}$$

where we let $\pi_{mk} \triangleq \frac{|\alpha_{mk}|}{\alpha_m}$ and $\alpha_m \triangleq \sum_{k=1}^{K} |\alpha_{mk}|$ and

$$\tilde{W}^{(n)} = \mathsf{diag}\left\{ d_{jk}^{(n)} \right\} \otimes I_2.$$

The new curvatures $d_{jk}^{(n)}$ are found by taking derivatives of the new Q_{L-SQS} (first line of (C.13)) and are expressed in terms of the previous maximum curvature:

$$d_{jk}^{(n)} = \sum_{m=1}^{M} \frac{|\alpha_{mk}|^2}{\pi_{mk}} c_{jm}^{(n)}.$$

Finally, we add this surrogate to that of the regularization term to obtain the final separable quadratic surrogate for (5.4).

$$\begin{aligned} Q_\Psi &= \Psi\left(\boldsymbol{z}^{(n)}, f^{(n)}\right) + \nabla\,\Psi\left(\boldsymbol{z}^{(n)}, f^{(n)}\right)\left(\boldsymbol{z} - \boldsymbol{z}^{(n)}\right) + \\ & \quad \frac{1}{2}\left(\boldsymbol{z} - \boldsymbol{z}^{(n)}\right)'\left(\mathsf{diag}\left\{d_{jk}^{(n)} + \beta r\right\} \otimes I_2\right)\left(\boldsymbol{z} - \boldsymbol{z}^{(n)}\right). \end{aligned} \tag{C.14}$$

The factor "r" depends on the choice of the regularizer $\mathsf{R}(\boldsymbol{z}_k)$ and is the maximum curvature of (5.6). For 2nd-order finite differences with the 8 nearest neighbors, this factor is $4 \cdot 4 \cdot (2 + 2/\sqrt{2})$. This leads to the natural iteration for updating $\boldsymbol{z}_k$ (where $a_k = \mathrm{real}\{x_k\}$ and $b_k = \mathrm{imag}\{x_k\}$):

$$\begin{bmatrix} \boldsymbol{a}_k^{(n+1)} \\ \boldsymbol{b}_k^{(n+1)} \end{bmatrix} = \begin{bmatrix} \boldsymbol{a}_k^{(n)} \\ \boldsymbol{b}_k^{(n)} \end{bmatrix} - \begin{bmatrix} \frac{\nabla_{\boldsymbol{a}_k}\,\Psi\left(f^{(n)}, \boldsymbol{z}_k^{(n)}\right)}{d_{jk}^{(n)} + \beta r} \\ \frac{\nabla_{\boldsymbol{b}_k}\,\Psi\left(f^{(n)}, \boldsymbol{z}_k^{(n)}\right)}{d_{jk}^{(n)} + \beta r} \end{bmatrix}. \tag{C.15}$$

One way to increase the speed of the algorithm is to only update the object estimate every few iterations. Because the object is a nuisance parameter and the initial estimate is very good (based on simulation results), occasional updates have only marginal effects on the final B_1^+ map estimates. Therefore, for examples in this paper, we updated the object only every 10 iterations. This decreases the computation time by a significant fraction (by 1/5 for simulation examples) with only a minimal increase in NRMSE for the same number of iterations.

APPENDIX D

B_1: Derivatives of F

This section derives the derivatives of F in terms of H and its derivatives, which are tabulated as explained in Section 5.2.2.

To simplify the derivations, we use an equivalent definition for F. We define $z = a + ib$ and rewrite (B.1) as follows:

$$\begin{aligned} F(z) &= \mathrm{e}^{\imath\angle z}\, H(\sqrt{a^2+b^2}) \\ &= \left(\frac{a}{\sqrt{a^2+b^2}} + \frac{ib}{\sqrt{a^2+b^2}}\right) H(\sqrt{a^2+b^2}). \end{aligned}$$

The final line follows from using Euler's formula for $\mathrm{e}^{\imath\angle z}$ and expressing $\cos$ and $\sin$ using the Pythagorean Theorem. Now, we define the real functions

$$\begin{aligned} h(r) &\triangleq \frac{H(r)}{r} \\ \dot{h}(r) &= \frac{r\dot{H}(r) - H(r)}{r^2} \\ \ddot{h}(r) &= \frac{r^2\ddot{H}(r) - 2r\dot{H}(r) + 2H(r)}{r^3}. \end{aligned}$$

We can either tabulate the function h directly or we can use the tabulated function H to calculate h. The derivatives of h can be numerically tabulated or expressed in terms of the previous equations. We can now express (B.1) as

$$F(z) = F(a+ib) = ah(|z|) + ibh(|z|) = zh(|z|). \tag{D.1}$$

The derivatives of (D.1) with respect to a and b are:

$$\begin{aligned}\frac{\partial}{\partial a}F(z) &= a\dot{h}(|z|)\frac{a}{|z|} + h(|z|) + ib\dot{h}(|z|)\frac{a}{|z|} \\ &= \frac{a^2}{|z|}\dot{h}(|z|) + \frac{iab}{|z|}\dot{h}(|z|) + h(|z|) \\ &= a\frac{z}{|z|}\dot{h}(|z|) + h(|z|). \qquad \text{(D.2)}\end{aligned}$$

$$\begin{aligned}\frac{\partial}{\partial b}F(z) &= a\dot{h}(|z|)\frac{b}{|z|} + i[b\dot{h}(|z|)\frac{b}{|z|} + h(|z|)] \qquad \text{(D.3)} \\ &= b\frac{z}{|z|}\dot{h}(|z|) + ih(|z|). \qquad \text{(D.4)}\end{aligned}$$

Combining these two derivatives, we obtain:

$$\begin{aligned}\frac{\partial}{\partial z}F(z) &\triangleq \frac{\partial}{\partial a}g(z) + i\frac{\partial}{\partial b}g(z) \qquad \text{(D.5)} \\ &= \frac{z^2}{|z|}\dot{h}(|z|). \qquad \text{(D.6)}\end{aligned}$$

Some equations in Appendix C require the derivatives of F_R and F_I. These can be separately derived from the definition of F_R and F_I or by simply calculating the real and imaginary parts of expressions (D.2) and (D.4) above. This also applies for the following derivative expressions (D.9),(D.10), and (D.11).

Note that $h_R = H_R/r$ and $h_I = H_I/r$. First, we derive F_R and F_I in terms of h as follows.

$$\begin{aligned}
F_R(z) &= \text{real}\{F(z)\} = real(zh(|z|)) \\
&= \text{real}\{a(h_R(|z|) + ih_I(|z|)) + ib(h_R(|z|) + ih_I(|z|))\} \\
&= ah_R(|z|) - bh_I(|z|). \qquad \text{(D.7)}
\end{aligned}$$

$$\begin{aligned}
F_I &= \text{imag}\{F(z)\} \\
&= \text{imag}\{a(h_R(|z|) + ih_I(|z|)) + ib(h_R(|z|) + ih_I(|z|))\} \\
&= ah_I(|z|) + bh_R(|z|). \qquad \text{(D.8)}
\end{aligned}$$

The derivative of (D.7) and (D.8) with respect to a and b are:

$$\begin{aligned}
\frac{\partial}{\partial a} F_R &= \frac{\partial}{\partial a}\left(ah_R(|z|) - bh_I(|z|)\right) \\
&= h_R(|z|) + \frac{a^2}{|z|}\dot{h}_R(|z|) - \frac{ab}{|z|}\dot{h}_I(|z|).
\end{aligned}$$

$$\begin{aligned}
\frac{\partial}{\partial a} F_I &= \frac{\partial}{\partial a}\left(ah_I(|z|) + bh_R(|z|)\right) \\
&= h_I(|z|) + \frac{a^2}{|z|}\dot{h}_I(|z|) + \frac{ab}{|z|}\dot{h}_R(|z|).
\end{aligned}$$

$$\begin{aligned}
\frac{\partial}{\partial b} F_R &= \frac{\partial}{\partial b}\left(ah_R(|z|) - bh_I(|z|)\right) \\
&= \frac{ab}{|z|}\dot{h}_R(|z|) - h_I(|z|) - \frac{b^2}{|z|}\dot{h}_I(|z|).
\end{aligned}$$

$$\begin{aligned}
\frac{\partial}{\partial b} F_I &= \frac{\partial}{\partial b}\left(ah_I(|z|) + bh_R(|z|)\right) \\
&= \frac{ab}{|z|}\dot{h}_I(|z|) + h_R(|z|) + \frac{b^2}{|z|}\dot{h}_R(|z|).
\end{aligned}$$

The second derivatives of F, which are used along with (C.6), (C.7), and (C.8) to find $c(y)$ in Appendix C are given by:

$$\begin{aligned} \frac{\partial^2}{\partial a^2}F(z) &= \frac{\dot{h}(|z|)}{|z|}\left(z + 2a - a^2\frac{z}{|z|^2}\right) \\ &\quad + \frac{\ddot{h}(|z|)}{|z|^2}(az). \end{aligned} \tag{D.9}$$

$$\begin{aligned} \frac{\partial^2}{\partial b^2}F(z) &= \frac{\dot{h}(|z|)}{|z|}\left(z + 2b - b^2\frac{z}{|z|^2}\right) \\ &\quad + \frac{\ddot{h}(|z|)}{|z|^2}(biz). \end{aligned} \tag{D.10}$$

$$\begin{aligned} \frac{\partial}{\partial a}\frac{\partial}{\partial b}F(z) &= \frac{\dot{h}(|z|)}{|z|}\left(ab + ia - ab\frac{z}{|z|^2}\right) \\ &\quad + \frac{\ddot{h}(|z|)}{|z|^2}(abz). \end{aligned} \tag{D.11}$$

The derivatives of the real and imaginary parts of F are:

$$\begin{aligned} \frac{\partial^2}{\partial a^2}F_{\mathrm{R}} &= \frac{\partial}{\partial a}\left(h_R(|z|) + \frac{a^2}{|z|}\dot{h}_R(|z|) - \frac{ab}{|z|}\dot{h}_I(|z|)\right) \\ &= \frac{a}{|z|}\dot{h}_R(|z|) + \frac{2a}{|z|}\dot{h}_R(|z|) - \frac{a^3}{|z|^2}\dot{h}_R(|z|) \\ &\quad + \frac{a^3}{|z|^2}\ddot{h}_R(|z|) - \frac{b}{|z|}\dot{h}_I(|z|) + \frac{a^2b}{|z|^2}\dot{h}_I(|z|) \\ &\quad - \frac{a^2b}{|z|}\ddot{h}_I(|z|). \end{aligned} \tag{D.12}$$

$$\begin{aligned}\frac{\partial^2}{\partial a^2}F_{\mathrm{I}} &= \frac{\partial}{\partial a}\left(h_I(|z|)+\frac{a^2}{|z|}\dot{h}_I(|z|)+\frac{ab}{|z|}\dot{h}_R(|z|)\right)\\ &= \frac{a}{|z|}\dot{h}_I(|z|)+\frac{2a}{|z|}\dot{h}_I(|z|)-\frac{a^3}{|z|^2}\dot{h}_I\\ &\quad +\frac{a^3}{|z|^2}\ddot{h}_I+\frac{b}{|z|}\dot{h}_R(|z|)-\frac{a^2b}{|z|^2}\dot{h}_R(|z|)\\ &\quad +\frac{a^2b}{|z|^2}\ddot{h}_R(|z|).\end{aligned}\tag{D.13}$$

$$\begin{aligned}\frac{\partial^2}{\partial b^2}F_{\mathrm{R}} &= \frac{\partial}{\partial b}\left(\frac{ab}{|z|}\dot{h}_R(|z|)-h_I(|z|)-\frac{b^2}{|z|}\dot{h}_I(|z|)\right)\\ &= \frac{a}{|z|}\dot{h}_R(|z|)-\frac{ab^2}{|z|^2}\dot{h}_R(|z|)-\frac{ab^2}{|z|^2}\ddot{h}_R(|z|)\\ &\quad -\frac{b}{|z|}\dot{h}_I(|z|)-\frac{2b}{|z|}\dot{h}_I(|z|)+\frac{b^3}{|z|^2}\dot{h}_I(|z|)\\ &\quad -\frac{b^3}{|z|^2}\ddot{h}_I(|z|).\end{aligned}\tag{D.14}$$

$$\begin{aligned}\frac{\partial^2}{\partial b^2}F_{\mathrm{I}} &= \frac{\partial}{\partial b}\left(\frac{ab}{|z|}\dot{h}_I(|z|)+h_R(|z|)+\frac{b^2}{|z|}\dot{h}_R(|z|)\right)\\ &= \frac{a}{|z|}\dot{h}_I(|z|)-\frac{ab^2}{|z|^2}\dot{h}_I(|z|)+\frac{ab^2}{|z|^2}\ddot{h}_I(|z|)\\ &\quad +\frac{b}{|z|}\dot{h}_R(|z|)+\frac{2b}{|z|}\dot{h}_R(|z|)-\frac{b^3}{|z|^2}\dot{h}_R(|z|)\\ &\quad +\frac{b^3}{|z|^2}\ddot{h}_R(|z|).\end{aligned}\tag{D.15}$$

$$\begin{aligned}\frac{\partial}{\partial a}\frac{\partial}{\partial b}F_{\mathrm{R}} &= \frac{\dot{h}_R(|z|)}{|z|}(b-\frac{a^2b}{|z|})+\frac{\ddot{h}_R(|z|)}{|z|^2}(a^2b)+\\ &\quad -\frac{\dot{h}_I(|z|)}{|z|}(a-\frac{ab^2}{|z|})-\frac{\ddot{h}_I(|z|)}{|z|^2}(ab^2).\end{aligned}\tag{D.16}$$

$$
\begin{aligned}
\frac{\partial}{\partial a}\frac{\partial}{\partial b}F_{\mathrm{I}} &= \frac{\dot{h_I}(|z|)}{|z|}(b-\frac{a^2b}{|z|})+\frac{\ddot{h_I}(|z|)}{|z|^2}(a^2b) \\
&\quad +\frac{\dot{h_R}(|z|)}{|z|}(a-\frac{ab^2}{|z|})+\frac{\ddot{h_R}(|z|)}{|z|^2}(ab^2). \qquad \text{(D.17)}
\end{aligned}
$$

APPENDIX E

B_1: Initial estimate for $\boldsymbol{f}$ and $\mathbf{x}$

The estimator requires a good initial estimate for $\boldsymbol{z}_k$ to ensure the estimator descends to a good local minimum. We need an initial estimate for the magnitude and phase of the B_1^+ maps and of the object

The standard double angle method (5.2) is a natural choice for estimating the magnitude of B_1^+. The DAM effectively estimates the composite maps $\mathbf{x}_m$ (5.8); by forming an appropriate $\tilde{\boldsymbol{\alpha}}$ (defined below in (E.2)) and inverting it, we estimate the desired coil maps $\boldsymbol{z}_k$. The DAM also requires that, for each composite map we estimate, we also take a second measurement where the relative amplitude of each coil is double that of the first measurement, *i.e.*, let $m = 2K$ and fix $\boldsymbol{\alpha}$ such that $\alpha_{m+k} = 2\alpha_m$ where $m = 1, \ldots, K$. If this condition is satisfied, we calculate the initial estimate $z_k^{(0)}$ as follows.

First, we estimate the magnitude and phase of the composite maps. Using the corresponding measurements (*i.e.*, $\boldsymbol{y}_m$ and $\boldsymbol{y}_{m+k}$) in (5.2), we find $\widehat{\mathbf{x}_m^{(0)}}$. Similarly, we use a method of moments estimator for the phase of B_1^+:

$$\widehat{\angle \mathbf{x}_{jm}} = \angle \boldsymbol{y}_{jm} - \angle H(\widehat{|\mathbf{x}_{jm}|}), \tag{E.1}$$

using our estimate of $|\mathbf{x}_{jm}|$ from (5.2). We next form the matrix

$$\tilde{\boldsymbol{\alpha}} = \begin{bmatrix} \boldsymbol{\alpha}_1 \\ \boldsymbol{\alpha}_2 \\ \vdots \\ \boldsymbol{\alpha}_k \end{bmatrix}, \tag{E.2}$$

so that

$$\boldsymbol{\alpha} = \begin{bmatrix} \tilde{\boldsymbol{\alpha}} \\ 2\tilde{\boldsymbol{\alpha}} \end{bmatrix}.$$

Then, our initial estimate of the B_1^+ map is

$$\hat{\boldsymbol{z}}^{(0)} = \tilde{\boldsymbol{\alpha}}^{-1}\hat{\mathbf{x}}. \tag{E.3}$$

Given $\hat{\boldsymbol{z}}^{(0)}$, we estimate the object $\hat{\boldsymbol{f}}^{(0)}$ using (5.7).

Alternatively, suppose that we only make $M = K + 1$ measurements, the minimum required to estimate both the object and each of the coil maps. We fix $\boldsymbol{\alpha}_{K+1} = 2\boldsymbol{\alpha}_1$ as before. Using these two measurements, we estimate the $\hat{\mathbf{x}_1}^{(0)}$ and $\boldsymbol{f}^{(0)}$ using (5.2), (E.1), and (5.7). If the coil combinations are chosen wisely, this estimate should have few “holes” and can be used as an initial estimate for the other coil combinations *i.e.*, $\hat{\mathbf{x}}_m^{(0)} = \hat{\mathbf{x}}_1^{(0)}$ for $m = 2, \dots K + 1$. Finally, we find the B_1^+ maps $\boldsymbol{z}_m$ using (E.3) and the same $\tilde{\boldsymbol{\alpha}}$ matrix (E.2) as before. We note, this estimate is not as good for the other coils and will likely require more iterations and a higher SNR than if all $M = 2K$ scans were used.

APPENDIX F

B_1: What if $\boldsymbol{\alpha}$ is complex?

Up to this point, we have assumed that $\boldsymbol{\alpha}$ consists of solely real values. However, $\boldsymbol{\alpha}$ could be complex *e.g.*, if we put a different phase on each coil along with changing the magnitude. This does make the derivation of cost function gradients and the final algorithm more complicated. Let us look at these derivations more closely.

Now, let $\alpha_{mk} = \alpha^R_{mk} + i\alpha^I_{mk}$ and $z_{jk} = a_{jk} + ib_{jk}$. Then,

$$\mathrm{real}\left\{\sum_{k=1}^{K} \alpha_{mk} z_{jk}\right\} = \sum_{k=1}^{K} \alpha^R_{mk} a_{jk} - \alpha^I_{mk} b_{jk},$$

and

$$\mathrm{imag}\left\{\sum_{k=1}^{K} \alpha_{mk} z_{jk}\right\} = \sum_{k=1}^{K} \alpha^R_{mk} b_{jk} + \alpha^I_{mk} a_{jk}.$$

Now, both $\mathrm{real}\left\{\sum_{k=1}^{K} \alpha_{mk} z_{jk}\right\}$ and $\mathrm{imag}\left\{\sum_{k=1}^{K} \alpha_{mk} z_{jk}\right\}$ contain both a_{jk} and b_{jk}. This causes difficulty in evaluating (C.4), (C.5), (C.6), (C.7), or (C.8) when the argument for a is $\mathrm{real}\left\{\sum_{k=1}^{K} \alpha_{mk} z_{jk}\right\}$ and the argument for b is $\mathrm{imag}\left\{\sum_{k=1}^{K} \alpha_{mk} z_{jk}\right\}$. For example, when $\boldsymbol{\alpha}$ is real, we can use the chain rule to solve for $\frac{\partial}{\partial a_j k} G(a, b)$ and finally get the same result as (D.2) with an extra factor of α_{mk}. When $\boldsymbol{\alpha}$ is complex, however, (D.2) is no longer suitable, because the new arguments "a" and "b" contain both a_{jk} and b_{jk}, so when we take a derivative with respect to a_{jk}, we have to consider both "a" and "b".

Therefore, we will require a new set of derivatives. Because $\frac{\partial}{\partial a}G_R$ and $\frac{\partial}{\partial a}G_I$ are required for all the second derivatives of the cost function (and we can solve all the first derivatives of the cost function using only these derivatives), we solve for these, rather than $\frac{\partial}{\partial a}G$.

For shorthand, we let

$$\mathrm{real}\{\cdot\} \triangleq \mathrm{real}\left\{\sum_{k=1}^{K} \alpha_{mk} z_{jk}\right\},$$

and

$$\mathrm{imag}\{\cdot\} \triangleq \mathrm{imag}\left\{\sum_{k=1}^{K} \alpha_{mk} z_{jk}\right\},$$

and we recall that

$$|z| = \sqrt{(\sum_{k=1}^{K} a_{jk})^2 + (\sum_{k=1}^{K} b_{jk})^2}.$$

$$\begin{aligned}
\frac{\partial}{\partial a_{jk}} F_R &= \frac{\partial}{\partial a_{jk}} \left(\mathrm{real}\{\cdot\}\, h_R(|z|) - \mathrm{imag}\{\cdot\}\, h_I(|z|)\right) \\
&= \alpha^R_{mk} h_R(|z|) + \alpha^R_{mk} \frac{\mathrm{real}^2\{\cdot\}}{|z|} \dot{h}_R(|z|) \\
&\quad + \alpha^I_{mk} \frac{\mathrm{real}\{\cdot\}\,\mathrm{imag}\{\cdot\}}{|z|} \dot{h}_R(|z|) - \alpha^I_{mk} h_I(|z|) \\
&\quad - \alpha^R_{mk} \frac{\mathrm{real}\{\cdot\}\,\mathrm{imag}\{\cdot\}}{|z|} \dot{h}_I(|z|) \\
&\quad - \alpha^I_{mk} \frac{\mathrm{imag}^2\{\cdot\}}{|z|} \dot{h}_I(|z|).
\end{aligned}$$

This expression is equivalent to the previous expression if $\alpha^I_{mk} = 0$. We can see that α_{mk} no longer factors simply out of these expressions; a naive incorrect application of the chain rule to the previous expressions would yield wrong results. Similar results apply for the other derivatives, shown below.

$$\begin{aligned}
\frac{\partial}{\partial a_{jk}} F_I &= \frac{\partial}{\partial a_{jk}} \left(\mathrm{real}\{\cdot\}\, h_I(|z|) + \mathrm{imag}\{\cdot\}\, h_R(|z|)\right) \\
&= \alpha_{mk}^{R} h_I(|z|) + \alpha_{mk}^{R} \frac{\mathrm{real}^2\{\cdot\}}{|z|} \dot{h}_I(|z|) \\
&\quad + \alpha_{mk}^{I} \frac{\mathrm{real}\{\cdot\}\,\mathrm{imag}\{\cdot\}}{|z|} \dot{h}_I(|z|) + \alpha_{mk}^{I} h_R(|z|) \\
&\quad - \alpha_{mk}^{I} \frac{\mathrm{real}\{\cdot\}\,\mathrm{imag}\{\cdot\}}{|z|} \dot{h}_R(|z|) \\
&\quad + \alpha_{mk}^{R} \frac{\mathrm{real}\{\cdot\}\,\mathrm{imag}\{\cdot\}}{|z|} \dot{h}_R(|z|).
\end{aligned}$$

$$\begin{aligned}
\frac{\partial}{\partial b_{jk}} F_R &= \frac{\partial}{\partial b_{jk}} \left(\mathrm{real}\{\cdot\}\, h_R(|z|) - \mathrm{imag}\{\cdot\}\, h_I(|z|)\right) \\
&= -\alpha_{mk}^{I} h_R(|z|) - \alpha_{mk}^{I} \frac{\mathrm{real}^2\{\cdot\}}{|z|} \dot{h}_R(|z|) \\
&\quad + \alpha_{mk}^{R} \frac{\mathrm{real}\{\cdot\}\,\mathrm{imag}\{\cdot\}}{|z|} \dot{h}_R(|z|) - \alpha_{mk}^{R} h_I(|z|) \\
&\quad + \alpha_{mk}^{I} \frac{\mathrm{real}\{\cdot\}\,\mathrm{imag}\{\cdot\}}{|z|} \dot{h}_I(|z|) \\
&\quad - \alpha_{mk}^{R} \frac{\mathrm{imag}^2\{\cdot\}}{|z|} \dot{h}_I(|z|).
\end{aligned}$$

$$\begin{aligned}
\frac{\partial}{\partial b_{jk}} F_I &= \frac{\partial}{\partial b_{jk}} \left(\mathrm{real}\{\cdot\}\, h_I(|z|) + \mathrm{imag}\{\cdot\}\, h_R(|z|)\right) \\
&= -\alpha_{mk}^{I} h_I - \alpha_{mk}^{I} \frac{\mathrm{real}^2\{\cdot\}}{|z|} \dot{h}_I(|z|) \\
&\quad + \alpha_{mk}^{R} \frac{\mathrm{real}\{\cdot\}\,\mathrm{imag}\{\cdot\}}{|z|} \dot{h}_I(|z|) + \alpha_{mk}^{R} h_R(|z|) \\
&\quad - \alpha_{mk}^{I} \frac{\mathrm{real}\{\cdot\}\,\mathrm{imag}\{\cdot\}}{|z|} \dot{h}_R(|z|) \\
&\quad + \alpha_{mk}^{R} \frac{\mathrm{imag}^2\{\cdot\}}{|z|} \dot{h}_R(|z|).
\end{aligned}$$

The other difficulty with a complex $\boldsymbol{\alpha}$ is deriving a separable quadratic surrogate. We can no longer use the same definition of π_{mk} and finding a valid π_{mk} for this case seems difficult at best. This is a matter for future work.

APPENDIX G

B_1: Spatial Resolution Analysis

We must choose values for the regularization parameter β to use the proposed regularized method. With conventional regularization, this selection requires tedious trial-and-error methods; preferably, values would be selected based on a quantitative measure, such as the amount of smoothing to introduce. Therefore, we analyzed the spatial resolution of the estimated B_1^+ map $\hat{\boldsymbol{z}}$. To simplify the analysis, we focused on the single coil case ($K = 1$) and assumed that f_j is known. Empirically, the spatial resolution of the multi-coil case matched the spatial resolution of the single coil case when we used $M = 2K$ and a uniform object and used the modified penalty described here. This analysis naturally led to a modified penalty design, allowing for a standard selection of β based on desired blur FWHM as well as providing more uniform spatial resolution independent of the particular characteristics of the B_1^+ maps.

The local impulse response of the estimator is equal to the gradient of the estimator multiplied by an impulse The gradient of the estimator has the following form:

$$\begin{aligned}
\nabla \hat{\boldsymbol{z}}(\boldsymbol{y}) &= [\nabla^{[2,0]}\,\Psi(\hat{\boldsymbol{z}}(\boldsymbol{y}),\boldsymbol{y})]^{-1} - \nabla^{[1,1]}\,\Psi(\hat{\boldsymbol{z}}(\boldsymbol{y}),\boldsymbol{y})] \\
&= [\nabla^{[2,0]}L(\boldsymbol{z},\boldsymbol{y}) + \nabla^2 \beta R(\boldsymbol{z})]^{-1} \\
&\quad [-\nabla^{[1,1]}L(\boldsymbol{z},\boldsymbol{y})]|_{z=\hat{z}(y)}, \qquad \text{(G.1)}
\end{aligned}$$

where $\nabla^{[p,q]}\,\Psi$ denotes the pth derivative of Ψ with respect to $\boldsymbol{z}$ and the qth derivative of Ψ with respect to $\boldsymbol{y}$.

The second derivative $\nabla^{[2,0]}L(\boldsymbol{z},\boldsymbol{y})$ introduces varying spatial resolution; this can partially be accounted for through clever choice of the regularizer; therefore, we derive this second derivative.

Because $\boldsymbol{z}$ and $\boldsymbol{y}$ are both complex quantities, for this analysis we treat the real and imaginary part of each as separate variables. We write z_{jks} where j denotes the voxel, k denotes the coil, and s denotes the real or the imaginary part (thus, $\frac{\partial}{\partial s} = \frac{\partial}{\partial a}$ if $s = R$ and $\frac{\partial}{\partial s} = \frac{\partial}{\partial b}$ if $s = I$. Then, the Hessian of L is:

$$[\nabla^{[2,0]}L(\boldsymbol{z},\boldsymbol{y})]_{jks,j'k's'} = \begin{cases} 0 & \text{if } j \neq j' \\ f_j d_{jks;jk's'}(\boldsymbol{z}) & \text{if } j = j' \end{cases}, \tag{G.2}$$

where

$$\begin{aligned} d_{jks;jk's'}(\boldsymbol{z}) \;=\; & \sum_{m=1}^{M} \alpha_{mk}\alpha_{mk'} \\ & \left(\frac{\partial}{\partial s}F_{\mathrm{R}}([\alpha\boldsymbol{z}_j]_m)\frac{\partial}{\partial s'}F_{\mathrm{R}}([\alpha\boldsymbol{z}_j]_m) + \right. \\ & \left. \frac{\partial}{\partial s}F_{\mathrm{I}}([\alpha\boldsymbol{z}_j]_m)\frac{\partial}{\partial s'}F_{\mathrm{I}}([\alpha\boldsymbol{z}_j]_m)\right). \end{aligned} \tag{G.3}$$

For purposes of analysis, we used the mean measurement vector for $\boldsymbol{y}$, *i.e.*

$$\boldsymbol{y} = \bar{\boldsymbol{y}} = f\,F(\mathrm{x}),$$

and then (G.3) has the same form as (C.6), (C.7), and (C.8) using appropriate values for s and accounting for the α_{mk} factors due to the chain rule for differentiation. Similarly, we derived

$$
\begin{aligned}
[\nabla^{[1,1]} L(\mathbf{x}, \boldsymbol{y})]_{jks,j'm's'} &\triangleq \frac{\partial}{\partial z_{jks}} \frac{\partial}{\partial z_{j'k's'}} L(\boldsymbol{z}, \boldsymbol{y}) \\
&= \begin{cases} 0 & \text{if } j \neq j' \\ f_j g_{j,k,s;j',m',s'} & \text{if } j = j' \end{cases}, \qquad \text{(G.4)}
\end{aligned}
$$

where

$$
g_{j,k,s;j',m',s'} = \alpha_{mk} \frac{\partial}{\partial s} F_{s'}([\alpha \boldsymbol{z}]_m) \frac{\partial}{\partial s} F_{s'}(\mathbf{x}_{jm'}), \qquad \text{(G.5)}
$$

again using the mean measurement vector. However, we note that as the regularization term goes to zero, in the limit, then (G.4) times the gradient of the mean measurement vector goes to (G.2) and understanding (G.4) becomes less necessary.

Although the Hessian is not “diagonal”, the diagonal elements are larger than the off-diagonal elements. Therefore, we ignore the off-diagonal elements for the remainder of the analysis.

The resulting spatial resolution for the estimated B_1^+ maps shown in (G.2) is inherently non-uniform. Areas with a low magnitude f_j will be smoothed more because these areas are more influenced by noise; this greater smoothing is desirable. Conversely, areas with a large magnitude, which have a greater degree of data fidelity, are smoothed less. We do not want the median magnitude of f_j to effect the amount of smoothing; therefore, we normalize the data by the median value of f in areas with large signal value (in this paper, greater than 10% of the object maximum using the first-pass estimate of the object) giving the object a median value of 1.

However, the effect of $d_{jks;jk's'}$ seems less desirable. Therefore, we modified our penalty using quadratic penalty design to create more uniform spatial resolution. This approach is based on certainty-based Fisher information approximation [29, 34]. This approach requires an estimate of $\boldsymbol{z}$, which is unknown. Therefore, our first step is to run the proposed algorithm through a few iterations (say, $n = 5$, where n is the number of iterations) to obtain a first-pass initial estimate of $\boldsymbol{z}$. We use a small β for the initial first pass through the algorithm (*e.g.*, we use $\beta = 2^{-10}$ in this paper), to allow a small level of regularization. We then use this initialization to define a "certainty" factor as follows:

$$\kappa_{jks} = \sqrt{d_{jks;jks}(\boldsymbol{z}^{n})}, \tag{G.6}$$

where $\boldsymbol{z}^{(n)}$ is our initial estimate. We note that because κ_{jks} is based on a noisy estimate of $\boldsymbol{z}$, areas where f_j is very small are particular noisy and create unreliable estimates for κ. Therefore, we set these certainty factors in areas with small magnitude (in this paper, less than 10% of the object maximum using the first-pass estimate of the object) to the average value of κ over the rest of the map. Then, we use the following modified penalty function:

$$\mathsf{R}(\boldsymbol{z}_k) = \sum_{j=1}^{N} \sum_{l \in \mathcal{N}_j} \kappa_{jks} \kappa_{lks} (z_{jks} - z_{lks})^2, \tag{G.7}$$

where $\mathcal{N}_j$ is a neighborhood of the jth pixel using second order differences. This creates approximately uniform average spatial resolution if $f_j = 1$. Thus, we eliminate most of the effect of $d_{jks;jk's'}$ from the spatial resolution, while still smoothing more in areas where f_j is small.

Finally, we can now choose β based on the amount of acceptable blur. Assuming that the modified penalty function (G.7) has made $d_{jks;jk's'} \approx 1$, we used the inverse 2D FFT to compute the PSF $\boldsymbol{z}$ and tabulated its FWHM as a function of $\beta / |f_j|$. This graph is shown in Fig 1 of [44]. Given the desired spatial resolution, we can pick the corresponding β for use in the algorithm. The resulting spatial resolution will be inherently non-uniform, with greater smoothing in low signal magnitude areas, effectively "interpolating" across signal voids.

APPENDIX H

B_1/T_1: Derivatives of Signal Models: SSI and AFI

We consider both signals to be real to simplify analysis. We consider the B_1^+ map and the T_1 to be the two unknown variables and use the matrix CRB. For both models, we assume that the same echo time is used for both sequences, and, for the AFI, for both repetition times. We also slightly modify the definition of E_1 and E_2 to accommodate the AFI pulse sequence

$$E_1 = \exp\left(-\frac{T_{R1}}{T_1}\right),$$

and

$$E_2 = \exp\left(-\frac{T_{R2}}{T_1}\right).$$

Then we can express the expectations as:

$$\begin{aligned} -\mathsf{E}\big[\nabla^2_{T_1} \ln \mathsf{p}\big(F_i^{SSI}; b, T_1\big)\big] &= \frac{1}{\sigma^2}\left(\frac{1-\cos(\phi_i)}{1-E_1\cos(\phi_i)}\right)^2 \\ &\quad \cdot \left(\frac{\sin(\phi_i)\, E_1 T_{R1}}{T_1^2\,(1-E_1\cos(\phi_i))}\right)^2 . \end{aligned} \tag{H.1}$$

$$-\mathsf{E}\big[\nabla_{T_1}\nabla_b \ln \mathsf{p}\big(F_i^{SSI}; b, T_1\big)\big] = \frac{-1}{\sigma^2}\frac{\alpha_i(1-E_1)E_1(\cos(\phi_i)-E_1)}{T_1^2(1-E_1\cos(\phi_i))^4} \cdot (1-\cos(\phi_i))\sin(\phi_i)\,T_R. \tag{H.2}$$

$$-\mathsf{E}\big[\nabla_b^2 \ln \mathsf{p}\big(F_i^{SSI}; b, T_1\big)\big] = \frac{1}{\sigma^2}\left(\frac{\alpha_i(1-E_1)}{(1-E_1\cos(\phi_i))^2}\right)^2 (\cos(\phi_i)-E_1)^2\,. \tag{H.3}$$

The relevant expressions for the CRB of the AFI are:

$$\begin{aligned}-\mathsf{E}\big[\nabla_b^2 \ln \mathsf{p}\big(F_{2i-1}^{AFI}; b, T_1\big)\big] = {} & \frac{1}{\sigma^2}\left(\frac{\alpha}{(1-E_1E_2\cos^2(\phi_i))^2}\right)^2 \\ & \Big(\cos(\phi_i)+E_1E_2\cos^3(\phi_i)-E_2\cos(\phi_i) \\ & -E_1E_2^2\cos^3(\phi_i)+2E_2\cos^2(\phi_i)-2E_1E_2\cos^2(\phi_i) \\ & -E_2-E_1E_2^2\cos^2(\phi_i)+E_1E_2 \\ & +E_1^2E_2^2\cos^2(\phi_i)-2E_1E_2\cos(\phi_i)+2E_1E_2^2\cos(\phi_i)\Big)^2,\end{aligned} \tag{H.4}$$

and the expression for F_{2i}^{AFI} just replaces E_1 with E_2 and vice versa.

$$
\begin{aligned}
-\mathsf{E}\big[\nabla_b \nabla_{T_1} \ln \mathsf{p}\big(F_1^{AFI}; b, T_1\big)\big] \quad = \quad & \frac{1}{\sigma^2}\frac{E_2}{T_1^2}\frac{\alpha \sin(\phi_i)}{(1 - E_1E_2\cos^2(\phi_i))^4} \\
& \Bigg(\cos(\phi_i) + E_1E_2\cos^3(\phi_i) - E_2\cos(\phi_i) \\
& - E_1E_2^2\cos^3(\phi_i) + 2E_2\cos^2(\phi_i) - 2E_1E_2\cos^2(\phi_i) \\
& - E_2 - E_1E_2^2\cos^2(\phi_i) + E_1E_2 \\
& + E_1^2E_2^2\cos^2(\phi_i) - 2E_1E_2\cos(\phi_i) + 2E_1E_2^2\cos(\phi_i) \Bigg) \\
& \Bigg(E_1\cos(\phi_i)(T_{R1} + T_{R2})(cos(\phi_i) - 1) \\
& + E_1E_2T_{R1}\cos^2(\phi_i)(cos(\phi_i) - 1) \\
& - T_{R2} + T_{R2}\cos(\theta) \Bigg).
\end{aligned} \tag{H.5}
$$

$$
\begin{aligned}
-\mathsf{E}\big[\nabla_{T_1}^2 \ln \mathsf{p}\big(F_{2i-1}^{AFI}; b, T_1\big)\big] \quad = \quad & \frac{1}{\sigma^2}\left(\frac{\sin(\phi_i)}{(1 - E_1E_2\cos^2(\phi_i))^2}\right)^2 \left(\frac{E_2}{T_1^2}\right)^2 \\
& \Bigg(E_1\cos(\phi_i)(T_{R1} + T_{R2})(cos(\phi_i) - 1) \\
& + E_1E_2T_{R1}\cos^2(\phi_i)(cos(\phi_i) - 1) \\
& - T_{R2} + T_{R2}\cos(\phi_i) \Bigg)^2.
\end{aligned} \tag{H.6}
$$

APPENDIX I

B_1^+,T_1: Derivation of cost function gradients

This section first considers a simplified version of the B_1^+ and T_1 map cost function and its gradient. Any gradient-based algorithm uses the first derivative of the cost function. Next, we apply the results to our cost function (6.19). The equations in this section rely heavily on derivatives of the function F which are derived (in terms of derivatives of H) in Appendix J (and are very similar to those in Appendix C with the addition of a third parameter for T_1).

First, consider a simple (one voxel, one measurement) version of (6.20). We can rewrite (6.20) as follows:

$$\begin{aligned}
\tilde{L}(\boldsymbol{z}, t, f) &= l\left(y, t, f, \mathrm{real}\left\{\sum_{k=1}^{K} \alpha_k z_k\right\}, \mathrm{imag}\left\{\sum_{k=1}^{K} \alpha_k z_k\right\}\right) \\
l(y, t, f, a, b) &\triangleq \frac{1}{2}\left|y - fG(a, b, t)\right|^2 \\
G(a, b, t) &\triangleq F(a + ib, t) = G_R(a, b, t) + iG_I(a, b, t), \qquad \text{(I.1)}
\end{aligned}$$

where $\boldsymbol{z} = (z_1, \ldots, z_K)$.

We simplify $l(\cdot)$ by ignoring terms independent of the unknown variables a or b (and recalling that f is constrained to be real):

$$\begin{aligned} l(y,t,f,a,b) &\triangleq -\operatorname{real}\{y\}\operatorname{real}\{fG(a,b,t)\} \\ &\quad -\operatorname{imag}\{y\}\operatorname{imag}\{fG(a,b,t)\} \\ &\quad +\frac{1}{2}|f|^2|G(a,b,t)|^2 . \end{aligned} \tag{I.2}$$

$$\begin{aligned} l(y,t,f,a,b) &\equiv -y_R f G_R(a,b,t) - y_I f G_I(a,b,t) \\ &\quad +\frac{1}{2}f^2|G(a,b,t)|^2 . \end{aligned} \tag{I.3}$$

The derivative of l with respect to the unknown variable a is:

$$\begin{aligned} \frac{\partial}{\partial a}l &= -y_R f \frac{\partial}{\partial a}G_R(a,b,t) - y_I f \frac{\partial}{\partial a}G_I(a,b,t) \\ &\quad +f^2 G_R(a,b,t)\frac{\partial}{\partial a}G_R(a,b,t) \\ &\quad +f^2 G_I(a,b,t)\frac{\partial}{\partial a}G_I(a,b,t) \\ &= -f(y_R - fG_R(a,b,t))\frac{\partial}{\partial a}G_R(a,b,t) \\ &\quad -f(y_I - fG_I(a,b,t))\frac{\partial}{\partial a}G_I(a,b,t) \\ &= -f(y_R - fG_R(a,b,t))\frac{\partial}{\partial a}G_R(a,b,t) \\ &\quad +if(y_I - fG_I(a,b,t))i\frac{\partial}{\partial a}G_I(a,b,t) \\ &= -f\operatorname{real}\left\{(y - fG(a,b,t))^* \frac{\partial}{\partial a}G(a,b,t)\right\} . \end{aligned} \tag{I.4}$$

Similarly, the derivative with respect to b is:

$$\begin{aligned}\frac{\partial}{\partial b} l &= -y_R f \frac{\partial}{\partial b} G_R(a,b,t) - y_I f \frac{\partial}{\partial b} G_I(a,b,t) \\ &\quad + |f|^2 G_R(a,b,t) \frac{\partial}{\partial b} G_R(a,b,t) \\ &\quad + |f|^2 G_I(a,b,t) \frac{\partial}{\partial b} G_I(a,b,t) \\ &= -f \,\mathrm{real}\left\{ (y - fG(a,b,t))^* \frac{\partial}{\partial b} G(a,b,t) \right\}. \end{aligned} \tag{I.5}$$

Similarly, the derivative with respect to t is:

$$\begin{aligned}\frac{\partial}{\partial t} l &= -y_R f \frac{\partial}{\partial t} G_R(a,b,t) - y_I f \frac{\partial}{\partial t} G_I(a,b,t) \\ &\quad + |f|^2 G_R(a,b,t) \frac{\partial}{\partial t} G_R(a,b,t) \\ &\quad + |f|^2 G_I(a,b,t) \frac{\partial}{\partial t} G_I(a,b,t) \\ &= -f \,\mathrm{real}\left\{ (y - fG(a,b,t))^* \frac{\partial}{\partial t} G(a,b,t) \right\}. \end{aligned} \tag{I.6}$$

When regularizing the object, the derivative with respect to f is needed. The derivative is:

$$\frac{\partial}{\partial f} l = -y_R G_R(a,b,t) - y_I G_I(a,b,t) + |f|\,|G(a,b,t)|^2 . \tag{I.7}$$

.

We also include the second derivatives for use in a Hessian calculation (for example, for a preconditioner for gradient descent algorithms, although not currently implemented in the algorithm). The second derivative of l with respect to the unknown variable a is:

$$\begin{aligned}\frac{\partial^2}{\partial a^2} l &= -f(y_R - fG_R(a,b,t)) \frac{\partial^2}{\partial a^2} G_R(a,b,t) \\ &\quad - f(y_I - fG_I(a,b,t)) \frac{\partial^2}{\partial a^2} G_I(a,b,t) \\ &\quad + |f|^2 \left(\left(\frac{\partial}{\partial a} G_R(a,b,t) \right)^2 + \left(\frac{\partial}{\partial a} G_I(a,b,t) \right)^2 \right). \end{aligned} \tag{I.8}$$

Similarly, the second derivative of l with respect to the unknown variable b is:

$$\begin{aligned}\frac{\partial^2}{\partial b^2}l &= -f(y_R - fG_R(a,b,t))\frac{\partial^2}{\partial b^2}G_R(a,b,t) \\ &\quad -f(y_I - fG_I(a,b,t))\frac{\partial^2}{\partial b^2}G_I(a,b,t) \\ &\quad +|f|^2\left(\left(\frac{\partial}{\partial b}G_R(a,b,t)\right)^2 + \left(\frac{\partial}{\partial b}G_I(a,b,t)\right)^2\right).\end{aligned} \tag{I.9}$$

The second derivative of l with respect to the unknown variable t is:

$$\begin{aligned}\frac{\partial^2}{\partial t^2}l &= -f(y_R - fG_R(a,b,t))\frac{\partial^2}{\partial t^2}G_R(a,b,t) \\ &\quad -f(y_I - fG_I(a,b,t))\frac{\partial^2}{\partial t^2}G_I(a,b,t) \\ &\quad +|f|^2\left(\left(\frac{\partial}{\partial t}G_R(a,b,t)\right)^2 + \left(\frac{\partial}{\partial t}G_I(a,b,t)\right)^2\right).\end{aligned} \tag{I.10}$$

The second derivative of l with respect to the unknown variable f is:

$$\frac{\partial^2}{\partial f^2}l = |G(a,b,t)|^2. \tag{I.11}$$

APPENDIX J

B_1^+, T_1: Derivatives of F

This section derives the derivatives of F in terms of H and its derivatives, which are tabulated (when using a non-ideal slice profile or incorporating B_0 field inhomogeneity) or explicitly derived (assuming an ideal sinc profile as the experiments in this thesis) as explained in Section 6.5.1.

To simplify the derivations, we use an equivalent definition for F. We define $z = a + ib$ and rewrite (6.26) as follows:

$$\begin{aligned} F(z,t) &= \mathrm{e}^{\imath \angle z} H(\sqrt{a^2+b^2}, t) \\ &= \left(\frac{a}{\sqrt{a^2+b^2}} + \frac{ib}{\sqrt{a^2+b^2}} \right) H(\sqrt{a^2+b^2}, t). \end{aligned}$$

The final line follows from using Euler's formula for $\mathrm{e}^{\imath \angle z}$ and expressing $\cos$ and $\sin$ using the Pythagorean Theorem.

Then,

$$\begin{aligned} F_R(a,b,t) &= \frac{a}{\sqrt{a^2+b^2}} H_R(\sqrt{a^2+b^2}, t) - \frac{b}{\sqrt{a^2+b^2}} H_I(\sqrt{a^2+b^2}, t) \\ F_I(a,b,t) &= \frac{b}{\sqrt{a^2+b^2}} H_R(\sqrt{a^2+b^2}, t) + \frac{a}{\sqrt{a^2+b^2}} H_I(\sqrt{a^2+b^2}, t). \end{aligned}$$

Using these equations, we can then find the derivatives

$$
\begin{aligned}
\frac{d}{da}F_R(a,b,t) &= \frac{1}{|z|}H_R(|z|\,,t) - \frac{a^2}{|z|^2}H_R(|z|\,,t) + \frac{a^2}{|z|^2}\nabla^{[10]}H_R(|z|\,,t) \\
&\quad + \frac{ab}{|z|^2}H_I(|z|\,,t) - \frac{ab}{|z|^2}\nabla^{[10]}H_I(|z|\,,t) \\
\frac{d}{db}F_R(a,b,t) &= \frac{-1}{|z|}H_I(|z|\,,t) - \frac{ab}{|z|^2}H_R(|z|\,,t) + \frac{ab}{|z|^2}\nabla^{[10]}H_R(|z|\,,t) \\
&\quad + \frac{b^2}{|z|^2}H_I(|z|\,,t) - \frac{b^2}{|z|^2}\nabla^{[10]}H_I(|z|\,,t) \\
\frac{d}{da}F_I(a,b,t) &= \frac{1}{|z|}H_I(|z|\,,t) - \frac{a^2}{|z|^2}H_I(|z|\,,t) + \frac{a^2}{|z|^2}\nabla^{[10]}H_I(|z|\,,t) \\
&\quad - \frac{ab}{|z|^2}H_R(|z|\,,t) + \frac{ab}{|z|^2}\nabla^{[10]}H_R(|z|\,,t) \\
\frac{d}{db}F_I(a,b,t) &= \frac{1}{|z|}H_R(|z|\,,t) - \frac{ab}{|z|^2}H_I(|z|\,,t) + \frac{ab}{|z|^2}\nabla^{[10]}H_I(|z|\,,t) \\
&\quad - \frac{b^2}{|z|^2}H_R(|z|\,,t) + \frac{b^2}{|z|^2}\nabla^{[10]}H_R(|z|\,,t) \\
\frac{d}{dt}F_R(a,b,t) &= \cos(\angle\boldsymbol{z})\,\nabla^{[01]}H_R(|z|\,,t) - \sin(\angle\boldsymbol{z})\,\nabla^{[01]}H_I(|z|\,,t) \\
&= \Re\left(\exp(i\angle\boldsymbol{z})\,\nabla^{[01]}H(|z|\,,t)\right) \\
\frac{d}{dt}F_I(a,b,t) &= \cos(\angle\boldsymbol{z})\,\nabla^{[01]}H_I(|z|\,,t) + \sin(\angle\boldsymbol{z})\,\nabla^{[01]}H_R(|z|\,,t) \\
&= \Im\left(\exp(i\angle\boldsymbol{z})\,\nabla^{[01]}H(|z|\,,t)\right).
\end{aligned}
$$

APPENDIX K

B_1^+, T_1: Initial estimate for B_1^+, T_1, and $\boldsymbol{f}$

The algorithm requires a good initial estimate for B_1^+ and T_1 to ensure the iterates descends to a good local minimum. We need an initial estimate for the magnitude and phase of the B_1^+ maps, the T_1 map, and the object.

Simple approach - Assume $TR = \infty$

We note that the standard approach for T_1 estimation (based on (6.14) assumes that the flip angle (and thus, the B_1^+ map) is known. Then, T_1 is estimated from the data using a transformation of the points and using a least-squares fit. Therefore, one approach to joint initial estimates is finding a good B_1^+ estimate and then use the standard T_1 estimate and use (6.24) to estimate the object. One obvious choice is assuming that $TR = \infty$ and using the standard double angle method using for estimating the magnitude of B_1^+. We use a method of moments estimator for the phase of B_1^+:

$$\widehat{\angle x_{jm}} = \angle y_{jm} - \angle H\left(\widehat{|x_{jm}|}, \boldsymbol{T}_j\right), \tag{K.1}$$

using our estimate of $|x_{jm}|$, where $\mathbf{x}_m$ are the composite maps (6.25). (Note that H is defined in (6.26).) Empirically, we found that while the phase B_1^+ maps are of sufficiently good quality, the magnitude B_1^+ maps, assuming an infinite repetition time, can be greatly improved.

An improvement over this method is using the regularized B_1^+ estimates from Chapter V with a small number of iterations. Generally, the more initial estimates introduced later in this appendix are based on our improved model and therefore perform better. However, with a low SNR, especially when only one coil is “on” at a time as in OAAT, the regularized B_1^+ estimate is more robust to noise and can work quite well. This method also has the advantage of only requiring $M = 2 * K$, though all estimates show the T_1 effects. One option is generating both the more complicated initial estimates as well as the simple B_1^+ estimate described above and choosing the one with less error compared to the measured data.

Triple angle method for multiple tip angles and constant TR

For our joint B_1^+/T_1 estimation, we used the following initialization when the TR is constant and there is a wide range of tip angles (see examples in Section 6.6.1). First, we write the simplified SSI signal model as:

$$S_i = A \sin \alpha_i b \frac{1 - X}{1 - \cos \alpha_i b X}, \tag{K.2}$$

where

$$X = \exp\left(-\frac{TR}{T_1}\right),$$

and

$$T_1 = \frac{-TR}{\log X}.$$

Similar to the double angle method (5.1) and (5.2), we require three signals such that

$$\begin{aligned} \alpha_2 &= 2\alpha_1 \\ \alpha_3 &= 3\alpha_1. \end{aligned}$$

Therefore, this method requires at least $M = 3 * K$. If we let $c \triangleq \cos(\alpha_1 b)$, using the double and triple angle trigonometric identities, then

$$\begin{aligned}
\cos(\alpha_2 b) &= 2c^2 - 1 \\
\cos(\alpha_3 b) &= 4c^3 - 3c \\
\sin(\alpha_1 b) &= \sqrt{1 - c^2} \\
\sin(\alpha_2 b) &= 2c\sqrt{1 - c^2} \\
\sin(\alpha_3 b) &= 3\sqrt{1 - c^2} - 4\left(\sqrt{1 - c^2}\right)^3 .
\end{aligned}$$

We then define the following ratios

$$\begin{aligned}
z_2 &= \frac{|S_2|}{|S_1|} \\
&= \frac{\sin(\alpha_2 b)}{\sin(\alpha_1 b)} \cdot \frac{1 - \cos(\alpha_1 b)\, X}{1 - \cos(\alpha_2 b)\, X} \\
&= \frac{2c(1 - cX)}{1 - (2c^2 - 1)X} \qquad \text{(K.3)}
\end{aligned}$$

and

$$\begin{aligned}
z_3 &= \frac{|S_3|}{|S_1|} \\
&= \frac{\sin(\alpha_3 b)}{\sin(\alpha_1 b)} \cdot \frac{1 - \cos(\alpha_1 b)\, X}{1 - \cos(\alpha_3 b)\, X} \\
&= (3 - 4(1 - c^2)) \cdot \frac{1 - cX}{1 - (4c^3 - 3c)X} . \qquad \text{(K.4)}
\end{aligned}$$

Then, we solve z_2 for X:

$$X = \frac{z_2 - 2c}{z_2(2c^2 - 1) - 2c^2} . \qquad \text{(K.5)}$$

Using this solution for X, we can solve for c with equation z_3 (using MATLAB's root, for example) solving the following equation:

$$\begin{aligned} 0 &= (8(z_3 - z_2) - 16)\, c^4 + (4z_2(1 - z_3))\, c^3 + (-8z_3 + 2z_2z_3 + 6z_2 + 4)\, c^2 \\ &\quad + (3z_2z_3 - z_2)\, c - z_2z_3 - z_2. \end{aligned} \tag{K.6}$$

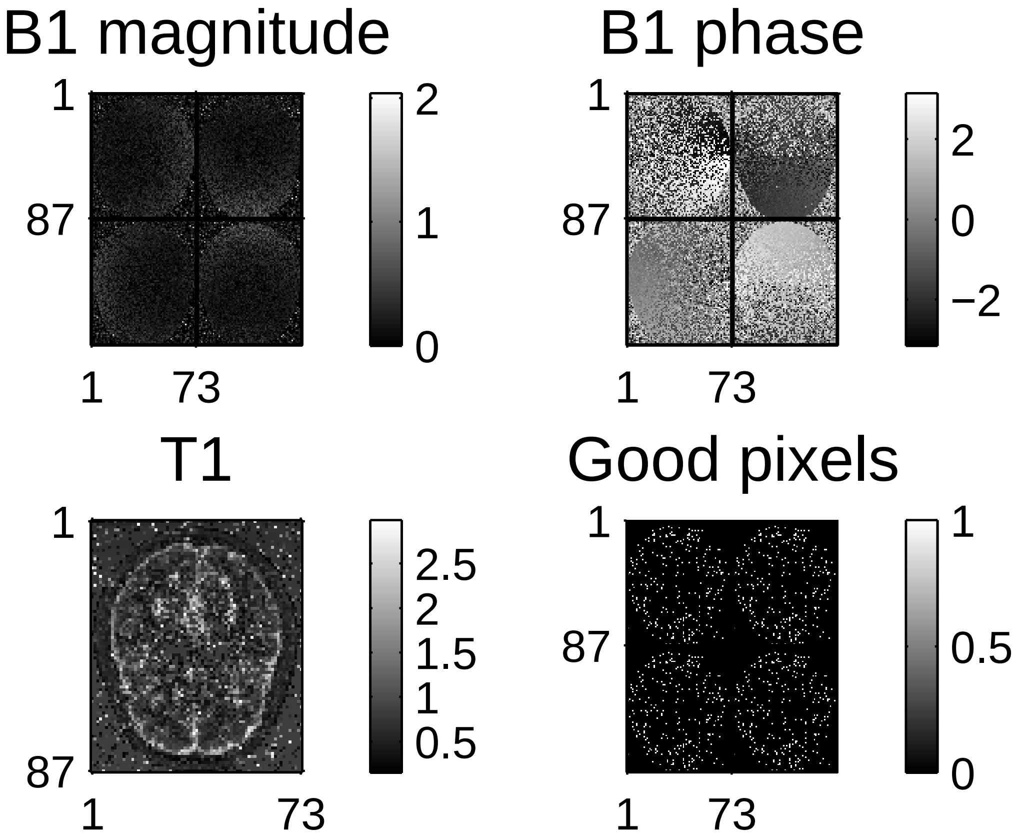

Figure K.1: Intermediate initial maps using triple angle method. Top: left: $|b|$ right: $\angle b$ Bottom: left: $\boldsymbol{T}$ right: $\boldsymbol{f}$. Data using LOO method at an SNR of 60 as in Section 6.6.1 using the true maps shown in Fig. 6.26.

We solve for c, and thus the magnitude of B_1^+ map, on a pixel-by-pixel basis. We preferentially choose those pixels with real roots such that $|c| \leq 1$ and the associated value of X (K.5) such that $0 < X < 1$. We also restrict the selection of this pixels to pixels where the magnitude of the data is sufficiently high. We then combine this magnitude B_1^+ map with the B_1^+ angle (K.1). An example of these interim maps is shown in Fig. K.1. Using the complex B_1^+ map values at the preferred pixels, we fit a two-dimensional polynomial function over the entire object (in this thesis, we use a fourth degree polynomial) for both the real and imaginary values of B_1^+. (We note that fitting instead to the magnitude and phase of B_1^+ would require meeting the constraint that $|b| \geq 0$.)

Finally, we use this new fitted B_1^+ map and (K.5) to get our initial estimate of T_1. This does seem susceptible to noise when the SNR is low (*e.g.*, around 30) but produces very good estimates with low noise and is used for the simulations. The final initial maps for this example are shown in Section 6.6.1 in Fig. 6.32, Fig. 6.33, Fig. 6.34, and Fig. 6.35.

Method when TR is varied

When we use the same flip angle for each measurement and instead vary the repetition time TR, neither of the above initializations apply. Here is another possible initialization method that we used with the phantom data described in Section 6.6.2. This method works when we have a good estimate of the T_1 map. In the phantom data, we knew that T_1 was roughly constant over the object and the approximate value ($\boldsymbol{T} = 1$ ms for the phantom used in this thesis). With this information, we fit, voxel by voxel, B_1^+ using the SSI model (6.27) assuming that T_1 is known and fixed by minimizing the norm of the difference (for example, using MATLAB's fminsearch). For the first set of phantom data, this initial B_1^+ is shown in Fig. K.2. We estimate the phase of B_1^+ using (K.1). By normalizing the data with respect to a reference image, we also calculated $\boldsymbol{f}$ over the object and set $\boldsymbol{f}$ to a constant value equal to its estimated mean.

When a combination of coils is used, we estimate the B_1^+ maps for the composite maps (5.8). One option is using these maps to estimate the composite maps and then finally solve for the individual maps at the end. This may not be desirable when there are coil cancellations. Another option is immediately estimating the individual coils

As in the triple angle method, we improve the initial B_1^+ map estimate by fitting a fourth order polynomial to weighted $|b|$ values inside the object (the weights inversely

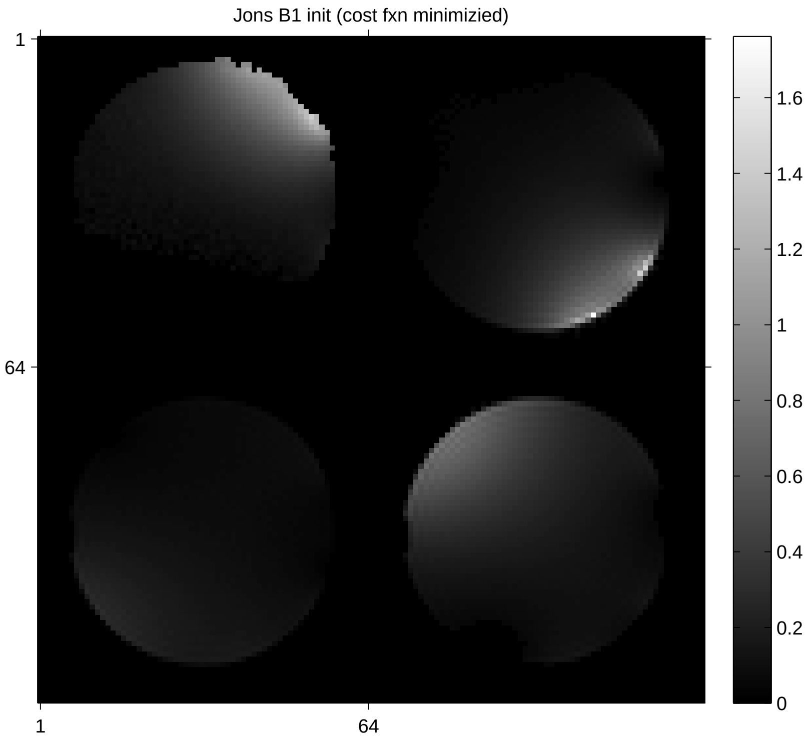

Figure K.2: Intermediate initial B_1^+ map when TR is varied. Initial OAAT phantom experiment B_1^+ estimate assuming known T_1.

proportional to the error of the data as measured between the measured magnitude data and the current estimated magnitude data). These initial estimates are shown in Fig. 6.45 for the first phantom experiment.

From the improved complex B_1^+ map estimate, we calculated an improved T_1 map estimate using the standard T_1 estimate and an improved $\boldsymbol{f}$ map estimate using (6.24).

APPENDIX L

B_1^+, T_1: Spatial Resolution Analysis

We must choose values for the regularization parameters β to use the proposed regularized method. With conventional regularization, this selection requires tedious trial-and-error methods; preferably, values would be selected based on a quantitative measure, such as the amount of smoothing to introduce.

Therefore, we analyzed the spatial resolution of the estimated B_1^+ map $\hat{\boldsymbol{z}}$ and T_1 map $\hat{\boldsymbol{T}}$ and the $\boldsymbol{f}$ $\hat{\boldsymbol{f}}$.

To simplify the analysis, we focused on the single coil case ($K = 1$). For B_1^+ map estimation, we assumed that f_j and $\boldsymbol{T}$ are known and fixed; for T_1 map estimation, we assumed that f_j and b are known and fixed. Empirically, the spatial resolution of the multi-coil case matched the spatial resolution of the single coil case when we used $M = 4K$ and a uniform object and used the modified penalty described here. This analysis naturally led to a modified penalty design, allowing for a standard selection of β based on desired blur FWHM as well as providing more uniform spatial resolution independent of the particular characteristics of the B_1^+ maps. Without this analysis, in conventional regularization each map would have (possibly drastically) different spatial resolution when using the same β. The goal of this analysis is that, when using the same β, an impulse added to the true map will result in a certain full-width half-maximum in the final estimated map.

The local impulse response of the estimator is equal to the gradient of the estimator multiplied by an impulse. The gradient of the estimator has the following general form (where $\boldsymbol{y}$ is the data and $\boldsymbol{z}$ is the variable):

$$\begin{aligned}
\boldsymbol{\nabla}\hat{\boldsymbol{z}}(\boldsymbol{y}) &= [\nabla^{[2,0]}\,\Psi(\hat{\boldsymbol{z}}(\boldsymbol{y}),\boldsymbol{y})]^{-1} - \nabla^{[1,1]}\,\Psi(\hat{\boldsymbol{z}}(\boldsymbol{y}),\boldsymbol{y})] \\
&= [\nabla^{[2,0]}L(\boldsymbol{z},\boldsymbol{y}) + \nabla^2\beta R(\boldsymbol{z})]^{-1} \\
&\ [-\nabla^{[1,1]}L(\boldsymbol{z},\boldsymbol{y})]|_{z=\hat{z}(y)},
\end{aligned} \tag{L.1}$$

where $\nabla^{[p,q]}\,\Psi$ denotes the pth derivative of Ψ with respect to $\boldsymbol{z}$ and the qth derivative of Ψ with respect to $\boldsymbol{y}$.

The second derivative $\nabla^{[2,0]}L(\boldsymbol{z},\boldsymbol{y})$ introduces varying spatial resolution; this can partially be accounted for through clever choice of the regularizer; therefore, we derive this second derivative.

First, we consider the spatial resolution of the B_1^+ map $\boldsymbol{z}$. Because $\boldsymbol{z}$ and $\boldsymbol{y}$ are both complex quantities, for this analysis we treat the real and imaginary part of each as separate variables. We write z_{jks} where j denotes the voxel, k denotes the coil, and s denotes the real or the imaginary part (thus, $\frac{\partial}{\partial s} = \frac{\partial}{\partial a}$ if $s = R$ and $\frac{\partial}{\partial s} = \frac{\partial}{\partial b}$ if $s = I$). Then, the Hessian of L is:

$$[\nabla^{[2,0]}L(\boldsymbol{z},\boldsymbol{y})]_{jks,j'k's'} = \begin{cases} 0 & \text{if } j \neq j' \\ f_j d_{jks;jk's'}(\boldsymbol{z}) & \text{if } j = j' \end{cases}, \tag{L.2}$$

where

$$\begin{aligned}
d_{jks;jk's'}(\boldsymbol{z}) &= \sum_{m=1}^{M} \alpha_{mk}\alpha_{mk'} \\
&\ \left(\frac{\partial}{\partial s}F_{\mathrm{R}}([\alpha\boldsymbol{z}_j]_m,t_j)\frac{\partial}{\partial s'}F_{\mathrm{R}}([\alpha\boldsymbol{z}_j]_m,t_j) + \right. \\
&\ \left. \frac{\partial}{\partial s}F_{\mathrm{I}}([\alpha\boldsymbol{z}_j]_m,t_j)\frac{\partial}{\partial s'}F_{\mathrm{I}}([\alpha\boldsymbol{z}_j]_m,t_j)\right).
\end{aligned} \tag{L.3}$$

For purposes of analysis, we used the mean measurement vector for $\boldsymbol{y}$, *i.e.*

$$\boldsymbol{y} = \bar{\boldsymbol{y}} = f\,F(\mathbf{x}, t),$$

and then (L.3) has the same form as (I.8) and (I.9). using appropriate values for s and accounting for the α_{mk} factors due to the chain rule for differentiation. Similarly, we derived

$$\begin{aligned}[\nabla^{[1,1]} L(\mathbf{x}, \boldsymbol{y})]_{jks,j'm's'} &\triangleq \frac{\partial}{\partial z_{jks}} \frac{\partial}{\partial z_{j'k's'}} L(\boldsymbol{z}, \boldsymbol{y}) \\ &= \begin{cases} 0 & \text{if } j \neq j' \\ f_j g_{j,k,s;j',m',s'} & \text{if } j = j' \end{cases}, \end{aligned} \tag{L.4}$$

where

$$g_{j,k,s;j',m',s'} = \alpha_{mk} \frac{\partial}{\partial s} F_{s'}([\alpha \boldsymbol{z}_j]_m, t_j) \frac{\partial}{\partial s} F_{s'}([\alpha \boldsymbol{z}_j]_{m'}, t_j), \tag{L.5}$$

again using the mean measurement vector. However, we note that as the regularization term goes to zero, in the limit, then (L.4) times the gradient of the mean measurement vector goes to (L.2) and understanding (L.4) becomes less necessary.

We repeated this analysis for an unknown T_1 map $\hat{\boldsymbol{T}}$ with a known B_1^+ map $\boldsymbol{z}$ and object $\boldsymbol{f}$. Now, the Hessian of L is:

$$[\nabla^{[2,0]} L(\boldsymbol{T}, \boldsymbol{y})]_{j,j'} = \begin{cases} 0 & \text{if } j \neq j' \\ f_j^2 d_{j;j}(\boldsymbol{z}) & \text{if } j = j' \end{cases}, \tag{L.6}$$

where

$$\begin{aligned} d_{j;j}(\boldsymbol{z}) &= \sum_{m=1}^{M} \left(\frac{\partial}{\partial t} F_{\mathrm{R}} \left([\alpha \boldsymbol{z}_j]_m, t_j \right) \right)^2 + \\ &\quad \left(\frac{\partial}{\partial t} F_{\mathrm{I}} \left([\alpha \boldsymbol{z}_j]_m, t_j \right) \right)^2 . \end{aligned} \tag{L.7}$$

We note that the variable transformation of $\boldsymbol{T}$ slightly modifies this equation as explained in Section M.

We repeated this analysis for an unknown object map (assuming that we are regularizing the object) $\hat{\boldsymbol{f}}$ with a known T_1 map $\boldsymbol{T}$ and B_1^+ map $\boldsymbol{z}$. Now, the Hessian of L is:

$$[\nabla^{[2,0]} L(\boldsymbol{f}, \boldsymbol{y})]_{j,j'} \begin{cases} 0 & \text{if } j \neq j' \\ r_{j,j}(\boldsymbol{z}) & \text{if } j = j' \end{cases}, \tag{L.8}$$

where

$$\begin{aligned} r_{j;j}(\boldsymbol{z}) \;&=\; \sum_{m=1}^{M} \left(F_{\mathrm{R}}\left([\alpha \boldsymbol{z}_j]_m, t_j\right)\right)^2 + \\ &\;\; \left(F_{\mathrm{I}}\left([\alpha \boldsymbol{z}_j]_m, t_j\right)\right)^2 . \end{aligned} \tag{L.9}$$

Although these Hessians are not “diagonal”, the diagonal elements are larger than the off-diagonal elements. Therefore, we ignore the off-diagonal elements for the remainder of the analysis.

The resulting spatial resolution for the estimated maps shown in (L.2), (L.6), and (L.8) is inherently non-uniform. Areas with a low magnitude f_j will be smoothed more because these areas are more influenced by noise; this greater smoothing is desirable. Conversely, areas with a large magnitude, which have a greater degree of data fidelity, are smoothed less. We do not want the median magnitude of f_j to effect the amount of smoothing; therefore, we normalize the data by the median value of f in areas with large signal value (in this paper, greater than 10% of the object maximum using the first-pass estimate of the object) giving the object a median value of 1.

However, the effect of $d_{jks;jk's'}$ and $d_{j,j}$ and $r_{j,j}$ seems less desirable. Therefore, we modified our penalties using quadratic penalty design to create more uniform spatial resolution. This approach is based on certainty-based Fisher information approximation [29, 34]. This approach requires an estimate of b or $\boldsymbol{T}$ or $\boldsymbol{f}$, which is unknown. One option is is to run the proposed algorithm through a few iterations (say, $n = 5$, where n is the number of iterations) to obtain a first-pass initial estimate of $\boldsymbol{z}$ and $\boldsymbol{T}$. and then use a small β for the initial first pass through the algorithm (*e.g.*, $\beta = 2^{-10}$), to allow a small level of regularization. A second option is to use the initial values of $\boldsymbol{z}$ or $\boldsymbol{T}$ used for the algorithm; we found the estimates described in Appendix K were sufficiently accurate to use to calculate an improved regularization scheme.

We then use these estimates to define a "certainty" factor as follows:

$$\kappa^{\boldsymbol{z}}_{jks} = \sqrt{d_{jks;jks}(\boldsymbol{z}^n)}, \tag{L.10}$$

and

$$\kappa^{\boldsymbol{T}}_{j} = \sqrt{d_{j;j}(\boldsymbol{T}^n)}, \tag{L.11}$$

and

$$\kappa^{\boldsymbol{f}}_{r} = \sqrt{r_{j;j}(f^n_j)}, \tag{L.12}$$

where $\boldsymbol{z}^{(n)}$ and $\boldsymbol{T}^{(n)}$ are our initial estimates. We note that because $\kappa^{\boldsymbol{z}}_{jks}$ and $\kappa^{\boldsymbol{T}}_{j}$ and $\kappa^{\boldsymbol{f}}_{r}$ are based on a noisy estimate of $\boldsymbol{z}$ or $\boldsymbol{T}$ or $\boldsymbol{f}$, areas where f_j is very small are particular noisy and create unreliable estimates for $\kappa^{\boldsymbol{z}}$ and $\kappa^{\boldsymbol{T}}$ and κ^{f_j}. Therefore, we set these certainty factors in areas with small magnitude (in this paper, less than 10% of the object maximum using the first-pass estimate of the object) to the average value of κ over the rest of the map. Then, we use the following modified penalty function:

$$\mathsf{R}(\boldsymbol{z}_k) = \sum_{j=1}^{N} \sum_{l \in \mathcal{N}_j} \kappa^{\boldsymbol{z}}_{jks} \kappa^{\boldsymbol{z}}_{lks} (z_{jks} - z_{lks})^2, \tag{L.13}$$

and

$$\mathsf{R}(\boldsymbol{T}) = \sum_{j=1}^{N} \sum_{l \in \mathcal{N}_j} \kappa_j^{\boldsymbol{T}} \kappa_l^{\boldsymbol{T}} (\boldsymbol{T}_j - \boldsymbol{T}_l)^2, \tag{L.14}$$

and

$$\mathsf{R}(f_j) = \sum_{j=1}^{N} \sum_{lin \mathcal{N}_j} \kappa_r^{\boldsymbol{T}} \kappa_l^{\boldsymbol{f}} (\boldsymbol{f}_j - \boldsymbol{f}_l)^2, \tag{L.15}$$

where $\mathcal{N}_j$ is a neighborhood of the jth pixel using second order differences. This creates approximately uniform average spatial resolution if $f_j = 1$ and assuming quadratic regularization. When tested under these assumptions, spatial resolution is quite uniform for B_1^+. Using the improved penalty (L.14) for T_1 (with quadratic regularization and a test T_1 with blocks of varying T_1 values) still results in some spatial resolution variation but is more uniform and predictable than the original penalty. However, when all other variables are known and kept constant, the improved penalty gives much more uniform spatial resolution. Thus, using the improved penalties (L.13) and (L.14) we eliminate most of the effect of $d_{jks;jk's'}$ and $d_{j,j}$ from the spatial resolution, while still smoothing more in areas where f_j is small.

Finally, we can now choose β based on the amount of acceptable blur. Assuming that the modified penalty function (L.13) has made $d_{jks;jk's'} \approx 1$ and (L.14) has made $d_{j;j} \approx 1$ and (L.15) has made $r_{j;j} \approx 1$, we can chose a FWHM as a function of $\beta / |f_j|$ based on the graph shown in Fig. 4.1. Given the desired spatial resolution, we can pick the corresponding β for use in the algorithm. The resulting spatial resolution will be inherently non-uniform, with greater smoothing in low signal magnitude areas, effectively "interpolating" across signal voids.

APPENDIX M

B_1^+, T_1: Constrained estimation for T_1

T_1 is physically constrained to be positive. Therefore, we wish to constrain

$$0 \leq \boldsymbol{T} < \boldsymbol{T}_{MAX},$$

where we let $\boldsymbol{T}_{MAX}$ be equal to the maximum value of T_1 we could physically expect in the field of view. In this paper, we set $\boldsymbol{T}_{MAX} = 3$ s. To enforce these constraints, we let $\boldsymbol{T} = \Gamma(\varsigma)$ where we chose Γ to be the sigmoid function

$$\Gamma(\varsigma) = \frac{\boldsymbol{T}_{MAX}}{1 + \exp(-\varsigma)}. \tag{M.1}$$

We then estimate the new variable ς. The cost function (6.19) becomes

$$\begin{aligned} (\hat{\boldsymbol{z}}, \hat{\boldsymbol{T}}, \hat{\boldsymbol{f}}) &= \underset{\boldsymbol{z}, \boldsymbol{T}: 0 < \boldsymbol{T}_j < \boldsymbol{T}_{MAX}, \boldsymbol{f}}{\arg\min} \Psi(\boldsymbol{z}, \boldsymbol{T}, \boldsymbol{f}), \\ (\hat{\boldsymbol{z}}, \hat{\varsigma}, \hat{\boldsymbol{f}}) &= \underset{\boldsymbol{z}, \varsigma, \boldsymbol{f}}{\arg\min} \tilde{\Psi}(\boldsymbol{z}, \varsigma, \boldsymbol{f}), \\ \tilde{\Psi}(\boldsymbol{z}, \varsigma, \boldsymbol{f}) &= L(\boldsymbol{z}, \Gamma(\varsigma), \boldsymbol{f}) + \beta_{\boldsymbol{z}} R(\boldsymbol{z}) + \beta_{\varsigma} R(\varsigma). \end{aligned} \tag{M.2}$$

Finally, we let $\hat{\boldsymbol{T}}_j = \Gamma(\hat{\varsigma})$.

We note that the cost function gradients as derived in Section I change only via the chain rule with the additional multiplication of the following factor:

$$\frac{\partial}{\partial \varsigma}\Gamma(\varsigma) = \frac{\boldsymbol{T}_{MAX} \exp^{-\varsigma}}{(1+\exp^{-\varsigma})^2}. \tag{M.3}$$

Then,

$$\frac{\partial}{\partial \varsigma_j}\,\Psi(\boldsymbol{z}, \boldsymbol{T}, \boldsymbol{f}) = \left(\frac{\partial}{\partial \boldsymbol{T}_j} L(\boldsymbol{z}, \boldsymbol{T}, \boldsymbol{f})\right)|_{\boldsymbol{T}=\Gamma(\varsigma)} \cdot \dot{\Gamma}(\varsigma_j) + \frac{\partial}{\partial \varsigma_j}\beta_\varsigma R(\varsigma).$$

The spatial resolution also changes slightly. As we are estimating and regularizing ς (L.11) will also require the additional multiplication factor (M.3) shown above.

In this paper, we first estimate T_1 as explained in Section K and then convert this via the inverse logistic function

$$\varsigma = -\ln\left(\frac{\boldsymbol{T}_{MAX}}{\boldsymbol{T}} - 1\right)$$

and then solve for ς as above. Finally, we convert this back into a T_1 map via (M.1).

BIBLIOGRAPHY

BIBLIOGRAPHY

[1] H. Erdoğan and J. A. Fessler. Ordered subsets algorithms for transmission tomography. *Phys. Med. Biol.*, 44(11):2835–51, November 1999.

[2] S. Akoka, F. Franconi, F. Seguin, and A. Le Pape. Radiofrequency map of an NMR coil by imaging. *Mag. Res. Im.*, 11(3):437–41, 1993.

[3] P. Aksit, J. A. Derbyshire, and J. L. Prince. Three-point method for fast and robust field mapping for EPI geometric distortion correction. In *Proc. IEEE Intl. Symp. Biomed. Imag.*, pages 141–4, 2007.

[4] B. Aubert-Broche, A. C. Evans, and D. L. Collins. A new improved version of the realistic digital brain phantom. *neuroimage*, 32(1):138–45, August 2006.

[5] B. Aubert-Broche, M. Griffin, G. B. Pike, A. C. Evans, and D. L. Collins. Twenty new digital brain phantoms for creation of validation image data bases. *IEEE Trans. Med. Imag.*, 25(11):1410–6, November 2006.

[6] M. A. Bernstein, M. Grgic, T. J. Brosnan, and N. J. Pelc. Reconstructions of phase contrast, phased array multicoil data. *Mag. Res. Med.*, 32(3):330–334, September 1994.

[7] K. T. Block, M. Uecker, and J. Frahm. Undersampled radial MRI with multiple coils. Iterative image reconstruction using a total variation constraint. *Mag. Res. Med.*, 57(6):1086–98, June 2007.

[8] D. Böhning and B. G. Lindsay. Monotonicity of quadratic approximation algorithms. *Ann. Inst. Stat. Math.*, 40(4):641–63, December 1988.

[9] L. Bokacheva, A. J. Huang, Q. Chen, N. Oesingmann, P. Storey, H. Rusinek, and V. S. Lee. Single breath-hold T_1 measurement using low flip angle TrueFISP. *Mag. Res. Med.*, 55(5):1186–90, May 2006.

[10] D. Brunner and K. Pruessmann. A matrix approach for mapping array transmit fields in under a minute. In *Proc. Intl. Soc. Mag. Res. Med.*, page 354, 2008.

[11] D. O. Brunner and K. P. Pruessmann. B1+ interferometry for the calibration of RF transmitter arrays. *Mag. Res. Med.*, 61(6):1480–8, June 2009.

[12] M. F. Callaghan, J. L. Ulloa, D. J. Larkman, P. Irarrazaval, and J. V. Hajnal. Measuring coil sensitivities of transmit and receive arrays with demonstration of RF shimming. In *Proc. Intl. Soc. Mag. Res. Med.*, page 2627, 2006.

[13] M. A. Castro, J. Yao, Y. Pang, C. Lee, E. Baker, J. Butman, I. E. Evangelou, and D. Thomasson. Template-based B1 inhomogeneity correction in 3T MRI brain studies. *IEEE Trans. Med. Imag.*, 29(11):1927–41, November 2010.

[14] L-C. Chang, C. G. Koay, P. J. Basser, and C. Pierpaoli. Linear least-squares method for unbiased estimation of T1 from SPGR signals. *Mag. Res. Med.*, 60(2):496–501, August 2008.

[15] N. Chen and A. M. Wyrwicz. Correction for EPI distortions using multi-echo gradient-echo imaging. *Mag. Res. Med.*, 41(6):1206–13, June 1999.

[16] H-L. M. Cheng and G. A. Wright. Rapid high-resolution T_1 mapping by variable flip angles: Accurate and precise measurements in the presence of radiofrequency field inhomogeneity. *Mag. Res. Med.*, 55(3):566–74, March 2006.

[17] P. L. Choyke, A. J. Dwyer, and M. V. Knopp. Functional tumor imaging with dynamic contrast-enhanced magnetic resonance imaging. *J. Mag. Res. Im.*, 17(5):509–20, May 2003.

[18] D. L. Collins, A. P. Zijdenbos, V. Kollokian, J. G. Sled, N. J. Kabani, C. J. Holmes, and A. C. Evans. Design and construction of a realistic digital brain phantom. *IEEE Trans. Med. Imag.*, 17(3):463–8, June 1998.

[19] R. T. Constable, R. C. Smith, and J. C. Gore. Signal-to-noise and contrast in fast spin echo (FSE) and inversion recovery FSE imaging. *J. Comp. Assisted Tomo.*, 16:41–7, 1992.

[20] C. H. Cunningham, J. M. Pauly, and K. S. Nayak. Saturated double-angle method for rapid B_1+ mapping. *Mag. Res. Med.*, 55(6):1326–33, June 2006.

[21] R. Cusack, M. Brett, and K. Osswald. An evaluation of the use of magnetic field-maps to undistort echo-planar images. *NeuroImage*, 18(1):127–42, January 2003.

[22] A. R. De Pierro. A modified expectation maximization algorithm for penalized likelihood estimation in emission tomography. *IEEE Trans. Med. Imag.*, 14(1):132–7, March 1995.

[23] R. Deichmann. Fast high-resolution T_1 mapping of the human brain. *Mag. Res. Med.*, 54(1):20–7, July 2005.

[24] S. C. L. Deoni. High-resolution T1 mapping of the brain at 3T with driven equilibrium single pulse observation of T1 with high-speed incorporation of RF field inhomogeneities (DESPOT1-HIFI). *J. Mag. Res. Im.*, 26(4):1106–11, October 2007.

[25] S. C. L. Deoni, T. M. Peters, and B. K. Rutt. Determination of optimal angles for variable nutation proton magnetic spin-lattice, T_1, and spin-spin, T_2, relaxation times measurement. *Mag. Res. Med.*, 51(1):194–9, January 2004.

[26] S. C. L. Deoni, B. K. Rutt, and T. M. Peters. Rapid combined T1 and T2 mapping using gradient recalled acquisition in the steady state. *Mag. Res. Med.*, 49(3):515–26, March 2003.

[27] J. A. Detre, J. S. Leigh, D. S. Williams, and A. P. Koretsky. Perfusion imaging. *Mag. Res. Med.*, 23(1):37–45, January 1992.

[28] N. G. Dowell and P. S. Tofts. Fast, accurate, and precise mapping of the RF field in vivo using the 180^0 signal null. *Mag. Res. Med.*, 58(3):622–30, September 2007.

[29] J. A. Fessler. Mean and variance of implicitly defined biased estimators (such as penalized maximum likelihood): Applications to tomography. *IEEE Trans. Im. Proc.*, 5(3):493–506, March 1996.

[30] J. A. Fessler. *Image reconstruction: Algorithms and analysis*. ?, 2006. Book in preparation.

[31] J. A. Fessler, N. H. Clinthorne, and W. L. Rogers. On complete data spaces for PET reconstruction algorithms. *IEEE Trans. Nuc. Sci.*, 40(4):1055–61, August 1993.

[32] J. A. Fessler, S. Lee, V. T. Olafsson, H. R. Shi, and D. C. Noll. Toeplitz-based iterative image reconstruction for MRI with correction for magnetic field inhomogeneity. *IEEE Trans. Sig. Proc.*, 53(9):3393–402, September 2005.

[33] J. A. Fessler and D. C. Noll. Iterative image reconstruction in MRI with separate magnitude and phase regularization. In *Proc. IEEE Intl. Symp. Biomed. Imag.*, pages 209–12, 2004.

[34] J. A. Fessler and W. L. Rogers. Uniform quadratic penalties cause nonuniform image resolution (and sometimes vice versa). In *Proc. IEEE Nuc. Sci. Symp. Med. Im. Conf.*, volume 4, pages 1915–9, 1994.

[35] J. A. Fessler and W. L. Rogers. Spatial resolution properties of penalized-likelihood image reconstruction methods: Space-invariant tomographs. *IEEE Trans. Im. Proc.*, 5(9):1346–58, September 1996.

[36] J. A. Fessler and B. P. Sutton. Nonuniform fast Fourier transforms using min-max interpolation. *IEEE Trans. Sig. Proc.*, 51(2):560–74, February 2003.

[37] J. A. Fessler, D. Yeo, and D. C. Noll. Regularized fieldmap estimation in MRI. In *Proc. IEEE Intl. Symp. Biomed. Imag.*, pages 706–9, 2006.

[38] L. Fleysher, R. Fleysher, S. Liu, W. Zaaraoui, and O. Gonen. Optimizing the precision-per-unit-time of quantitative MR metrics: Examples for T_1, T_2, and DTI. *Mag. Res. Med.*, 57(2):380–7, February 2007.

[39] R. Fleysher, L. Fleysher, M. Inglese, and D. Sodickson. TROMBONE: T1-relaxation-oblivious mapping of transmit radio-frequency field (B1) for MRI at high magnetic fields. *Mag. Res. Med.*, 2011.

[40] A. Funai and J. A. Fessler. Cramer Rao bound analysis of joint B1/T1 mapping methods in MRI. In *Proc. IEEE Intl. Symp. Biomed. Imag.*, pages 712–5, 2010.

[41] A. Funai, J. A. Fessler, W. Grissom, and D. C. Noll. Regularized B1+ map estimation in MRI. In *Proc. IEEE Intl. Symp. Biomed. Imag.*, pages 616–9, 2007.

[42] A. K. Funai, J. A. Fessler, W. Grissom, and D. C. Noll. Regularized B1+ map estimation with slice selection effects. In *Proc. Intl. Soc. Mag. Res. Med.*, page 3145, 2008.

[43] A. K. Funai, J. A. Fessler, and D. C. Noll. Estimating K transmit B1+ maps from K+1 scans for parallel transmit MRI. In *Proc. Intl. Soc. Mag. Res. Med.*, page 2609, 2009.

[44] A. K. Funai, J. A. Fessler, D. T. B. Yeo, V. T. Olafsson, and D. C. Noll. Regularized field map estimation in MRI. *IEEE Trans. Med. Imag.*, 27(10):1484–94, October 2008.

[45] C. Ganter. Off-resonance effects in the transient response of SSFP sequences. *Mag. Res. Med.*, 52(2):368–75, August 2004.

[46] S. J. Garnier, G. L. Bilbro, J. W. Gault, and W. E. Snyder. Magnetic resonance image restoration. *J. Math. Im. Vision*, 5(1):7–19, February 1995.

[47] G. Glover. Multipoint Dixon technique for water and fat proton and susceptibility imaging. *J. Mag. Res. Im.*, 1(5):521–30, September 1991.

[48] G. Golub and V. Pereyra. Separable nonlinear least squares: the variable projection method and its applications. *Inverse Prob.*, 19(2):R1–26, April 2003.

[49] M. I. Grivich and D. P. Jackson. The magnetic field of current-carrying polygons: An application of vector field rotations. *Amer. J. Phys.*, 68(5):469–74, May 2000.

[50] T. Guo, S. C. L. Deoni, K. W. Finnis, A. G. Parrent, and T. M. Peters. Application of T1 and T2 maps for stereotactic deep-brain neurosurgery planning @u doi 10.1109/IEMBS.2005.1615707. In *Proc. Int'l. Conf. IEEE Engr. in Med. and Biol. Soc.*, pages 5416–9, 2005.

[51] E. M. Haacke, R. W. Brown, M. R. Thompson, and R. Venkatesan. *Magnetic resonance imaging: Physical principles and sequence design.* Wiley, New York, 1999.

[52] T. B. Harshbarger and D. B. Twieg. Iterative reconstruction of single-shot spiral MRI with off-resonance. *IEEE Trans. Med. Imag.*, 18(3):196–205, March 1999.

[53] G. Helms, H. Dathe, and P. Dechent. Quantitative FLASH MRI at 3T using a rational approximation of the Ernst equation. *Mag. Res. Med.*, 59(3):667–72, March 2008.

[54] D. Hernando, J. P. Haldar, B. P. Sutton, J. Ma, P. Kellman, and Z-P. Liang. Joint estimation of water/fat images and field inhomogeneity map. *Mag. Res. Med.*, 59(3):571–80, March 2008.

[55] D. M. Higgins, J. P. Ridgway, A. Radjenovic, U. Mohan Sivananthan, and M. A. Smith. T1 measurement using a short acquisition period for quantitative cardiac applications. *Med. Phys.*, 32(6):1738–46, June 2005.

[56] D. I. Hoult. Sensitivity and power deposition in a high-field imaging experiment. *J. Mag. Res. Im.*, 12(1):46–67, July 2000.

[57] J. Hsu, G. Zaharchuk, and G. Glover. Fast simultaneous measurement of the RF flip angle and the longitudinal relaxation time for quantitative MRI. In *Proc. Intl. Soc. Mag. Res. Med.*, page 360, 2008.

[58] J-J. Hsu, G. Zaharchuk, and G. H. Glover. Rapid methods for concurrent measurement of the RF-pulse flip angle and the longitudinal relaxation time. *Mag. Res. Med.*, 61(6):1319–25, June 2009.

[59] L-Y. Hsu, K. L. Rhoads, J. E. Holly, P. Kellman, A. H. Aletras, and A. E. Arai. Quantitative myocardial perfusion analysis with a dual-bolus contrast-enhanced first-pass MRI technique in humans. *J. Mag. Res. Im.*, 23(3):315–22, March 2006.

[60] P. J. Huber. *Robust statistics*. Wiley, New York, 1981.

[61] P. Irarrazabal, C. H. Meyer, D. G. Nishimura, and A. Macovski. Inhomogeneity correction using an estimated linear field map. *Mag. Res. Med.*, 35(2):278–82, February 1996.

[62] M. W. Jacobson and J. A. Fessler. Properties of MM algorithms on convex feasible sets: extended version. Technical Report 353, Comm. and Sign. Proc. Lab., Dept. of EECS, Univ. of Michigan, Ann Arbor, MI, 48109-2122, November 2004.

[63] M. W. Jacobson and J. A. Fessler. An expanded theoretical treatment of iteration-dependent majorize-minimize algorithms. *IEEE Trans. Im. Proc.*, 16(10):2411–22, October 2007.

[64] P. M. Jakob, C. M. Hillenbrand, T. Wang, G. Schultz, D. Hahn, and A. Haase. Rapid quantitative lung ^{1}H T1 mapping. *J. Mag. Res. Im.*, 14(6):795–9, December 2001.

[65] P. Jezzard and R. S. Balaban. Correction for geometric distortion in echo planar images from B_0 field variations. *Mag. Res. Med.*, 34(1):65–73, July 1995.

[66] P. Jezzard and S. Clare. Sources of distortion in functional MRI data. *Hum. Brain Map.*, 8(2-3):80–5, 1999.

[67] U. Katscher, P. Brnert, C. Leussler, and J. S. van den Brink. Transmit SENSE. *Mag. Res. Med.*, 49(1):144–50, January 2003.

[68] A. B. Kerr, C. H. Cunningham, J. M. Pauly, R. O. Giaquinto, R. D. Watkins, and Y. Zhu. Self-calibrated transmit SENSE. In *Proc. Intl. Soc. Mag. Res. Med.*, page 2561, 2006.

[69] Y. Kim, J. A. Fessler, and D. C. Noll. Smoothing effect of sensitivity map on fMRI data using a novel regularized self-calibrated estimation method. In *Proc. Intl. Soc. Mag. Res. Med.*, page 1267, 2008.

[70] R. K-S. Kwan, A. C. Evans, and G. B. Pike. MRI simulation-based evaluation of image-processing and classification methods. *IEEE Trans. Med. Imag.*, 18(11):1085–97, November 1999.

[71] K. Lange. *Numerical analysis for statisticians*. Springer-Verlag, New York, 1999.

[72] K. Lange, D. R. Hunter, and I. Yang. Optimization transfer using surrogate objective functions. *J. Computational and Graphical Stat.*, 9(1):1–20, March 2000.

[73] H. B. W. Larsson, J. Frederiksen, J. Petersen, A. Nordenbo, I. Zeeberg, O. Henriksen, and J. Olesen. Assessment of demyelination, edema, and gliosis by in vivo determination of T1 and T2 in the brain of patients with acute attack of multiple sclerosis. *Mag. Res. Med.*, 11(3):337–48, September 1989.

[74] S. Lee, J. A. Fessler, and D. Noll. A simultaneous estimation of field inhomogeneity and R2* maps using extended rosette trajectory. In *Proc. Intl. Soc. Mag. Res. Med.*, page 2327, 2002.

[75] S. Lee, J. A. Fessler, and D. C. Noll. A dynamic R2*-and-field-map-corrected imaging for single shot rosette trajectories. In *Proc. Intl. Soc. Mag. Res. Med.*, page 2515, 2006.

[76] J. M. N. Leitāo and Mário A T Figueiredo. Absolute phase image reconstruction: a stochastic nonlinear filtering approach. *IEEE Trans. Im. Proc.*, 7(6):868–82, June 1998.

[77] W. Li. A very fine title that i need to find! In *Proc. Intl. Soc. Mag. Res. Med.*, 2005.

[78] Z-P. Liang and P. C. Lauterber. *Principles of magnetic resonance imaging*. IEEE, New York, 2000.

[79] D. C. Look and D. R. Locker. Time saving in measurement of NMR and EPR relaxation times. *Rev Sci Instrum*, 41(2):250–1, February 1970.

[80] K. Lu, T. T. Liu, and M. Bydder. Optimal phase difference reconstruction: comparison of two methods. *Mag. Res. Im.*, 26(1):142–5, January 2007.

[81] A. Lutti, C. Hutton, J. Finsterbusch, G. Helms, and N. Weiskopf. Optimization and validation of methods for mapping of the radiofrequency transmit field at 3T. *Mag. Res. Med.*, 64(1):229–38, July 2010.

[82] C. Ma, D. Xu, K. F. King, and Z. P. Liang. Joint design of spoke trajectories and RF pulses for parallel excitation. *Mag. Res. Med.*, 65(4):973–85, April 2011.

[83] A. Macovski. Noise in MRI. *Mag. Res. Med.*, 36(3):494–7, September 1996.

[84] R. Materne, A. M. Smith, F. Peeters, J. P. Dehoux, A. Keyeux, Y. Horsmans, and B. E. V. Beers. Assessment of hepatic perfusion parameters with dynamic MRI. *Mag. Res. Med.*, 47(1):135–42, January 2002.

[85] E. R. McVeigh, R. M. Henkelman, and M. J. Bronskill. Noise and filtration in magnetic resonance imaging. *Med. Phys.*, 12(5):586–91, September 1985.

[86] D. R. Messroghli, A. Radjenovic, S. Kozerke, D. M. Higgins, M. U. Sivananthan, and J. P. Ridgway. Modified Look-Locker inversion recovery (MOLLI) for high-resolution T_1 mapping of the heart. *Mag. Res. Med.*, 52(1):141–6, July 2004.

[87] K. S. Nayak and D. G. Nishimura. Automatic field map generation and off-resonance correction for projection reconstruction imaging. *Mag. Res. Med.*, 43(1):151–4, January 2000.

[88] K. S. Nayak, C-M. Tsai, C. H. Meyer, and D. G. Nishimura. Efficient off-resonance correction for spiral imaging. *Mag. Res. Med.*, 45(3):521–4, March 2001.

[89] K. Nehrke. On the steady-state properties of actual flip angle imaging (AFI). *Mag. Res. Med.*, 61(1):84–92, January 2009.

[90] K. Nehrke and P. Bornert. Improved B1-mapping for multi RF transmit systems. In *Proc. Intl. Soc. Mag. Res. Med.*, page 353, 2008.

[91] K. Nehrke and P. Bornert. Eigenmode analysis of transmit coil array for tailored B1 mapping. *Mag. Res. Med.*, 63(3):754–64, March 2010.

[92] D. G. Nishimura. Principles of magnetic resonance imaging, 1996. Unpublished textbook.

[93] D. C. Noll, J. A. Fessler, and B. P. Sutton. Conjugate phase MRI reconstruction with spatially variant sample density correction. *IEEE Trans. Med. Imag.*, 24(3):325–36, March 2005.

[94] D. C. Noll, C. H. Meyer, J. M. Pauly, D. G. Nishimura, and A. Macovski. A homogeneity correction method for magnetic resonance imaging with time-varying gradients. *IEEE Trans. Med. Imag.*, 10(4):629–37, December 1991.

[95] R. J. Ogg and P. B. Kingsley. Optimized precision of inversion-recovery T_1 measurements for constrained scan time. *Mag. Res. Med.*, 51(3):625–30, March 2004.

[96] V. Olafsson, J. A. Fessler, and D. C. Noll. Dynamic update of R2* and field map in fMRI. In *Proc. Intl. Soc. Mag. Res. Med.*, page 45, 2004.

[97] G. J. M. Parker, G. J. Barker, and P. S. Tofts. Accurate multislice gradient echo T1 measurement in the presence of non-ideal RF pulse shape and RF field nonuniformity. *Mag. Res. Med.*, 45(5):838–45, May 2001.

[98] J. Pauly, D. Nishimura, and A. Macovski. A k-space analysis of small-tip-angle excitation. *J. Mag. Res.*, 81(1):43–56, January 1989.

[99] C. Preibisch and R. Deichmann. Influence of RF spoiling on the stability and accuracy of T1 mapping based on spoiled FLASH with varying flip angles. *Mag. Res. Med.*, 61(1):125–35, January 2009.

[100] A. N. Priest, E. D. Vita, D. L. Thomas, and R. J. Ordidge. EPI distortion correction from a simultaneously acquired distortion map using TRAIL. *J. Mag. Res. Im.*, 23(4):597–603, April 2006.

[101] P. J. Reber, E. C. Wong, R. B. Buxton, and L. R. Frank. Correction of off resonance-related distortion in echo-planar imaging using EPI-based field maps. *Mag. Res. Med.*, 39(2):328–30, February 1998.

[102] S. Saekho, F. E. Boada, D. C. Noll, and V. A. Stenger. Small tip angle three-dimensional tailored radiofrequency slab-select pulse for reduced B_1 inhomogeneity at 3 T. *Mag. Res. Med.*, 53(2):479–84, February 2005.

[103] K. Scheffler and Jürgen Hennig. T1 quantification with inversion recovery TrueFISP. *Mag. Res. Med.*, 45(4):720–3, April 2001.

[104] J. F. Schenck. The role of magnetic susceptibility in magnetic resonance imaging: MRI magnetic compatibility of the first and second kinds. *Med. Phys.*, 23(6):815–50, June 1996.

[105] P. Schmitt, M. A. Griswold, P. M. Jakob, M. Kotas, V. Gulani, M. Flentje, and A. Haase. Inversion recovery TrueFISP: Quantification of T_1, T_2, and spin density. *Mag. Res. Med.*, 51(4):661–7, April 2004.

[106] E. Schneider and G. Glover. Rapid in vivo proton shimming. *Mag. Res. Med.*, 18(2):335–47, April 1991.

[107] K. Sekihara, S. Matsui, and H. Kohno. NMR imaging for magnets with large nonuniformities. *IEEE Trans. Med. Imag.*, 4(4):193–9, December 1985.

[108] K. Setsompop, L. L. Wald, V. Alagappan, B. A. Gagoski, and E. Adalsteinsson. Magnitude least squares optimization for parallel radio frequency excitation design demonstrated at 7 Tesla with eight channels. *Mag. Res. Med.*, 59(4):908–15, April 2008.

[109] J. Sheng and L. Ying. A variable projection approach to parallel magnetic resonance imaging. In *Proc. IEEE Intl. Symp. Biomed. Imag.*, pages 1027–30, 2008.

[110] R. Stollberger and P. Wach. Imaging of the active B_1 field in vivo. *Mag. Res. Med.*, 35(2):246–51, February 1996.

[111] K. Sung and K. S. Nayak. B1+ compensation in 3T cardiac imaging using short 2DRF pulses. *Mag. Res. Med.*, 59(3):441–6, March 2008.

[112] K. Sung and K. S. Nayak. Measurement and characterization of RF nonuniformity over the heart at 3T using body coil transmission. *J. Mag. Res. Im.*, 27(3):643–48, March 2008.

[113] B. P. Sutton, J. A. Fessler, and D. Noll. Iterative MR image reconstruction using sensitivity and inhomogeneity field maps. In *Proc. Intl. Soc. Mag. Res. Med.*, page 771, 2001.

[114] B. P. Sutton, D. C. Noll, and J. A. Fessler. Fast, iterative image reconstruction for MRI in the presence of field inhomogeneities. *IEEE Trans. Med. Imag.*, 22(2):178–88, February 2003.

[115] B. P. Sutton, D. C. Noll, and J. A. Fessler. Dynamic field map estimation using a spiral-in / spiral-out acquisition. *Mag. Res. Med.*, 51(6):1194–204, June 2004.

[116] R. Treier, A. Steingoetter, M. Fried, W. Schwizer, and P. Boesiger. Optimized and combined T_1 and B_1 mapping technique for fast and accurate T_1 quantification in contrast-enhanced abdominal MRI. *Mag. Res. Med.*, 57(3):568–76, March 2007.

[117] T-K. Truong, D. W. Chakeres, and P. Schmalbrock. Effects of B_0 and B_1 inhomogeneity in ultra-high field MRI. In *Proc. Intl. Soc. Mag. Res. Med.*, page 2170, 2004.

[118] D. B. Twieg. Parsing local signal evolution directly from a single-shot MRI signal: A new approach for fMRI. *Mag. Res. Med.*, 50(5):1043–52, November 2003.

[119] M. Unser, A. Aldroubi, and M. Eden. Recursive regularization filters: design, properties, and applications. *IEEE Trans. Patt. Anal. Mach. Int.*, 13(3):272–7, March 1991.

[120] J. T. Vaughan, M. Garwood, C. M. Collins, W. Liu, L. DelaBarre, G. Adriany, P. Andersen, H. Merkle, R. Goebel, M. B. Smith, and K. Ugurbil. 7T vs. 4T: RF power, homogeneity, and signal-to-noise comparison in head images. *Mag. Res. Med.*, 46(1):24–30, July 2001.

[121] R. Venkatesan, W. Lin, and E. Mark Haacke. Accurate determination of spin-density and T_1 in the presence of RF-field inhomogeneities and flip-angle miscalibration. *Mag. Res. Med.*, 40(4):592–602, October 1998.

[122] T. Voigt, K. Nehrke, O. Doessel, and U. Katscher. T1 corrected B1 mapping using multi-TR gradient echo sequences. *Mag. Res. Med.*, 2010.

[123] J. Vymazal, A. Righini, R. A. Brooks, M. Canesi, C. Mariani, M. Leonardi, and G. Pezzoli. T1 and T2 in the brain of healthy subjects, patients with Parkinson disease, and patients with multiple system atrophy: relation to iron content. *Radiology*, 211(2):489–95, May 1999.

[124] D. Wang, L. Shi, Y-X. J. Wang, J. Yuan, D. K. W. Yeung, A. D. King, A. T. Ahuja, and P. A. Heng. Concatenated and parallel optimization for the estimation of T1 map in FLASH MRI with multiple flip angles. *Mag. Res. Med.*, 63(5):1431–6, May 2010.

[125] H. Z. Wang, S. J. Riederer, and J. N. Lee. Optimizing the precision in T1 relaxation estimation using limited flip angles. *Mag. Res. Med.*, 5(5):399–416, November 1987.

[126] J. Wang, W. Mao, M. Qiu, M. B. Smith, and R. Todd Constable. Factors influencing flip angle mapping in MRI: RF pulse shape, slice-select gradients, off-resonance excitation, and B0 inhomogeneities. *Mag. Res. Med.*, 56(2):463–68, August 2006.

[127] J. Wang, M. Qiu, and R. T. Constable. In vivo method for correcting transmit/receive nonuniformities with phased array coils. *Mag. Res. Med.*, 53(3):666–74, March 2005.

[128] J. Wang, M. Qiu, Q. X. Yang, M. B. Smith, and R. T. Constable. Measurement and correction of transmitter and receiver induced nonuniformities in vivo. *Mag. Res. Med.*, 53(2):408–17, February 2005.

[129] Y. Wang. Description of parallel imaging in MRI using multiple coils. *Mag. Res. Med.*, 44(3):495–9, September 2000.

[130] J. B. M. Warntjes, O. Dahlqvist, and P. Lundberg. Novel method for rapid, simultaneous T_1, $T^*{}_2$, and proton density quantification. *Mag. Res. Med.*, 57(3):528–537, March 2007.

[131] P. Williamson, D. Pelz, H. Merskey, S. Morrison, S. Karlik, D. Drost, T. Carr, and P. Conlon. Frontal, temporal, and striatal proton relaxation times in schizophrenic patients and normal comparison subjects. *Am J Psychiatry*, 149:549–51, 1992.

[132] C. Windischberger, S. Robinson, A. Rauscher, M. Barth, and E. Moser. Robust field map generation using a triple-echo acquisition. *J. Mag. Res. Im.*, 20(4):730–4, October 2004.

[133] R. C. Wright, S. J. Riederer, J. N. Lee, F. Farzaneh, and J. B. D. Castro. High-speed techniques for estimating T1, T2, and density images. *IEEE Trans. Med. Imag.*, 6(2):165–8, June 1987.

[134] D. Xu, K. F. King, Y. Zhu, G. C. McKinnon, and Z-P. Liang. A noniterative method to design large-tip-angle multidimensional spatially-selective radio frequency pulses for parallel transmission. *Mag. Res. Med.*, 58(2):326–34, August 2007.

[135] D. Xu, K. F. King, Y. Zhu, G. C. McKinnon, and Z-P. Liang. Designing multichannel, multidimensional, arbitrary flip angle RF pulses using an optimal control approach. *Mag. Res. Med.*, 59(3):547–60, March 2008.

[136] V. L. Yarnykh. Actual flip-angle imaging in the pulsed steady state: A method for rapid three-dimensional mapping of the transmitted radiofrequency field. *Mag. Res. Med.*, 57(1):192–200, January 2007.

[137] V. L. Yarnykh. Optimal radiofrequency and gradient spoiling for improved accuracy of T1 and B1 measurements using fast steady-state techniques. *Mag. Res. Med.*, 63(6):1610–26, June 2010.

[138] L. Ying, J. Sheng, and B. Liu. Joint estimation of image and coil sensitivities in parallel MRI. In *Proc. IEEE Intl. Symp. Biomed. Imag.*, pages 17–20, 2006.

[139] C. Yip, J. A. Fessler, and D. C. Noll. Iterative RF pulse design for multidimensional, small-tip-angle selective excitation. *Mag. Res. Med.*, 54(4):908–17, October 2005.

[140] C. Yip, J. A. Fessler, and D. C. Noll. Advanced three-dimensional tailored RF pulse for signal loss recovery in T2*-weighted fMRI. In *Proc. Intl. Soc. Mag. Res. Med.*, page 3001, 2006.

[141] D. F. Yu and J. A. Fessler. Edge-preserving tomographic reconstruction with nonlocal regularization. *IEEE Trans. Med. Imag.*, 21(2):159–73, February 2002.

[142] A. C. Zelinski, L. L. Wald, K. Setsompop, V. Alagappan, B. A. Gagoski, V. K. Goyal, and E. Adalsteinsson. Fast slice-selective radio-frequency excitation pulses for mitigating B+1 inhomogeneity in the human brain at 7 Tesla. *Mag. Res. Med.*, 59(6):1355–64, June 2008.

[143] A. C. Zelinski, L. L. Wald, K. Setsompop, V. K. Goyal, and E. Adalsteinsson. Sparsity-enforced slice-selective MRI RF excitation pulse design. *IEEE Trans. Med. Imag.*, 27(9):1213–29, September 2008.

[144] H. Zhang, S. M. Shea, V. Park, D. Li, P. K. Woodard, R. J. Gropler, and J. Zheng. Accurate myocardial T_1 measurements: Toward quantification of myocardial blood flow with arterial spin labeling. *Mag. Res. Med.*, 53(5):1135–42, May 2005.

[145] Z. Zhang, C-Y. Yip, W. Grissom, D. C. Noll, F. E. Boada, and V. A. Stenger. Reduction of transmitter B_1 inhomogeneity with transmit SENSE slice-select pulses. *Mag. Res. Med.*, 57(5):842–7, May 2007.

[146] K. Zhong and O. Speck. Simultaneous fast quantitation of B1 and T1 maps at 7T using the TESSA principle. In *Proc. Intl. Soc. Mag. Res. Med.*, page 359, 2008.

[147] D. C. Zhu and R. D. Penn. Full-brain T_1 mapping through inversion recovery fast spin echo imaging with time-efficient slice ordering. *Mag. Res. Med.*, 54(3):725–31, September 2005.

[148] Y. Zhu. Parallel excitation with an array of transmit coils. *Mag. Res. Med.*, 51(4):775–84, April 2004.

ABSTRACT

Regularized Estimation of Main and RF Field Inhomogeneity and Longitudinal Relaxation Rate in Magnetic Resonance Imaging

by

Amanda K. Funai

Chair: Jeffrey A. Fessler

In designing pulses and algorithms for magnetic resonance imaging, several simplifications to the Bloch equation are used. However, as magnetic resonance (MR) imaging requires higher temporal resolution and faster pulses are used, simplifications such as uniform main field (B_0) strength and uniform radio-frequency (RF) transmit coil field (B_1^+) strength no longer apply. Ignoring these non-uniformities can cause significant distortions. Accurate maps of the main and RF transmit coil field inhomogeneity are required for accurate pulse design and imaging. Standard estimation methods yield noisy maps, particularly in image regions having low spin density, and ignore other important factors, such as slice selection effects in B_1 mapping and T_2 effects in B_0 mapping. This thesis uses more accurate signal models for the MR scans to derive iterative regularized estimators that show improvements over the conventional unregularized methods through Cramér-Rao Bound analysis, simulations, and real MR data.

In fast MR imaging with long readout times, field inhomogeneity causes image distortion and blurring. This thesis first describes regularized methods for estimation of the off-resonance frequency at each voxel from two or more MR scans having different echo times, using algorithms that decrease monotonically a regularized least-squares cost function.

A second challenge is that RF transmit coils produce non-uniform field strengths, so an excitation pulse will produce tip angles that vary substantially over the field of view. This thesis secondly describes a regularized method for B_1^+ map estimation for each coil and for two or more tip angles. Using these scans and known slice profile, the iterative algorithm estimates both the magnitude and phase of each coil's B_1^+ map.

To circumvent the challenge in conventional B_1^+ mapping sequences of an long repetition time, this thesis thirdly describes a regularized method for joint B_1^+ and T_1 map estimation using a regularized method based on a penalized-likelihood cost function using the steady-state incoherent (SSI) imaging sequence with several scans with varying tip angles or repetition times.